Annular Mode-Like Responses to External Forcings in a Simple Atmospheric General Circulation Model

by

Michael John Ring

S.B., Physics (2001), MIT
S.B., Earth, Atmospheric, and Planetary Sciences (2001), MIT

Submitted to the Department of Earth, Atmospheric, and Planetary Sciences
in partial fulfillment of the requirements for the degree of

Doctor of Philosophy

at the

MASSACHUSETTS INSTITUTE OF TECHNOLOGY

February 2008

© Massachusetts Institute of Technology 2008. All rights reserved.

Author . . . .
Department of Earth, Atmospheric, and Planetary Sciences
December 11, 2007

Certified by. . . . .
R. Alan Plumb
Professor of Meteorology
Thesis Supervisor

Accepted by . . . .
Maria T. Zuber
E.A. Griswold Professor of Geophysics
Head, Department of Earth, Atmospheric and Planetary Sciences

MASSACHUSETTS INSTITUTE
OF TECHNOLOGY
APR 2 3 2008
ARCHIVES

Annular Mode-Like Responses to External Forcings in a Simple Atmospheric General Circulation Model

by

Michael John Ring

S.B., Physics (2001), MIT

S.B., Earth, Atmospheric, and Planetary Sciences (2001), MIT

Submitted to the Department of Earth, Atmospheric, and Planetary Sciences
on December 11, 2007, in partial fulfillment of the
requirements for the degree of
Doctor of Philosophy

Abstract

In this thesis, I investigate the response of a simple atmospheric general circulation model to applied forcings to learn whether the annular mode patterns are a preferred model response to the forcings. The thesis is inspired by the appearance of annular mode patterns in Earth's atmosphere in response to a number of forcings.

Climatologies of the model under the influence of applied torques or perturbations to the reference temperature profile are compiled and compared to a control run with neither type of forcing. In most cases the differences in climatologies are annular mode-like, suggesting the patterns are the preferred response of the model to the forcings. The strength of the response typically increases for either an increase in the strength of the forcing, or an increase in the strength of the projection of the forcing on the model's annular mode patterns. Trials with a response which was not annular mode-like usually featured a poor projection of the forcing on the annular modes, or substantial interference with tropical dynamics.

A zonally symmetric version of the model is also used to test the direct response of the model to the forcing versus the response caused by changes in eddy feedback processes. The direct forcing alone is found to be insufficient to produce either the correct strength or shape of the annular mode patterns. Instead the changes in eddy fluxes must be included to produce the correct shape and amplitude of the anomalies.

Thesis Supervisor: R. Alan Plumb
Title: Professor of Meteorology

Acknowledgments

I cannot possibly thank my family, and particularly my parents, enough for all they have done for me. My parents always stressed to me the importance of education. From preschool to graduate school, my parents have sacrificed both time and treasure for me, and I am forever grateful to their commitment and belief in me. I also wish to thank especially my father for proofreading this manuscript.

I also especially wish to thank my thesis adviser, Alan Plumb, for his valuable counsel and insight over the past six years. He has always been enthusiastic and supportive of my work, keeping me focused and never growing frustrated at me for my wrong turns. Alan has always been willing to find time for me in his own busy schedule, and I cannot imagine completing this work without his support.

I also wish to thank a group of my fellow graduate students and one research scientist for their support as well. Greg Lawson, Rob Korty, Nikki Prive, and Jeff Scott have been wonderful mentors and friends over the past six years, always willing to answer questions, give advice, or provide a much-needed Friday afternoon of bridge after a tough week at work.

This thesis is based on work supported by the National Science Foundation through grant ATM-0314094. I also acknowledge the support of MIT's Presidential Fellows program.

Contents

1 Introduction **27**

1.1 Historical Overview and Observations 27

1.1.1 The North Atlantic Oscillation 27

1.1.2 The Southern Annular Mode 28

1.1.3 The Arctic Oscillation 33

1.2 Annular Modes and an Eddy Feedback 37

1.3 Links to Other Climate Problems 38

1.4 Motivation 43

2 Model Setup **45**

2.1 Introduction 45

2.2 Resolution 46

2.3 Radiation 48

2.4 Friction and Hyperdiffusion 49

2.5 A Note on Zonal Symmetry 52

2.6 Summary 53

3 Climatology of the Control Run **55**

3.1 Introduction 55

3.2 Zonal- and Time-Mean Climatological Fields 55

3.3 Zonal Variations in the Unforced Run 60

3.4 Variability of the Unforced Run 62

3.5 Summary 73

4 Mechanically Forced Trials **75**
4.1 Introduction 75
4.2 Nature of the Applied Forcing 75
4.3 Climatology of an Example Run 77
4.4 Differences in Climatologies for Variation of Forcing Location 86
4.5 Differences in Climatologies of Barotropically Forced Trials 101
4.6 Differences in Climatologies of Trials Using Different Forcing Magnitudes 107
4.7 Summary 111

5 Thermally Forced Trials **113**
5.1 Introduction 113
5.2 Trials with Hemisphere-Scale Thermal Forcing 114
5.3 Trials With Forcing Confined Poleward of 45° 121
5.4 Summary 134

6 Zonally Symmetric Trials **137**
6.1 Introduction 137
6.2 Setup 138
6.3 Control Climatology of the Zonally Symmetric Run 139
6.4 Results of the Zonally Symmetric Model for Mechanically Forced Trials 143
6.5 Results of the Zonally Symmetric Model for Thermally Forced Trials 153
6.6 Summary 158

7 Comparison of Forcing and Response Strengths **165**
7.1 Introduction 165
7.2 Fluctuation-Dissipation Theory 166
7.3 Simple Comparisons of Forcing and Response Strength 167
7.4 Mathematical Formulation of the Effective Forcing 171
7.5 Principal Oscillation Pattern Analysis 181
7.6 Discussion 194

8 Conclusions 199
8.1 Introduction 199
8.2 Summary 199
8.3 Suggestions for Future Work 202
8.4 Implications for Earth's Atmosphere 204

A Reference Temperature Profile 209

B Mathematical Formulation of the POP Analysis 211

List of Figures

1-1 Patterns of zonal wind and geopotential height variability associated with the annular modes. Reproduced from Thompson and Wallace (2000). 30

1-2 Patterns of zonal wind variability associated with SAM. Reproduced from Lorenz and Hartmann (2001). 32

1-3 Patterns of zonal wind variability associated with AO during winter. Reproduced from Lorenz and Hartmann (2003). 35

1-4 Wintertime AO trends in the surface air temperature, precipitation, and sea-level pressure fields. Reproduced from Thompson et al. (2000). 40

1-5 Composites of 18 events featuring a weak polar vortex and 30 events featuring a strong polar vortex, showing the downward propagation of AO anomalies. Contour interval is 0.25 of nondimensional AO index for each color; values less than 0.25 are not shaded. White contours feature contour interval of 0.5. From Baldwin, M. P. and T. J. Dunkerton, 2001: "Stratospheric harbingers of anomalous weather regimes." *Science*, **294**, 581-584. Reprinted with permission from AAAS. 42

2-1 Zonal- and time-mean zonal wind for the T42 test run. Contour interval is 5 $m\ s^{-1}$; zero contour is dashed. 46

2-2 First and second EOFs of zonal-mean zonal wind anomalies in the T42 test run. Solid lines are contours of the leading EOF; dashed lines are contours of the second EOF. Contours are in units of 1 $m\ s^{-1}$; vertical lines indicate positions of time-mean jets. 47

2-3 Reference temperature for the unforced model run. Contour interval is 10 K. 49

2-4 Zonal- and time-mean zonal wind for the test run using maximum mechanical damping rate of 1 day^{-1}. Contour interval is 5 $m\ s^{-1}$; zero contour is dashed. 50

2-5 First and second EOFs of zonal-mean zonal wind anomalies in the test run using maximum mechanical damping rate of 1 day^{-1}. Solid lines are contours of the leading EOF; dashed lines are contours of the second EOF. Contours are in units of 1 $m\ s^{-1}$. 51

3-1 Zonal- and time-mean zonal wind for the unforced model run. Contour interval is 5 $m\ s^{-1}$; zero contour is dashed. 56

3-2 Zonal-mean zonal wind from a selected day of model climatology, showing the double-jet structure. Contouring as in Figure 3-1. 57

3-3 Climatological streamfunction for the unforced model run. Contour interval is $3 \times 10^{10} kg\ s^{-1}$; zero contour is omitted. 57

3-4 Climatological temperature for the unforced model run. Contour interval is 10 K. 58

3-5 Time-mean E-P fluxes and divergence from control run with vectors plotted according to the scaling in Edmon et al. (1980). Divergence is contoured; interval is 4 $m\ s^{-1}\ day^{-1}$ acceleration of zonal wind until 20 $m\ s^{-1}\ day^{-1}$ and 20 $m\ s^{-1}\ day^{-1}$ thereafter. Arrows represent E-P flux; sample arrow at bottom left represents $5 \times 10^{20}\ m^3\ Pa$ of upward flux; an equivalent length in the horizontal represents $6.47 \times 10^{15}\ m^3$ of meridional flux. 59

3-6 Time-mean barotropic E-P flux divergence. Contour interval is 1 $m\ s^{-1}\ day^{-1}$ acceleration of zonal wind. Solid lines are positions of time-mean jets. 60

3-7 Time-mean zonal wind at 250 hPa. Contour interval is 5 $m\ s^{-1}$. . . . 61

3-8 As in Figure 3-7, but for the time-mean temperature at 750 hPa. Contour interval is 5 K. 61

3-9 Fourier coefficients for the zonal wind at SH jet center (37° S and 250 hPa). The coefficients are computed daily, and the mean of their absolute value for each wavenumber is plotted. 62

3-10 (Top) First EOF of surface pressure anomalies in the NH. Contour interval is 50 Pa; negative contours are dashed. (Bottom) As in the top panel, but for the SH. 63

3-11 First and second EOFs of zonal-mean zonal wind anomalies. Solid lines are contours of the leading EOF; dashed lines are contours of the second EOF. Contours are in units of 1 $m\ s^{-1}$; vertical lines indicate positions of time-mean jets. 64

3-12 As in Figure 3-11, but for EOFs 3 and 4 of the zonal-mean zonal wind anomalies. Solid lines are contours of EOF3; dashed lines are contours of EOF4. Contours are in units of 0.5 $m\ s^{-1}$; vertical lines indicate positions of time-mean jets. 65

3-13 Principal component timeseries associated with first four EOFs. Magnitude is non-dimensional. 66

3-14 Autocorrelation of first four principal component timeseries. 66

3-15 Histograms indicating number of days for which the value of PC1 (top) and PC2 (bottom) fell between the indicated values. 67

3-16 (Left) Histogram of the daily PC value of NAM at 500 hPa, as compiled by Baldwin. (Right) Histogram of monthly mean value of SAM at surface, as compiled by NCDC. Figure courtesy of R. A. Plumb. . . 68

3-17 Leading spatial patterns of E-P flux divergence anomalies derived from SVD analysis with the zonal wind anomalies. Solid lines indicate the leading pattern; dashed lines indicate the second pattern. Contour interval is 0.5 $m\ s^{-1}\ day^{-1}$ acceleration of zonal wind until 5 $m\ s^{-1}\ day^{-1}$ and 5 $m\ s^{-1}\ day^{-1}$ thereafter. 69

3-18 Anomalous E-P flux divergence found in SVD patterns 1 and 2 added to the climatological E-P flux divergence. Contour interval 4 $m\ s^{-1}\ day^{-1}$ acceleration of zonal wind until 20 $m\ s^{-1}\ day^{-1}$ and 20 $m\ s^{-1}\ day^{-1}$ thereafter. 70

3-19 As in Figure 3-18, but for the patterns found in SVD patterns 1 and 2 subtracted from the climatological E-P flux divergence. Contour interval 4 $m\ s^{-1}\ day^{-1}$ acceleration of zonal wind until 20 $m\ s^{-1}\ day^{-1}$ and 20 $m\ s^{-1}\ day^{-1}$ thereafter. 71

3-20 Leading spatial patterns of barotropic E-P flux divergence anomalies derived from SVD analysis with the zonal wind anomalies. Solid lines indicate the leading pattern; dashed lines indicate the second pattern. Contour interval is 0.5 $m\ s^{-1}\ day^{-1}$; solid vertical lines are positions of the time-mean jets. 71

3-21 (Top) E-P flux divergence anomalies from SVD1 pattern averaged over all pressure levels for each latitude. Vertical black line is position of time-mean SH jet. (Bottom) As in top panel, except for SVD2 pattern and NH. 72

3-22 Cross-correlation of timeseries associated with the first (solid line) and second (dashed line) singular vectors of wind and E-P flux divergence. 73

4-1 Torque applied in Trial L1. Forcing contours are in $m\ s^{-1}\ day^{-1}$ tendency of angular momentum, divided by Earth's radius. Dotted lines are leading EOFs of zonal-mean zonal wind. 76

4-2 As in Figure 4-1, but for Trial L3. 77

4-3 Zonal- and time-mean zonal wind for Trial L3. Contour interval is 5 $m\ s^{-1}$; zero contour is dashed. 78

4-4 Climatological streamfunction for Trial L3. Contour interval is $3 \times 10^{10}\ kg\ s^{-1}$; zero contour is omitted. 79

4-5 Climatological temperature for Trial L3. Contour interval is 10 K. . . 80

4-6 Time-mean E-P fluxes and divergence from Trial L3 with vectors plotted according to the scaling in Edmon et al. (1980). Divergence is contoured; interval is 4 $m\ s^{-1}\ day^{-1}$ acceleration of zonal wind until 20 $m\ s^{-1}\ day^{-1}$ and 20 $m\ s^{-1}\ day^{-1}$ thereafter. Negative contours are dashed and zero contour is omitted. Arrows represent E-P flux; sample arrow at bottom left represents $5 \times 10^{20}\ m^3\ Pa$ of upward flux; an equivalent length in the horizontal represents $6.47 \times 10^{15}\ m^3$ of meridional flux. 80

4-7 Time-mean barotropic E-P flux divergence for Trial L3. Contour interval is 1 $m\ s^{-1}\ day^{-1}$ acceleration of zonal wind. Zero contour is omitted. 81

4-8 Time-mean zonal wind at 250 hPa from Trial L3. Contour interval is 5 $m\ s^{-1}$. 82

4-9 As in Figure 4-8, but for the time-mean temperature at 750 hPa. Contour interval is 5 K. 82

4-10 Fourier coefficients for the zonal wind at 37° S and 250 hPa for Trial L3. The coefficients are computed daily, and the mean of their absolute value for each wavenumber is plotted. 83

4-11 First and second EOFs of zonal-mean zonal wind anomalies in Trial L3. Solid lines are contours of the leading EOF; dashed lines are contours of the second EOF. Contours are in units of 1 $m\ s^{-1}$; vertical lines indicate positions of time-mean jets. 83

4-12 As in Figure 4-11, but for EOFs 3 and 4 of the zonal-mean zonal wind anomalies. Solid lines are contours of EOF3; dashed lines are contours of EOF4. Contours are in units of 0.5 $m\ s^{-1}$; vertical lines indicate positions of time-mean jets. 84

4-13 Autocorrelation of first four principal component timeseries from Trial L3. 85

4-14 Leading spatial patterns of E-P flux divergence anomalies derived from SVD analysis with the zonal wind anomalies in Trial L3. Solid lines indicate the leading pattern; dashed lines indicate the second pattern. Contour interval is 0.5 $m\ s^{-1}\ day^{-1}$ acceleration of zonal wind until 5 $m\ s^{-1}\ day^{-1}$ and 5 $m\ s^{-1}\ day^{-1}$ thereafter. 85

4-15 Change in time-mean zonal wind at 250 hPa for Trial L3 versus the control. Contour interval is 1 $m\ s^{-1}$. 87

4-16 Change in time-mean zonal-mean zonal wind for the indicated trials versus the control. Contour interval is 1 $m\ s^{-1}$ in the upper two panels and 2 $m\ s^{-1}$ in the lower two panels. 88

4-17 Change in time-mean zonal-mean zonal wind for the indicated trials versus the control. Contour interval is 1 $m\ s^{-1}$ for all panels. 89

4-18 As in Figure 4-16, but for the change in streamfunction. Contour interval is $1 \times 10^9\ kg\ s^{-1}$ in the upper left panel and $5 \times 10^9\ kg\ s^{-1}$ in the other panels. 91

4-19 As in Figure 4-17, but for the change in streamfunction. Contour interval is $5 \times 10^9\ kg\ s^{-1}$ in all panels. 92

4-20 As in Figure 4-16, but for the change in temperature. Contour interval is .25 K in all panels. 93

4-21 As in Figure 4-17, but for the change in temperature. Contour interval is .25 K in all panels. 94

4-22 As in Figure 4-16, but for the change in E-P flux divergence. Contour interval is 0.5 $m\ s^{-2}$ acceleration of zonal wind until 2.5 $m\ s^{-2}$ and 2.5 $m\ s^{-2}$ thereafter in all panels except bottom right, where contour interval is 1 $m\ s^{-2}$ acceleration of zonal wind until 5 $m\ s^{-2}$ and 5 $m\ s^{-2}$ thereafter. 96

4-23 As in Figure 4-17, but for the change in E-P flux divergence. Contour interval is 0.5 $m\ s^{-2}$ acceleration of zonal wind until 2.5 $m\ s^{-2}$ and 2.5 $m\ s^{-2}$ thereafter in all panels except bottom right, where contour interval is 1 $m\ s^{-2}$ acceleration of zonal wind until 5 $m\ s^{-2}$ and 5 $m\ s^{-2}$ thereafter. 97

4-24 As in Figure 4-16, but for the change in meridional E-P flux divergence. Contour interval is 0.1 $m\ s^{-2}$ zonal wind tendency in top left panel, 0.5 $m\ s^{-2}$ tendency in bottom right panel, and 0.25 $m\ s^{-2}$ in other panels. 98

4-25 As in Figure 4-17, but for the change in meridional E-P flux divergence. Contour interval is 0.25 $m\ s^{-2}$ in all panels. 99

4-26 Change in time-mean zonal-mean zonal wind for the indicated trials versus the control. Contour interval is 2 $m\ s^{-1}$ in the upper two panels and 1 $m\ s^{-1}$ in the lower two panels. 102

4-27 As in Figure 4-26, but for the change in streamfunction. Contour interval is 5×10^9 $kg\ s^{-1}$ in all panels. 103

4-28 As in Figure 4-26, but for the change in temperature. Contour interval is .25 K in all panels. 104

4-29 As in Figure 4-26, but for the change in E-P flux divergence. Contour interval is 1 $m\ s^{-2}$ acceleration of zonal wind until 5 $m\ s^{-2}$ and 5 $m\ s^{-2}$ thereafter in top panels and 0.5 $m\ s^{-2}$ acceleration of zonal wind until 2.5 $m\ s^{-2}$ and 2.5 $m\ s^{-2}$ thereafter in bottom panels. 105

4-30 As in Figure 4-26, but for the change in the meridional portion of E-P flux divergence. Contour interval is 0.5 $m\ s^{-2}$ acceleration of zonal wind in top two panels and 0.25 $m\ s^{-2}$ acceleration of zonal wind in bottom two panels. 106

4-31 Change in time-mean zonal-mean zonal wind for the indicated trials versus the control. Contour interval is 0.5 $m\ s^{-1}$ in all panels. 108

4-32 Change in time-mean zonal-mean zonal wind for the indicated trials versus the control. Contour interval is 1 $m\ s^{-1}$ in all panels. 110

4-33 Change in time-mean zonal-mean zonal wind for the indicated trials versus the control. Contour interval is 2 $m\ s^{-1}$ in both panels. 110

5-1 (Left) Difference in reference temperature versus the control for a trial with maximum perturbation of 5 K, just off the equator. Contour interval is 1 K. (Right) The meridional gradient of the reference temperature difference. Contour interval is $2.5 \times 10^{-7}\ K\ m^{-1}$. 115

5-2 As in Figure 5-1, but for a trial with maximum perturbation of $-5\ K$ at the poles. 116

5-3 Change in zonal-mean, time-mean zonal wind for the indicated runs versus the control run. Contour interval is 1 $m\ s^{-1}$. 117

5-4 As in Figure 5-3, but for the changes in streamfunction. Contour interval is $5 \times 10^{9}\ kg\ s^{-1}$. 118

5-5 As in Figure 5-3, but for the changes in time-mean, zonal-mean temperature. Contour interval is 0.5 K. 119

5-6 As in Figure 5-3, but for the changes in time-mean E-P flux divergence. Contour interval is 1 $m\ s^{-2}$ acceleration of zonal wind until 5 $m\ s^{-2}$ and 5 $m\ s^{-2}$ thereafter. 120

5-7 (Left) Change in relaxation temperature for the indicated run versus the control run. Contour interval is 0.5 K. (Right) The meridional gradient of the reference temperature difference. Contour interval is $2.5 \times 10^{-7}\ K\ m^{-1}$. 123

5-8 Change in zonal-mean, time-mean zonal wind for the indicated runs versus the control run. Contour interval is 0.5 $m\ s^{-1}$ in upper left panel and 1 $m\ s^{-1}$ otherwise. 123

5-9 Change in zonal-mean, time-mean zonal wind for the indicated runs versus the control run. Contour interval is 1 $m\ s^{-1}$ except 2 $m\ s^{-1}$ for bottom right panel. 124

5-10 As in Figure 5-8, but for the changes in streamfunction. Contour interval is $5 \times 10^{9}\ kg\ s^{-1}$. 126

5-11 As in Figure 5-9, but for the changes in streamfunction. Contour interval is 5×10^9 $kg\ s^{-1}$ except 1×10^{10} $kg\ s^{-1}$ in bottom right panel. 127

5-12 As in Figure 5-8, but for the changes in temperature. Contour interval is .25 K in top left panel, .5 K in top right and bottom left panel, and 1 K in bottom right panel. 128

5-13 As in Figure 5-9, but for the changes in temperature. Contour interval is .25 K in top left panel, .5 K in top right and bottom left panel, and 1 K in bottom right panel. 129

5-14 As in Figure 5-8, but for the changes in time-mean E-P flux divergence. Contour interval is 1 $m\ s^{-2}$ acceleration of zonal wind until 5 $m\ s^{-2}$ and 5 $m\ s^{-2}$ thereafter. 130

5-15 As in Figure 5-9, but for the changes in time-mean E-P flux divergence. Contour interval is 1 $m\ s^{-2}$ acceleration of zonal wind until 5 $m\ s^{-2}$ and 5 $m\ s^{-2}$ thereafter. 131

5-16 As in Figure 5-8, but for the changes in time-mean meridional E-P flux divergence. Contour interval is 0.25 $m\ s^{-2}$ acceleration of zonal wind in top panels and 0.5 $m\ s^{-2}$ in bottom panels. 132

5-17 As in Figure 5-9, but for the changes in time-mean meridional E-P flux divergence. Contour interval is 0.25 $m\ s^{-2}$ acceleration of zonal wind in top panels and 0.5 $m\ s^{-2}$ in bottom panels. 133

6-1 Forcing of zonal wind due to eddy flux terms calculated in Equation 6.1. Contour interval is 1 $m\ s^{-1}\ day^{-1}$ rate of change of zonal wind. Negative contours are dashed and zero contour is omitted. 140

6-2 As in Figure 6-1, but for the forcing in temperature as calculated from Equation 6.2. Contour interval is 0.5 $K\ day^{-1}$ rate of change of temperature. Negative contours are dashed and zero contour is omitted. . 141

6-3 Zonal wind for the control zonally symmetric run. Contour interval is 5 $m\ s^{-1}$; zero contour is dashed. 142

6-4 Streamfunction for the control zonally symmetric run. Contour interval is $3 \times 10^{10}\ kg\ s^{-1}$; zero contour is omitted. 142

6-5 Temperature for the control zonally symmetric run. Contour interval is 10 K. 143

6-6 Change in zonal wind for the indicated trials versus the control for the zonally symmetric runs, including direct forcing only. Contour interval is 0.5 $m\ s^{-1}$ in top left panel and 1 $m\ s^{-1}$ in other panels; zero contour is omitted. 144

6-7 As in Figure 6-6, but for the streamfunction. Contour interval is $1 \times 10^9\ kg\ s^{-1}$ in top two panels and $2 \times 10^9\ kg\ s^{-1}$ in the bottom two panels. Zero contour is omitted. 146

6-8 As in Figure 6-6, but for the temperature. Contour interval is 0.25 K in top left panel, 0.5 K in bottom left panel, and 1 K in right panels. 147

6-9 Changes in tendency of of zonal wind due to eddy flux terms for each trial versus the control. Contour interval is 0.5 $m\ s^{-1}\ day^{-1}$ rate of change of zonal wind. Zero contour is omitted. 148

6-10 As in Figure 6-9, but for the changes in temperature tendency. Contour interval is 0.1 $K\ day^{-1}$. Zero contour is omitted. 149

6-11 Change in zonal wind for the indicated trials versus the control for the zonally symmetric runs, including both direct forcing and changes in eddy fluxes. Contour interval is 2 $m\ s^{-1}$ in the top right panel and 1 $m\ s^{-1}$ in the other panels. Vertical lines are positions of time-mean jets. 150

6-12 As in Figure 6-11, but for the streamfunction. Contour interval is $5 \times 10^9 kg\ s^{-1}$ in all panels. 151

6-13 As in Figure 6-11, but for the temperature. Contour interval is 0.5 K in all panels. 152

6-14 Change in zonal wind for the indicated trials versus the control for the zonally symmetric runs, including direct forcing only. Contour interval is 0.25 $m\ s^{-1}$ in left panels and 0.5 $m\ s^{-1}$ in right panels. 155

6-15 As in Figure 6-14, but for the streamfunction. Contour interval is $0.25 \times 10^9 kg\ s^{-1}$ in all panels. Zero contour is omitted. 156

6-16 As in Figure 6-14, but for the temperature. Contour interval is 0.25 K in left panels and 0.5 K in right panels. 157

6-17 Changes in forcing of of zonal wind due to eddy flux terms for each trial versus the control. Contour interval is 0.1 $m\ s^{-1}\ day^{-1}$ rate of change of zonal wind in top left panel; 0.25 $m\ s^{-1}\ day^{-1}$ in bottom left panel, and 0.5 $m\ s^{-1}\ day^{-1}$ in right panels. Zero contour is omitted. . 158

6-18 As in Figure 6-17, but for the changes in temperature forcing. Contour interval is 0.025 $K\ day^{-1}$ in top left panel; 0.1 $K\ day^{-1}$ in bottom right panel; and 0.05 $K\ day^{-1}$ in other panels. Zero contour is omitted. . . 159

6-19 Change in zonal wind for the indicated trials versus the control for the zonally symmetric runs, including both direct forcing and changes in eddy fluxes. Contour interval is 0.5 $m\ s^{-1}$ in the left panels and 1 $m\ s^{-1}$ in the right panels. Vertical lines are positions of time-mean jets. 160

6-20 As in Figure 6-19, but for the streamfunction. Contour interval is $1 \times 10^9\ kg\ s^{-1}$ in the top left panel, $2 \times 10^9\ kg\ s^{-1}$ in the bottom left panel, $3 \times 10^9\ kg\ s^{-1}$ in the top right panel, and $5 \times 10^9\ kg\ s^{-1}$ in the bottom right panel. 161

6-21 As in Figure 6-19, but for the temperature. Contour interval is 0.25 K in left panels and 0.5 K in right panels. 162

7-1 Projection of SH zonal wind response on SAM of the unforced model run versus the forcing projected on SAM of unforced model run, for the mechanically forced trials. Dashed line is best linear least-squares fit. 168

7-2 As in Figure 7-1, but for the NAM and NH. 169

7-3 First and second SVD patterns of temperature anomalies found from cross-covariance with zonal wind anomalies. Solid lines indicate leading pattern; dashed lines indicate second pattern. Contour interval is 0.25 K; zero contours are omitted. 170

7-4 Projection of SH response versus projection of forcing. Response includes the temperature anomaly of each run weighted by the variance of the temperature of the unforced run and the zonal wind anomaly of each run weighted by the variance of the zonal wind of the unforced model run. Forcing is also weighted by the appropriate variance. Circles indicate mechanically forced trials; squares thermally forced trials. Dashed line is best linear least-squares fit. 171

7-5 As in Figure 7-4, but for the NH. 172

7-6 Instantaneous streamfunction response to indicated forcings in the 2-D elliptic model. Contour interval is $1 \times 10^9 kg\ s^{-1}$. 179

7-7 Applied torques (left panels) and "effective forcings" (right panel) for the indicated trials. Units are $m^2\ s^{-2}$ in each panel. 180

7-8 Buoyancy forcing (left panels, units $10^{-13}\ s^{-3}$) and "effective forcing" (right panels, units $m^2\ s^{-2}$) for the indicated trials. 182

7-9 First and second eigenvectors of V and W for the four-EOF system, using a 10-day lag. Units are nondimensional. 188

7-10 As in Figure 7-9, but for a 40-day lag. 189

7-11 As in Figure 7-9, but for a six-EOF system. 190

7-12 As in Figure 7-9, but for an eight-EOF system. 191

7-13 SH zonal wind response projected on W^T of the unforced model run versus the forcing projected on same pattern. Circles indicate mechanically forced trials; squares indicate thermally forced trials. Dashed line is best least-squares fit; solid line is prediction based on decorrelation time of pattern in unforced run. 193

7-14 As in Figure 7-13, but for the NAM and NH. 194

7-15 As in Figure 7-13, but for the points with strengths of response projection below the median value. 195
7-16 As in Figure 7-15, but for the NAM and NH. 195

List of Tables

4.1 Summary of trials with imposed vertically localized angular momentum forcings of peak magnitude 1 $m\ s^{-1}\ day^{-1}$. 86
4.2 Summary of trials with imposed barotropic angular momentum forcings. 101
4.3 Summary of trials with forcing of same shape as that in Trial L3, but of different magnitudes. 108

5.1 Summary of trials with hemisphere-scale changes to reference temperature. 116
5.2 Summary of trials with imposed reference temperature perturbations localized poleward of 45°. 122

7.1 Eigenvalues of B for the indicated trials. 192

Chapter 1

Introduction

1.1 Historical Overview and Observations

1.1.1 The North Atlantic Oscillation

While the term “annular modes” has only recently come into widespread use in meteorology, the study of large-scale, low-frequency variability has a much longer history in the field. Indeed, one of the most active topics of research in atmospheric science throughout the twentieth century was the North Atlantic Oscillation (NAO).

The name “NAO” was granted to the pressure anomalies over the North Atlantic Ocean by Walker (1924). Walker and Bliss (1932) noted this variability was associated with an anti-correlation of pressure anomalies over the Azores and over Iceland, and defined the first index of the NAO by weighting temperature and pressure data from nine stations in the North Atlantic region. Other expressions for the index include a simple difference of surface pressure between the Azores and Iceland, or an empirical orthogonal function (EOF) of surface pressure over the North Atlantic basin (Marshall et al., 2001), but however the index is defined it expresses the same basic pattern: a dipole of pressure anomalies, with a region of one polarity over the subtropical North Atlantic, and a region of opposite polarity over the subpolar North Atlantic.

While the NAO and other similar phenomena are traditionally considered in terms of pressure anomalies, they of course have associated patterns of variability in other fields. One well-known manifestation of the NAO is the "see-saw" of temperature between Northern Europe and Greenland. The tendency for unusually mild winters in Northern Europe to be correlated with unusually harsh winters in Greenland, and vice-versa, was the subject of much work as early as the 1930s (e.g. Angström, 1935; Loewe, 1937).

The anomalous patterns associated with the NAO have a signature in the wind field as well. Rossby (1939) constructed a "zonal index", a measure of the strength of the zonally-averaged winds between 35° N and 55° N. Namias (1950) argued that variation in the zonal index was linked to meridional displacement of the jet. A unification of the pressure and wind perspectives was achieved by Lorenz (1951), who found a link between the zonal-mean zonal wind at 55° N and the strength of the NAO's pressure patterns. Indeed, it is well-known today that the anomalously high pressure in the Azores region is linked to a poleward displacement of westerlies in the Atlantic sector, and vice versa.

1.1.2 The Southern Annular Mode

The topic of climate variability in the Northern Hemisphere has clearly been of paramount interest to meteorology for many decades. The study of large-scale, low-frequency variability in the Southern Hemisphere (SH) has a shorter history than that of its northern counterpart — an unsurprising fact given the historical scarcity of data south of the equator. However, analysis of the variability in the SH has been ongoing for several decades now, and strong zonal symmetries have been found to dominate the variability in the SH extratropics.

The leading mode of variability in the SH is a dipole of pressure or geopotential, with one region of anomalies centered over Antarctica, and an annulus of opposite polarity stretching about the mid-latitudes. The pattern emerges whether one examines pressure anomalies at sea level (Rogers and van Loon, 1982; Szeredi and Karoly, 1987; Gong and Wang, 1999) or geopotential at various levels of the troposphere (Rogers and van Loon, 1982; Kidson, 1988b; Shiotani, 1990; Karoly, 1990).

Recently, Thompson and Wallace (2000) described this pattern as the SH's "annular mode". Their study, making use of a 40-year record of NCEP-NCAR reanalysis data, examined the geopotential height fields at 850 hPa, and 50 hPa during November (a month when the stratosphere and troposphere are strongly coupled in the SH), and found the dipolar patterns of geopotential in both fields, confirming the earlier studies. Thompson and Wallace (2000) noted the geopotential patterns are highly zonally symmetric, likely owing to the relative scarcity of large-scale topography or land-sea contrast in the SH. While the tropospheric signature of the annular mode is strongest in winter, Thompson and Wallace (2000) found the pattern persists year-round.

Thompson and Wallace (2000) showed the amplitude and spatial pattern of the SH annular mode (SAM) in their Figure 1, which is reproduced here as Figure 1-1. The authors obtained this pattern by regressing the monthly-mean 850 hPa geopotential height field upon the annular mode time series, defined by Thompson and Wallace (2000) as the leading principal component time series of 850 hPa geopotential height, and displaying the amplitude at one standard deviation. The pattern indicates anomalies of 40 m found over Antarctica, with opposite-signed anomalies of about 10 m occurring in a belt paralleling the Southern Ocean. This pattern is defined to be the "positive phase" of the annular mode, while anomalously high geopotential over Antarctica and anomalously low geopotential over the mid-latitudes is considered to be the annular mode's "negative phase". Though the amplitude of the pattern is not perfectly zonally symmetric (the geopotential anomalies are slightly stronger in the Australian sector than in the South American sector), anomalies of the same sign may be found at all longitudes in the mid-latitude belt. The spatial structure of the leading mode is similar to those found by Rogers and van Loon (1982) for the geopotential height at 500 hPa and Karoly (1990) at 300 hPa, and by Gong and Wang (1999) for the surface pressure.

The pattern of variability in the geopotential height field also extends to the stratosphere during southern late spring, a time during which, as noted by Thompson and Wallace (2000), large-scale propagation of planetary waves from the troposphere to the stratosphere is permitted (Charney and Drazin, 1961). Thompson and Wallace

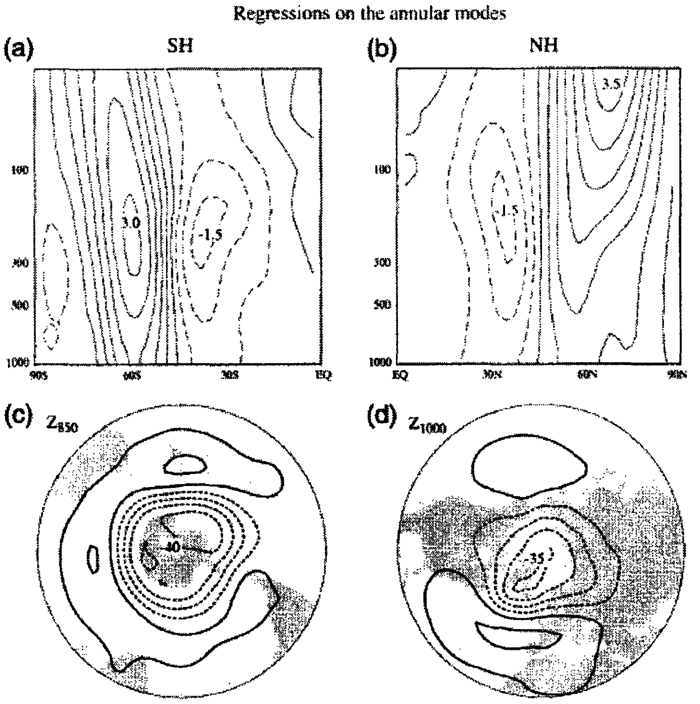

FIG. 1. (top) Zonal-mean geostrophic wind and (bottom) lower-tropospheric geopotential height regressed on the standardized indices of the annular modes (the AO and its SH counterpart) based upon monthly data, Jan 1958–Dec 1997. *Left panels are for the SH, right panels are for the NH.* Units are m s^{-1} (top) and m per std dev of the respective index time series (bottom). Contour intervals are 10 m (−15, −5, 5, . . .) for geopotential height and 0.5 m s^{-1} (−0.75, −0.25, 0.25) for zonal wind.

Figure 1-1: Patterns of zonal wind and geopotential height variability associated with the annular modes. Reproduced from Thompson and Wallace (2000).

(2000) found the SAM pattern at 50 hPa for November data, with a value of 290 m for the geopotential height anomaly over Antarctica. The strong annular mode pattern in the stratosphere does not occur either in southern summer (stratospheric easterlies prohibit stationary wave propagation) or southern winter (the westerly vortex is too strong for stationary wave propagation).

As with the NAO, the extratropical variability in the SH is most often defined in terms of pressure or geopotential, but its signature may be found in other fields as well. Thompson and Wallace (2000), for example, found anomalies of up to 1.1° C at Antarctic stations by regressing surface air temperature against their annular mode index, with a colder central Antarctica (but warmer Antarctic peninsula) associated with the positive phase of the annular mode. During the spring active season, the positive annular mode index is also associated with colder polar stratospheric temperatures. Regressions performed by Thompson and Wallace (2000) also indicate the positive phase of the SAM is associated with positive temperature anomalies in the mid-latitudes.

Particularly notable is the annular mode signature of the zonal wind field (Yoden et al., 1987; Kidson, 1988a; Hartmann and Lo, 1998; Thompson and Wallace, 2000), which indicates a shifting of the mid-latitude westerlies in the different phases of the mode. This pattern was especially examined recently by Lorenz and Hartmann (2001).

Lorenz and Hartmann (2001) found the leading EOF of the zonal-mean zonal wind anomalies, using daily data obtained from the NCEP-NCAR reanalysis, is a dipole. This pattern is shown in their Figure 2, which is reproduced here as Figure 1-2. The westerly anomaly is centered near 60° S, the easterly anomaly near 40° S, and a nodal line near 50° S — the mean position of the SH's eddy-driven jet. Hence, Lorenz and Hartmann (2001) characterized the annular mode's signature in the zonal wind field as a wobble of the eddy-driven jet about its time-mean position. Regressing the wind data against their leading principal component, Lorenz and Hartmann (2001) obtained a maximum amplitude of over 4 $m\ s^{-1}$ for the westerly lobe at jet level, and over 3 $m\ s^{-1}$ for the easterly lobe. However, both lobes are deep, vertically coherent structures, and the surface wind anomalies found by Lorenz and Hartmann (2001) exceed 2 $m\ s^{-1}$ in the westerly lobe and 1 $m\ s^{-1}$ in the easterly lobe. The patterns found by Lorenz and Hartmann (2001) from purely the wind data are similar to those found by Thompson and Wallace (2000) by regressing the wind data on their annular mode index, and Lorenz and Hartmann (2001) also noted the extremely high correlation coefficient between the zonal wind anomalies and the geopotential height anomalies.

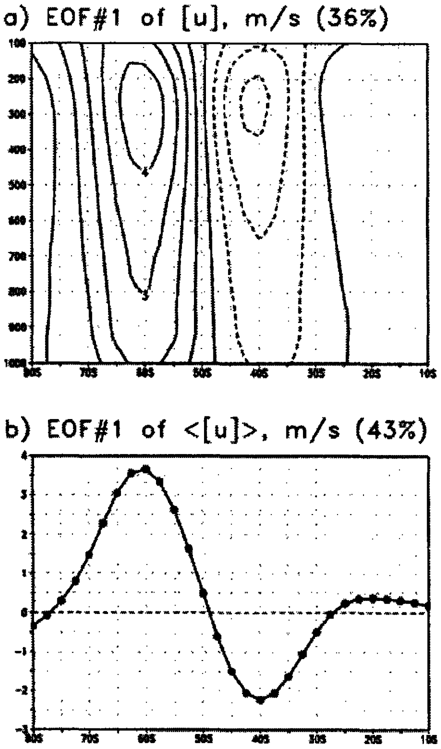

FIG. 2. (a) EOF1 of the zonal-mean zonal wind; (b) EOF1 of the vertical and zonal-mean zonal wind. The percent variance explained is given at top-right corner of plot.

Figure 1-2: Patterns of zonal wind variability associated with SAM. Reproduced from Lorenz and Hartmann (2001).

While Lorenz and Hartmann (2001) did not examine stratospheric changes, the regression maps of Thompson and Wallace (2000) indicate the westerly anomalies associated with the positive phase of the mode extend into the stratosphere during the period of strong coupling in the spring. These stratospheric westerly anomalies are associated with a stronger polar vortex, and are therefore consistent with the colder stratospheric temperatures observed during this phase.

To summarize, the SAM is a highly zonally symmetric pattern of variability, explaining more variance in the extratropics of the SH as compared to any other pattern. The variability may be examined through several different meteorological fields, all of which are closely linked to each other. In the mode's positive phase, anomalously high geopotential is found in the mid-latitudes and anomalously low geopotential over the pole. The eddy-driven westerlies are found poleward of their climatological position. The mid-latitudes enjoy anomalously warm temperatures while Antarctica experiences anomalously cold temperatures. A negative phase of the mode is associated with the opposite patterns. Finally, the SAM's patterns of variability extend to the stratosphere during southern late spring, the time of dynamic coupling between the stratosphere and troposphere.

1.1.3 The Arctic Oscillation

Traditionally, most interest in the Northern Hemisphere (NH) low-frequency climatological patterns has focused around regional-scale anomalies such as the NAO and the Pacific-North America pattern (Wallace and Gutzler 1981), rather than hemisphere-scale variability. The work of Thompson and Wallace (1998, 2000) and Thompson et al. (2000) has encouraged discussion on more zonally symmetric patterns of variability.

Thompson and Wallace (1998) noted that the variation in Eurasian surface air temperature is more closely correlated to hemisphere-wide pressure variability than to solely the NAO, with warmer temperatures correlating strongly with abnormally high mid-latitude surface pressure. They also found strong correlations between the patterns at the surface and at the 50 hPa level, which were primarily zonal in nature though with the negative center tilted toward Greenland, rather than directly over the North Pole. This "Arctic Oscillation" (AO), as the authors termed the phenomenon, is a more longitudinally symmetric expression of climate variability than the traditional view through the NAO.

Thompson and Wallace (2000) defined the AO index using the 1000 hPa geopotential height and then followed procedures similar to those they used in the SH to obtain the spatial patterns. They found, as shown in Figure 1-1, that the leading pattern of height variability is a dipole. As with the SAM, a positive phase of the AO is defined such that the mid-latitudes experience positive height anomalies and the polar regions negative height anomalies. At the 1000 hPa level, the authors computed an anomaly of 35 m over the pole and anomalies of about $5 - 10$ m in the mid-latitudes. The NH pattern displays more zonal asymmetry than its SH counterpart, with Thompson and Wallace (2000) finding the maximum mid-latitude amplitude in the Euro-Atlantic region, a secondary maximum over the Pacific, and relative minima over the North American and Asian continents. The amplitude of the tropospheric pattern in the NH is more seasonal than its SH counterpart as well, though the pattern may still be discerned during northern summer.

The dipolar geopotential anomalies may be found at other altitudes as well. Thompson and Wallace (1998), confining their analysis to the November-April season, found a dipole at several levels of the atmosphere, with 40 m anomalies centered over the pole at 1000 hPa, 70 m anomalies at 500 hPa, and 170 m anomalies at 50 hPa. Extending this analysis, Baldwin and Dunkerton (1999) found the AO signature in geopotential height at nine levels, ranging from the surface to 10 hPa. As noted above the surface pattern features enhanced amplitude in the Euro-Atlantic and Pacific sectors, and a wavenumber-2 pattern may also be discerned at the mid-tropospheric levels as well, which Thompson and Wallace (1998) suggested is associated with the land-sea contrasts in the NH. The patterns in the stratosphere are more zonal, however, with little evidence of a wave-2 component.

The stratospheric signature of the annular mode in the NH is found by Thompson and Wallace (2000) throughout the greater winter season, in contrast to the SH, where it was limited to late spring. As the winter polar vortex in the NH is weaker than that found in the SH, planetary waves tend not to be excluded by overly strong westerlies as in the SH, and the period of dynamic stratosphere-troposphere coupling is longer in the NH than in the SH. The patterns of variability in the stratosphere associated with the positive annular mode phase — anomalously low geopotential over the pole, an unusually strong polar vortex, and an abnormally cold polar stratosphere — are similar between the hemispheres.

As in the SH, the zonal wind variability in the NH comprises a dipole of westerly and easterly anomalies, centered about the position of the time-mean eddy-driven jet. These patterns are shown in their Figure 3, reproduced here as Figure 1-3. Lorenz and Hartmann (2003), performing an EOF analysis of December-March monthly-mean zonal wind data and regressing the daily wind time series upon the EOFs, found a maximum westerly anomaly of 3 $m\ s^{-1}$ centered near 55° N and a maximum easterly anomaly of 2.5 $m\ s^{-1}$ centered near 32° N, with a nodal line near 42° N. As in the SH, the zonal wind patterns are vertically coherent, with westerly surface anomalies between $1 - 1.5\ m\ s^{-1}$ and easterly surface anomalies of $0.5 - 1\ m\ s^{-1}$ found in the regression patterns.

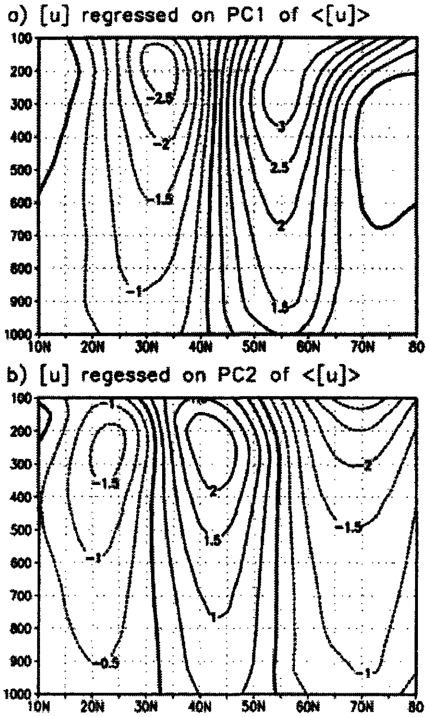

FIG. 3. Leading EOFs of monthly mean zonal wind after linearly removing ENSO variability. (a) Zonal-mean zonal wind regressed on PC1 of the vertical- and zonal-mean zonal wind using monthly data. ENSO has been linearly removed from the data. The units are m s⁻¹. (b) Same as (a) except for PC2.

Figure 1-3: Patterns of zonal wind variability associated with AO during winter. Reproduced from Lorenz and Hartmann (2003).

The variability described by the AO is similar to that of the SAM. The positive phase of the pattern indicates anomalously high pressure in the mid-latitudes, and a poleward shift of the eddy-driven westerlies. The negative phase describes the opposite pattern. As for the SAM in the SH, stratospheric extensions of the AO patterns may be found for the period during which the stratosphere and troposphere are strongly dynamically coupled. There is more seasonal variability in the amplitude of the NH patterns as compared to the SH patterns. Additionally, the NH patterns contain more asymmetries as compared to their SH counterparts.

The presence of these asymmetries has made the zonally symmetric perspective adopted by Thompson and Wallace (1998, 2000) and Thompson et al. (2000) controversial, and while the AO and NAO explain much of the same variability, which of the two is the more meaningful paradigm is a subject of debate (Wallace, 2000). The controversy is mainly because of weak correlations between the centers of action in the subtropical Atlantic and Pacific (Deser, 2000; Ambaum et al., 2001) that would suggest the NAO as a better paradigm. Wallace and Thompson (2002) argued this discrepancy is caused by the Pacific-North America pattern (Wallace and Gutzler, 1981), and that removing anomalies associated with this pattern results in more zonally symmetric anomalies.

While the characterization of the low-frequency variability in the NH as either primarily regional or primarily planetary in scale continues to be debated, there is more agreement that either of the observed phenomena are manifestations of the same processes. In fact, while disputing the zonally symmetric perspective for the NH, Ambaum et al. (2001) noted many of the dynamical mechanisms proposed in relation to the annular modes could also be valid in their regional perspective. Cash et al. (2002) found in an aquaplanet GCM that while the long-time variability in their model runs was zonally symmetric, individual events during which dipolar behavior was observed were more zonally localized. Vallis et al. (2004), using a stochastic forcing of a barotropic model, produced longitudinally symmetric dipolar patterns of variability for statistically zonally uniform forcing, but localized dipolar patterns for more meridionally confined forcings. This was further confirmed in the simple models of Gerber and Vallis (2005), who found in their stochastic model that a zonally symmetric EOF pattern could be produced even when the dynamics were more localized.

In any case, a number of authors have adopted a hemispheric perspective for climate variability in the NH since the publication of Thompson and Wallace (1998), and the variability observed using a NAO perspective is, except for the longitudinal confinement, very similar to that viewed in the SH for the SAM. Further, it appears that the same dynamical mechanisms are responsible for either regional, NAO-like anomalies or hemispheric, AO-like anomalies. One of the most investigated dynamical mechanisms is the role of eddies, which I shall review next.

1.2 Annular Modes and an Eddy Feedback

The prominence and the persistence of the annular modes suggest that they are sustained by a dynamical process internal to the atmosphere. The link between the annular modes and eddy fluxes, and the investigation into whether a feedback exists between the two quantities, have been recent topics of research interest.

Relationships between the eddy activity and anomalies in the zonal-mean flow have been noted for some time, having been found in observations (e.g. Karoly, 1990; Hartmann and Lo, 1998; Feldstein and Lee, 1998) and reproduced in model simulations (e.g. Yu and Hartmann, 1993; Robinson, 1994, 1996; Lee and Feldstein, 1996; Feldstein and Lee, 1996). Limpasuvan and Hartmann (2000) examined both the NCEP-NCAR reanalysis data and a GFDL model run, and found in each case the extrema of anomalous eddy momentum flux convergence were very nearly co-located with the latitudes of anomalous zonal wind related to the annular modes.

An additional question regarding the eddies is whether their role goes beyond impulsive forcing of the annular mode patterns, and instead constitutes maintenance by a feedback process. Robinson (2000) proposed a baroclinic mechanism by which the annular modes and eddy fluxes could be associated in a feedback loop. He noted that while the eddies initially seek to reduce local baroclinicity, their equatorward propagation results in westerly momentum transport into the eddy source region. He additionally hypothesized that surface friction could reduce the westerly anomalies at the surface, resulting in increased baroclinicity and conditions favorable for increased eddy generation.

Several authors have found evidence for an eddy-zonal flow feedback, although the details of the relationship differ among the studies. Feldstein and Lee (1998), for example, found an eddy feedback for the zonal-mean flow anomalies with high-frequency eddies, but dissipative tendencies for cross-frequency and low-frequency eddies. DeWeaver and Nigam (2000), taking an NAO perspective of the variability in the NH, discerned a positive feedback between stationary waves and the NAO-related wind anomalies. Lorenz and Hartmann (2001, 2003) further addressed this issue from an annular mode perspective and found a positive feedback between the eddy momentum fluxes and the zonal-mean flow anomalies in both hemispheres. Unlike DeWeaver and Nigam (2000), however, they found that the synoptic-scale eddies are the most important contributors to the feedback in both hemispheres, with the stationary waves contributing more to poleward propagation of anomalies in the NH.

While the nature of the disturbances providing the feedback differs from study to study, there is evidence of an eddy feedback which sustains the annular modes. Hence, any study of the annular modes must also closely scrutinize eddy fluxes to understand further the nature of the zonal anomalies.

1.3 Links to Other Climate Problems

Much of the recent interest in the annular modes has stemmed from their appearance in relation to a number of other problems in weather and climate. The annular modes' linkage to other meteorological phenomena suggests that the modes are a preferred response of the atmospheric circulation, and that an understanding of the other problems will necessitate a better knowledge of the annular modes themselves.

No problem in weather and climate has received more attention in the past two decades than global warming. It is well-known that the concentration of the greenhouse gas carbon dioxide has risen by about 30 percent since the beginning of the Industrial Revolution, and the concentrations of other greenhouse gases have risen as well. It has also been observed that the global mean surface air temperature of Earth has risen by 0.6° C since the beginning of the twentieth century (IPCC, 2001b). Should future warming continue to occur, it is important to understand what impacts the higher temperatures and other associated changes will have on weather and climate.

In addition to the short-term behavior of the annular modes, decadal trends in the patterns may be observed as well. Thompson et al. (2000) noted a trend toward positive indices in the last few decades of the twentieth century. The authors found the trends in each hemisphere. The trend for the AO during winter was particularly strong over the authors' 1968-1997 dataset; in January and February the linear trend exceeded two standard deviations for the 30-year period. The authors' Figure 1, showing AO-related trends in sea-level pressure, surface air temperature, and precipitation, is reproduced here as Figure 1-4.

Feldstein (2002), motivated by a concomitant increase in variance in the AO timeseries in the late twentieth century, also examined the trend of the index. Though he found that the behavior of the NH annular mode index throughout the first sixty years of the twentieth century could be accounted for by internal variability, he argued external forcing of the climate system or coupling to the ocean or cryosphere was needed to explain more recent behavior.

The annular modes, as they are represented in modeling studies, tend to respond to the greenhouse warming simulated in computer runs (e.g. Shindell et al., 1999; Fyfe et al., 1999; Kushner et al., 2001; Shindell et al., 2001; Rind et al., 2002; Gillett et al., 2002), usually by shifting to the positive phase of the annular mode (Rind et al., 2005). For example, Kushner et al. (2001), in examining the response of the SH to greenhouse warming in their model, found a poleward shift of the jet which projected strongly on their model's SAM. Shindell et al. (1999), Fyfe et al. (1999), and Gillett et al. (2002) found similar behavior in the NH, with a strong positive projection on the AO, though some authors (Osborn et al., 1999; Zorita and Gonzales-Rouco, 2000) obtained a negative projection, and Rind et al. (2002) found strong positive projections in some of their runs but strong negative projections in others. In any case, the existence of decade-long trends in the annular mode timeseries, and the appearance of the annular modes as a preferred response to greenhouse warming in modeling studies, suggest it is important to consider the climate impacts of the annular modes when considering future climate change.

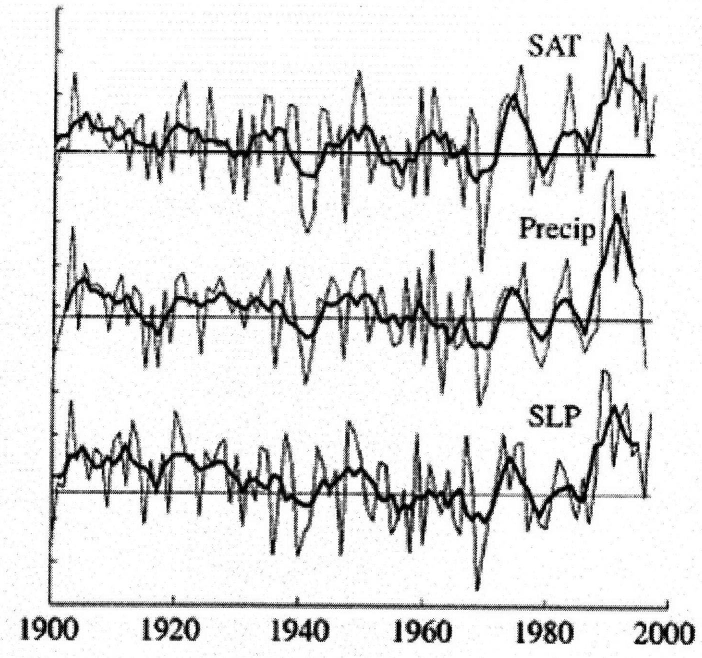

FIG. 1. Standardized JFM proxy AO indices based on SAT, precipitation, and SLP. Correlation statistics are presented in Table 1. Light lines indicate JFM seasonal means; heavy lines indicate 5-yr running means. The interval between tick marks on the vertical axis is one standard deviation.

Figure 1-4: Wintertime AO trends in the surface air temperature, precipitation, and sea-level pressure fields. Reproduced from Thompson et al. (2000).

Another active area of research in the atmospheric sciences is the interaction between the stratosphere and the troposphere. The annular modes may be an important intermediary in a suspected downward influence of the middle atmosphere on the lower atmosphere.

For much of the year there is little dynamical connection between the stratosphere and the troposphere; upward-propagating Rossby waves become evanescent in the weak easterlies which dominate for much of the year in the stratosphere (Charney and Drazin, 1961). During "active seasons", however, when westerly winds (which are not so strong as to also exclude the waves) predominate, a dynamical linkage between troposphere and stratosphere may be accomplished through the upward propagating planetary-scale waves, and the dipolar annular mode patterns of geopotential height may be found in the middle atmosphere (Thompson and Wallace, 2000).

Observations of a downward propagation of zonal wind anomalies from the stratosphere to the troposphere have been noted before the recent focus on the annular modes. Kodera et al. (1990) found that upper-stratospheric westerly anomalies, early in the NH winter, tended to precede tropospheric westerly anomalies in middle to late winter. Kodera and Koide (1997) found that, at least in the Atlantic sector, decadal climate trends could be related to variability of the stratospheric polar night jet. Kuroda and Kodera (1999) found that Eliassen-Palm flux convergence propagated downward in concert with zonal-mean zonal wind anomalies.

Using the AO perspective, Baldwin and Dunkerton (1999) noted the downward propagation of anomalies in geopotential height associated with the AO from the stratosphere to the troposphere, with an average downward propagation time of about three weeks. The anomalies typically occurred once or twice each northern winter. Figure 1-5, reproduced here from Figure 2 of Baldwin and Dunkerton (2001), is a composite of both the positive and negative AO events. Investigating the effects of these downward-propagating anomalies on surface climate, Baldwin and Dunkerton (2001) found an effect on storm tracks up to 60 days after the onset of the stratospheric anomalies, with the Atlantic storm track shifting northward under the influence of positive anomalies, and vice-versa. In their modeling studies, Polvani and Kushner (2002) and Kushner and Polvani (2004) found an annular-mode like response in the troposphere in response to stratospheric cooling. Thompson et al. (2006) obtained both observational and model results showing the balanced response to stratospheric wave drag and radiative anomalies could account for annular mode-like changes in the troposphere.

The mechanism by which the downward propagation of anomalies from stratosphere to troposphere occurs is still a matter of dispute. Hartley et al. (1998) and Black (2002) cited the remote effects of stratospheric potential vorticity anomalies on circulation in the troposphere. Perlwitz and Harnik (2003) instead invoked the

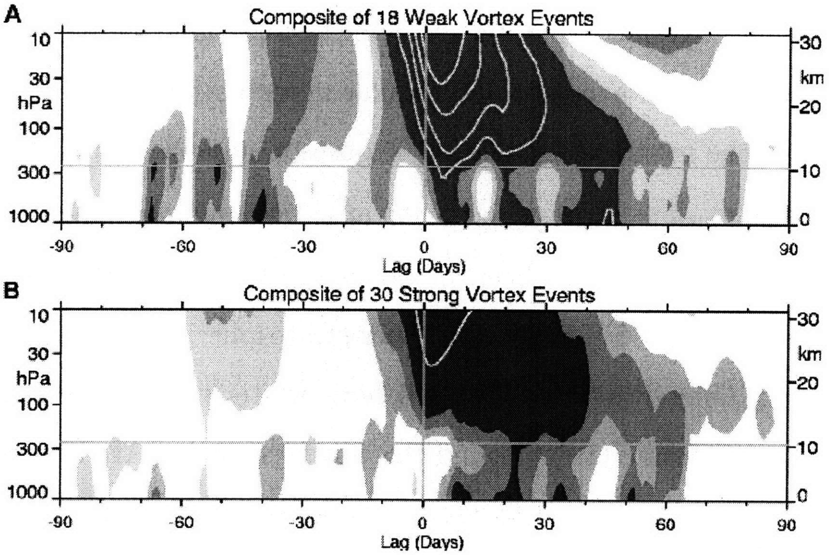

Figure 1-5: Composites of 18 events featuring a weak polar vortex and 30 events featuring a strong polar vortex, showing the downward propagation of AO anomalies. Contour interval is 0.25 of nondimensional AO index for each color; values less than 0.25 are not shaded. White contours feature contour interval of 0.5. From Baldwin, M. P. and T. J. Dunkerton, 2001: "Stratospheric harbingers of anomalous weather regimes." *Science*, **294**, 581-584. Reprinted with permission from AAAS.

reflection of planetary waves. Plumb and Semeniuk (2003) argued the downward propagation occurs through local wave-mean flow interaction. Song and Robinson (2004) tested the theory of "downward control" (Haynes et al., 1991) with eddy forcing as a potential mechanism, but rejected it based on their model runs. Controversy also remains about whether internal tropospheric dynamics are needed to amplify a response from the stratosphere (Kushner and Polvani, 2004; Song and Robinson, 2004; Thompson et al., 2006). Throughout the different mechanisms proposed, however, the annular modes appear in the stratosphere-troposphere coupling.

Another problem in atmospheric science for which the annular modes appear to be a preferred response is ozone depletion. This behavior is somewhat related to the response to the stratospheric cooling investigated by Kushner and Polvani (2004), as the depletion of ozone is associated with stratospheric cooling. Thompson and Wallace (2000) found the annular mode signature by examining Dobson units of column ozone, and Thompson and Solomon (2002) found tropospheric trends in the SH are associated with changes to the polar vortex in the lower stratosphere, which they further noted has been affected by ozone loss. Gillett and Thompson (2003) were able to reproduce high-latitude SH climate trends using only stratospheric ozone depletion as a model forcing.

The annular modes appear in the discussion of a number of other atmospheric phenomena, occurring in both reanalysis data and modeling studies. Their prominence in these studies suggests they are a preferred means of response to atmospheric perturbations. That is the essence of what is tested in this thesis, as I outline below.

1.4 Motivation

As discussed above, the annular modes are large components of variability in the atmosphere, explaining more variability in the extratropics of each hemisphere as compared to any other pattern. Less clear from such reanalysis studies, however, is whether the annular modes are truly "mode-like", in that they appear not only in the climatological variability, but also as a preferred response of the general circulation to a given perturbation.

Modeling studies suggest that the annular modes are, indeed, a preferred response. Kushner and Polvani (2004), for example, altered the reference temperature profile of the stratosphere in their model, yet they produced changes in tropospheric westerlies which reflected annular mode-like patterns. The SH warming considered by Kushner et al. (2001) projected well on their model's annular mode, while Rind et al. (2002) found annular mode-like responses as well for simulated carbon dioxide increases and changes in solar forcing related to the quasi-biennial oscillation. Song and Robinson (2004) used artificial torques placed in the stratosphere to force their model, yet the responses they produced were similar to their model's annular mode.

While examples of studies in which the annular modes respond to an atmospheric forcing are scattered throughout the literature, there is no systemic study of whether, in fact, the response of a model to a suite of generic forcings is expressed in terms of the annular mode patterns. That is the question I seek to answer here: *Are the annular modes a preferred response of the atmospheric circulation to a generic forcing?*, or, put more simply, *Are the annular modes truly "mode-like?"* If the phenomena are preferred responses, then they should arise for myriad types of perturbations. I will test this contention using a simple general circulation model, inserting forcings into the model and comparing the results of the forced trials to those of a control run, with no external forcing applied. I will choose both artificial momentum torques and perturbations to the model's reference temperature and see if the changes in climatology under the influence of these forcings resemble the model's annular modes.

Should the annular modes prove to be a preferred response of the atmosphere to a given forcing, it is also worthwhile to consider why they are, in fact, the selected pattern. As noted above, a number of studies have found that eddies play an important role in the maintenance of the annular modes. In fact, Lorenz and Hartmann (2001, 2003) found a feedback between the eddy forcing and zonal wind anomalies. Given the large amount of evidence suggesting an important role for the eddies in relation to the zonal wind, I will pay special attention to whether an eddy feedback is responsible for the patterns by using a zonally symmetric model. This will allow for the separation of the directly applied forcing and the changes in eddy fluxes, and allow comparisons for the effects of each.

In Chapter 2 of this thesis, I discuss the setup of the model used. The climatology of the control model run is presented in Chapter 3. Chapter 4 examines the results of trials under the influence of the artificial torques, while the results of the trials with reference temperature perturbations are shown in Chapter 5. In Chapter 6, I discuss the results using the zonally symmetric version of the model. Chapter 7 contains further discussion on the similarities and differences of the responses between the mechanically and thermally forced cases, using a fluctuation-dissipation theory framework. Finally, conclusions are presented in Chapter 8.

Chapter 2

Model Setup

2.1 Introduction

The approach of this thesis is to use a simple general circulation model to discern whether the model's annular modes are preferred responses to generic forcings. Specifically, I use the dynamical core of the GFDL atmospheric general circulation model in this study. This model has been used by a number of other authors (e.g. Kushner and Polvani, 2004; Song and Robinson, 2004; Chen et al., 2007) in their studies of the annular modes or related phenomena.

The GFDL dynamical core is a dry, primitive-equation, hydrostatic model. The prognostic variables are vorticity and the divergence of the horizontal flow, temperature, and the logarithm of surface pressure. The techniques of solution are spectral transforms in the horizontal, and Simmons and Burridge (1981) differencing in the vertical. Sigma is used as the vertical coordinate.

The model includes Rayleigh friction and Newtonian cooling to a specified reference temperature (which here is perpetually solstitial) as its dissipative schemes. Hyperdiffusion is also applied. A zonally symmetric setup is chosen here as no topography is imposed upon the model and a longitudinally symmetric reference temperature is chosen.

In the rest of the chapter, I will discuss more extensively several aspects of the setup used in the model.

2.2 Resolution

For the model runs presented later in this thesis, a T30 spectral resolution is selected. This results in an equivalent grid spacing of 3.75° in the horizontal. Twenty vertical levels, equally spaced from $\sigma = 0.025$ to $\sigma = 0.975$, are employed.

As with all computer modeling studies, there is a trade-off between the resolution employed and the length of time needed to compile model runs. For the system used here, it took about eight hours to complete a model run of 500 days at T30 resolution. Given the tendency of the annular modes in the model to have an unrealistically large temporal persistence (which is discussed by Gerber et al. (2007) and will be shown for the runs here in the subsequent chapters), it was necessary to compile long climatologies, with 5,000 days being the usual choice of length here. This naturally placed a premium on minimizing computing time.

The model resolution was tested by comparing the control model run compiled at T30 resolution with runs employing T42 and T63 resolution. Fortunately, the runs conducted at higher resolution were very similar to that at T30 resolution. An illustration of the similarity may be found by comparing Figure 2-1 below and the control climatology in Chapter 3.

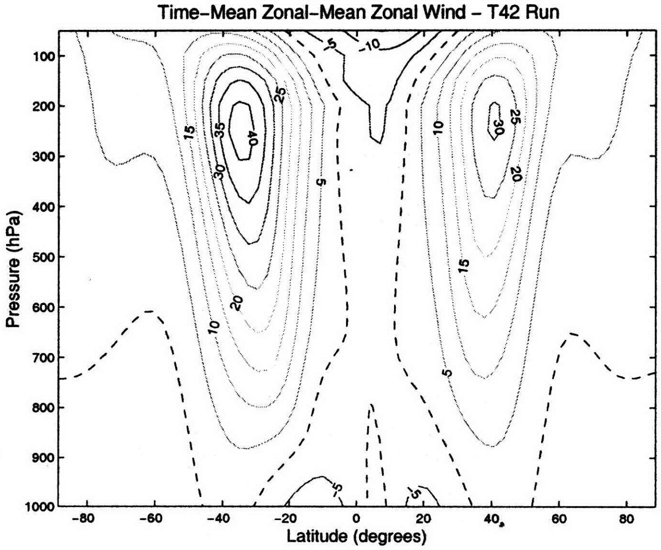

Figure 2-1: Zonal- and time-mean zonal wind for the T42 test run. Contour interval is 5 $m\ s^{-1}$; zero contour is dashed.

Figure 2-1 shows the zonal-mean zonal wind, for a 5,000-day climatology, sampled once daily. The resolution here is T42, but the other parameters are the same as those discussed below (and used for the T30 climatology shown in Chapter 3). Here the westerly jet peaks at 41 $m\ s^{-1}$ strength at 36° S latitude; this compares favorably to the coordinates in the climatology shown in Figure 3-1 (43 $m\ s^{-1}$ strength at 37° S). The magnitudes and positions of the jets in the NH are similar as well (31 $m\ s^{-1}$ at 41° here versus 32 $m\ s^{-1}$ at 41° in the T30 climatology).

As an additional test, the EOFs of zonal-mean zonal wind were computed for the T42 run and compared to the EOFs found in the T30 run (shown in Chapter 3). The former are shown in Figure 2-2; the latter are shown in Figure 3-11. The time-mean values are removed and the data weighted by the square root of cosine of latitude (North et al., 1982) before computing the EOFs. The EOFs are computed on the global domain; however with no spatial overlap between the two leading patterns they are shown here on the same plot. In both cases, each EOF forms a vertically coherent dipole of wind about the jet's time-mean position. The strongest EOF is found in the SH, with the second-strongest EOF found in the NH.

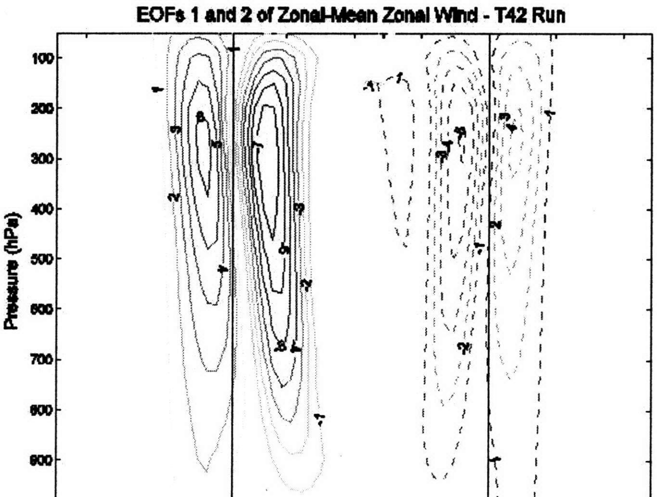

Figure 2-2: First and second EOFs of zonal-mean zonal wind anomalies in the T42 test run. Solid lines are contours of the leading EOF; dashed lines are contours of the second EOF. Contours are in units of 1 $m\ s^{-1}$; vertical lines indicate positions of time-mean jets.

Other climatological fields in the T42 run were similar to those of the T30 run. Additionally, there was little difference among the run conducted at T63 resolution (not shown) and the runs at T42 and T30 resolution. Since the climatology at T30 resolution is similar to those produced at higher resolution, the T30 truncation will be chosen for the model runs here.

2.3 Radiation

The model uses Newtonian cooling as its parameterization for thermodynamic processes. This is a linear relaxation to a prescribed reference temperature profile. The results shown here use a damping coefficient of $\frac{1}{40}$ day^{-1} above $\sigma = 0.7$, linearly increasing to $\frac{1}{4}$ day^{-1} at the surface. With many of Earth's radiative processes occurring at the surface, the more rapid relaxation time there is a sensible choice. The vertical variation of the coefficient is similar to that used by Held and Suarez (1994), although they employ a variation with latitude of the relaxation parameter within the boundary layer below $\sigma = 0.7$ that is not used here. Removal of this variation was found to improve slightly the decay time of the annular mode patterns' autocorrelation while not otherwise altering their magnitude or structure, so the meridional variation was not employed here.

The reference temperature profile to which the model is relaxed is similar to that used by Held and Suarez (1994), although some modifications are made. The exact formula of the reference profile will be shown in the Appendix; the profile is displayed in Figure 2-3. A solstitial pattern is imparted to the reference temperature profile by two means. First, the point of maximum reference temperature is displaced off-equator slightly. Second, a sinusoidal term, equal at the surface to 10 K multiplied by the sine of latitude, is added to the profile. The profile decays away from the point of maximum reference temperature following the fourth power of cosine of latitude.

As seen in Figure 2-3, the point of maximum equilibrium temperature of 315 K occurs on the NH side of the equator. The equator-pole reference temperature gradient is 50 K in the NH but 70 K in the SH. Hence the SH will be the winter hemisphere

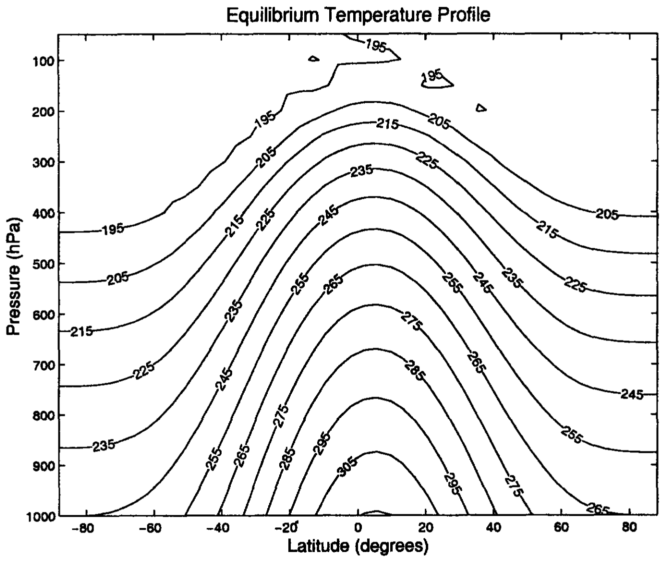
Equilibrium Temperature Profile

Figure 2-3: Reference temperature for the unforced model run. Contour interval is 10 K.

in these runs, while the NH is the summer hemisphere.

As a consequence of this reference temperature profile, the strengths of the annular modes will be different between the two hemispheres. This has already been seen in Figure 2-2 for the T42 test run, and it will hold as well in the T30 model runs discussed later in this thesis. The stronger annular mode occurs in the winter hemisphere, but the summer hemisphere also features an annular mode which represents the largest amount of variability in that hemisphere. This is also consistent with observations of the annular modes in Earth's atmosphere (e.g. Thompson and Wallace, 2000).

2.4 Friction and Hyperdiffusion

A linear drag below $\sigma = 0.7$ is the model's representation of surface friction. The coefficient of friction, which is zero above this level, increases linearly to 2 day^{-1} at the surface.

The damping coefficient used here is twice the value used by Held and Suarez (1994). The increase of friction improves the decorrelation times of the patterns, as will be discussed below. Several checks were conducted to insure that the change in parameter value did not significantly alter the behavior of the jets and their annular modes. Fortunately, the changes brought about by the increased mechanical damping were minor.

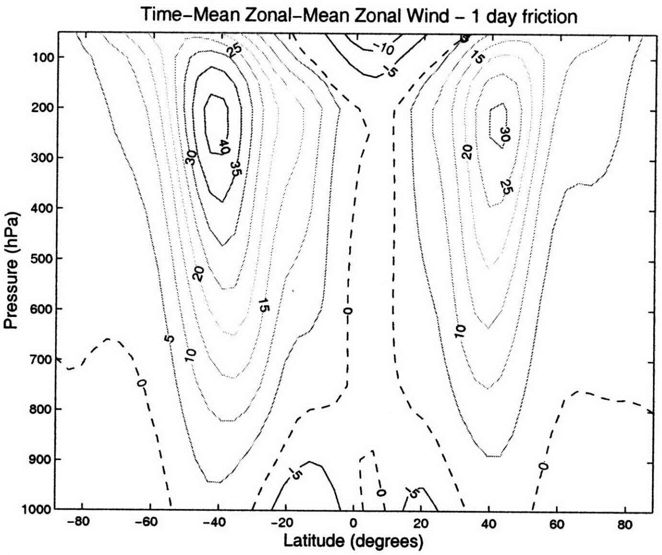

Figure 2-4: Zonal- and time-mean zonal wind for the test run using maximum mechanical damping rate of 1 day^{-1}. Contour interval is 5 $m\ s^{-1}$; zero contour is dashed.

The climatological zonal-mean zonal wind using a damping coefficient of 1 day^{-1} at the surface (in other words, the strength used by Held and Suarez (1994) and half the strength of the friction used in the model runs in the rest of the thesis) is shown in Figure 2-4. Comparing with a run using the higher coefficient of friction shown in Chapter 3 (Figure 3-1), the increase of the damping coefficient results in the jets moving equatorward by several degrees. This behavior is also noted in the GFDL model by Chen et al. (2007), who analyze the latitudinal movement extensively. The behavior was also found by Robinson (1996) in his two-layer model.

The SH jet is centered at 41° here, and the NH jet at 43°. Their positions in the control trial shown in Chapter 3 with 2 day^{-1} friction at the surface are 37° S and 41° N. The jets shown in Figure 2-4 also display more prominent "kinks" in the wind contours on the jets' equatorward flanks as compared to the profiles in Figure 3-1. This is indicative of a greater separation in this trial of the mid-latitude westerlies generated by eddy momentum flux convergence, and the subtropical westerlies gen-

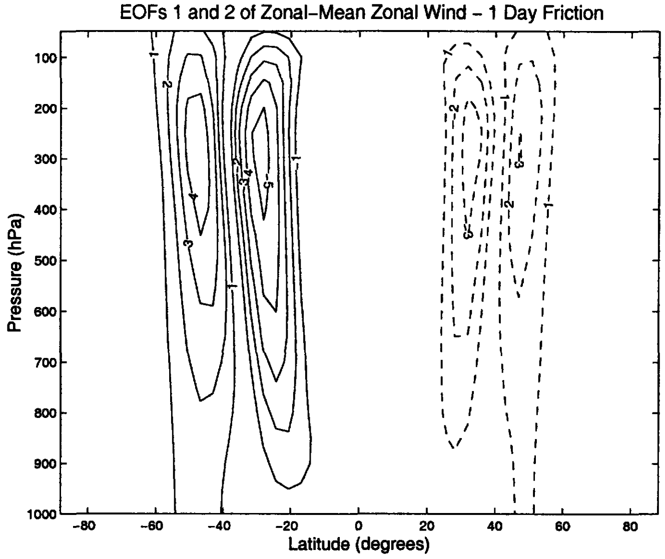

Figure 2-5: First and second EOFs of zonal-mean zonal wind anomalies in the test run using maximum mechanical damping rate of 1 day^{-1}. Solid lines are contours of the leading EOF; dashed lines are contours of the second EOF. Contours are in units of 1 $m\ s^{-1}$.

erated by Coriolis deflection of the meridional circulation.

As should be expected, the magnitude of the surface westerlies is reduced by the increased friction. The peak value at the surface is 3.7 $m\ s^{-1}$ as compared to 2.3 $m\ s^{-1}$ for the control trial in Chapter 3. However, westerlies still occur at the surface and throughout the jet column, and the peak strength of the jet at tropopause level is unaffected by the increased boundary layer friction.

In cases using both lower and higher rates of friction, the leading EOF of the zonal-mean zonal wind anomalies is a dipole of opposite-signed centers of wind anomalies, one on each side of the jet's time-mean position. The leading patterns for the case with weaker mechanical damping are shown in Figure 2-5; they are similar to the patterns for the case in Figure 3-11 with stronger friction. While the EOF patterns are similar in each case, the autocorrelation of the timeseries decayed more rapidly using the higher mechanical damping. Therefore, the 2 day^{-1} rate at the surface is used in the runs to follow.

A ∇^6 hyperdiffusion is chosen in the model runs. Here the smallest wavenumber is damped on a timescale of $\frac{7}{10}$ day; when runs of higher resolution were employed to test model resolution, this parameter was appropriately scaled. The model was also tested by varying this timescale by a factor of two; the climatology produced was not significantly different.

2.5 A Note on Zonal Symmetry

As stated in the Introduction, there is considerable debate over whether the dominant patterns of anomalous pressure and wind in the NH constitute a hemisphere-scale phenomenon (e.g. Thompson and Wallace, 2000), or a regional pattern focused on the North Atlantic Basin (e.g. Ambaum et al., 2001).

The model runs employed here use a zonally symmetric reference temperature profile, and no topography is imposed upon the surface. As such, to the extent that one is interested in the behavior of the NH, the perspective taken in this thesis is more reflective of that of the former authors than that of the latter. However, while arguing the variability in the NH is best understood on a regional basis, Ambaum et al. (2001) do not reject the annular mode paradigm in the SH. They additionally note that many of the mechanisms used to explain the Arctic Oscillation may be equally valid for the North Atlantic Oscillation.

The zonally symmetric approach is also more appealing since it allows use of a body of theory on the interactions between the zonal mean state and the eddies. Within the context of the annular modes, such work has been conducted by Limpasuvan and Hartmann (2000) and Lorenz and Hartmann (2001, 2003), for example. In Chapter 6 of this thesis, I will use a zonally symmetric version of the model to separate the direct effects of the applied forcing from those caused by the changes in eddy fluxes. The partition could not be accomplished if a zonally asymmetric system were considered.

Since the runs to follow are zonally symmetric, the importance of non-zonality to the flow anomalies in the NH cannot be addressed here. However, even if one views the zonal inhomogeneity as critical to processes to the NH, the runs conducted in this model will still prove to be a reasonable analog for the behavior of Earth's annular mode in the SH, and should prove interesting from a theoretical standpoint as well.

2.6 Summary

In this chapter, I have discussed the setup of the GCM dynamical core used here and explained the damping parameters chosen. Test runs using higher resolutions or perturbed damping coefficients were found to produce climatologies similar to the one to follow in the next chapter, with the annular modes in each case being the most prominent expression of variability in each hemisphere. The climatology of the control model run produced under the selected parameters will be discussed extensively in the next chapter.

In later chapters, I will present trials in which the model is subjected to an external torque, or trials which use an altered relaxation temperature profile. Hence these runs are used to study the behavior of the model in response to mechanical and thermal forcings, respectively, to determine whether the annular modes are indeed a mode-like response. The nature of the forcing for the mechanically forced trials will be discussed at the beginning of Chapter 4, while the nature of the thermal forcing will be discussed at the beginning of Chapter 5.

Chapter 3

Climatology of the Control Run

3.1 Introduction

Before beginning the suite of trials in which the model is subjected to an external forcing, I first compile a climatology of the model with no applied external forcing. This climatology, consisting of 7,200 days of model data, sampled once daily after the model had spun up from rest, is presented in this chapter. The climatology shown below is robust and reproducible from smaller segments of the model dataset. As may be expected from the given conditions, the model's climatology is highly longitudinally symmetric. It also contains annular modes similar to those observed in the real atmosphere.

3.2 Zonal- and Time-Mean Climatological Fields

The time-mean, zonal-mean zonal wind is shown in Figure 3-1. The most prominent features are the two westerly jets, one in each hemisphere, associated primarily with the convergence of eddy momentum flux. The SH (winter) jet occurs at about 37° latitude, reaching a peak amplitude of 43 $m\ s^{-1}$ at 250 hPa. The NH (summer) jet's peak magnitude of 32 $m\ s^{-1}$ occurs at 41° latitude and 250 hPa.

In both hemispheres the peak westerly surface wind speed is slightly more than 2 meters per second, occurring at about the same latitude as the upper jet. Easterly

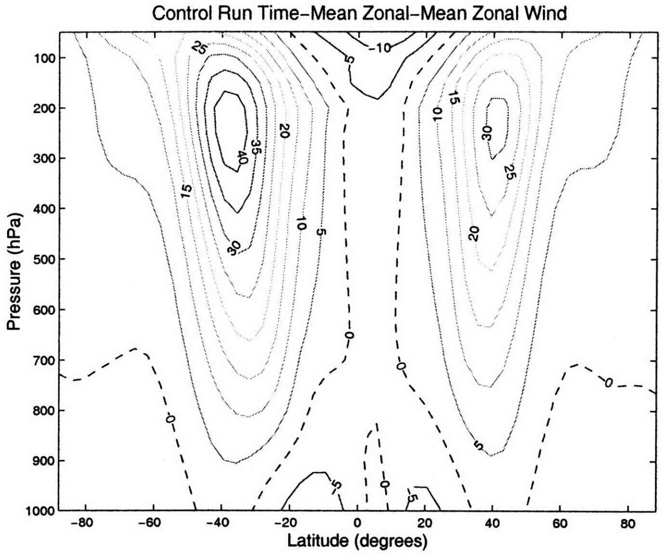

Figure 3-1: Zonal- and time-mean zonal wind for the unforced model run. Contour interval is 5 $m\ s^{-1}$; zero contour is dashed.

surface flow is found equatorward of 30° in each hemisphere.

The model output also contains westerlies associated with the tropical meridional overturning circulation, although these winds are less prominent than those produced by the eddy fluxes. However, they can be discerned on many days of the individual climatology as a bulge on the equatorward side of the jet. On some days of the climatology, a distinct double jet may be noted, as shown in Figure 3-2.

The climatological meridional streamfunction is shown in Figure 3-3. The strongest overturning cell extends from the tropical NH across the equator into the SH, as expected from the model's relaxation temperature profile. The winter Ferrel cell may also be noted, as well as weaker overturning circulations in the summer hemisphere. Consistent with the streamfunction shown in Figure 3-3, the strongest upward velocities are found north of the equator, with the strongest sinking motion in the subtropical SH. Strong cross-equatorial northerlies are found at tropopause level, with vigorous cross-equatorial southerlies at the surface.

The climatological zonal-mean temperature profile is displayed in Figure 3-4. The warmest point is naturally in the tropics, although the temperature is cooler than the prescribed reference temperature (Figure 2-3). The meridional gradient of the

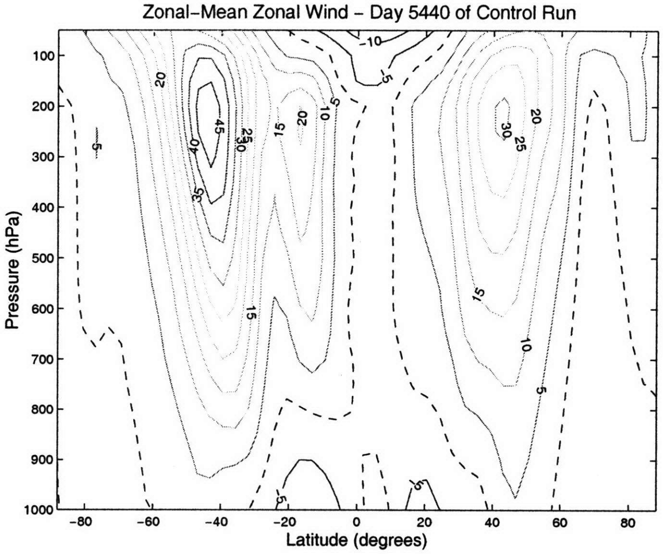

Figure 3-2: Zonal-mean zonal wind from a selected day of model climatology, showing the double-jet structure. Contouring as in Figure 3-1.

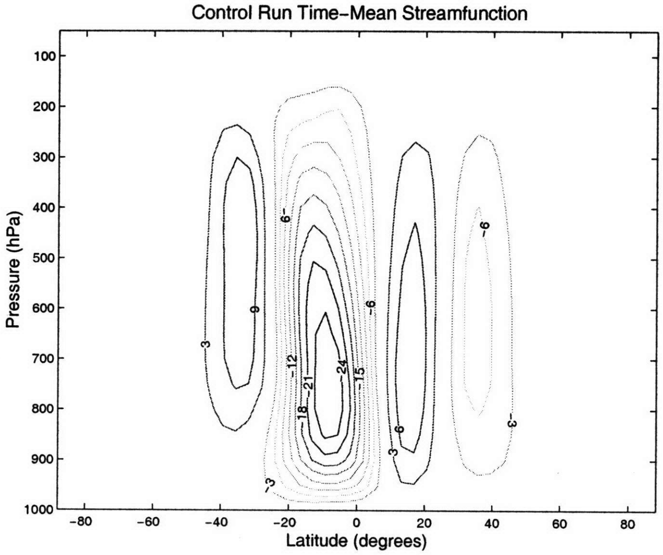

Figure 3-3: Climatological streamfunction for the unforced model run. Contour interval is $3 \times 10^{10} kg\ s^{-1}$; zero contour is omitted.

temperature in the tropics is nearly zero, while strong temperature gradients occur in mid-latitudes. The South Pole is 20 K cooler than the North Pole, reflecting the seasonality imparted in the reference profile.

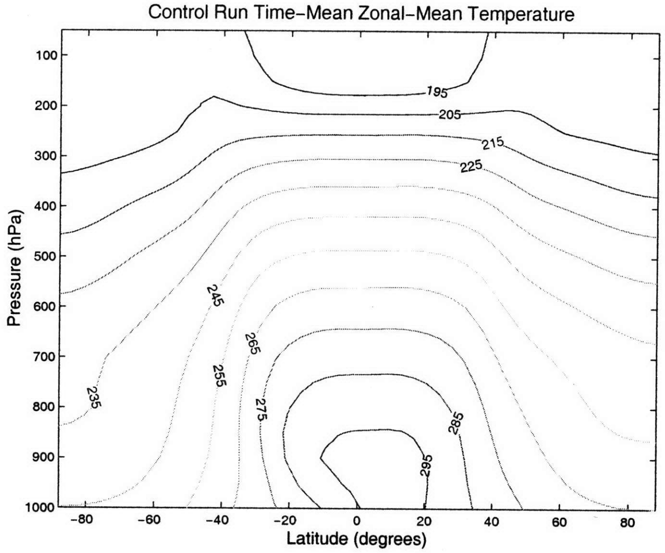
Control Run Time-Mean Zonal-Mean Temperature

Figure 3-4: Climatological temperature for the unforced model run. Contour interval is 10 K.

Figure 3-5 illustrates the climatological Eliassen-Palm flux and divergence. The E-P flux vectors are plotted according to the conventions in Edmon et al. (1980). The divergence is weighted by $(a\cos\phi)^{-1}$ so as to represent units of acceleration of zonal wind. As expected, the dominant pattern in this field is divergence near the surface and convergence at upper levels, indicating the generation of eddies at low levels, upward propagation, and dissipation at upper levels.

The components of the Eliassen-Palm flux in the meridional and vertical directions may be written, respectively, as

$$F_\phi = a\cos\phi\left(-\overline{u'v'} + \overline{v'\theta'}\,\frac{\partial\overline{u}}{\partial p}\left(\frac{\partial\overline{\theta}}{\partial p}\right)^{-1}\right) \tag{3.1}$$

$$F_p = a\cos\phi\left(\left(f - \frac{\frac{\partial(\overline{u}\cos\phi)}{\partial\phi}}{a\cos\phi}\right)\overline{v'\theta'}\left(\frac{\partial\overline{\theta}}{\partial p}\right)^{-1} - \overline{u'\omega'}\right), \tag{3.2}$$

where the overbars indicate zonal means, the primes departures from the zonal mean, and the notation of meteorological variables is standard.

Most of the divergence shown in Figure 3-5 is "baroclinic" (that is, stemming from the component of the divergence associated with Equation 3.2), but the "barotropic" divergence (or, that associated with Equation 3.1) is important as well, particularly in the upper troposphere. Indeed, when considering the integrated angular momentum budget, the surface baroclinic divergence will be cancelled by baroclinic convergence in the free troposphere. The barotropic component of the divergence, and not the baroclinic part, affects the integrated angular momentum budget.

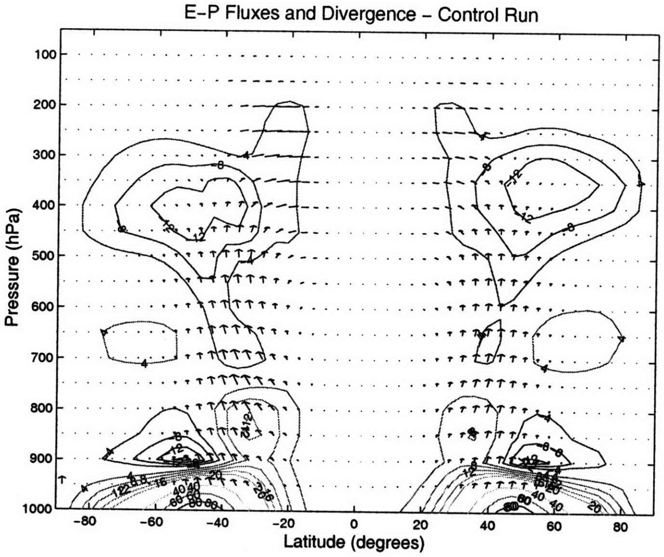

Figure 3-5: Time-mean E-P fluxes and divergence from control run with vectors plotted according to the scaling in Edmon et al. (1980). Divergence is contoured; interval is 4 $m\ s^{-1}\ day^{-1}$ acceleration of zonal wind until 20 $m\ s^{-1}\ day^{-1}$ and 20 $m\ s^{-1}\ day^{-1}$ thereafter. Arrows represent E-P flux; sample arrow at bottom left represents $5 \times 10^{20}\ m^3\ Pa$ of upward flux; an equivalent length in the horizontal represents $6.47 \times 10^{15}\ m^3$ of meridional flux.

The barotropic portion of the divergence (weighted by $(a \cos\phi)^{-1}$) is displayed in Figure 3-6. Note that, in each hemisphere, the maximum of the barotropic E-P flux divergence's contribution to acceleration occurs at the jet center in the upper troposphere, again suggesting the jets seen in Figure 3-1 are driven primarily by eddy activity.

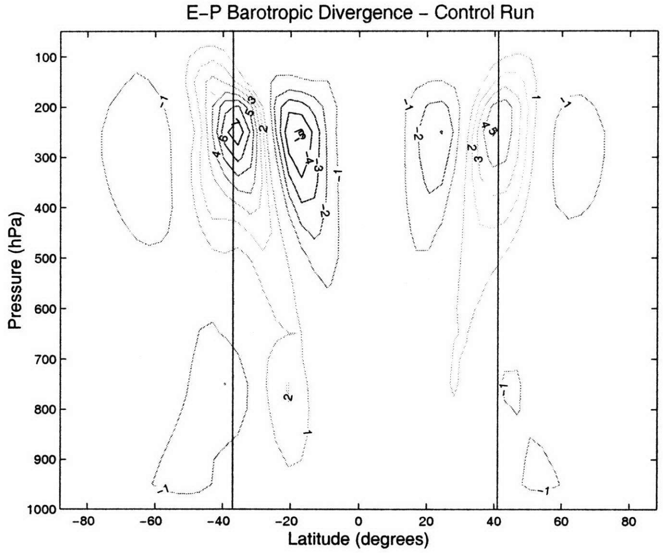

Figure 3-6: Time-mean barotropic E-P flux divergence. Contour interval is 1 $m\ s^{-1}\ day^{-1}$ acceleration of zonal wind. Solid lines are positions of time-mean jets.

3.3 Zonal Variations in the Unforced Run

In the above discussion, I have focused on the zonal-mean climatology of the model. As the model contains no topography or land-sea contrast, and there is no longitudinal variation in the reference temperature profile, little variation in the model's climatology with latitude should be expected. Indeed, that is the case, as shown by the next two figures. Figure 3-7 displays the cross-section of time-mean zonal wind at 250 hPa, while Figure 3-8 displays the cross-section of time-mean temperature at 750 hPa. Both fields are highly zonal with very little variation in the longitudinal direction. These results are typical of those found at other pressure levels.

While the time-mean climatological fields are highly zonal, longitudinal variation of course exists on individual days of the run. To diagnose this variation, Fourier analysis is performed on each day of the flow, and the absolute values of the Fourier coefficients of u found on each day are averaged. Figure 3-9 is a bar graph of these average Fourier coefficients for the flow at the center of the climatological jet (37° S and 250 hPa). The largest coefficients are found for large synoptic-scale eddies (wavenumbers 5 and 6), with the planetary-scale eddies (wavenumbers 1 through 4) contributing

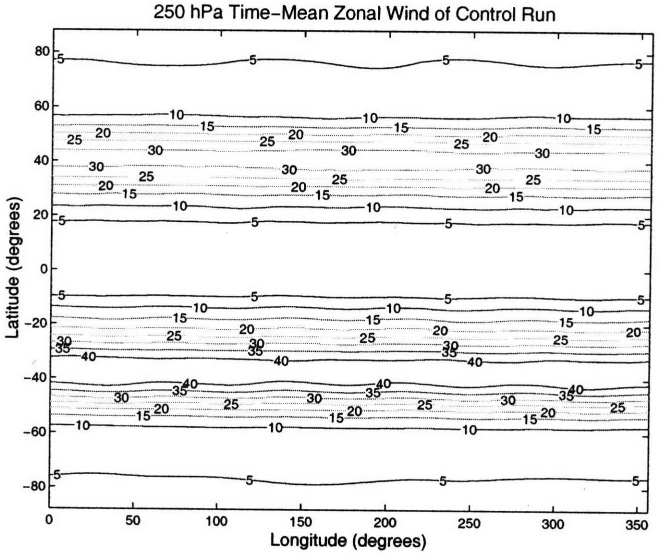

Figure 3-7: Time-mean zonal wind at 250 hPa. Contour interval is 5 $m\ s^{-1}$.

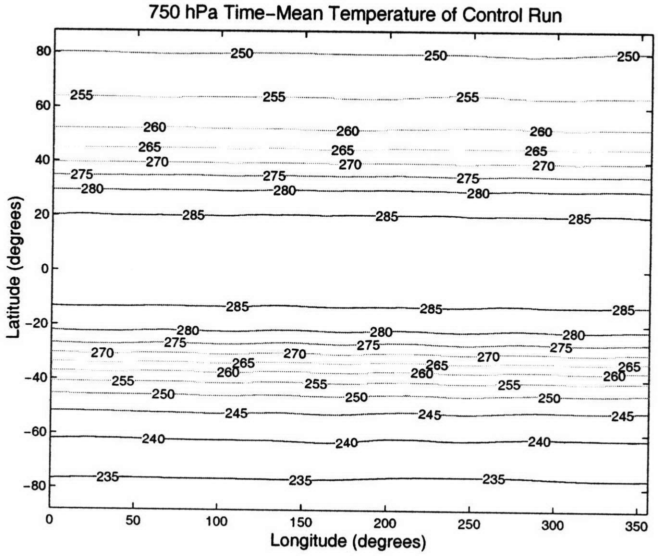

Figure 3-8: As in Figure 3-7, but for the time-mean temperature at 750 hPa. Contour interval is 5 K.

as well. This distribution is typical of those found in the model's climatology at upper levels at and near the jet centers, although at lower altitudes on the flanks of the jets, the coefficients associated with the planetary scale eddies are larger than those associated with the large synoptic eddies.

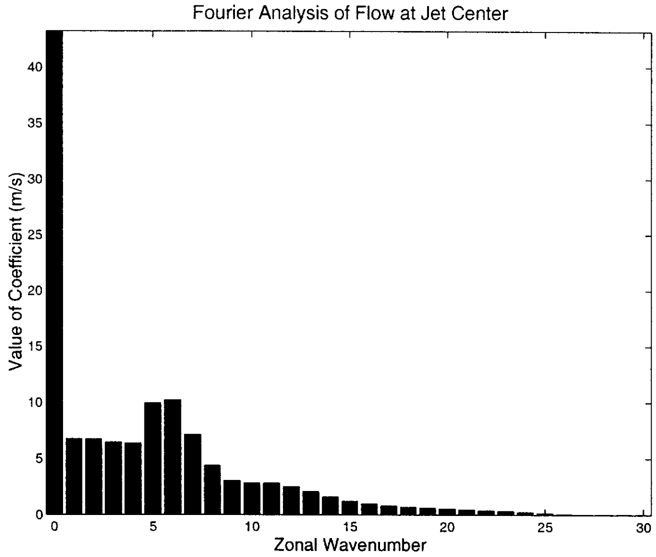

Figure 3-9: Fourier coefficients for the zonal wind at SH jet center (37° S and 250 hPa). The coefficients are computed daily, and the mean of their absolute value for each wavenumber is plotted.

Having examined the climatological means produced by the control run of the model, I now discuss the variability found in the unforced model's climatology.

3.4 Variability of the Unforced Run

In this section, the variability of the model's climatology is examined through the use of empirical orthogonal functions (EOFs).

First, I examine the first EOF of the surface pressure anomalies in each hemisphere. The patterns in Figure 3-10 have been regressed against the pressure field. The time-mean field is subtracted before computing the anomalies, and the data are weighted by the square root of cosine of latitude (North et al. (1982)). Both the SH and NH feature a pattern which is similar to that of the observed annular mode (Figure 3-10). Each domain contains two belts of anomalous pressure encircling the globe:

a ring of lower pressure closer to the pole and a ring of higher pressure nearer the equator. The belts show a high degree of longitudinal symmetry and no longitudinal structure is evident. Similar results may be obtained for EOFs of the geopotential height field at various levels of the model atmosphere. The longitudinal symmetry of these pressure EOFs reinforces the choice of a zonal-mean perspective, and I so choose below in the examination of the wind field.

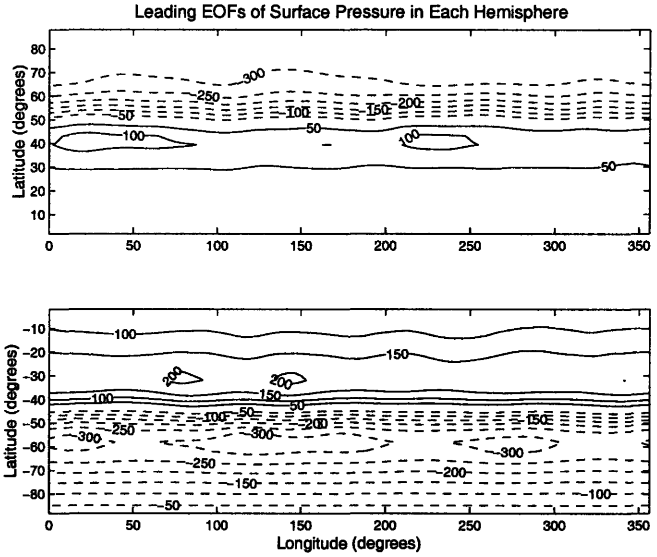

Figure 3-10: (Top) First EOF of surface pressure anomalies in the NH. Contour interval is 50 Pa; negative contours are dashed. (Bottom) As in the top panel, but for the SH.

Figure 3-11 displays the leading EOFs in the zonal-mean zonal wind field. The patterns in Figure 3-11 have been regressed against the zonal-mean zonal wind. As done with the pressure field, the wind data were weighted, and their means subtracted, before computing the EOFs. Unlike the pressure EOFs shown above (which were calculated separately in each hemisphere), the wind EOFs are computed on the global domain; however with no spatial overlap between the two leading patterns they are shown here on the same plot. These EOFs may also be reproduced using smaller segments of the control climatology.

EOF1, which explains 53 percent of the variability, is confined to the SH, while EOF2, which explains 17 percent of the variability, appears only in the NH. The structure of each pattern is clearly dipolar, with a positive lobe to the poleward

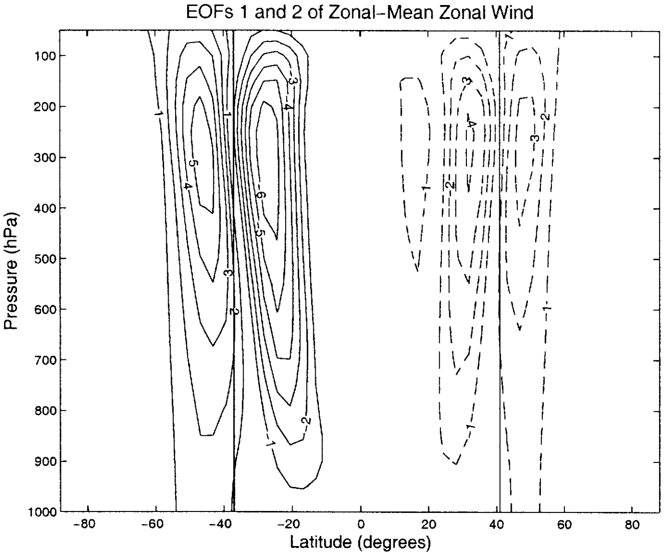

Figure 3-11: First and second EOFs of zonal-mean zonal wind anomalies. Solid lines are contours of the leading EOF; dashed lines are contours of the second EOF. Contours are in units of 1 $m\ s^{-1}$; vertical lines indicate positions of time-mean jets.

side of the jet's time-mean position in each hemisphere and a negative lobe to the equatorward side. This is the "wobble" of the jet described by Lorenz and Hartmann (2001, 2003) as the signature of the annular mode in the zonal wind field. While the strongest amplitudes occur at the jet level, the dipoles extend from the surface to the top of the model atmosphere. The patterns obtained from global data shown here are very similar to those obtained by examining each hemisphere separately.

The third and fourth EOFs of the zonal-mean zonal wind are shown in Figure 3-12. As above, these patterns are similar to those obtained examining each hemisphere separately. EOF3 is limited to the austral hemisphere and EOF4 to the boreal hemisphere, so I again display them on one plot. These patterns are not dipolar but tripolar, featuring a positive lobe at the jet centers and negative lobes on their poleward and equatorward flanks. These two patterns represent what Lorenz and Hartmann (2001, 2003) described as a strengthening and tightening of the jet. Here EOF3 explains 10 percent of the variability and EOF4 4 percent of the variability, so the amount of variability explained by these patterns has been significantly reduced as compared to the two leading patterns. Hence my focus will be on the two leading patterns.

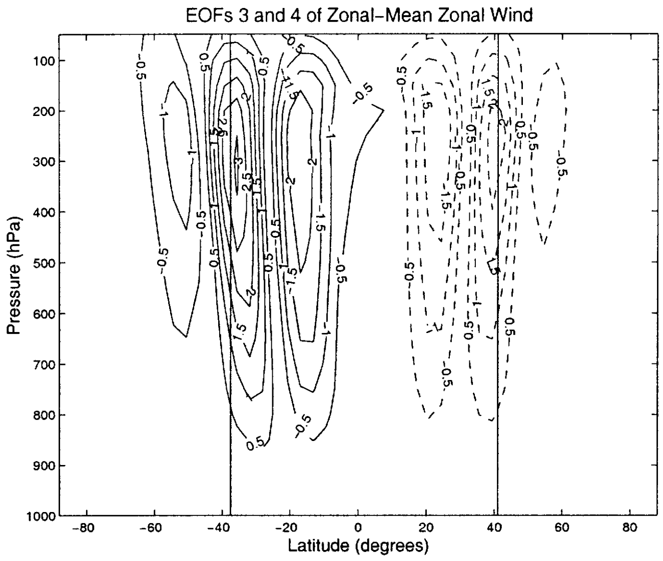

Figure 3-12: As in Figure 3-11, but for EOFs 3 and 4 of the zonal-mean zonal wind anomalies. Solid lines are contours of EOF3; dashed lines are contours of EOF4. Contours are in units of 0.5 $m\ s^{-1}$; vertical lines indicate positions of time-mean jets.

In addition to the spatial patterns shown above, I examine the temporal structure of the variability. Figure 3-13 shows the principal component timeseries associated with each of the four EOFs. The first two patterns are clearly more slowly varying than the third and fourth patterns. I further investigate this by examining the autocorrelation of the first four patterns (Figure 3-14). EOFs 1 and 2 decay slowly, with the decorrelation of EOF1 being about 58 days and EOF2 48 days. Their decorrelations follow approximately exponential curves. EOFs 3 and 4 decorrelate much more rapidly — their e-folding times are 7 days and 6 days, respectively. These two curves are less exponential than the former two — each features a plateau in the decorrelation at about 20 days.

The long decorrelation timescale is one area where the model deviates significantly from observations (Gerber et al., 2007). Feldstein (2000) found that the decorrelation time of the northern annular mode at the surface was about 10 days. Similarly, Baldwin et al. (2003) found decorrelation values for the annular mode in the troposphere to range from 10 to 20 days, depending on season and atmospheric level. In any case, the timescales obtained here are about four to six times too long as compared to observations. This finding in the model data has necessitated the long model runs.

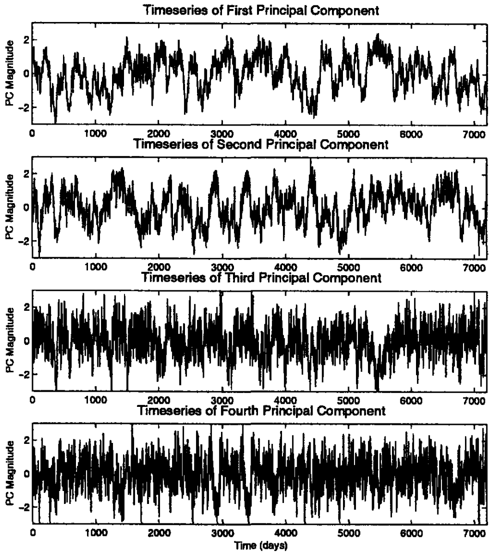

Figure 3-13: Principal component timeseries associated with first four EOFs. Magnitude is non-dimensional.

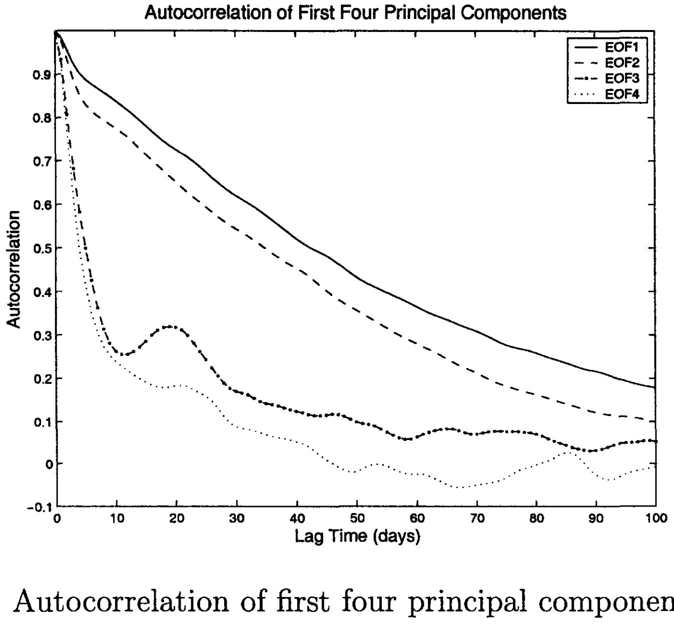

Figure 3-14: Autocorrelation of first four principal component timeseries.

However, the distribution of positive and negative events in the model's annular modes more closely resembles those found in real life. Figure 3-15 are histograms, showing the number of days in the 7,200 day model run for which the value of the principal component timeseries associated with EOF1 and EOF2, respectively, was of a certain value. They are similar to the distributions of the AO maintained by Baldwin, and the SAM maintained by the NCDC (Figure 3-16). The figure containing the observed data is provided courtesy of R. A. Plumb.

The distribution of events is unimodal in each hemisphere. Both EOFs of the model data have a median value tilted toward the positive phase, and this tendency is stronger in EOF1 than EOF2. While the distributions are skewed, they show no evidence of a bimodal probability distribution where the patterns favor either a strongly positive or negative phase.

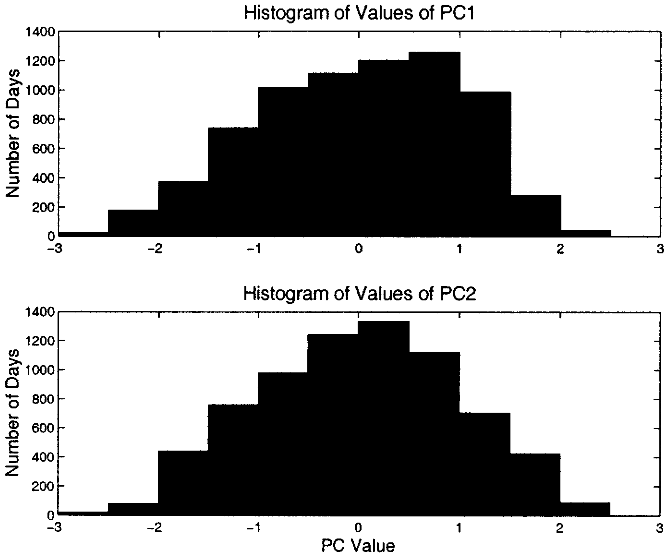

Figure 3-15: Histograms indicating number of days for which the value of PC1 (top) and PC2 (bottom) fell between the indicated values.

Next, I examine the variability found in the eddies. The leading EOFs of the E-P flux divergence are dipolar with height in each hemisphere, showing increased eddy generation at lower altitudes and dissipation at upper altitudes. These results are not particularly elucidating for understanding the variability of the annular modes, so instead I will examine the cross-covariance of zonal wind and E-P flux divergence.

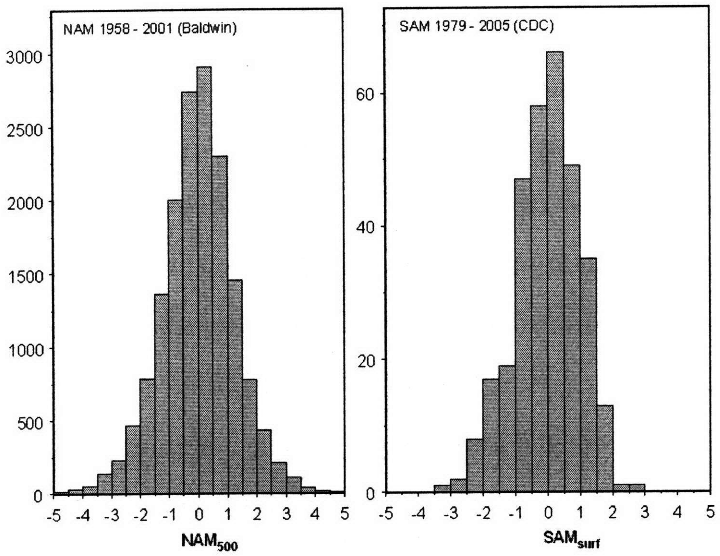

Figure 3-16: (Left) Histogram of the daily PC value of NAM at 500 hPa, as compiled by Baldwin. (Right) Histogram of monthly mean value of SAM at surface, as compiled by NCDC. Figure courtesy of R. A. Plumb.

A singular value decomposition (SVD) of the cross-covariance matrix between the zonal wind and E-P flux divergence anomalies is computed, according to the procedure in Bretherton et al. (1992). As shown by those authors, the left singular vectors found from this analysis will contain information on one of the variables (here, the zonal-mean zonal wind) and the right singular vectors will contain information on the other (here, the E-P flux divergence). The zonal wind patterns contained in the first few left singular vectors are virtually identical to the EOFs of the zonal wind, but the E-P flux divergence patterns obtained from the right singular vectors are quite different than those found through the EOF analysis of that field.

The first and second patterns of E-P flux divergence obtained from the SVD analysis are shown in Figure 3-17. The patterns are multiplied by $(a\cos\phi)^{-1}$, so they reflect the acceleration of zonal wind suggested by the divergence. Again, the first pattern occurs in the SH, the second pattern in the NH, and the two patterns are displayed on the same plot. In each hemisphere, the leading pattern shows a strong dipole near the surface, in the region of eddy generation, suggesting the eddy generation migrates with the zonal jet. On the poleward side of the jet's time-mean position, there are positive E-P flux divergence anomalies, suggesting increased eddy generation and a westerly torque on the zonal flow there. On the other side of the jet is anomalous convergence, and hence, an easterly forcing of the zonal flow. There is evidence of a similar dipole at the tropopause level as well, though the structure of the patterns in the middle troposphere is more complex.

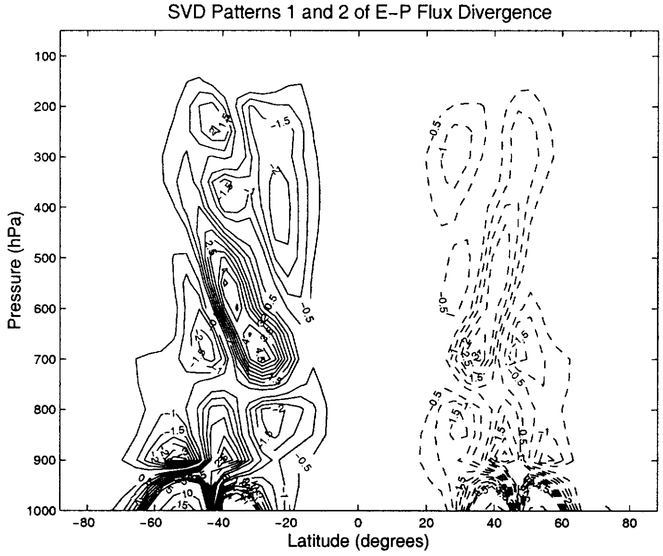

Figure 3-17: Leading spatial patterns of E-P flux divergence anomalies derived from SVD analysis with the zonal wind anomalies. Solid lines indicate the leading pattern; dashed lines indicate the second pattern. Contour interval is 0.5 $m\ s^{-1}\ day^{-1}$ acceleration of zonal wind until 5 $m\ s^{-1}\ day^{-1}$ and 5 $m\ s^{-1}\ day^{-1}$ thereafter.

To better understand the effects of the E-P flux divergence anomalies, the patterns shown in Figure 3-17 are added to (Figure 3-18) and subtracted from (Figure 3-19) the climatological E-P flux divergence shown in Figure 3-5. Addition of the SVD anomalies to the climatological divergence causes the region of maximum baroclinic eddy generation to shift poleward with the wind. In each hemisphere, for example, the 60 $m\ s^{-1}\ day^{-1}$ contour spans the the $40° - 60°$ range at the surface when the SVD patterns are added. Upon subtraction of the pattern, however, this contour does not reach 60° in either hemisphere but dips well equatorward of 40° in both hemispheres.

The migration of regions of E-P flux convergence may be noted in the upper troposphere. The regions of convergence between 20° and 30° and 500 hPa and 200 hPa are much stronger when the anomalies are added rather than subtracted. On the other hand, the regions of convergence exceeding 12 $m\ s^{-1}\ day^{-1}$, which occur in the mid-latitudes, are more expansive when the SVD anomalies are subtracted rather than added. This is especially noticeable in the SH, and indicates that when the zonal wind shifts poleward, E-P flux convergence in the upper troposphere shifts equatorward, and vice-versa. Hence, when the annular mode is in its positive phase, there is anomalous E-P flux *divergence* in the mid-latitudes. When the annular mode is in its negative phase, this anomalous divergence is found in the subtropics. Both the surface baroclinic zone and the regions of anomalous E-P flux divergence in the upper troposphere are seen to move in conjunction with the shifts of the jet described by the annular modes.

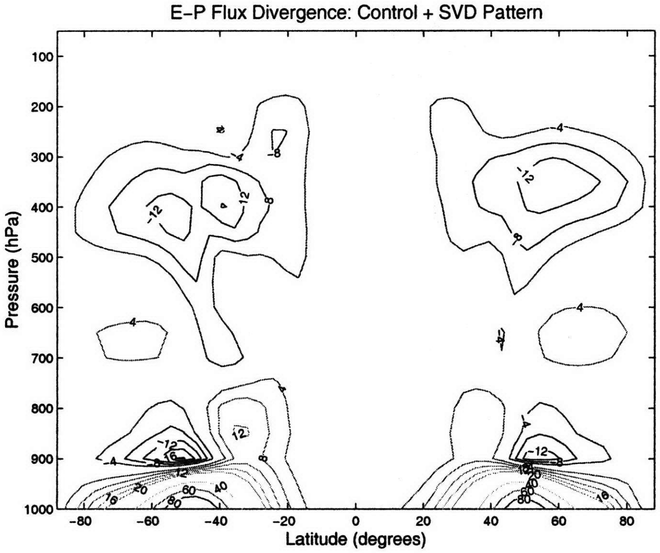

Figure 3-18: Anomalous E-P flux divergence found in SVD patterns 1 and 2 added to the climatological E-P flux divergence. Contour interval 4 $m\ s^{-1}\ day^{-1}$ acceleration of zonal wind until 20 $m\ s^{-1}\ day^{-1}$ and 20 $m\ s^{-1}\ day^{-1}$ thereafter.

As an additional check on the behavior in the upper troposphere, I perform SVD analysis on the cross-covariance between the zonal wind and the barotropic divergence. The leading barotropic divergence patterns found through this analysis are shown in Figure 3-20. Near the level at which the jet is strongest, anomalous divergence is found poleward of the jet center, and anomalous convergence equatorward of the jet center. The dipoles of barotropic divergence tilt toward the equator as one approaches the ground, but at middle and lower levels of the model atmosphere the contribution from the baroclinic divergence is larger.

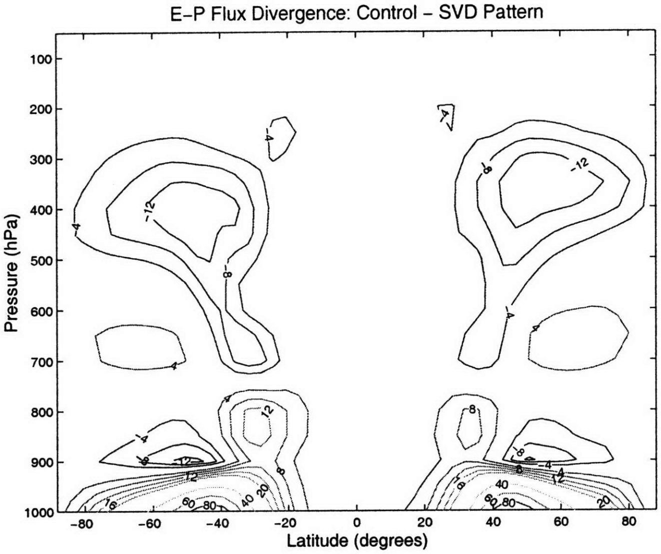

Figure 3-19: As in Figure 3-18, but for the patterns found in SVD patterns 1 and 2 subtracted from the climatological E-P flux divergence. Contour interval 4 $m\ s^{-1}\ day^{-1}$ acceleration of zonal wind until 20 $m\ s^{-1}\ day^{-1}$ and 20 $m\ s^{-1}\ day^{-1}$ thereafter.

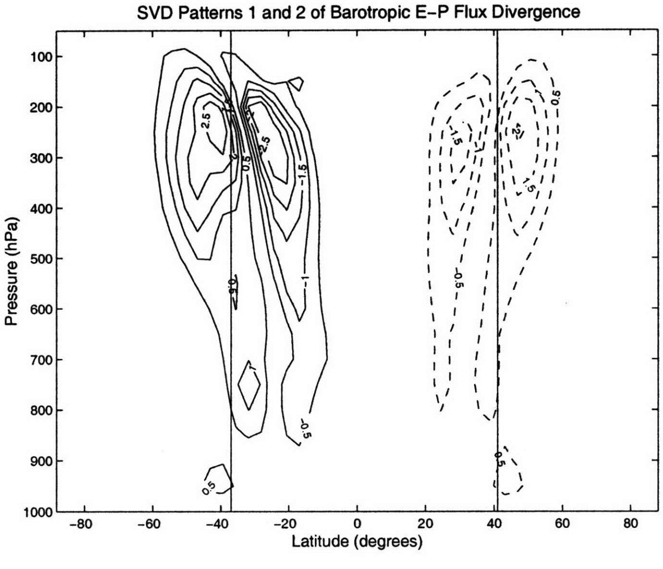

Figure 3-20: Leading spatial patterns of barotropic E-P flux divergence anomalies derived from SVD analysis with the zonal wind anomalies. Solid lines indicate the leading pattern; dashed lines indicate the second pattern. Contour interval is 0.5 $m\ s^{-1}\ day^{-1}$; solid vertical lines are positions of the time-mean jets.

The graphs in Figure 3-21 show the E-P flux divergence found from the SVD patterns, averaged over all pressure levels for each latitude. The anomalies are again weighted by $(a \cos \phi)^{-1}$ so as to show the zonal wind tendency. The results in Figure 3-21 again emphasize that the eddy forcing which seeks to accelerate the zonal wind migrates along with the zonal wind. These results demonstrate a positive correlation between the zonal wind and E-P flux divergence.

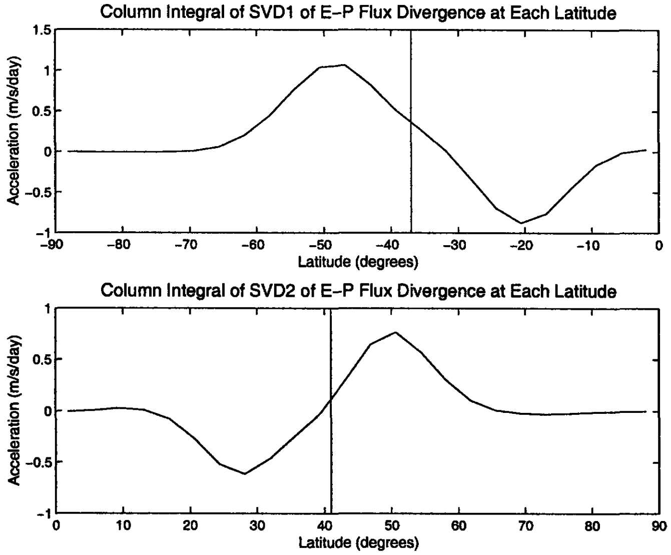

Column Integral of SVD1 of E–P Flux Divergence at Each Latitude

Column Integral of SVD2 of E–P Flux Divergence at Each Latitude

Figure 3-21: (Top) E-P flux divergence anomalies from SVD1 pattern averaged over all pressure levels for each latitude. Vertical black line is position of time-mean SH jet. (Bottom) As in top panel, except for SVD2 pattern and NH.

Finally, I examine the timescales associated with the E-P flux divergence. In Figure 3-22, the cross-correlations of the timeseries associated with the left singular vectors (wind patterns) and right singular vectors (E-P flux divergence patterns) are shown. In both hemispheres there is a remarkable persistence, with the anomalies decaying much more slowly than would be expected by considering Earth's annular modes. These results, as do those shown in Figure 3-14, reinforce the need for long model runs to compensate for the persistence of the annular mode patterns.

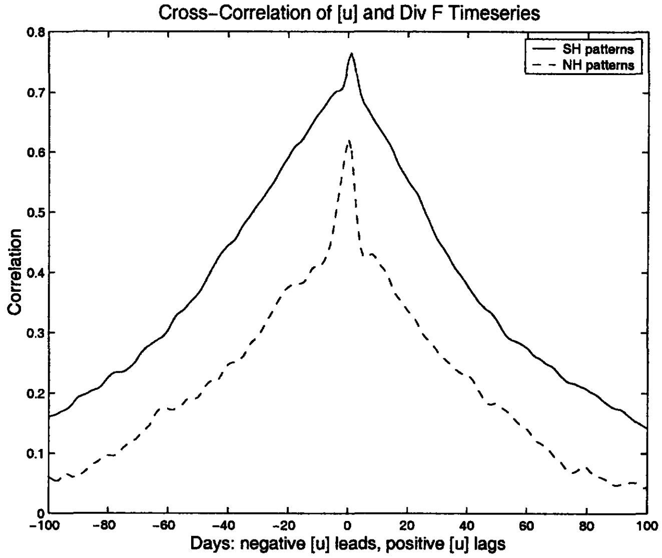

Figure 3-22: Cross-correlation of timeseries associated with the first (solid line) and second (dashed line) singular vectors of wind and E-P flux divergence.

3.5 Summary

In this chapter, I have examined the climatology of a model run with no external forcing applied. The model produces a climatology similar to that of Earth, although differences of course do exist. The means shown here are highly zonal and reproducible from smaller segments of the model climatology. The most prominent features in each hemisphere are the westerly jets, each associated with E-P flux divergence.

Next I examine the variability in each hemisphere, using EOF and SVD analysis. The model produces EOF patterns similar to those observed on Earth in the various meteorological fields. The two strongest EOFs are the dipoles — one in the winter hemisphere and one in the summer hemisphere — associated with the wobble of the jet about its time-mean position. Through SVD analysis, it is shown that both the surface baroclinic zone and a region of anomalous E-P flux divergence in the upper troposphere shift along with the wind.

The most crucial difference between the model's annular modes and those of the real atmosphere is that the decay timescales of the former are much longer than those of the latter. Hence, here and in the upcoming forced trials, long climatologies will be necessary to compensate for the unrealistically long annular mode timescales.

With the discussion of the control climatology complete, I will examine in the next chapter a suite of trials under which the model is subjected to an applied angular momentum forcing.

Chapter 4

Mechanically Forced Trials

4.1 Introduction

In this chapter, I present the results of a number of trials under which the model is subjected to an imposed, external momentum forcing. The differences between the climatologies here and that of the control run are generally annular mode-like, suggesting the patterns are preferred responses of the model to a generic perturbation.

The first section of this chapter discusses the torques applied in these cases. I next illustrate extensively the climatology of a single run which is typical of the broader group. Then I examine the changes between the forced trial and control run found in all the trials performed.

4.2 Nature of the Applied Forcing

I choose a forcing which is designed not to mimic the nature of the annular modes. Specifically, while the annular modes are dipolar in each hemisphere, the applied torque is monopolar in each hemisphere. For each trial, a torque is added to the SH and a torque of equal strength but opposite polarity added to the NH, so no net angular momentum is added globally to the model.

A number of trials are conducted for which the applied torque looks like a bullseye. These forcings are similar to those used by Song and Robinson (2004). For these trials,

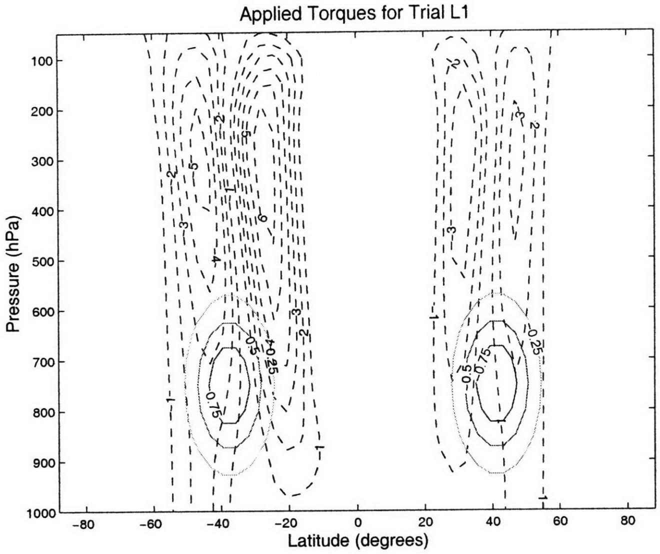

Figure 4-1: Torque applied in Trial L1. Forcing contours are in $m\ s^{-1}\ day^{-1}$ tendency of angular momentum, divided by Earth's radius. Dotted lines are leading EOFs of zonal-mean zonal wind.

the torque applied is independent of longitude, and Gaussian in latitude and pressure. The forcing magnitude decays to $1/e$ of its maximum value over about 11° of latitude and 150 hPa in the vertical. Illustrations of the torques in two of these trials are shown in Figures 4-1 and 4-2, respectively.

In the first suite of trials, the strength of the torque, in terms of rate of change of angular momentum, is held fixed, and the placement of the torque is varied. The westerly torque is added to the SH and the easterly torque to the NH. I choose trials with the torques in both the lower and upper atmosphere, at the centers of the jets and on the poleward and equatorward flanks of the jets. These trials are summarized in Table 4.1, found in Section 4.4 below.

I examine a second set of model runs with a different shape of torque. Specifically, these trials use barotropic forcing, in which the strength of the torque is held fixed with height. The forcings in these trials retain the Gaussian decay of strength with latitude. The total amount of torque, integrated over the pressure column, applied in these trials is equal to that of the analogous trials with bullseye-shaped forcings. Table 4.2, in Section 4.5 below, lists these trials.

Finally, the third set of trials in this chapter examines a set of runs for which the

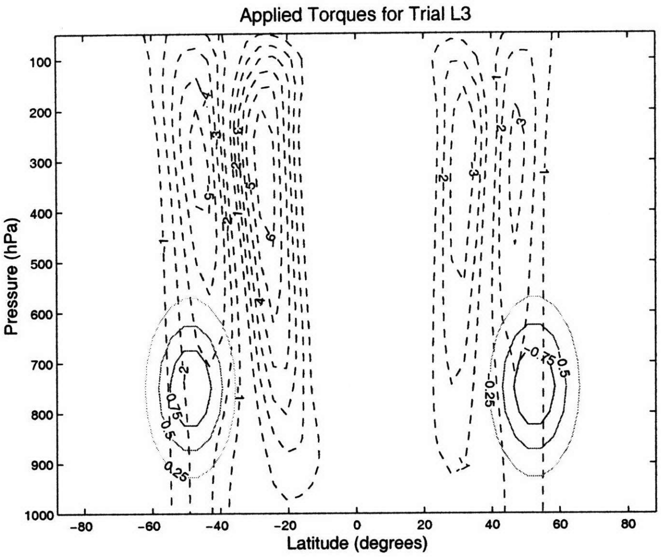

Figure 4-2: As in Figure 4-1, but for Trial L3.

position of the torque is held fixed (at the location of the forcing in Figure 4-2) but the magnitude of the torque is changed for each model run. A list of these trials is presented in Table 4.3 in Section 4.6.

In all of the aforementioned trials, the forcing is switched on smoothly over a period of 20 days, then held fixed. A climatology of the model is then compiled after granting a sufficient time to allow the model to spin up. In most of the trials presented below, this period for which the climatology is compiled is 5,000 days, but for several trials (which will be noted below) a 7,000 day climatology is used. Selected trials were repeated using a lengthened period over which the forcing was turned on, but this change did not result in climatologies statistically different from those obtained using the 20-day switch-on period.

4.3 Climatology of an Example Run

I examine in detail the climatology of the case which was forced with torques centered in the lower troposphere, on the jet's poleward flank (Trial L3). The climatology of this trial is typical of the other forced cases. The climatology produced by the model under the influence of the forcing is similar to that of the control run; hence the effect of the applied torque is a modification, but not a drastic shift, of the fields produced in the control trial.

The time-mean zonal-mean zonal wind found in Trial L3 is shown in Figure 4-3. The wind profile is similar to that of the control trial (Figure 3-1). As in the control case, the most prominent features are the westerly jets in each hemisphere, associated with the eddy momentum fluxes. The SH jet is slightly stronger and appears several degrees poleward of its position in the unforced climatology. The NH jet, in contrast, appears a few degrees equatorward of its former position. Similarly, the surface midlatitude westerlies in the SH here are stronger than in the control case, while the NH surface westerlies are weaker than those in the control run.

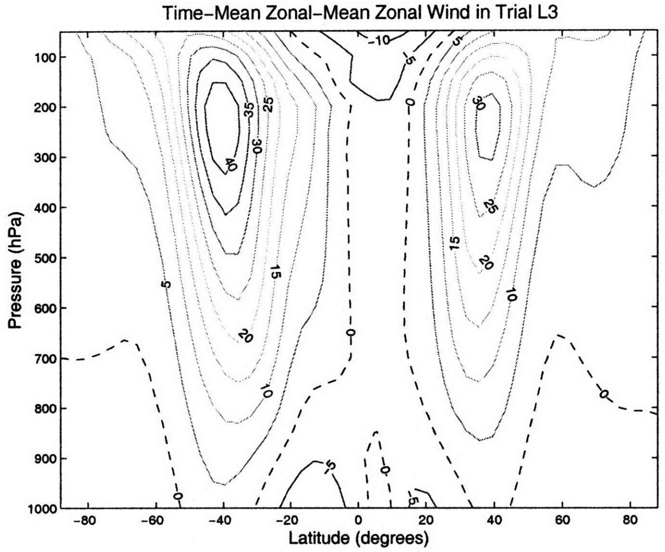
Time-Mean Zonal-Mean Zonal Wind in Trial L3

Figure 4-3: Zonal- and time-mean zonal wind for Trial L3. Contour interval is 5 $m\ s^{-1}$; zero contour is dashed.

The climatological meridional streamfunction for Trial L3 is shown in Figure 4-4. The overturning circulation is similar to that found in the control trial (Figure 3-3). The largest upward flow still occurs in the tropical NH, with the strongest sinking motion in the subtropical SH.

The zonal-mean, time-mean temperature found in Trial L3 is shown in Figure 4-5. As with the previous two figures, the climatology displayed is similar to that found in the control model run (Figure 3-4). The warmest point in the model atmosphere is

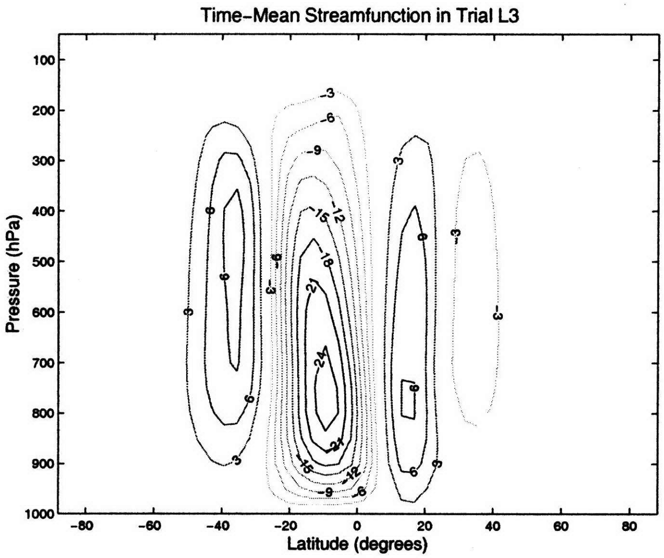

Figure 4-4: Climatological streamfunction for Trial L3. Contour interval is $3 \times 10^{10}\ kg\ s^{-1}$; zero contour is omitted.

still found in the NH. The nearly flat tropical meridional temperature gradients and the 20 K difference between the North and South Poles are noted here, as they were in the control.

The time-mean E-P flux and divergence produced in Trial L3 are shown in Figure 4-6 (compare to the unforced run in Figure 3-5). Again, strong divergence at the surface in the mid-latitudes is prominent, with upward and equatorward propagation of eddies and the strongest convergence in the upper troposphere. The barotropic portion of this divergence (Figure 4-7) comprises a pattern similar to that of the unforced model run (Figure 3-6), with somewhat larger extrema of divergence in the SH, and somewhat smaller extrema in the NH.

The zonal-mean fields produced by the model under the influence of the torque are similar to those of the control climatology. Examination of cross-sections in longitude and latitude indicate that, as in the control run, the time-mean flow in Trial L3 is highly zonal. Figures 4-8 and 4-9 display the time-mean zonal wind at 250 hPa and temperature at 750 hPa, respectively. As in the control run (Figures 3-7 and 3-8), there is no discernible longitudinal structure in the fields. A Fourier analysis of the time-mean zonal wind field at 250 hPa and 37° S (Figure 4-10) is similar to that of

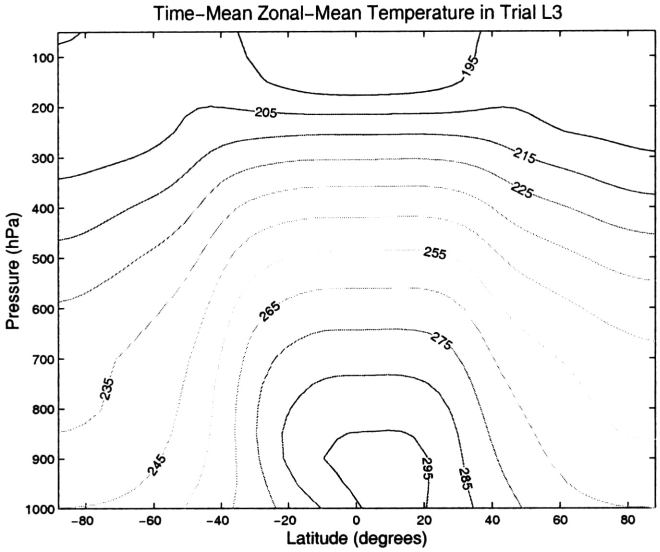

Figure 4-5: Climatological temperature for Trial L3. Contour interval is 10 K.

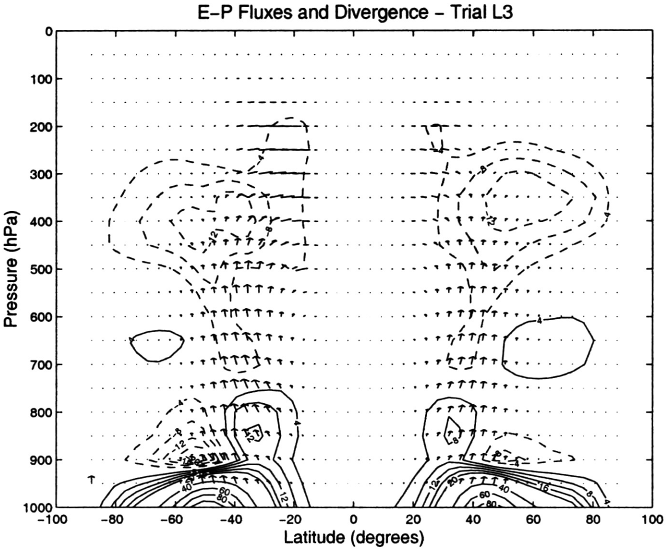

Figure 4-6: Time-mean E-P fluxes and divergence from Trial L3 with vectors plotted according to the scaling in Edmon et al. (1980). Divergence is contoured; interval is 4 $m\ s^{-1}\ day^{-1}$ acceleration of zonal wind until 20 $m\ s^{-1}\ day^{-1}$ and 20 $m\ s^{-1}\ day^{-1}$ thereafter. Negative contours are dashed and zero contour is omitted. Arrows represent E-P flux; sample arrow at bottom left represents $5 \times 10^{20}\ m^3\ Pa$ of upward flux; an equivalent length in the horizontal represents $6.47 \times 10^{15}\ m^3$ of meridional flux.

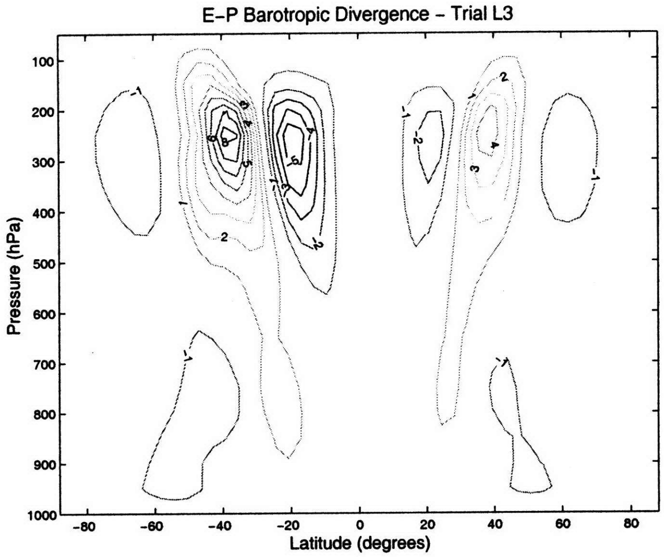

Figure 4-7: Time-mean barotropic E-P flux divergence for Trial L3. Contour interval is 1 $m\ s^{-1}\ day^{-1}$ acceleration of zonal wind. Zero contour is omitted.

the control run as well (Figure 3-9).

Having shown that the nature of the time-mean fields in the forced case is similar to that of the control run, I next examine the variability found in Trial L3, using the same procedures outlined in Chapter 3. As in the control trial, the variability of Trial L3 is composed primarily of the annular modes.

Figure 4-11 displays the first two EOFs of zonal-mean zonal wind anomalies for the data in Trial L3. As with the patterns in the control run (Figure 3-11), the means are removed and the data weighted by the square root of the cosine of latitude before computing the EOFs. The leading EOFs are dipoles, indicating the wobble about the jet's time-mean position as in the control case. The amount of variability explained by each pattern (49 percent for EOF1 and 18 percent for EOF2) is very close to that of the control case. EOFs 3 and 4 (explaining 12 percent and 4 percent of the variability, respectively) also have the expected tripole shape in each hemisphere (Figure 4-12).

The decorrelation times of the wind patterns in Trial L3 are longer than those of the observed annular modes, as seen in Figure 4-13. Here the first principal component of zonal wind has an e-folding timescale of about 55 days, while the second principal

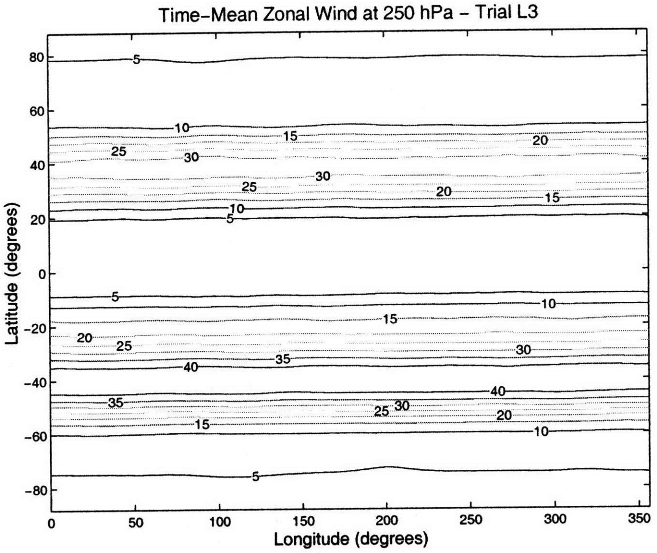

Figure 4-8: Time-mean zonal wind at 250 hPa from Trial L3. Contour interval is 5 $m\ s^{-1}$.

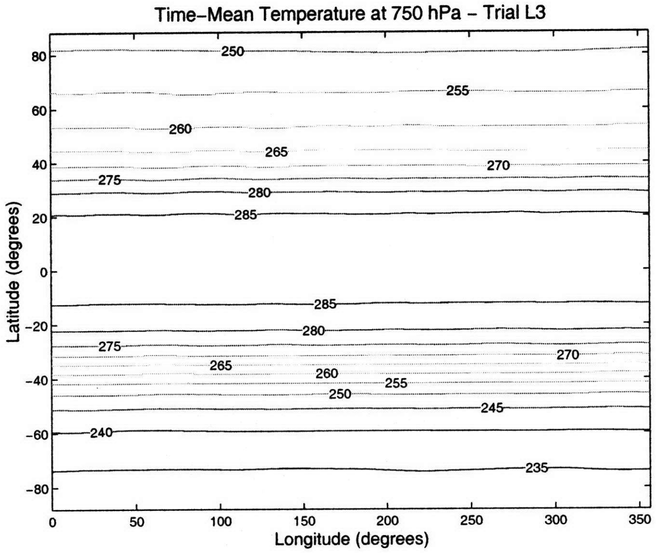

Figure 4-9: As in Figure 4-8, but for the time-mean temperature at 750 hPa. Contour interval is 5 K.

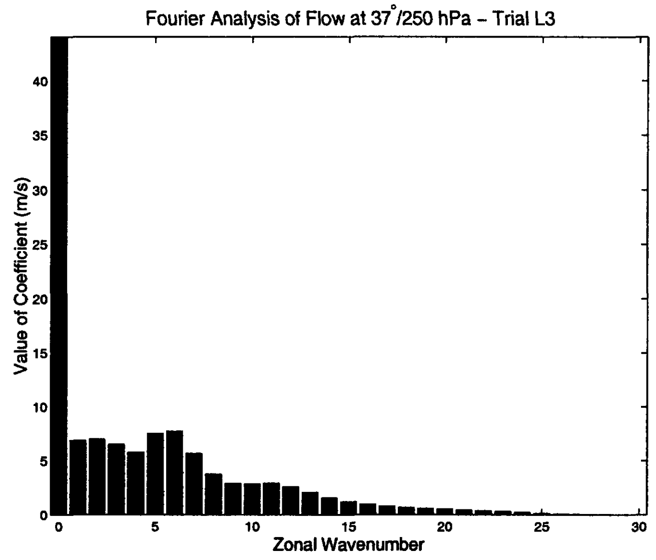

Figure 4-10: Fourier coefficients for the zonal wind at 37° S and 250 hPa for Trial L3. The coefficients are computed daily, and the mean of their absolute value for each wavenumber is plotted.

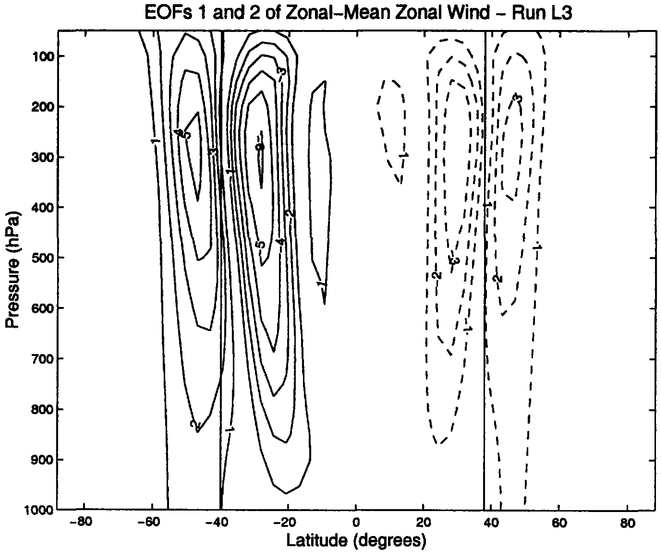

Figure 4-11: First and second EOFs of zonal-mean zonal wind anomalies in Trial L3. Solid lines are contours of the leading EOF; dashed lines are contours of the second EOF. Contours are in units of 1 $m\ s^{-1}$; vertical lines indicate positions of time-mean jets.

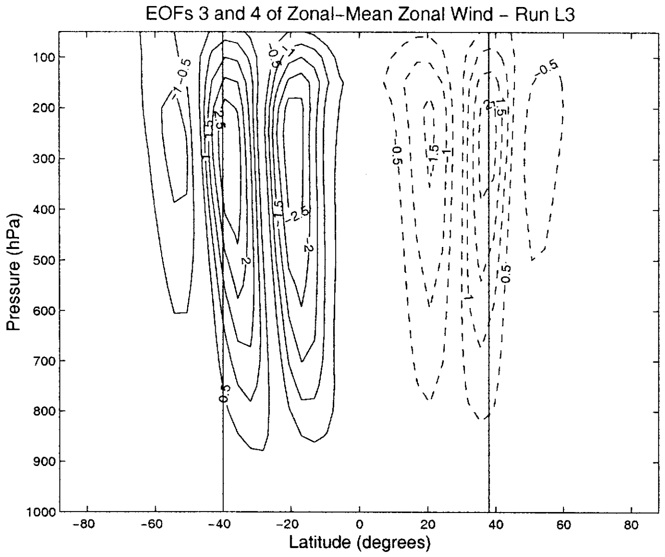

Figure 4-12: As in Figure 4-11, but for EOFs 3 and 4 of the zonal-mean zonal wind anomalies. Solid lines are contours of EOF3; dashed lines are contours of EOF4. Contours are in units of 0.5 $m\ s^{-1}$; vertical lines indicate positions of time-mean jets.

component features a timescale of about 45 days. These timescales are similar to those computed for the control run (Figure 3-14).

The singular value decomposition of the cross-covariance matrix between the zonal-mean zonal wind anomalies and E-P flux divergence anomalies (Figure 4-14) reveals patterns similar to those seen in the control run (Figure 3-17). The shift of E-P flux divergence at the surface, as well as a similar pattern in the upper troposphere associated with the barotropic component of the divergence, are again both present.

In summary, the climatology produced in Trial L3 is similar to that of the control. Westerly jets associated primarily with the convergence of eddy fluxes are the dominant feature in each hemisphere. The time-mean flow is highly zonal, and most of the variability in the climatology is expressed by the annular modes, now centered about the new positions of the time-mean jets. These results are typical of those for the other model runs.

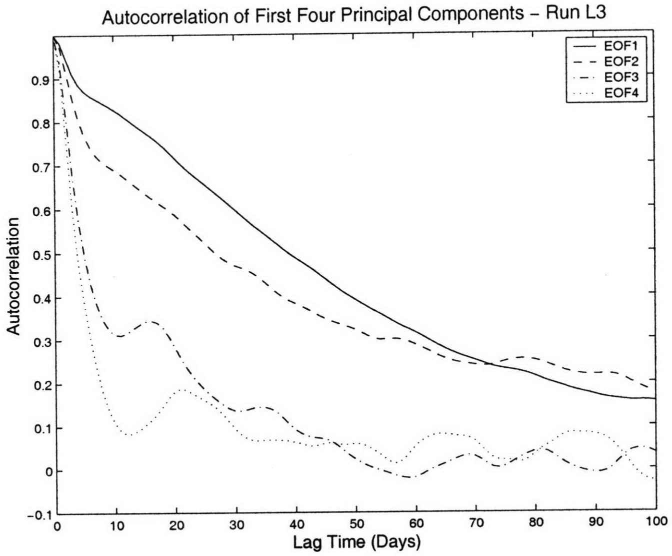

Figure 4-13: Autocorrelation of first four principal component timeseries from Trial L3.

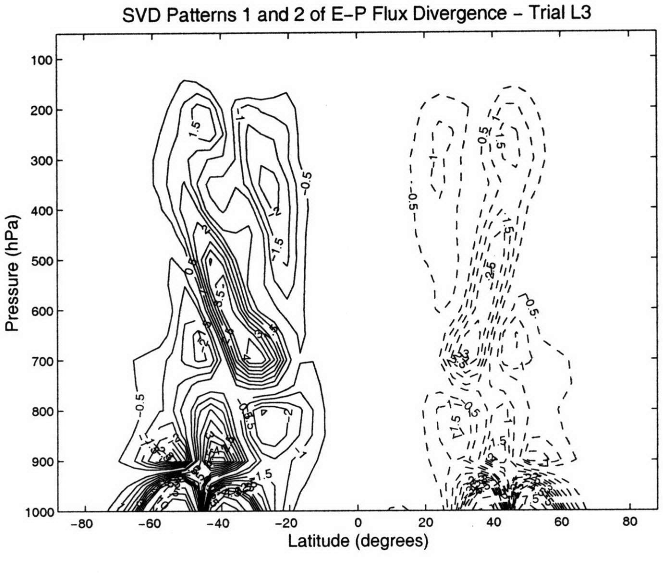

Figure 4-14: Leading spatial patterns of E-P flux divergence anomalies derived from SVD analysis with the zonal wind anomalies in Trial L3. Solid lines indicate the leading pattern; dashed lines indicate the second pattern. Contour interval is 0.5 $m\ s^{-1}\ day^{-1}$ acceleration of zonal wind until 5 $m\ s^{-1}\ day^{-1}$ and 5 $m\ s^{-1}\ day^{-1}$ thereafter.

Trial Number	Latitude of Forcing Center	Level of Forcing Center
L1	jet center	750 hPa
L2	jet center	250 hPa
L3	11° poleward of jet center	750 hPa
L4	11° poleward of jet center	250 hPa
L5	11° equatorward of jet center	750 hPa
L6	11° equatorward of jet center	250 hPa
L7	5.5° poleward of jet center	750 hPa
L8	16.5° poleward of jet center	750 hPa

Table 4.1: Summary of trials with imposed vertically localized angular momentum forcings of peak magnitude 1 $m\ s^{-1}\ day^{-1}$.

4.4 Differences in Climatologies for Variation of Forcing Location

Having discussed the climatology of a typical forced model run, I now turn attention to the differences between the forced model runs and the control trial. For most trials, the differences in the climatologies are expressed as the annular mode patterns, indicating that the annular modes are indeed a preferred response of the model to the forcing. The trials in this section use the Gaussian-bullseye forcing, and while the forcing magnitude is held fixed among the trials, the location of the forcing is varied, as summarized in Table 4.1. A 5,000 day climatology is obtained for most trials; Trial L6 uses a 7,000 day climatology.

Before beginning the discussion of changes to the zonal-mean fields, I note that the changes in the climatologies between the forced runs and the control run display a high degree of zonality. As an example, I plot the difference in time-mean zonal wind at 250 hPa between Trial L3 and the control in Figure 4-15. The belts of anomalous zonal wind circle the globe, and the zonal variation seen in the anomalous belts is much weaker than the mean values in those regions. As noted before, these results should not be surprising given the zonally symmetric setup of the model and the longitudinal symmetry of the forcing applied. Confirming the symmetry in the difference fields allows for a zonal-mean perspective to be taken, as shall be done in

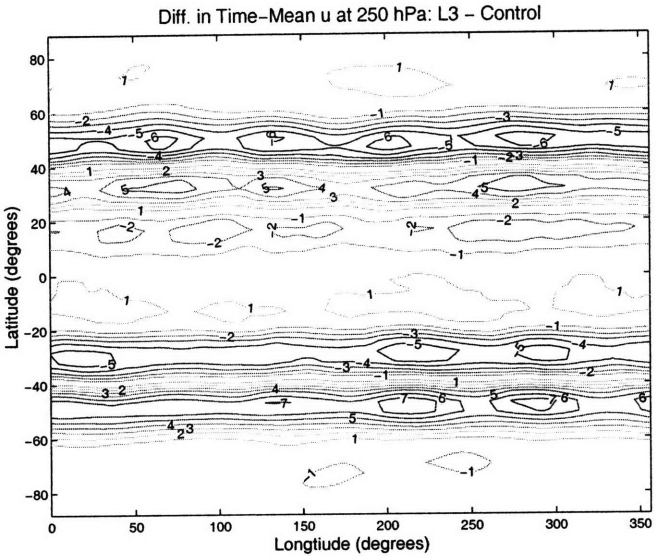

Figure 4-15: Change in time-mean zonal wind at 250 hPa for Trial L3 versus the control. Contour interval is 1 $m\ s^{-1}$.

the rest of this section.

The changes in zonal-mean zonal wind between the forced and control model runs are shown in Figures 4-16 (for Trials L1 through L4) and 4-17 (for Trials L5 through L8). Six of the eight trials with the bullseye forcing varying by location feature anomalous wind responses which look like the annular modes.

In Trials L3 through L8, the differences in the time-mean, zonal-mean zonal wind as compared to the control run are annular mode-like. These trials feature dipoles of anomalous wind in each hemisphere arising in response to the monopolar forcing. The magnitude of the response varies from trial to trial, with responses as high as 10 $m\ s^{-1}$ (Trial L4) but weaker ($2 - 4\ m\ s^{-1}$) in other trials (L5 and L6). Still, the responses of the six forced runs all contain the essential features of the annular mode signature of the wind field — dipolar anomalies of zonal wind, extending through the model atmosphere, with a positive anomaly on one side of the unforced jet's time-mean position, a negative anomaly on the other side, and a node at the latitudinal position of the unforced jet. In these six trials, the annular mode patterns may also be found by comparing a smaller segment of the forced model's climatology to that of the control, suggesting these patterns are robust.

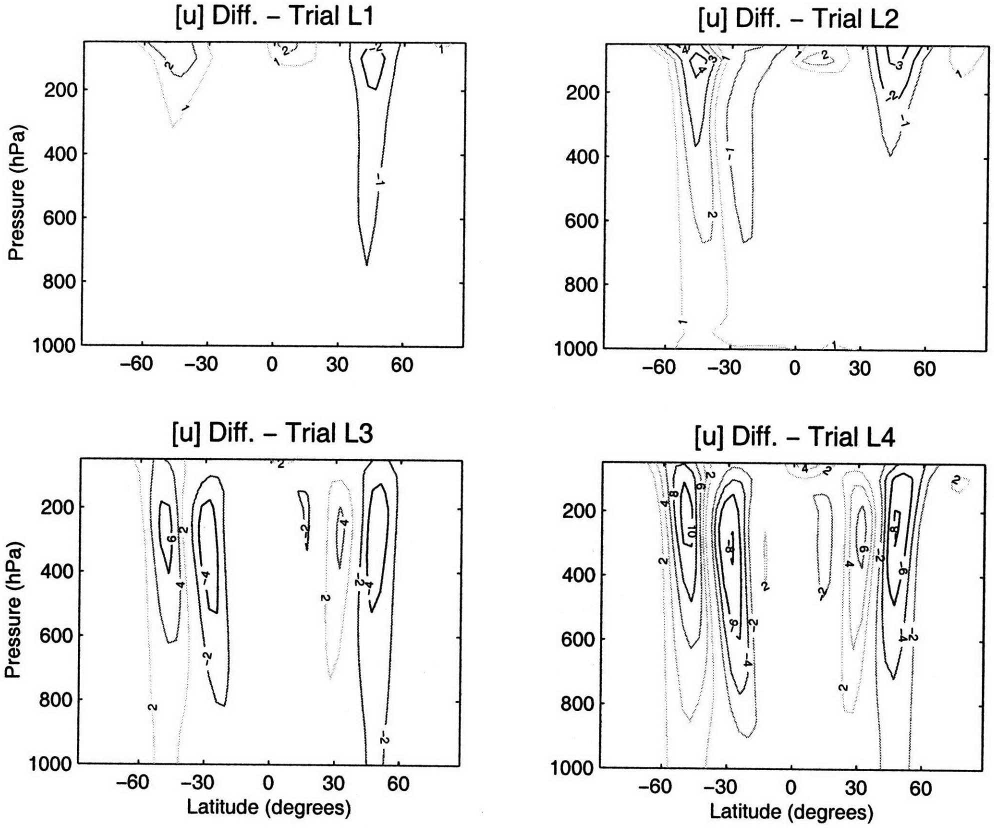

Figure 4-16: Change in time-mean zonal-mean zonal wind for the indicated trials versus the control. Contour interval is 1 $m\ s^{-1}$ in the upper two panels and 2 $m\ s^{-1}$ in the lower two panels.

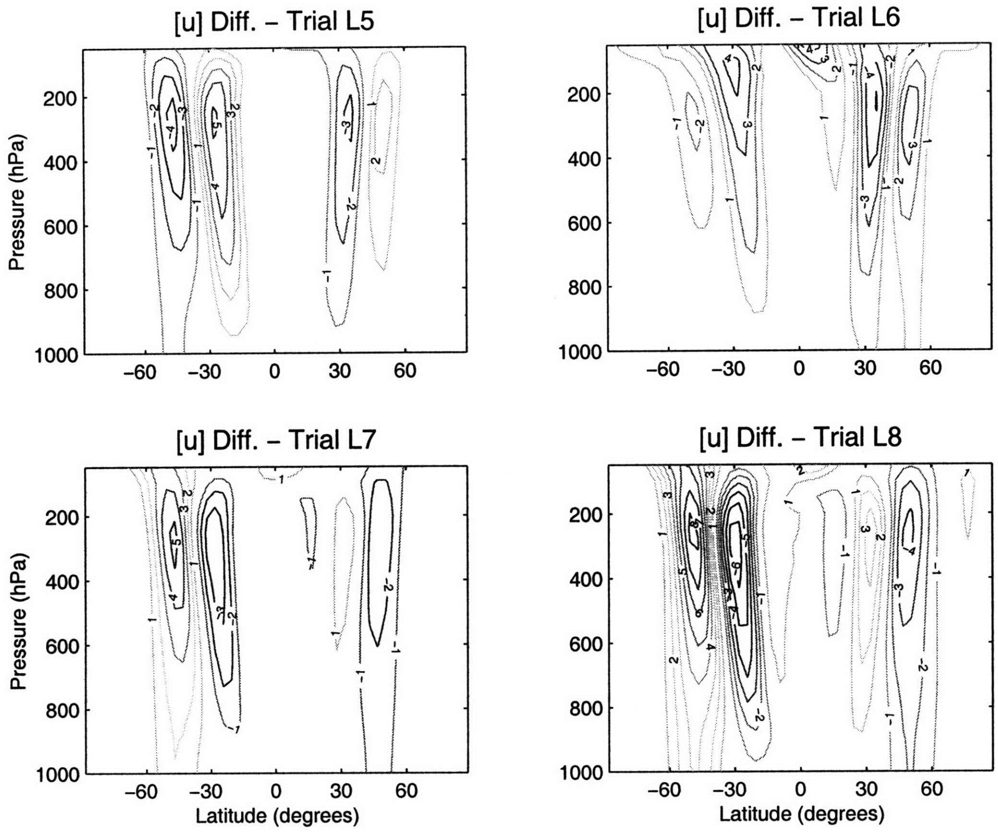

Figure 4-17: Change in time-mean zonal-mean zonal wind for the indicated trials versus the control. Contour interval is 1 $m\ s^{-1}$ for all panels.

In contrast, the zonal wind anomalies of Trials L1 and L2 do not display annular mode-like behavior. The closest analog among the results of the two trials may be found in the SH of Trial L2, where there is a dipolar structure in the upper troposphere. However, unlike the annular modes, this dipole does not extend all the way to the surface — the wind change in the lowest layers of the atmosphere is monopolar. Additionally, the responses found in the NH for Trial L2, and in both hemispheres for Trial L1, are monopolar and weaker in magnitude than those derived from the other six trials.

The next two figures examine the changes in streamfunction between the eight trials and the control. As may be expected from the wind changes displayed in Figures 4-16 and 4-17, there is a difference in the changes found for Trials L3 through L8 versus Trials L1 and L2.

In the six trials which feature the annular-mode like response, the change in streamfunction, is, at least to some extent, dipolar within each hemisphere. In some trials (L3 and L4) this behavior is very clear, while in other trials (L5 and L6) the picture is more muddied (in Trial L6, for example, the midlatitude response in the SH is weaker than $5 \times 10^9\ kg\ s^{-1}$). However, common features may be observed in the plots. A strongly anomalous cell is centered in the subtropics of each hemisphere, with another anomalous cell of opposite sign found in the mid-latitudes for each case.

These anomalies in the overturning circulation are associated with shifts in the locations of the overturning cells. Comparing the locations of the anomalies in Figures 4-18 and 4-19 with the control streamfunction in Figure 3-3 indicates the anomalies are large at nodal lines in the control streamfunction. In Trial L3, for example, the sinking in between the SH Hadley and Ferrel cells has shifted poleward of its positions in the unforced run, while the similar sinking in the NH has slid a few degrees equatorward.

The streamfunction changes for Trials L1 and L2, as shown in Figure 4-18, are different than those in the other six cases. The change in the SH of Trial L2 is dipolar but much weaker than many of the other examples considered, while the change in the NH is weak and strictly monopolar, as is the case for both hemispheres in Trial L1.

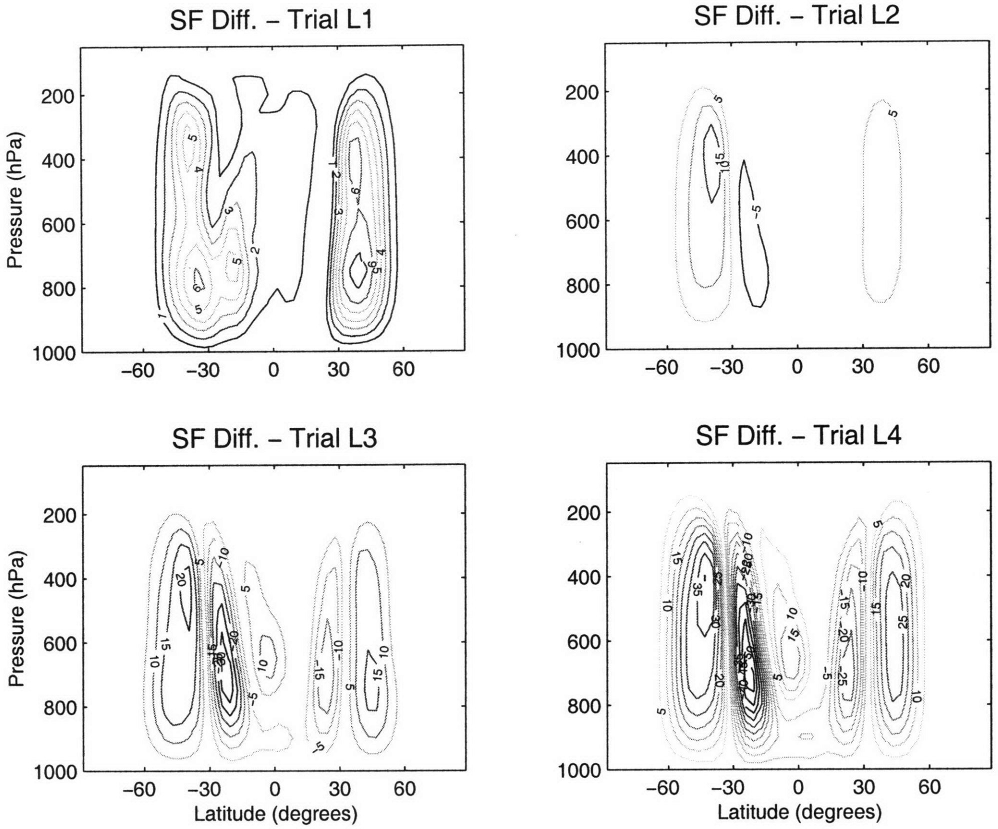
SF Diff. - Trial L1

SF Diff. - Trial L2

SF Diff. - Trial L3

SF Diff. - Trial L4

Figure 4-18: As in Figure 4-16, but for the change in streamfunction. Contour interval is 1×10^9 $kg\ s^{-1}$ in the upper left panel and 5×10^9 $kg\ s^{-1}$ in the other panels.

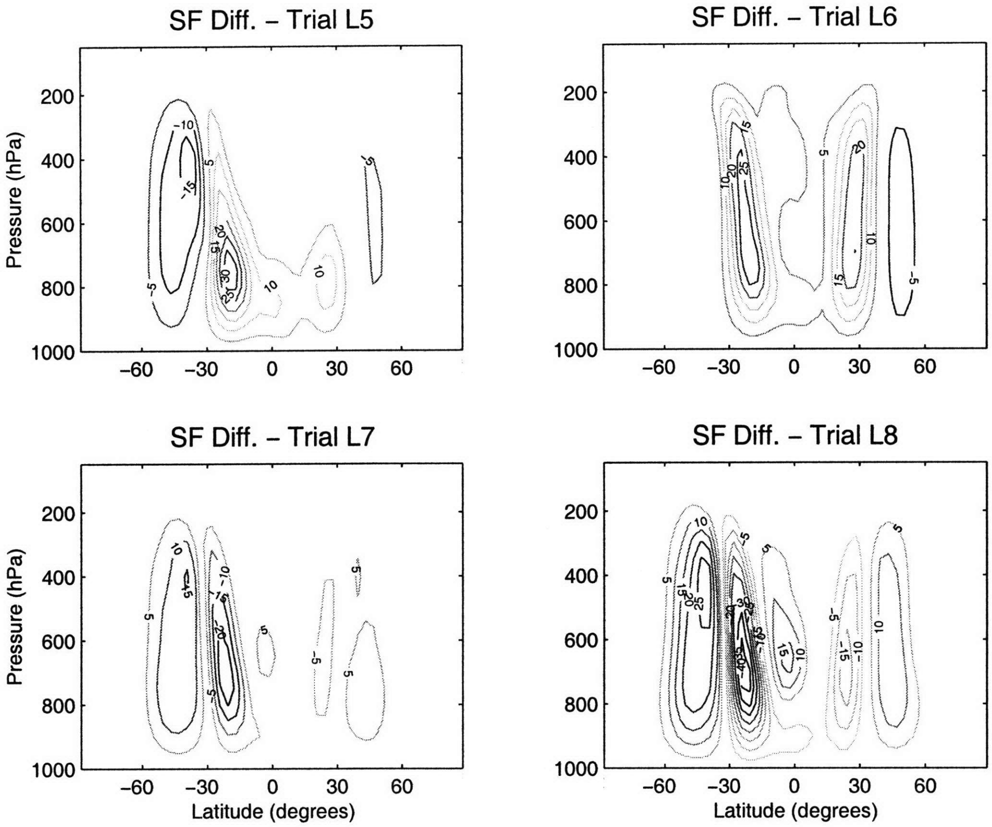

Figure 4-19: As in Figure 4-17, but for the change in streamfunction. Contour interval is 5×10^9 $kg\ s^{-1}$ in all panels.

Next, I consider the changes in zonal-mean temperature between each of the eight forced trials and the control run. These results are plotted in Figures 4-20 and 4-21. When the annular mode-like response is present, the most prominent feature in the temperature difference fields is a ribbon of anomalously warm or cold air centered at about 35° latitude, extending from the tropopause level to the surface. The anomaly reaches above 2 K in the trials with the strongest responses. This temperature anomaly is associated with dynamic warming or cooling resulting from the changes in pressure velocity associated with the overturning circulations. Generally, this is accompanied by a region of opposite-signed temperature anomalies on the poleward side of the ribbon, although this feature may be weak (Trials L5 and L6). As is typical of the other climatological fields, the differences in temperature between Trial L2 and the control bear some resemblance to that of the other trials in the SH but not in the NH. Trial L1 shows no evidence of the pattern in either hemisphere.

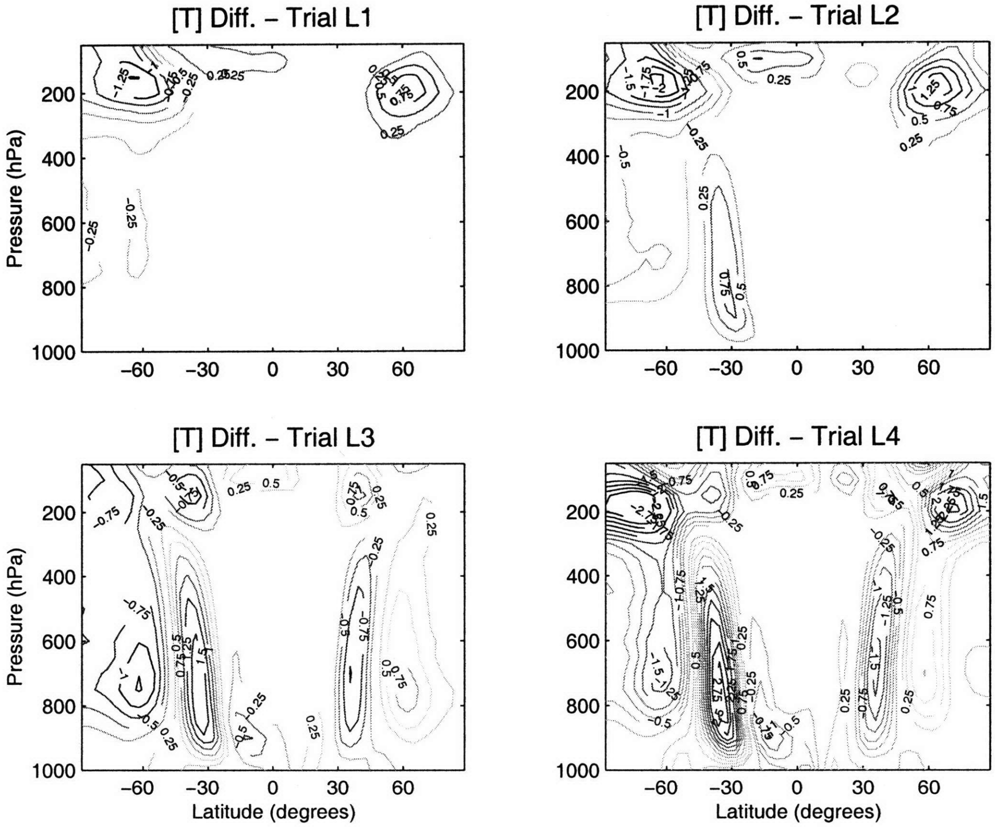

Figure 4-20: As in Figure 4-16, but for the change in temperature. Contour interval is .25 K in all panels.

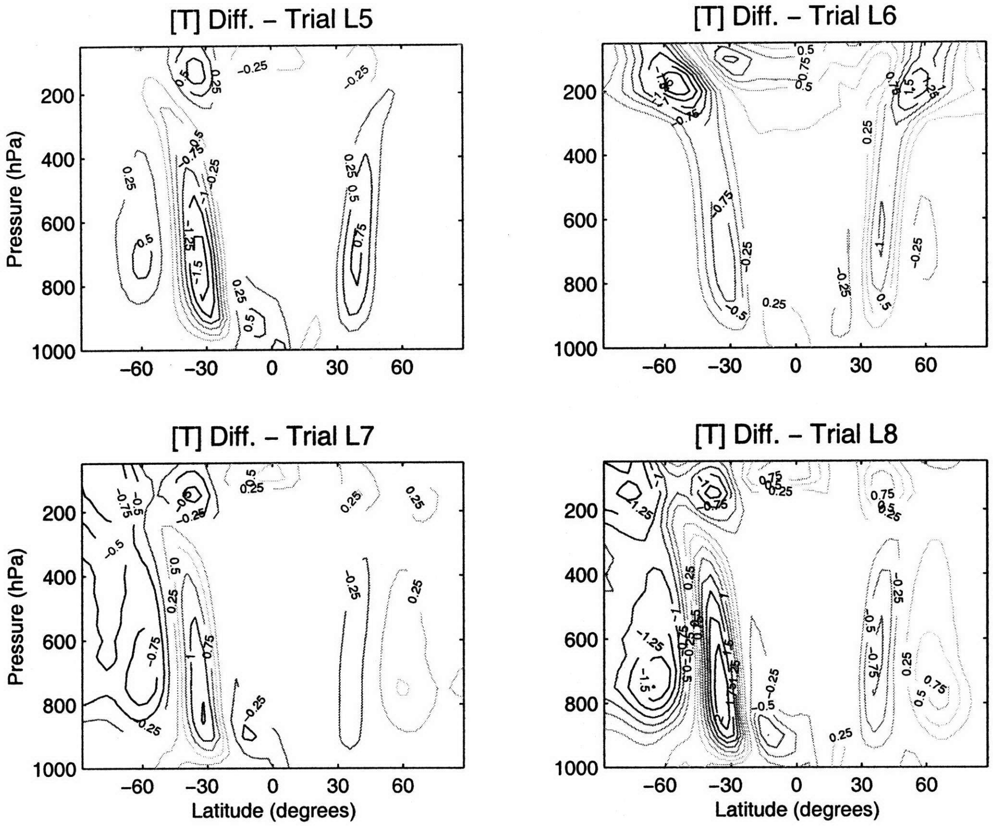

Figure 4-21: As in Figure 4-17, but for the change in temperature. Contour interval is .25 K in all panels.

The differences between the time-mean E-P flux divergence in each of the forced trials and the control trial are shown in Figures 4-22 and 4-23. Again, differences may be seen between trials with strong annular mode-like responses and those without. The changes in E-P flux divergence replicate the patterns found in the SVD analysis performed for the control run (Figure 3-17) if an annular mode-like response is present. A dipole of anomalous eddy generation is present at the ground, which may be observed in all trials L3 through L8, inclusive. Additionally, the structure of the divergence patterns in the upper troposphere is similar to those found in the SVD analysis, with a maximum of anomalous divergence at the same latitude as the spike in divergence at the ground, and an area of convergence co-located at the same latitude as the feature of same polarity at the ground. These features in the upper troposphere are weaker, but may be observed in most of the trials at the shown contour interval, at least for the SH, although the differences from Trial L6 are less faithful in this regard.

In contrast, the changes in E-P flux divergence in Trials L1 and L2 do not resemble this pattern. Most notably, the changes in E-P flux at the surface tend to be monopolar and not dipolar as seen in the other trials.

The changes in the E-P flux divergence in the upper troposphere may be better illustrated by considering only the meridional part of the divergence, as is done in Figures 4-24 and 4-25. The dipole of barotropic divergence, which was evident from the SVD analysis of that quantity with zonal wind, appears in the difference fields, with the stronger divergence patterns occurring for the cases with the stronger zonal wind patterns. The first two trials again show changes which are weaker and less annular mode-like than the other trials; the changes in Trial L1 are particularly weak.

In this subsection, I have found that in most trials, the change in zonal-mean zonal wind is annular mode-like. Two trials (Trials L1 and L2) did not fit this pattern, however. These two trials featured an applied torque placed at the time-mean position of the jet in the unforced model run (see Figure 4-1 for Trial L1). This placement also meant that the forcings were placed along the nodal line of the

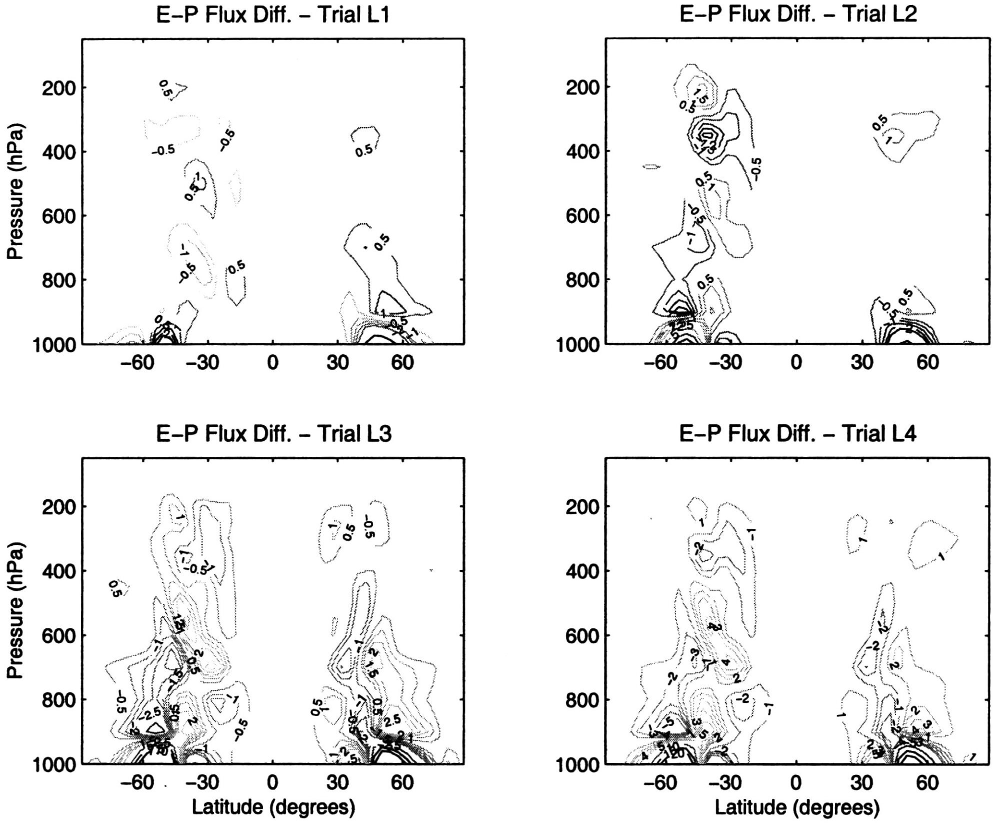

E–P Flux Diff. - Trial L1

E–P Flux Diff. - Trial L2

E–P Flux Diff. - Trial L3

E–P Flux Diff. - Trial L4

Figure 4-22: As in Figure 4-16, but for the change in E-P flux divergence. Contour interval is 0.5 $m\ s^{-2}$ acceleration of zonal wind until 2.5 $m\ s^{-2}$ and 2.5 $m\ s^{-2}$ thereafter in all panels except bottom right, where contour interval is 1 $m\ s^{-2}$ acceleration of zonal wind until 5 $m\ s^{-2}$ and 5 $m\ s^{-2}$ thereafter.

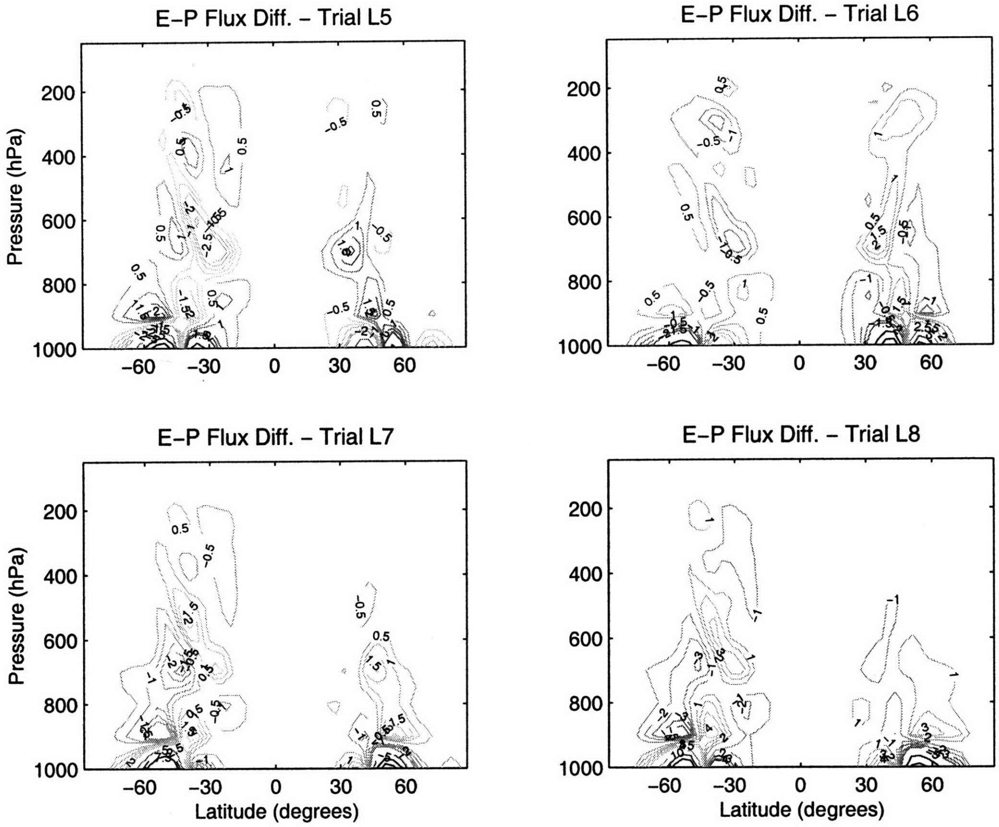

Figure 4-23: As in Figure 4-17, but for the change in E-P flux divergence. Contour interval is 0.5 $m\ s^{-2}$ acceleration of zonal wind until 2.5 $m\ s^{-2}$ and 2.5 $m\ s^{-2}$ thereafter in all panels except bottom right, where contour interval is 1 $m\ s^{-2}$ acceleration of zonal wind until 5 $m\ s^{-2}$ and 5 $m\ s^{-2}$ thereafter.

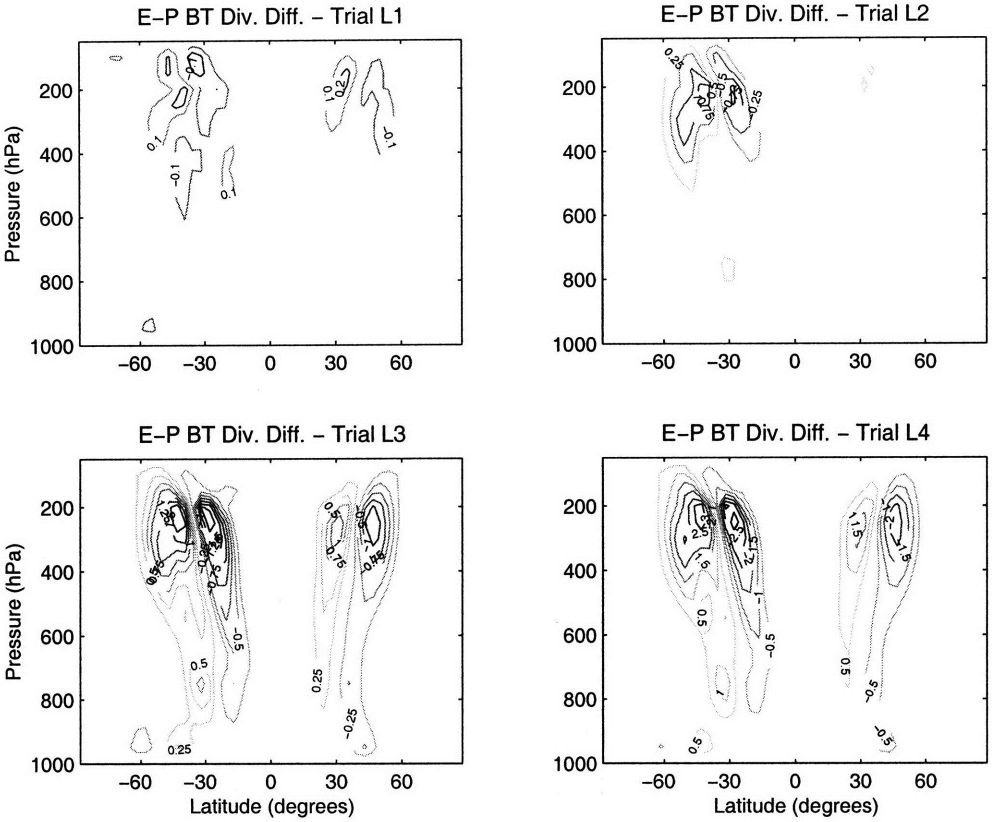

E–P BT Div. Diff. – Trial L1

E–P BT Div. Diff. – Trial L2

E–P BT Div. Diff. – Trial L3

E–P BT Div. Diff. – Trial L4

Figure 4-24: As in Figure 4-16, but for the change in meridional E-P flux divergence. Contour interval is 0.1 $m\ s^{-2}$ zonal wind tendency in top left panel, 0.5 $m\ s^{-2}$ tendency in bottom right panel, and 0.25 $m\ s^{-2}$ in other panels.

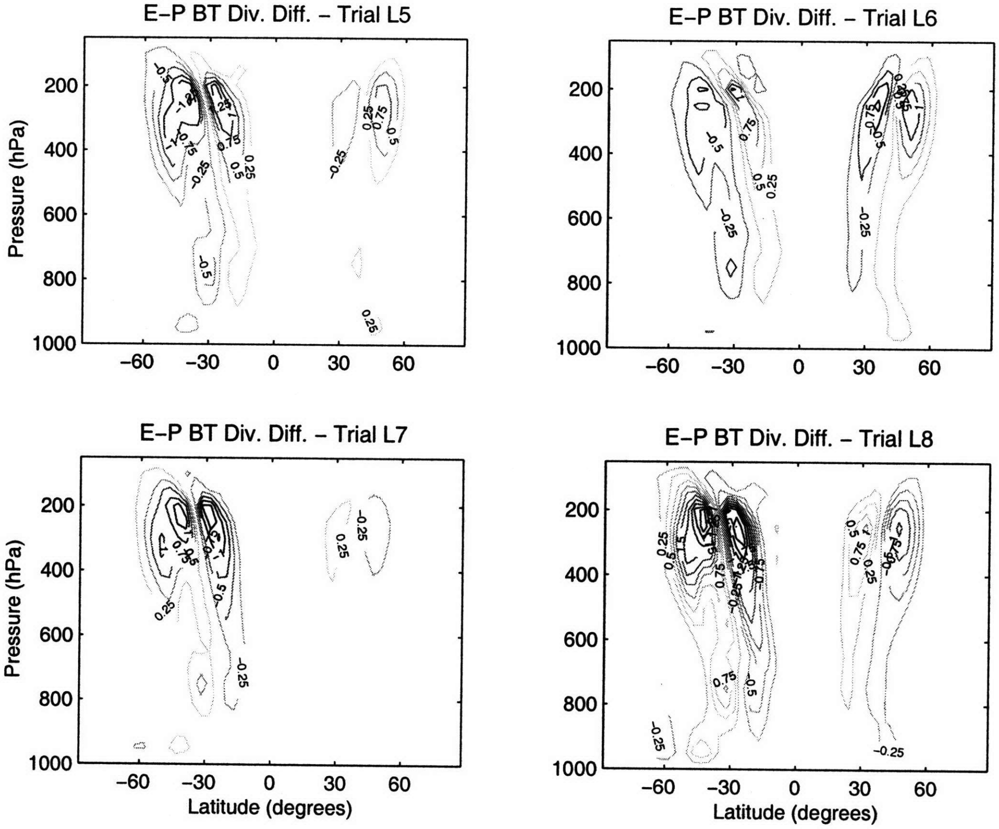

Figure 4-25: As in Figure 4-17, but for the change in meridional E-P flux divergence. Contour interval is 0.25 $m\ s^{-2}$ in all panels.

EOF of the control run's annular mode. Hence, in each case, a portion of the torque projected upon the positive lobe of the EOF but a similar portion projected upon the negative lobe, and the total projection of the forcing on the EOF was small.

The other six cases feature torques displaced from the nodal line of the EOF. These cases, which all have non-zero projections on the unforced modes, feature the annular mode-like response. From these trials, it appears that a non-zero projection on the EOFs of the unforced model run will dictate a response in the EOFs' shape.

The strengths of the responses among the six trials are also different. Trial L4 consistently produced the strongest anomalies in the various climatological fields examined. This case featured forcings centered 11° poleward of the jet and at 250 hPa. As may be discerned from Figure 4-2, this location is also a center of one of the lobes of the EOF. Hence, a case with a very strong projection of forcing on the annular mode produces a strong annular mode-like response.

However, one of the weaker responses among the six cases was seen in Trial L6, which used forcings centered 11° equatorward of the jet and at 250 hPa. This similarly offered a strong projection upon the annular mode, but the response was not as strong. As an additional check this trial was run for 7,000 days, but the additional data did not greatly affect the climatological means. I hypothesize that the response to this forcing, placed in the subtropics, retained more of a tropical flavor which complicated the response as compared to trials such as L4, which were purely extratropical. In Section 4.5 below, I will consider two cases with barotropic forcings placed on the equatorward side of the jet and find a similar discrepancy.

I especially wish to note, from the changes in E-P flux divergence shown in Figures 4-22 and 4-23, that changes in zonal wind which are annular mode-like are accompanied by changes in the E-P flux divergence which mimic the SVD pattern obtained from the cross-covariance of the divergence and zonal wind anomalies.

Numerous authors (e.g. Limpasuvan and Hartmann, 2000) have noted the relationship between the eddy divergences and the zonal wind anomalies associated with the annular modes. Lorenz and Hartmann (2001, 2003) postulated a positive feedback between the eddies and the zonal-mean flow. The presentation of similar patterns

Trial Number	Latitude of Forcing Center	Polarity of SH Forcing
B1	11° poleward of jet center	positive
B2	11° poleward of jet center	negative
B3	11° equatorward of jet center	positive
B4	11° equatorward of jet center	negative

Table 4.2: Summary of trials with imposed barotropic angular momentum forcings.

between the forced climatologies and SVD analysis indicates there is a relationship here, although the mere similarity of the patterns does not in itself constitute a feedback. Still, the similarity encourages a closer look at the role of eddies in creating the model's zonal wind anomalies. In Chapter 6 of this thesis, I will discuss results using a zonally symmetric model, in which the eddy fluxes may be held fixed, to determine the response obtained from direct forcing alone versus that including the changes to the eddy fluxes. There I will show that the changes in eddy fluxes are indeed necessary to capture both the strength and the shape of the annular mode patterns.

4.5 Differences in Climatologies of Barotropically Forced Trials

The preceding section discussed trials in which the forcing was localized in both latitude and pressure. Here I will show results from four trials using forcing whose magnitude did not vary with height. The torques are presented in Table 4.2. To review, there are four trials – two trials with forcing on the equatorward side of the jet and two with forcing on the poleward side, each set having one run with westerly torque in the SH and easterly torque in the NH, and vice versa. The integrated amount of forcing added in these trials is the same as that in the similar bullseye trials, so the magnitude of maximum forcing here is reduced by approximately a factor of four.

The difference in time-mean, zonal-mean zonal wind between the four trials and the control is shown in Figure 4-26. In Trials B1 and B2, the zonal wind response is annular mode-like, with a prominent dipolar structure extending from the surface to the top of the model atmosphere, visible in each model run.

The latter two trials, featuring the equatorward-flank forcing, present a different picture, however. The response in Trial B3 is reminiscent of that in Trial L6. While bands of anomalous westerlies and easterlies are found in each hemisphere, the response is weak (the 1 $m\ s^{-1}$ easterly anomaly in the SH is not statistically significant). Trial B4 features an annular mode response in only the SH, with an extremely weak (less than 1 $m\ s^{-1}$) monopolar response in the NH. The behavior of the model in response to the poleward-flank forcings is different than that in response to the equatorward-flank forcings. As an additional check on the behavior, the climatologies for Trials B3 and B4 were extended to 7,000 days, but the climatologies were not affected by the additional data.

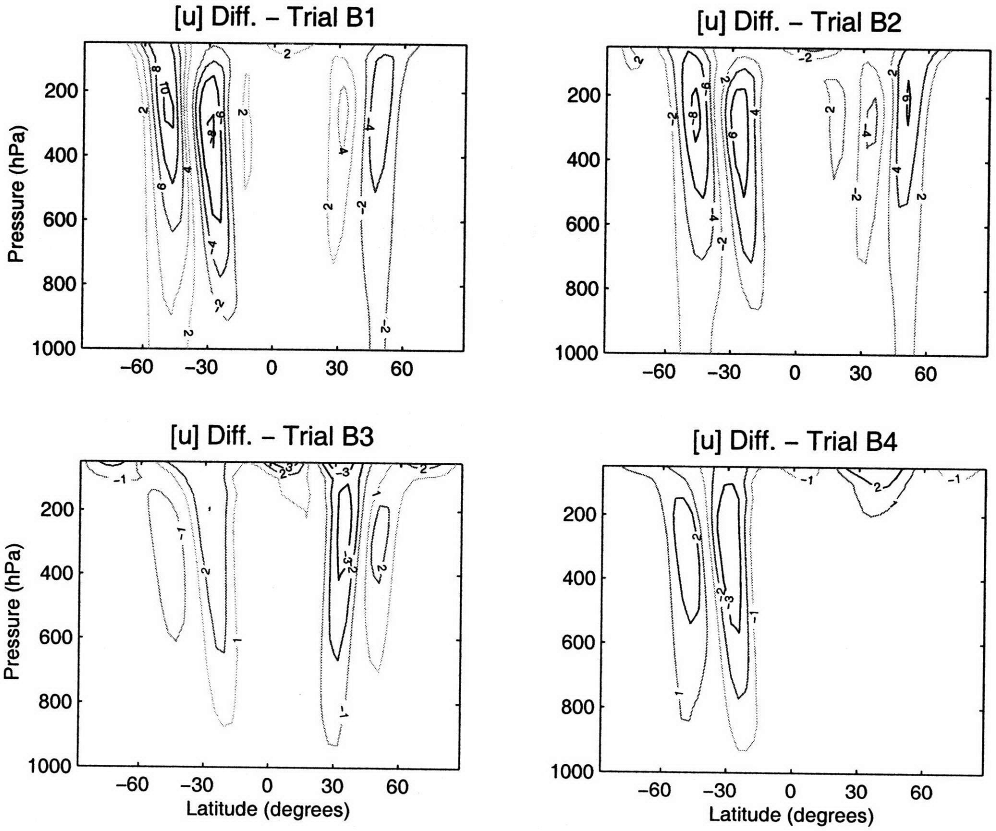

Figure 4-26: Change in time-mean zonal-mean zonal wind for the indicated trials versus the control. Contour interval is 2 $m\ s^{-1}$ in the upper two panels and 1 $m\ s^{-1}$ in the lower two panels.

The changes in streamfunction for the four barotropic trials are shown in Figure 4-27. While all four trials feature extrema of anomalous streamfunction in the subtropics, the extratropical anomalies are strong only in Trials B1 and B2. Also notably, the subtropical extrema for the two runs with extratropical forcing are of a larger magnitude, particularly for the SH.

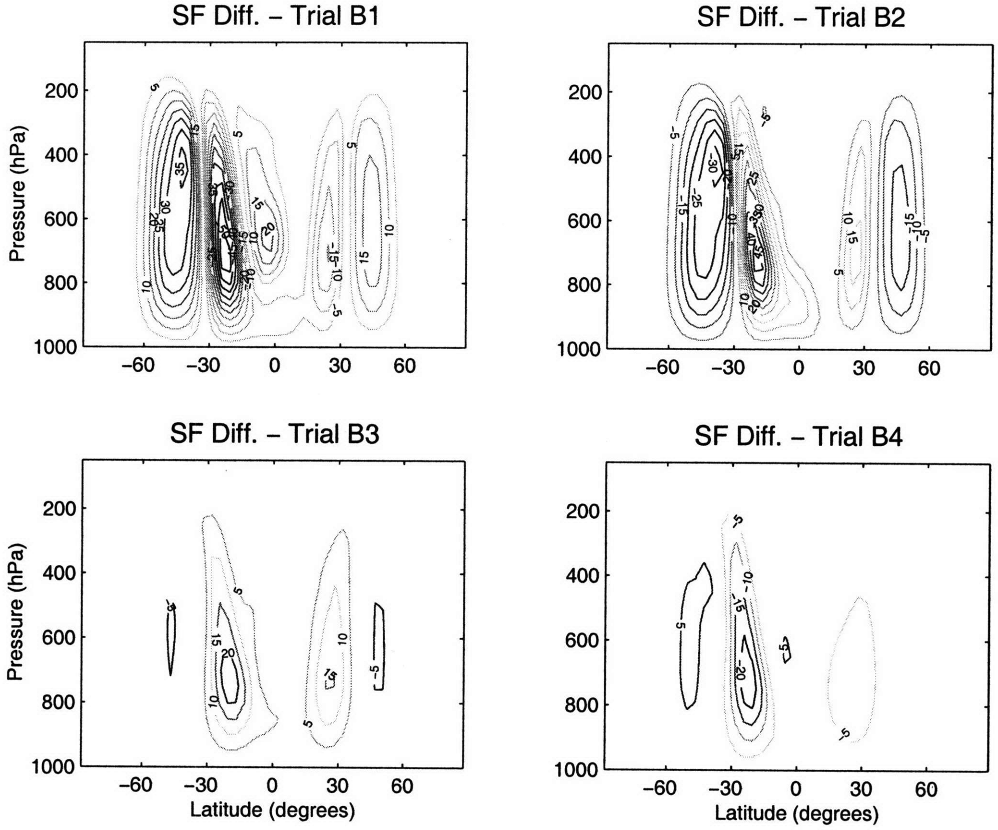
SF Diff. - Trial B1

SF Diff. - Trial B2

SF Diff. - Trial B3

SF Diff. - Trial B4

Figure 4-27: As in Figure 4-26, but for the change in streamfunction. Contour interval is 5×10^9 $kg\ s^{-1}$ in all panels.

The behavior of the temperature anomalies versus the control, as shown in Figure 4-28, is as expected based on the data previously shown. The changes in Trials B1 and B2 are strong (exceeding 2 K in the regions of dynamic cooling or warming near 35°), with opposite-signed anomalies on the poleward side. The changes in Trials B3 and B4 are weaker and do not include the anomalies closer to the pole. In fact, the changes in the lower troposphere of the NH in Trial B4 do not even reach .25 K.

Finally, I examine the changes in E-P fluxes and divergence among the four trials with barotropic forcing versus the control. The results are again consistent with those

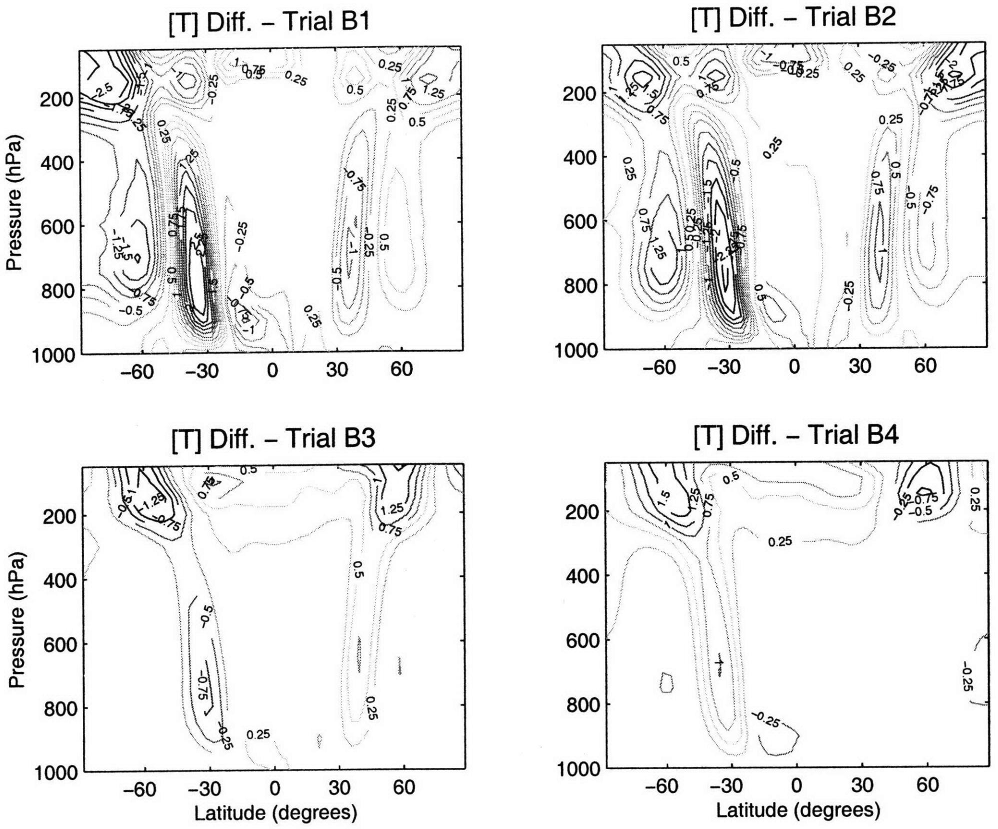

Figure 4-28: As in Figure 4-26, but for the change in temperature. Contour interval is .25 K in all panels.

shown for the other meteorological fields (Figure 4-29). The former two trials show a dipole of anomalous convergence and divergence at the surface, and a structure in the upper atmosphere similar to that found through SVD analysis. The surface dipoles are present in the latter two trials, but they are weaker, as are the extrema of divergence and convergence in the upper layers of the model atmosphere. This final point is confirmed by looking at the barotropic portion of the divergence (Figure 4-30), which is much stronger in the former two trials than in the latter two.

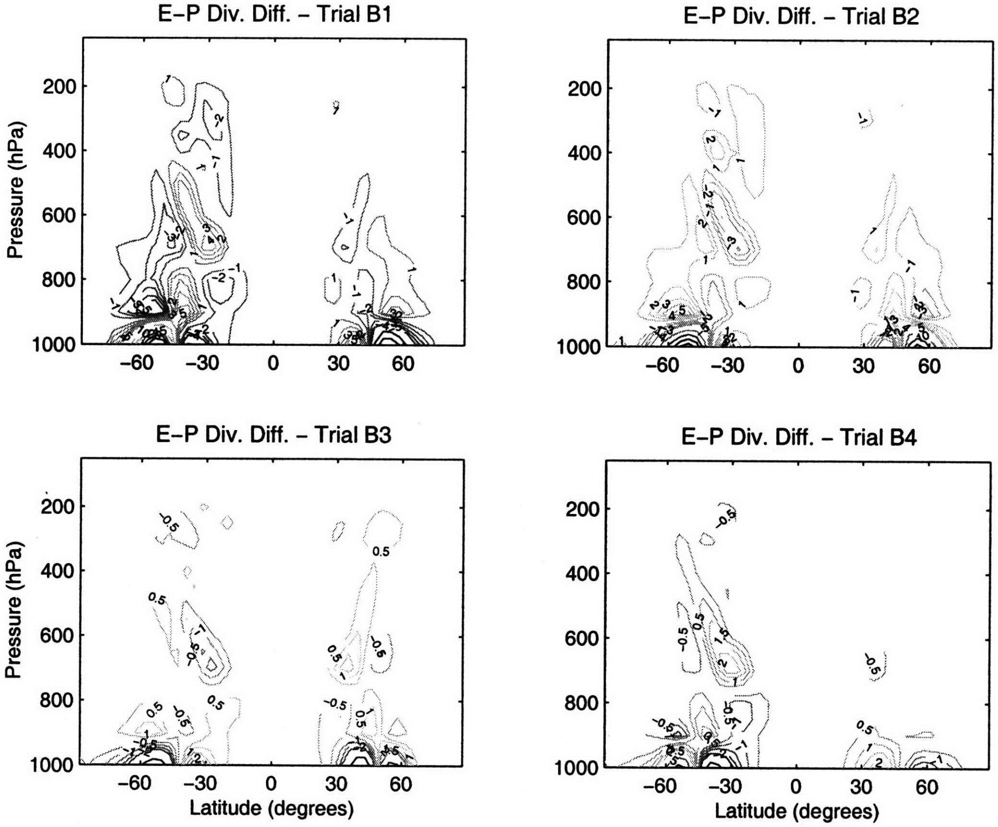

Figure 4-29: As in Figure 4-26, but for the change in E-P flux divergence. Contour interval is 1 $m\ s^{-2}$ acceleration of zonal wind until 5 $m\ s^{-2}$ and 5 $m\ s^{-2}$ thereafter in top panels and 0.5 $m\ s^{-2}$ acceleration of zonal wind until 2.5 $m\ s^{-2}$ and 2.5 $m\ s^{-2}$ thereafter in bottom panels.

The results found in this section are similar to those for analogous trials with torques in the shape of Gaussian bullseyes. Both Trials B1 and B2, which use forcing placed on the poleward flank of the jet, produce robust annular mode patterns, as do the trials with vertically localized forcing placed in the same location. The trials with

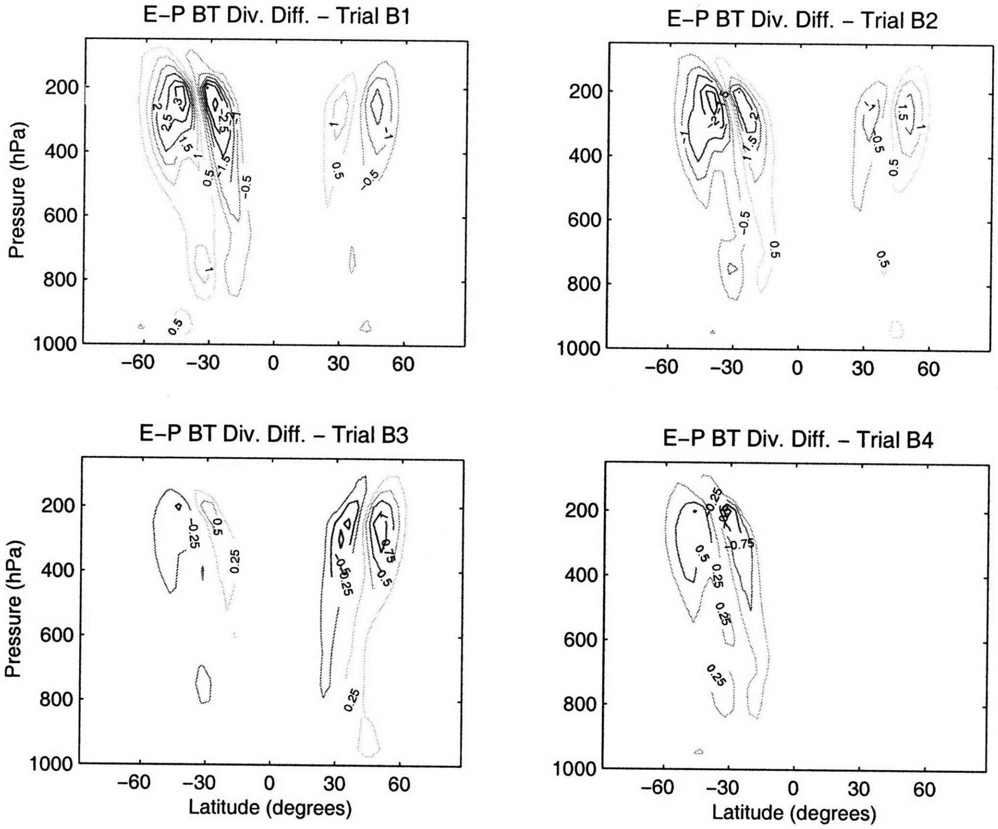

Figure 4-30: As in Figure 4-26, but for the change in the meridional portion of E-P flux divergence. Contour interval is 0.5 $m\ s^{-2}$ acceleration of zonal wind in top two panels and 0.25 $m\ s^{-2}$ acceleration of zonal wind in bottom two panels.

forcing placed on the equatorward flank feature weaker dipolar responses. However, this result is consistent with those from the bullseye-forcing cases as well — the responses in Trial L6 were the weakest amongst the six trials with a Gaussian forcing offset from the jet's center. There is a difference in the response of the model to forcings placed on the poleward flank and forcings placed on the equatorward flank. I will explore this discrepancy further through use of the zonally symmetric model in Chapter 6.

4.6 Differences in Climatologies of Trials Using Different Forcing Magnitudes

In this section, I present the results of a series of trials where the magnitude of the forcing is changed from run to run. In all these cases, the forcing is of the shape used in Trial L3 — a Gaussian bullseye, centered in the lower troposphere and on the poleward flank of the jet (which, as seen earlier, projects very well onto the annular mode pattern). However, as shown in Table 4.3, the strength of the applied torque is allowed to vary. Here I consider runs using forcing as weak as 25 percent of that used in Trial L3, and runs with forcing as strong as 150 percent. Additionally, I choose a trial with the same strength of forcing, but opposite sign as that used in Trial L3, as an additional check on the effects of polarity in the model response.

As the anomalies in the various climatological fields arising in response to the torques have already been extensively discussed, and it has been shown that the structure of the responses in fields such as temperature, streamfunction, and E-P flux divergence are all similar for trials which produce annular mode-like anomalies, I will focus on a single field here, presenting the difference in time-mean zonal mean zonal wind for each trial versus the control. The structures of the other climatological fields were similar in these trials to those presented in the former two sections, and the strengths of the responses of other fields in these trials varied similarly to the variation in the zonal mean wind response.

Trial Number	Relative Strength of Forcing Center
L3	1
S1	1/4
S2	3/8
S3	7/16
S4	15/32
S5	1/2
S6	17/32
S7	3/4
S8	-1
S9	5/4
S10	3/2

Table 4.3: Summary of trials with forcing of same shape as that in Trial L3, but of different magnitudes.

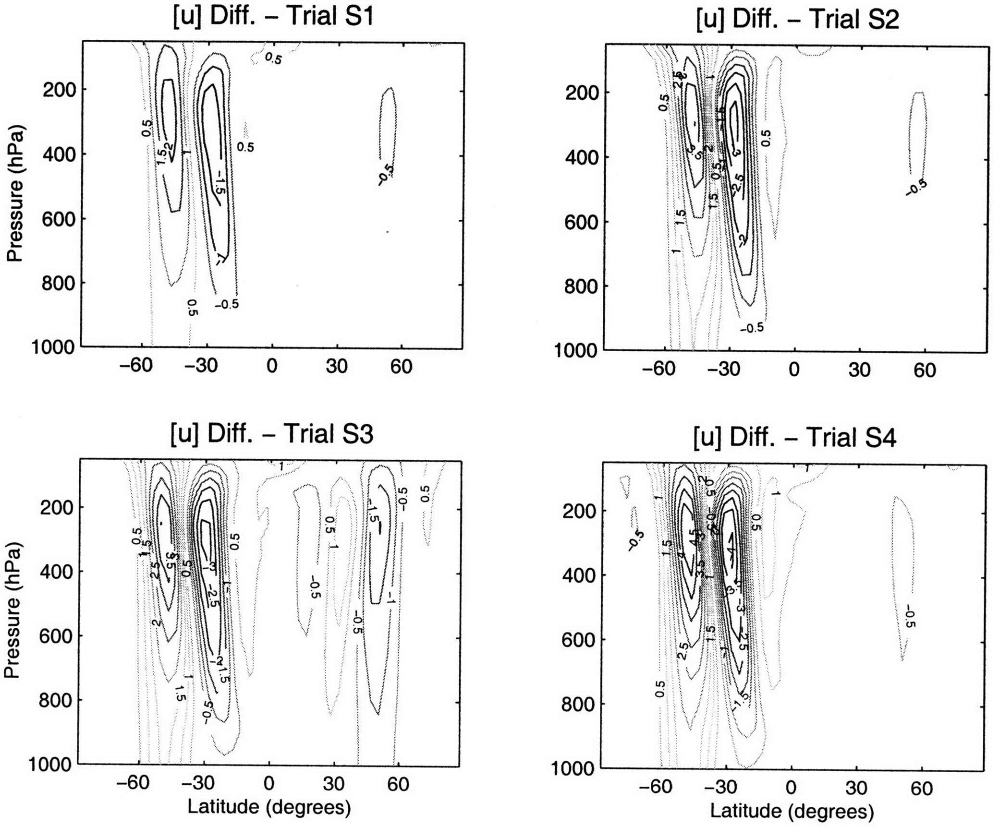

Figure 4-31: Change in time-mean zonal-mean zonal wind for the indicated trials versus the control. Contour interval is 0.5 $m\ s^{-1}$ in all panels.

The zonal wind responses found for Trials S1 through S4 are shown in Figure 4-31. The responses in the SH mimic the pattern of the annular mode. As may be expected, the weakest response is for Trial S1, which uses the weakest forcing, with the changes in time-mean zonal mean zonal wind becoming larger as the forcing magnitude grows. The results from the NH are different; here the changes in zonal wind are much weaker. The negative center of the dipole is less than 1 $m\ s^{-1}$ in magnitude in three of the four cases, and the positive center is less than 0.5 $m\ s^{-1}$ in magnitude in the same cases. In one case (Trial S3), there is an observed dipole in the Northern Hemisphere of strength greater than 1 $m\ s^{-1}$ in each lobe, but the results are still too weak to be statistically significant at the 95 percent level from those in the control run.

Figure 4-32 shows the responses of trials S5 through S8. In the NH, the responses are getting stronger as would be expected, for the increase in forcing strength. There is a peculiarity in the SH, however, as the response for Trial S5 (with relative forcing magnitude 1/2) is unexpectedly strong, while the response for Trial S6 (with relative forcing magnitude 17/32) is unexpectedly weak. Trials S5 and S6 were extended to 7,000 days, but the addition of the extra data did not alter the climatologies of the runs. The behavior of the zonal wind response in these two trials therefore appears robust, although the magnitudes in Trials S5 and S6 are unexpected, and there is no obvious explanation for the unusual strengths of the anomalies.

Trial S8 is a repeat of Trial L3, except that the polarities of the forcings are swapped. In Trial S8, the westerly torque is now in the NH, and the easterly torque in the SH. In each hemisphere the annular mode pattern is produced, with opposite polarity as that found for Trial L3. The results here are similar to those found in Trials B1 and B2, for the barotropic forcing placed on the jet's poleward flank, in that the annular mode pattern will arise for either polarity of the forcing.

Finally, Figure 4-33 displays the change in climatological zonal wind versus the control for Trials S9 and S10. As expected, these trials feature stronger responses than that seen in Trial L3.

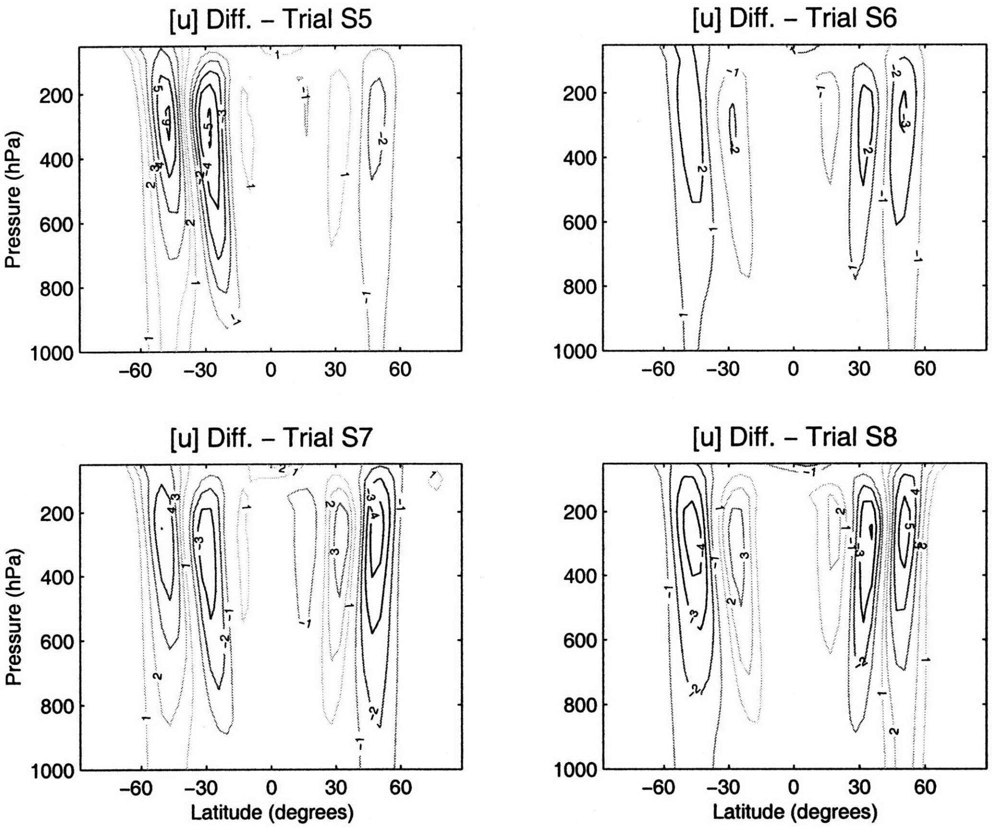

Figure 4-32: Change in time-mean zonal-mean zonal wind for the indicated trials versus the control. Contour interval is 1 $m\ s^{-1}$ in all panels.

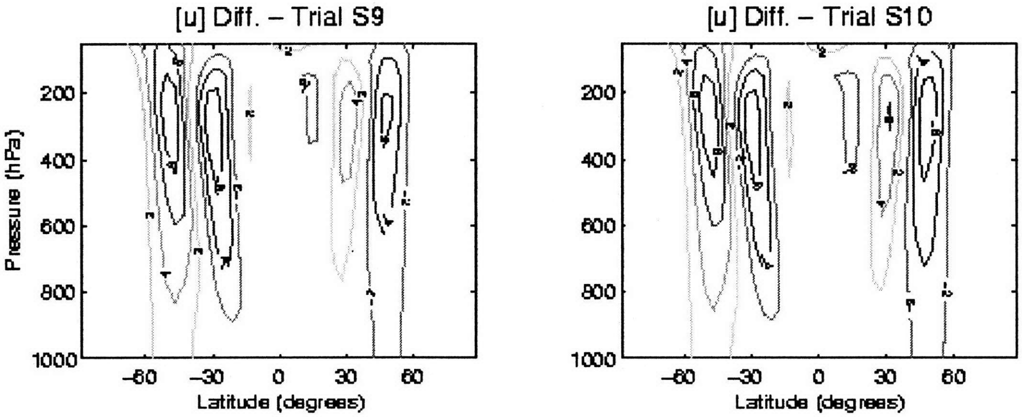

Figure 4-33: Change in time-mean zonal-mean zonal wind for the indicated trials versus the control. Contour interval is 2 $m\ s^{-1}$ in both panels.

4.7 Summary

In this section, I have analyzed the response of the model to a number of different angular momentum forcings. The annular mode pattern is found as a response in the vast majority of these trials, suggesting that the annular modes are indeed preferred components of the atmospheric circulation.

As noted in the Introduction to this thesis, an eddy feedback is presumed to maintain the annular mode patterns (e.g. Lorenz and Hartmann, 2001, 2003). Consequently, I have also focused on the changes to the E-P flux divergence fields and their relationship to the zonal wind field. For the cases in which the annular mode appears, the changes in E-P flux divergence strongly resemble the pattern found through SVD analysis of the covariance between zonal wind and flux divergence in the control model run. I will further explore these changes in eddy fluxes, and their relationship to the zonal wind changes, using a zonally symmetric model in Chapter 6.

The trials which did not produce a strong annular mode pattern fall into one of two groups. The first group includes trials with forcings placed at the center of the unforced jet. As noted above, these forcings are centered on the nodal line of the unforced model's annular mode and thus project poorly. The other trials with a weak annular mode response include several cases where forcing on the equatorward flank is used.

With the exception of the poorly-performing trials using equatorward-flank forcing, the strongest responses were noted for trials with an excellent projection of applied torque on the unforced run's annular modes. The trials with forcing strength generally showed an increased response for increasing forcing magnitude. These results suggests that, for a given forcing, the strength of the annular mode response may be increased either by increasing the magnitude of the forcing, or by improving the projection of the forcing onto the annular modes of the unforced run. In Chapter 7, the relationship between forcing and response strength will be further explored.

Chapter 5

Thermally Forced Trials

5.1 Introduction

In the previous chapter, I investigated the response of the model to the application of artificial torques and found the annular mode patterns typically captured the differences in climatology among the forced model runs and a control run. This suggests that the annular modes are a preferred response to atmospheric perturbations. However, if they are indeed a preferred pattern, then they should arise in response to forcings other than the torques used in Chapter 4.

Hence, in this chapter, I will force the model thermally, rather than mechanically, to see whether the annular modes are again a prominent pattern of response. The forcing will be accomplished by altering the reference temperature profile among the model runs. Below I describe the perturbations made to the equilibrium temperature profile. Later in the chapter, I discuss the differences among the trials using the changed reference temperature profiles and the control climatology.

As with the previous two chapters, the climatologies are examined and found to be similar to that of the control run. The westerly jets remain the dominant climatological features in all trials. The variability of each trial below is dominated by the dipolar annular mode patterns — oppositely-signed lobes of wind about the jet's new time-mean position. The climatologies of the runs below, as with the control run, are highly zonally symmetric.

As these properties have been discussed extensively for the control climatology in Chapter 3, and an example run in Chapter 4, I will simply note the similarities here rather than repeating in print the thorough climatological examination. Thus, for the rest of this chapter, my focus will be on the differences in climatologies among the control case and these new forced cases.

In these trials, the "forcing" of the model, as compared to the control run, is a change in the relaxation temperature profile. The runs here fall into three categories: trials with hemisphere-scale forcing maximized at the equator; trials with hemisphere-scale forcing maximized at the pole, and trials where the temperature forcing is applied only poleward of 45°. The next section discusses the results of the former two cases.

5.2 Trials with Hemisphere-Scale Thermal Forcing

The differences in relaxation temperature for two of the trials where hemisphere-scale forcing is applied are shown in Figures 5-1 and 5-2, along with the anomalous gradients. In each case, the difference is accomplished by changing the value of the maximum reference temperature (and thus the value of the prescribed equator-pole temperature gradient). This is similar to the procedure used in Son and Lee (2005, 2006).

The first profile is for a case (Trial T1) with the largest change in reference temperature prescribed just north of the equator, at the point where the reference temperature in the control run also happens to be largest. The temperature perturbation declines from 5 K at this point to zero at the poles. The temperature perturbation also declines to zero at tropopause level, with the vertical structure of the decay the same as that used for the decline of the value of the control reference temperature from its surface to its stratospheric value. A second trial (Trial T2) uses the inverse of this change, with a 5 K reduction of equilibrium temperature instead of the increase.

Trials T3 and T4 instead place the largest change at the pole. In Trial T3 (shown in Figure 5-2), there is a 5 K cooling of reference temperature at the poles, decreasing

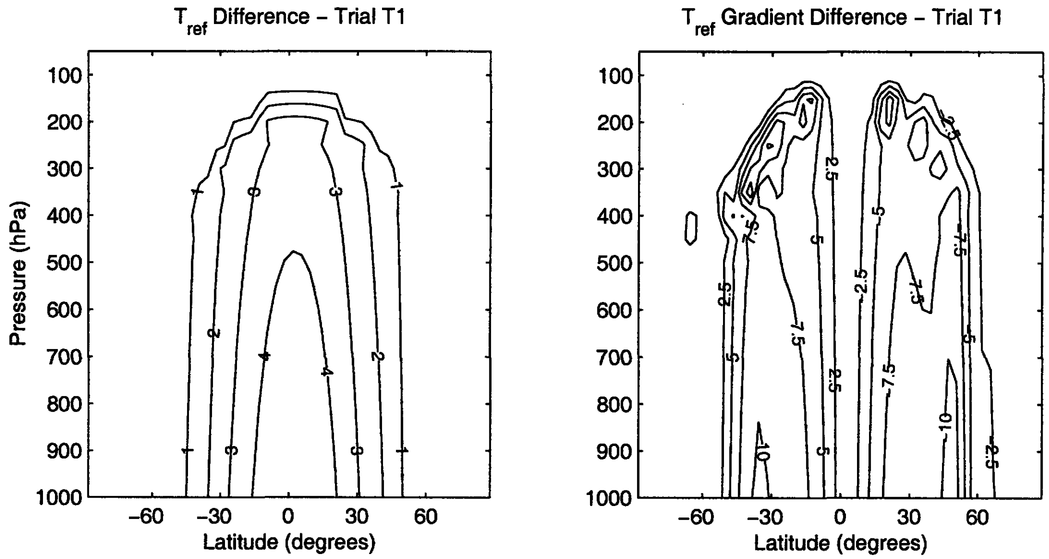

Figure 5-1: (Left) Difference in reference temperature versus the control for a trial with maximum perturbation of 5 K, just off the equator. Contour interval is 1 K. (Right) The meridional gradient of the reference temperature difference. Contour interval is 2.5×10^{-7} $K\ m^{-1}$.

to zero toward the equator. Trial T4 features the same difference pattern, but a polar warming instead of polar cooling. Again, the temperature perturbation decays in the vertical along with the background temperature.

While the regions of maximum reference temperature change are different among the four trials, the regions in which the largest change in the gradient of reference temperature occurs are similar, with the largest changes in gradient occurring in the subtropics to mid-latitudes. The anomalous gradients for Trials T1 and T3 are shown in Figures 5-1 and 5-2, indicating the largest changes occur in a broad swath centered on the mid-latitudes for both trials. Since the meridional temperature gradient is linked to the thermal wind shear, it is worthwhile to note the similarities here.

It may additionally be noted that these changes in reference temperature will alter the static stability of the atmosphere. For Trials T1 and T2, these changes will occur predominately at the tropical tropopause, while in Trials T3 and T4 the changes are focused at the polar tropopause.

The four trials with hemisphere-scale alterations to the reference temperature are summarized in Table 5.1. Note that trials T1 and T3 increase the equator-pole

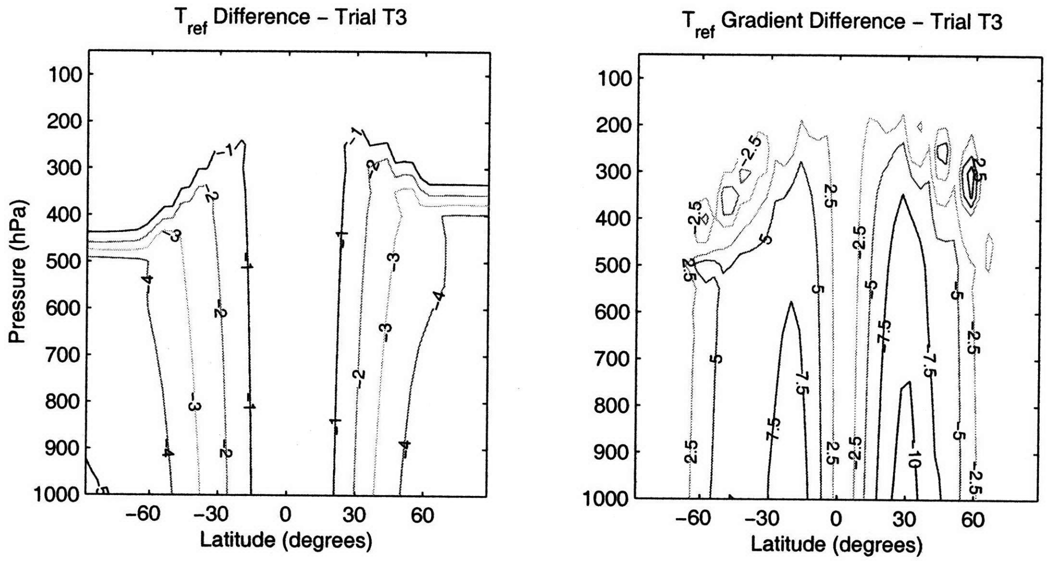

Figure 5-2: As in Figure 5-1, but for a trial with maximum perturbation of -5 K at the poles.

Trial Number	Maximum Change in T_{eq}	Location of Maximum Change
T1	5 K	equator
T2	-5 K	equator
T3	-5 K	pole
T4	5 K	pole

Table 5.1: Summary of trials with hemisphere-scale changes to reference temperature.

temperature difference, while Trials T2 and T4 decrease this difference.

These trials are allowed to spin up from rest under the influence of the perturbed reference temperature profiles. A climatology of 5,000 days, sampled once daily, is compiled after this spin-up period, and the climatologies of the perturbed trials are compared to that of the control.

The changes in zonal-mean, zonal wind among the four trials outlined in Table 5.1 and the control are shown in Figure 5-3. There are dipolar centers of wind anomalies found for each trial, but the picture is not as clean as in most of the momentum forcing trials. The first two trials, which feature the change in reference temperature concentrated in equatorial regions, do not show a change of zonal wind with dipolar anomalies of approximately equal strength as seen in the annular modes. While each trial generates a region of strong wind change around 50°, the centers of wind

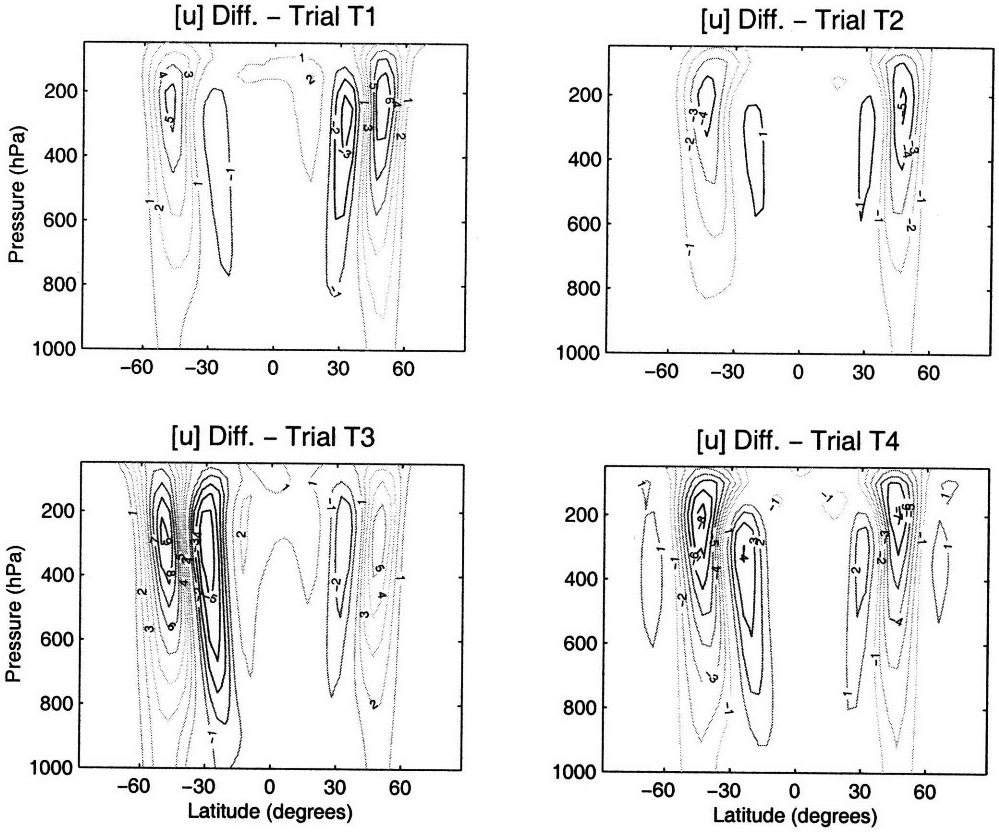

Figure 5-3: Change in zonal-mean, time-mean zonal wind for the indicated runs versus the control run. Contour interval is 1 $m\ s^{-1}$.

anomalies located on the equatorward side of the jet are much weaker. The changes appear as an amalgamation of a monopolar and dipolar response, rather than a response which is purely dipolar. Nor do the nodes in the anomalous zonal-mean wind response align with those of the unforced annular mode — the lines of zero anomalous zonal-mean zonal wind response are too far equatorward here.

In the latter two trials, the flavor of the response is more annular mode-like, in that the wind anomalies on the equatorward side in each hemisphere are closer in magnitude to the poleward-side anomalies. However, they still lag behind the strength of the poleward centers. The wind anomalies in Trial T4 are also displaced from the location of the annular mode dipole. In the SH, the dipole in the pattern of Trial T4 is at 31°, not 37° as with the annular modes. The NH nodal line is also off by a similar amount (35° versus 41°). The nodal lines for Trial T3 are closer to the positions of those in the unforced model's annular modes, however.

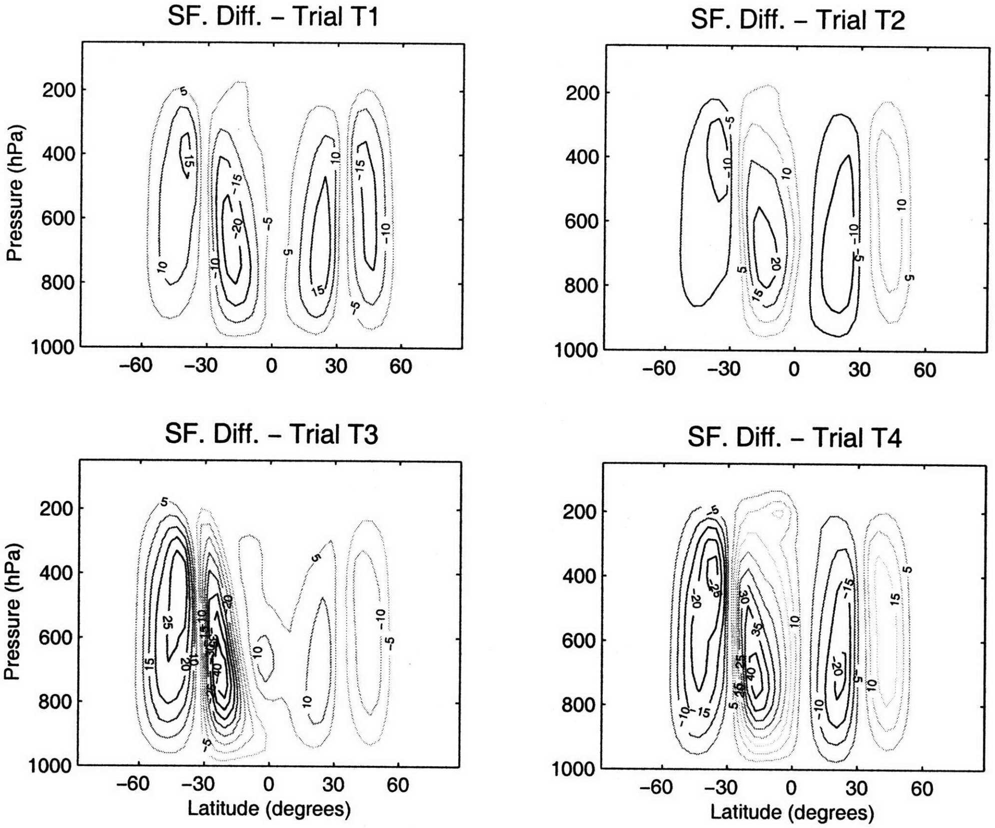

Figure 5-4: As in Figure 5-3, but for the changes in streamfunction. Contour interval is 5×10^9 $kg\ s^{-1}$.

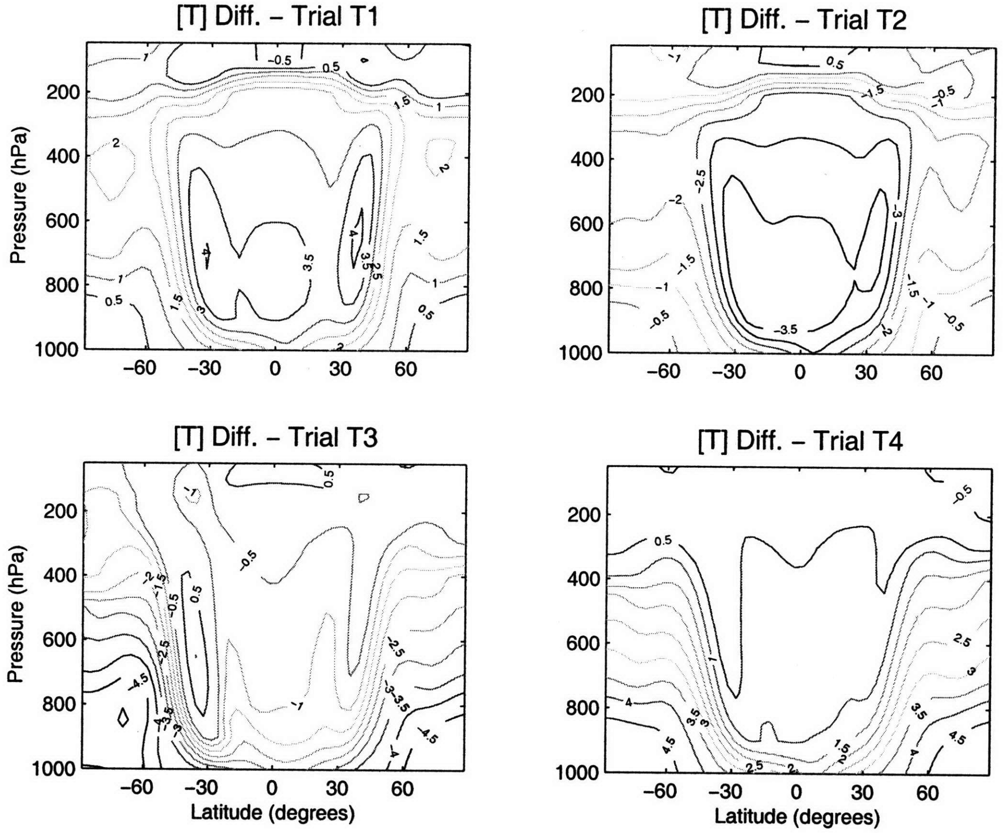
[T] Diff. - Trial T1

[T] Diff. - Trial T2

[T] Diff. - Trial T3

[T] Diff. - Trial T4

Figure 5-5: As in Figure 5-3, but for the changes in time-mean, zonal-mean temperature. Contour interval is 0.5 K.

The changes in climatological streamfunction for the four trials versus the control are displayed in Figure 5-4. Unlike the streamfunction changes seen in Chapter 4 (for example, the lower panels in Figure 4-18), which were focused in the mid-latitudes, the changes here include wider anomalies on the equatorward side, which extend further into the deep tropics. Hence the patterns suggest a strengthening and weakening of the existing cells. There is some shift in the position of the cells — in Trial T1, for example, the Hadley cells expand slightly poleward while in Trial T2 they contract slightly equatorward — but overall the change in streamfunction is more dominated by the strengthening and weakening of patterns rather than the meridional shifts seen in Chapter 4. Of the four trials, the anomalous streamfunction found for Trial T3 is the closest to those found in Chapter 4.

Figure 5-5 examines the changes in temperature among the four model runs and the control. In each case, the pattern of reference temperature differences (see Fig-

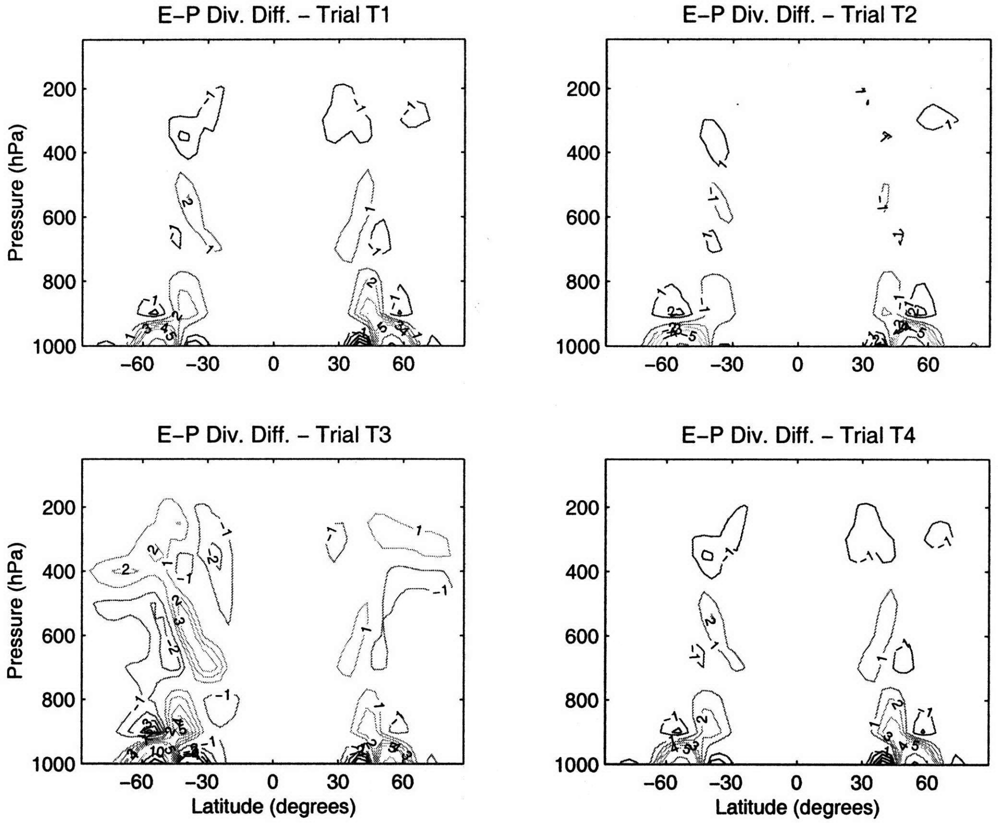

Figure 5-6: As in Figure 5-3, but for the changes in time-mean E-P flux divergence. Contour interval is 1 $m\ s^{-2}$ acceleration of zonal wind until 5 $m\ s^{-2}$ and 5 $m\ s^{-2}$ thereafter.

ure 5-1) is obvious, though the dynamic warming or cooling may also be discerned in the mid-latitudes. As should be expected from the above figures, the changes due to the dynamics are largest for Trial T3 and weaker for the other trials.

The differences in E-P flux divergence between each of the four trials and the control are shown in Figure 5-6. The changes here are similar to those of the other climatological fields. Trial T2 has the least annular-mode like response, as the anomalous surface convergence in the SH is not matched by a region of anomalous divergence. Trials T1 and T4 show a divergence dipole at the surface, although in each case the poleward lobe is stronger than the equatorward lobe. Again, the pattern in Trial T3 is the most similar to the changes found in Chapter 4.

Son and Lee (2006), using a tropical heating profile much more concentrated than that used here (their heating was confined equatorward of 10°), also noted poor predictability of the annular mode patterns in such runs when the tropical heating was high. They speculated an equatorward expansion of the baroclinic zone in their runs due to the stronger subtropical jet resulted in a more complex extratropical wind response than the simple annular mode patterns. While the forcing chosen here is much more broad than that of Son and Lee (2006), it appears the obfuscation of the extratropical dynamics occurs here as well.

Generally speaking, the results here do not show as clean and unambiguous of an annular mode pattern as those produced in Chapter 4. While some annular-mode like traits in the responses may be found (particularly for Trial T3), the perturbations in reference temperature produced changes which differed from the annular modes in several ways, particularly for the first two trials.

5.3 Trials With Forcing Confined Poleward of 45°

In the trials above, the response of the model to the applied reference temperature perturbations was generally not annular mode-like. This could be noted especially in the streamfunction anomalies (Figure 5-4), which suggested more of the response was concentrated in the tropics as compared to the trials in Chapter 4.

It therefore might be worthwhile to consider several cases whose forcings are exclusively extratropical. I do that here by presenting a suite of runs where the thermal forcing is limited to poleward of 45°. The region of maximum perturbation to the temperature gradient also shifts poleward, as compared to the "T" runs above. In these cases, as will be seen below, the annular mode response is strong.

For the trials below, an additional term is added to the reference temperature setup of the control run. At the ground, the term has the structure

$$T_{pert} = A\cos(2\phi); \quad |\phi| \; > \; 45^\circ \tag{5.1}$$

$$T_{pert} = 0; \quad |\phi| \; \leq \; 45^\circ \tag{5.2}$$

where A is the amplitude of temperature perturbation at the pole. Hence equator-

Trial Number	Strength of Maximum Forcing	Polarity of Forcing
P1	2 K	warming
P2	4 K	warming
P3	6 K	warming
P4	10 K	warming
P5	2 K	cooling
P6	4 K	cooling
P7	6 K	cooling
P8	10 K	cooling

Table 5.2: Summary of trials with imposed reference temperature perturbations localized poleward of 45°.

ward of 45°, no perturbation reference temperature is applied, and the strength of the perturbation increases sinusoidally from 45° to the pole. The vertical structure prescribed is the same as that for the unperturbed equilibrium temperature. Figure 5-7 shows an example for one trial; the other seven trials feature the same shape of reference temperature perturbations, but different magnitudes or polarities. In all cases, both the applied temperature perturbations, and anomalous gradients, are more latitudinally confined than in the previous cases. The list of trials using this type of reference temperature perturbation is shown in Table 5.2.

The time-mean, zonal mean zonal wind changes for these eight trials versus the control are shown in Figure 5-8 for Trials P1 through P4, and Figure 5-9 for Trials P5 through P8. Here, the annular mode responses are much more prominent in each hemisphere throughout the trials. The first four trials, which feature polar warming, generally contain easterly anomalies coinciding with the poleward lobe of the annular mode, and westerly anomalies co-located with the equatorward lobe of the annular mode. While the wind response in Trial P1 is weak, the other three trials all feature a robust annular mode response. The relative magnitudes of the anomalies in each lobe are closer than those in the "T" trials above, and the nodal lines of the anomalous wind patterns coincide with the nodal lines of the annular modes of the unforced run.

The trials featuring polar cooling of the reference temperature display strongly the annular mode patterns in all four trials, as seen in Figure 5-9. Here there are

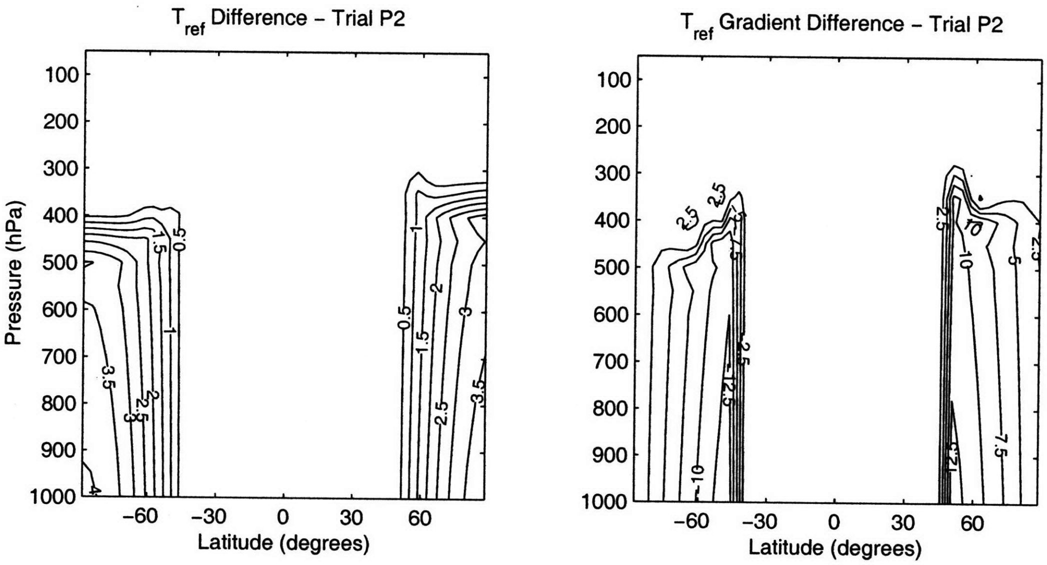

Figure 5-7: (Left) Change in relaxation temperature for the indicated run versus the control run. Contour interval is 0.5 K. (Right) The meridional gradient of the reference temperature difference. Contour interval is 2.5×10^{-7} $K\ m^{-1}$.

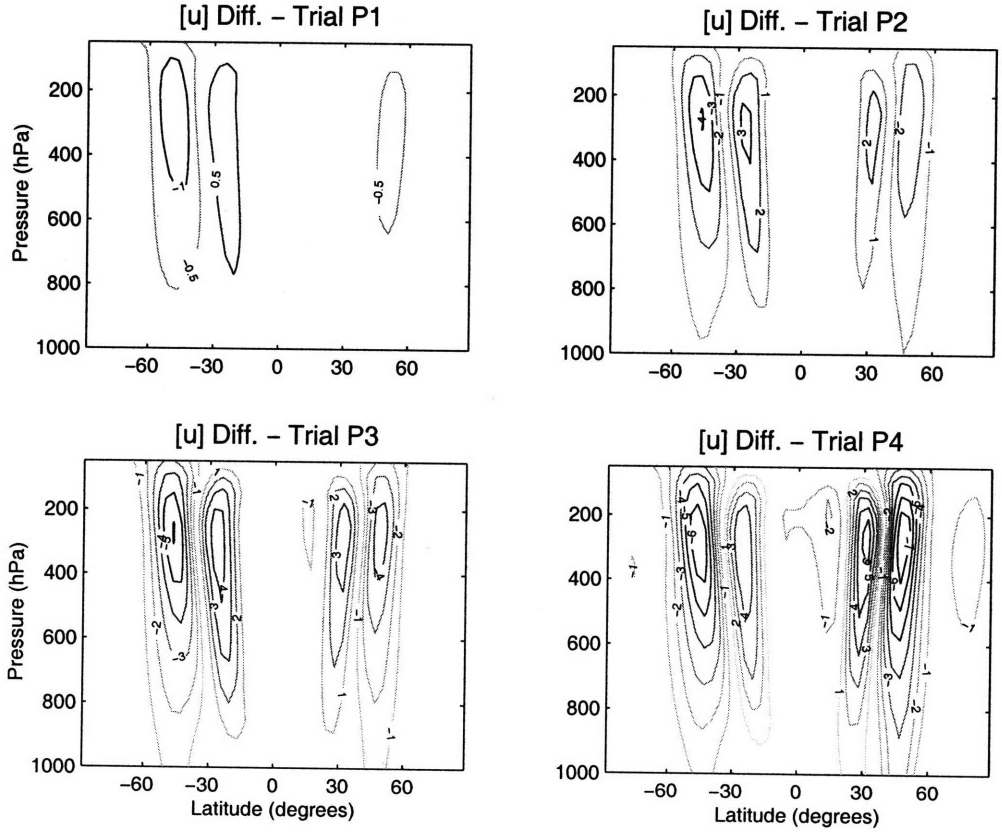

Figure 5-8: Change in zonal-mean, time-mean zonal wind for the indicated runs versus the control run. Contour interval is 0.5 $m\ s^{-1}$ in upper left panel and 1 $m\ s^{-1}$ otherwise.

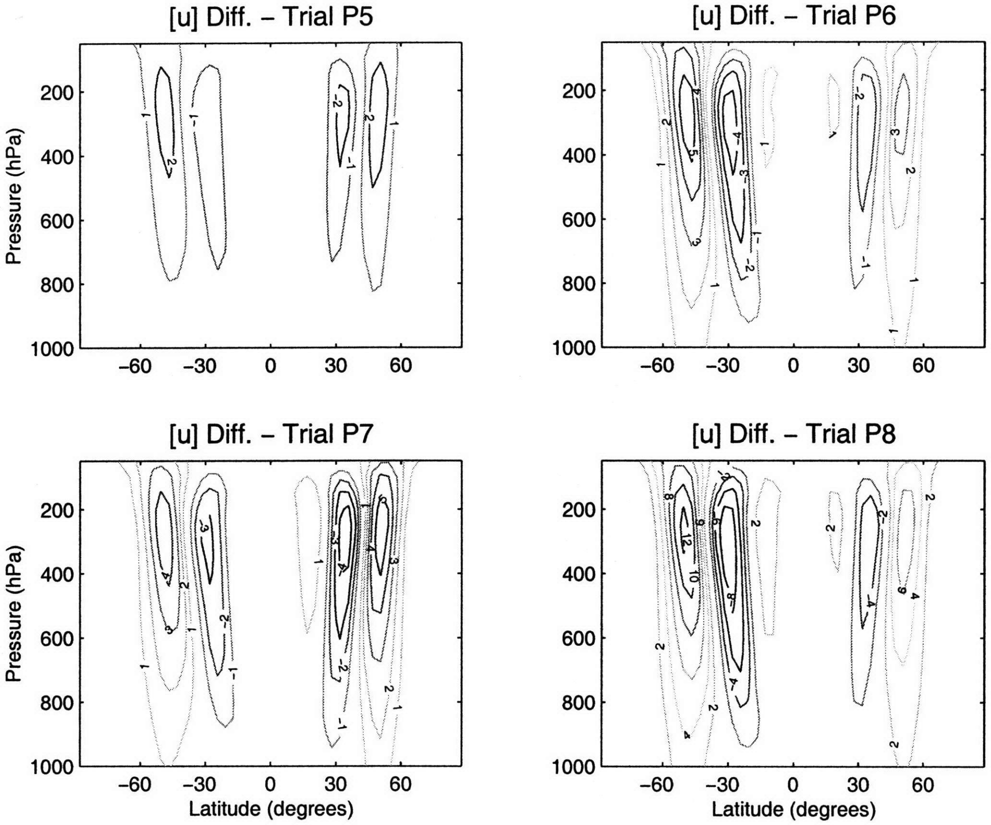

Figure 5-9: Change in zonal-mean, time-mean zonal wind for the indicated runs versus the control run. Contour interval is 1 $m\ s^{-1}$ except 2 $m\ s^{-1}$ for bottom right panel.

anomalous westerlies coinciding with the poleward lobe of the annular mode and easterly anomalies co-located with the equatorward lobe. The magnitudes of the anomalies in each lobe are also similar, and the strength of the patterns generally increases for stronger perturbations to the reference temperature.

The next two figures (5-10 and 5-11) show the changes in climatological streamfunction among these trials and the control. The changes are much more reminiscent of those found in Chapter 4 than for the "T" trials shown earlier in this chapter. Notably, there are smaller changes to the streamfunction in the deep tropics; the equatorial lobes of anomalous streamfunction are more meridionally confined, as in the responses in Chapter 4. Instead the largest changes in streamfunction are found in the subtropics and mid-latitudes, suggesting changes to the indirect overturning circulation associated with the eddy activity dominates the streamfunction field. The changes are especially intense for Trial P8, for which the strongest wind response was found.

The changes in temperature for the eight trials are presented in Figures 5-12 and 5-13. As in the cases above, the changes in reference temperature are still prominent in these difference fields. However, the mid-latitude changes in temperature associated with dynamic warming or cooling may be detected in these plots. As should be expected, the strength of this dynamic response is larger for the trials with larger perturbations of reference temperature.

The changes to E-P flux divergence are examined in Figures 5-14 and 5-15. Here it is easy to see the dipole of eddy flux divergence at the surface, which has been so prominent for the other cases in which an annular mode-like response appears. Only in Trial P1 does this feature not appear. In Trials P2 through P4, however, the surface dipoles of divergence and convergence are prominent. One notable difference among these cases and the runs shown in Chapter 4 is that the changes in surface divergence associated with the poleward lobe of the anomalies tend to be latitudinally more expansive, with regions of opposite polarity in the free troposphere also extending into the polar regions. This may be understood as an effect of the imposition of the anomalous reference temperature over a wider latitude than the torques used in

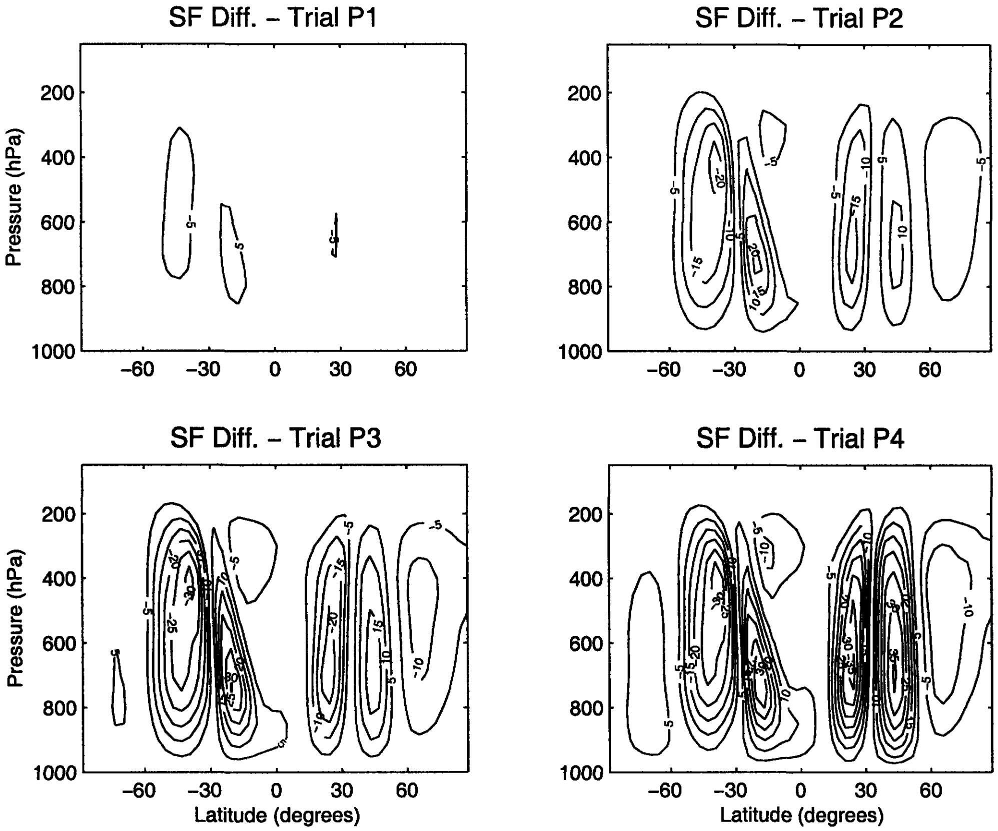

SF Diff. - Trial P1

SF Diff. - Trial P2

SF Diff. - Trial P3

SF Diff. - Trial P4

Figure 5-10: As in Figure 5-8, but for the changes in streamfunction. Contour interval is 5×10^9 $kg\ s^{-1}$.

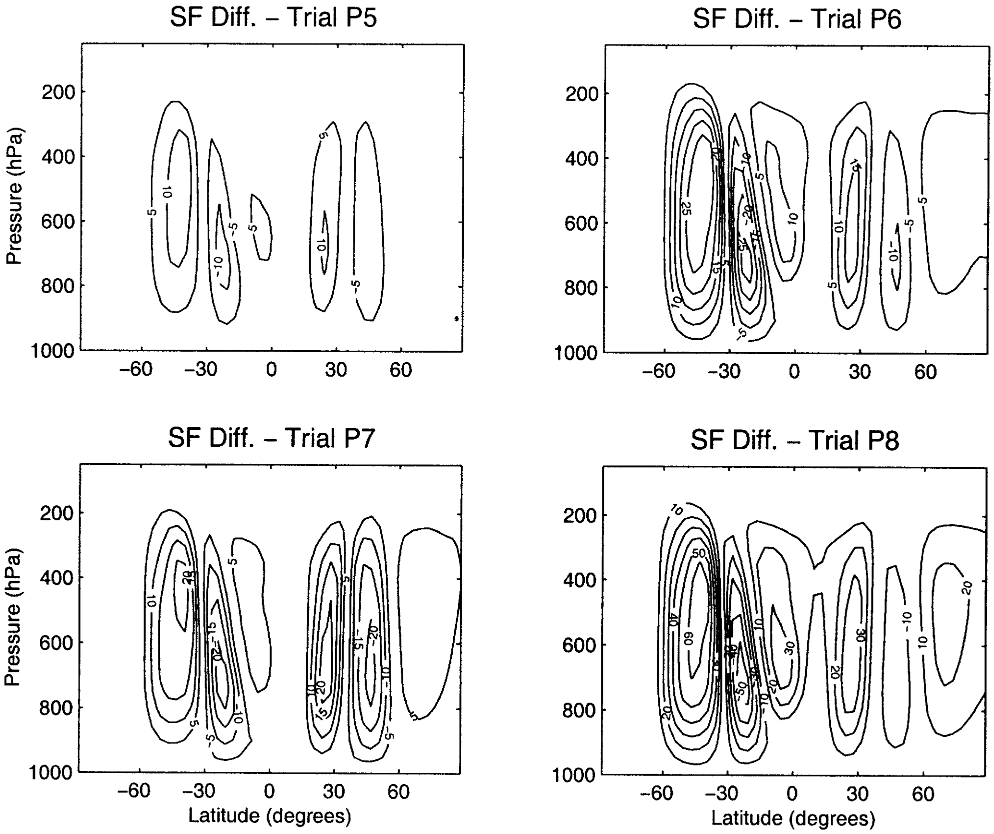

Figure 5-11: As in Figure 5-9, but for the changes in streamfunction. Contour interval is 5×10^9 $kg\ s^{-1}$ except 1×10^{10} $kg\ s^{-1}$ in bottom right panel.

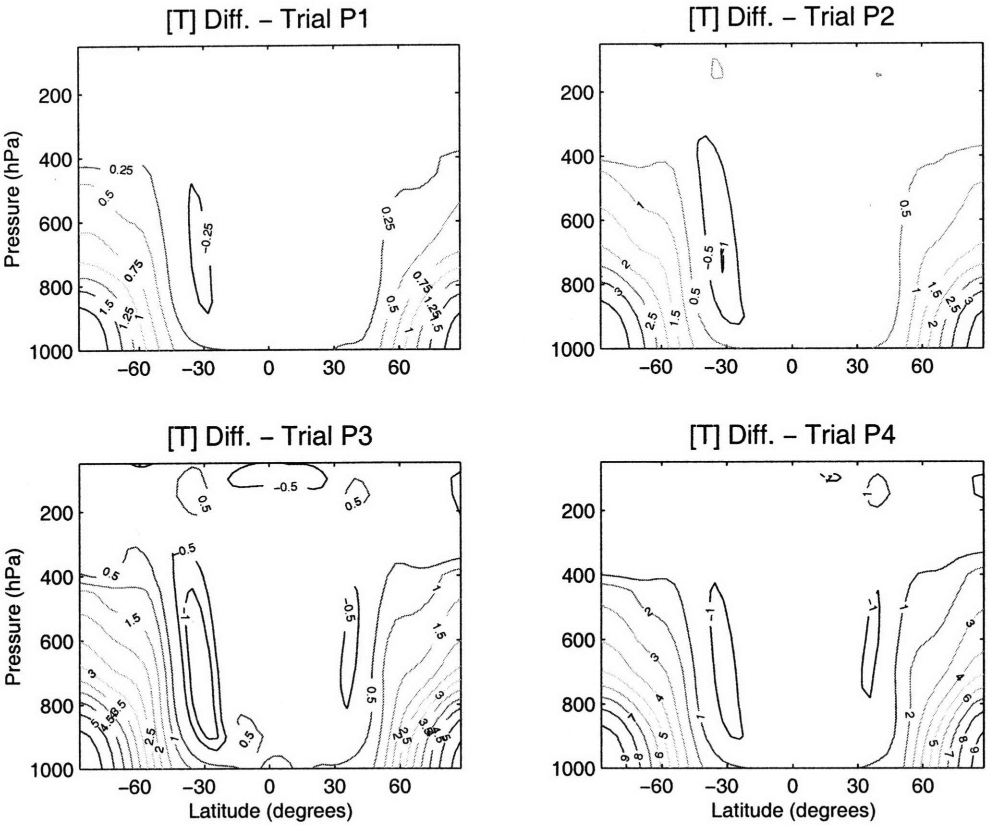

Figure 5-12: As in Figure 5-8, but for the changes in temperature. Contour interval is .25 K in top left panel, .5 K in top right and bottom left panel, and 1 K in bottom right panel.

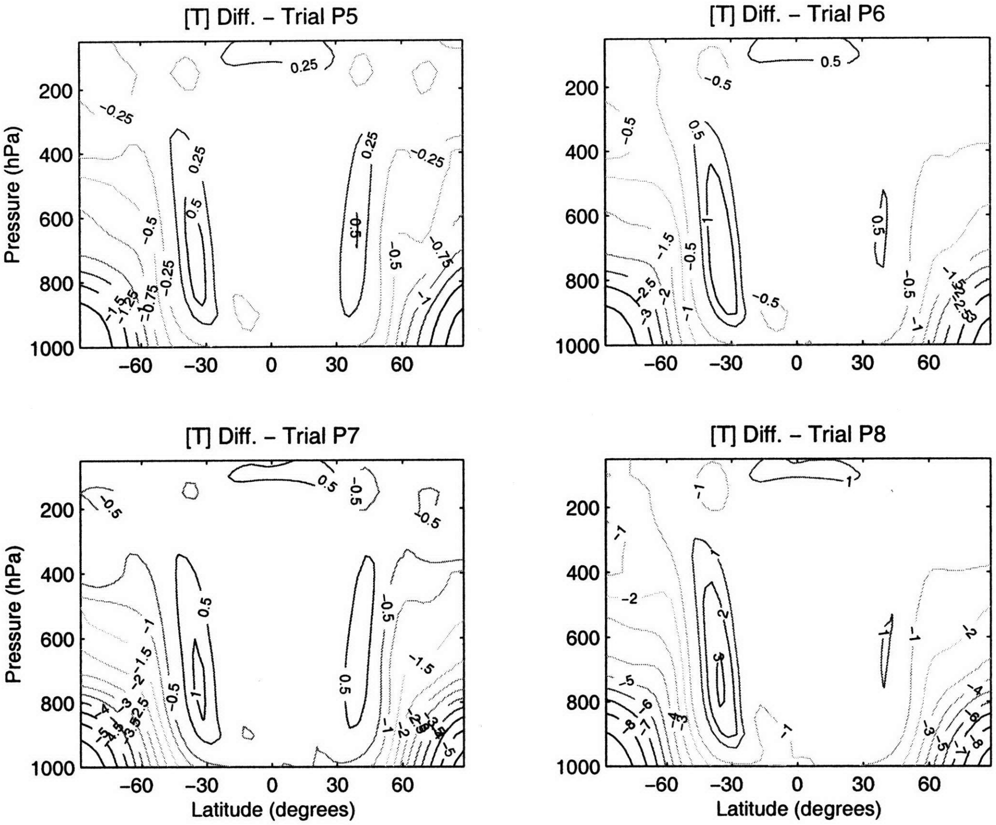

[T] Diff. - Trial P5

[T] Diff. - Trial P6

[T] Diff. - Trial P7

[T] Diff. - Trial P8

Figure 5-13: As in Figure 5-9, but for the changes in temperature. Contour interval is .25 K in top left panel, .5 K in top right and bottom left panel, and 1 K in bottom right panel.

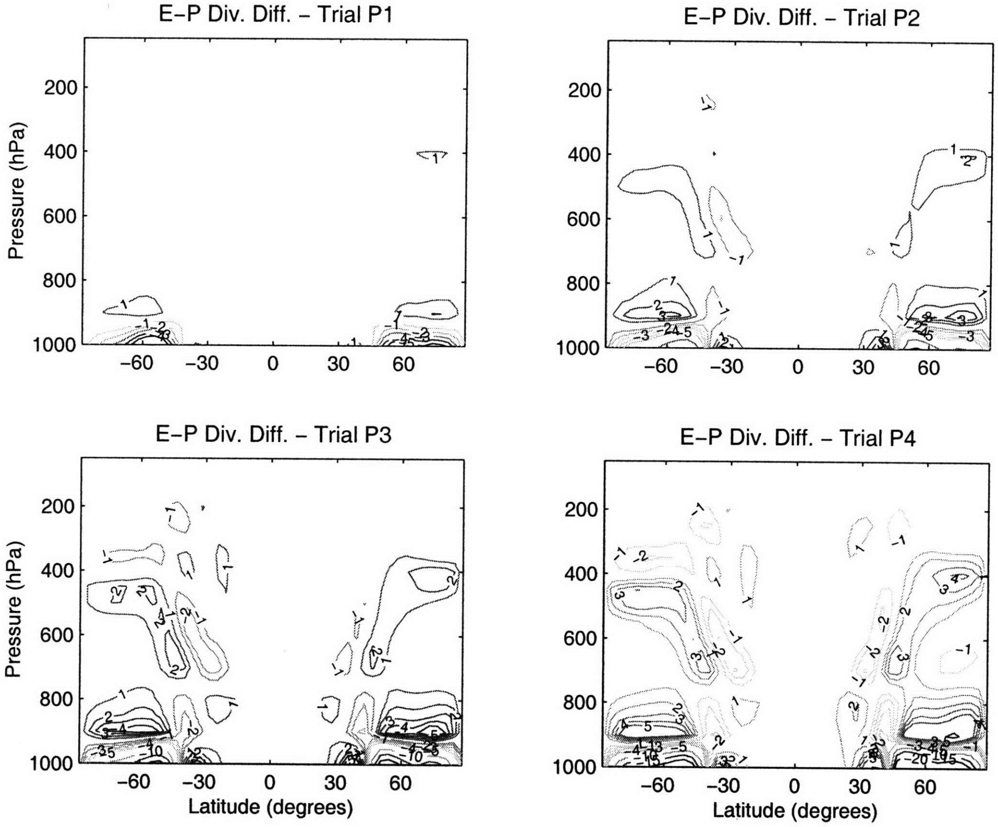

Figure 5-14: As in Figure 5-8, but for the changes in time-mean E-P flux divergence. Contour interval is 1 $m\ s^{-2}$ acceleration of zonal wind until 5 $m\ s^{-2}$ and 5 $m\ s^{-2}$ thereafter.

Chapter 4, which is affecting the baroclinicity (and hence the eddy generation rates) well into the polar region.

In Trials P5 through P8, the dipole of E-P flux divergence is prominent at the surface in all four trials. The similarities in the upper tropospheric structure of the anomalous E-P fluxes and the pattern found through SVD analysis is also especially noticeable in Trial P8.

Finally, I look at the changes in the barotropic portion of the E-P flux divergence in Figures 5-16 and 5-17. In the cases with polar warming of the reference temperature, I find anomalous barotropic convergence on the poleward side of the jet's position and divergence on the equatorward side, suggesting decreased equatorward propagation of eddies in these cases, and a resultant weaker momentum transport from the subtropics to the mid-latitudes. The response is again weak for Trial P1

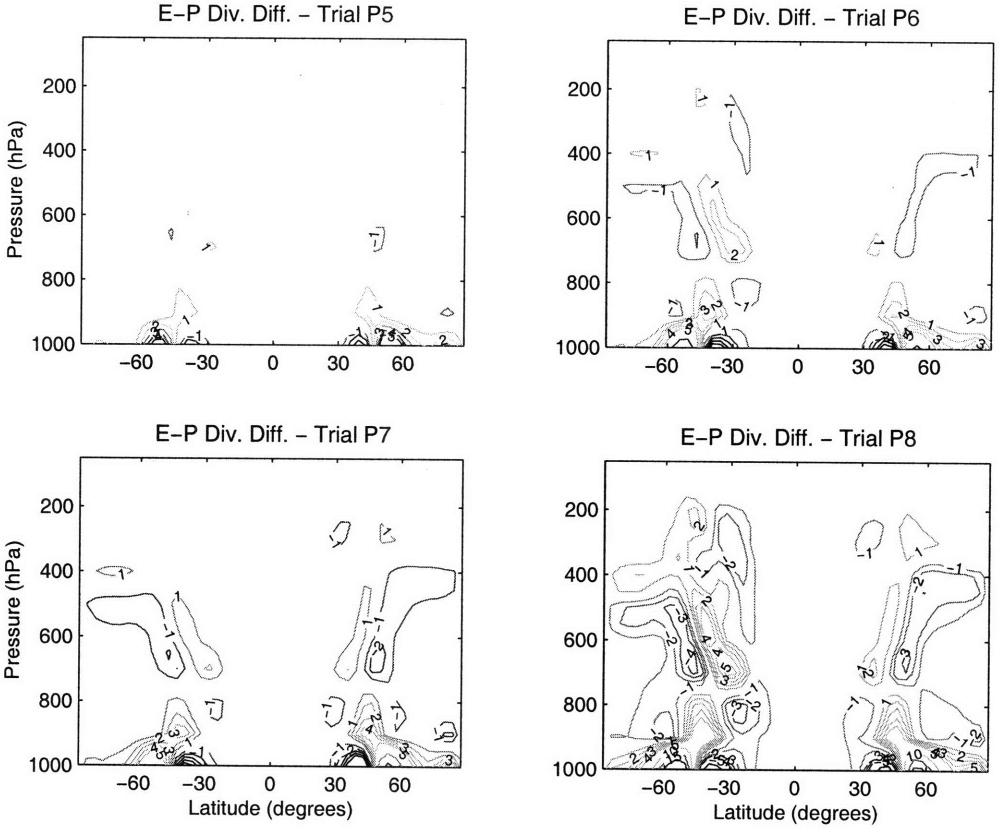

Figure 5-15: As in Figure 5-9, but for the changes in time-mean E-P flux divergence. Contour interval is 1 $m\ s^{-2}$ acceleration of zonal wind until 5 $m\ s^{-2}$ and 5 $m\ s^{-2}$ thereafter.

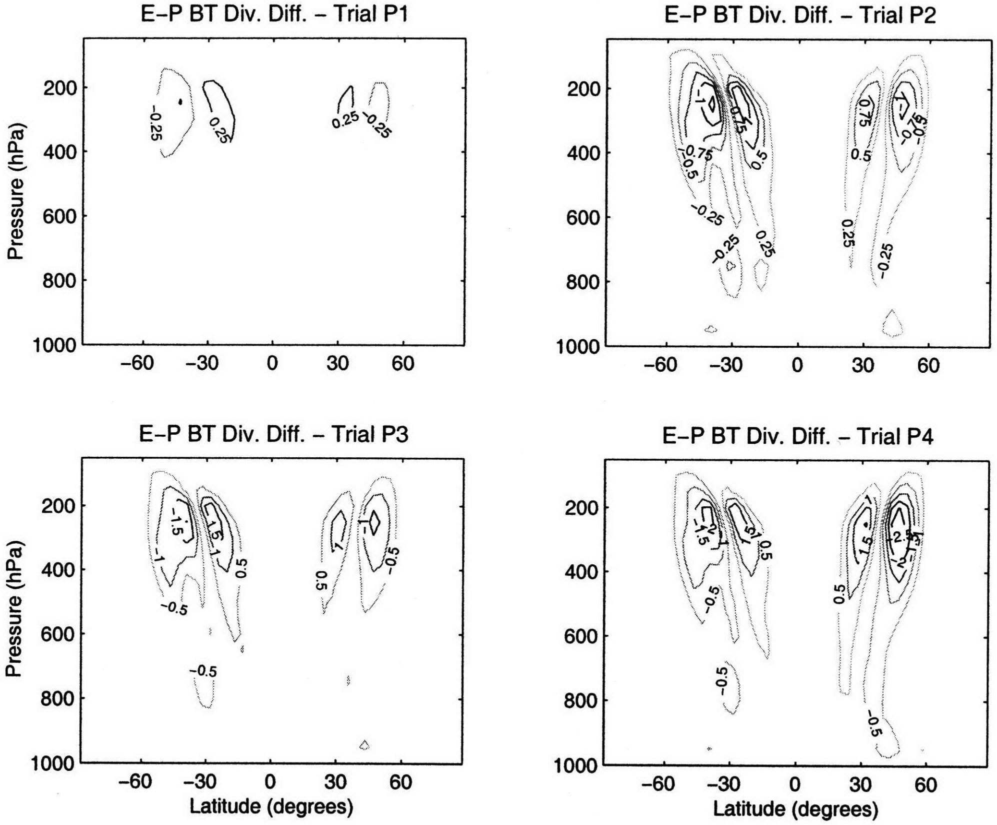

Figure 5-16: As in Figure 5-8, but for the changes in time-mean meridional E-P flux divergence. Contour interval is 0.25 $m\ s^{-2}$ acceleration of zonal wind in top panels and 0.5 $m\ s^{-2}$ in bottom panels.

but robust for the other trials. In Trials P5 through P8, which used polar cooling, anomalous divergence is found to coincide with the westerly anomalies in the upper troposphere, and convergence with the easterly anomalies. This suggests more intense equatorward eddy propagation, and consequently a larger poleward eddy-driven westerly momentum transport than in the control run.

As in the previous section, the results may be compared to those of Son and Lee (2006), who performed several trials using cooling confined to the polar regions. With their cooling, they found wind responses which included both annular mode-like wobbling behavior and poleward propagation, which they considered to be a blending of the EOF1-EOF2 behavior. Examining the basic state of their setup indicates their EOF2 (the tripole, strengthening-sharpening pattern) explains a much larger fraction of variance as compared to their EOF1 than does the EOF2 in my basic state. The

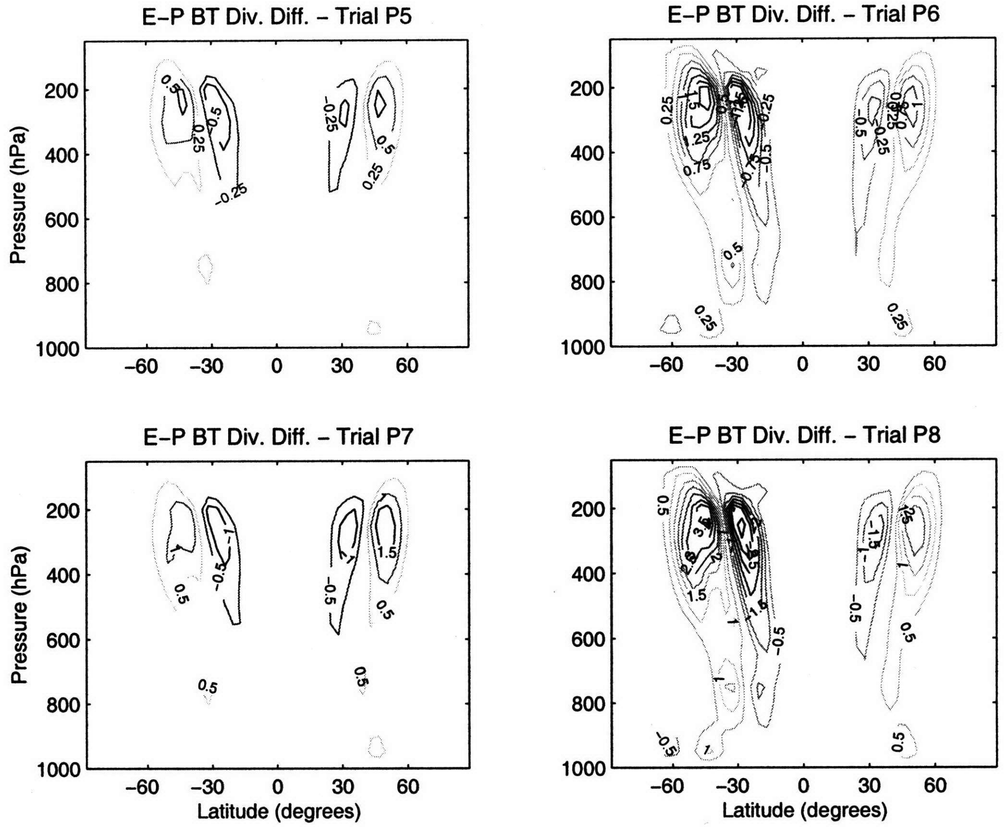

Figure 5-17: As in Figure 5-9, but for the changes in time-mean meridional E-P flux divergence. Contour interval is 0.25 $m\ s^{-2}$ acceleration of zonal wind in top panels and 0.5 $m\ s^{-2}$ in bottom panels.

larger fraction of variance encapsulated in EOF2 in their runs accounts for its more prominent behavior in their difference fields as compared to mine.

5.4 Summary

In this chapter, the response of the model to thermal forcings is tested, to determine whether the annular modes are a preferred response to these forcings. The forcing is accomplished by running the model with a reference temperature profile altered from that of the control, and the climatologies of each run using an altered profile and the control run are compared.

The first set of trials employed temperature forcing of a hemisphere-wide scale. These trials did not produce clear annular-mode like patterns in the response. Trials with the maximum temperature perturbations in the tropics did an especially poor job in producing annular mode-like changes to climatology. The trials with forcing maximized in the polar regions produced changes more similar to the annular mode-like patterns, but still did not reproduce the patterns as well as the runs in Chapter 4.

Next, a suite of runs was performed where the temperature perturbations were limited to poleward of 45°, resulting in a poleward shift of the region of the maximum perturbed reference temperature gradient as compared to the earlier runs. These trials were successful in consistently producing the annular mode pattern, except for Trial P1, for which the forcing was apparently too weak to produce a robust response. In the cases featuring a strong annular mode response, the changes in eddy fluxes are similar to the patterns emerging from SVD analysis, again suggesting a linkage between the zonal wind and eddy anomalies that will be further explored in the next chapter.

In Chapter 4 I showed that the annular modes appear as a response of the model atmosphere to a number of momentum forcings. The annular modes appear here as well in response to several temperature perturbations. From the results of these two chapters, the annular modes do appear to be a preferred response of the atmosphere to the applied forcings. However, the patterns can be difficult to discern for cases where the forcing extends deeply into the tropics.

It is difficult to compare directly the strength of the responses among the cases using momentum forcings and temperature forcings, as the nature of the two forcings are quite different. But it is of course tempting to find a way to unite the results of the two sets of trials. In Chapter 7, I will examine this problem and propose a means of comparing the responses under the different forcings. First, however, I turn to examine more closely the role of eddies in determining the responses through use of a zonally symmetric model in the next chapter.

Chapter 6

Zonally Symmetric Trials

6.1 Introduction

In most of the trials considered in the previous two chapters, the model has responded in an annular mode-like fashion in response to a generic forcing. This suggests the annular modes are a preferred response of the circulation to a given forcing. Additionally, the changes in E-P flux divergence found in each trial are similar to the patterns of E-P flux divergence found through the SVD analysis of the control run.

In observational studies of Earth's annular modes (e.g. Limpasuvan and Hartmann, 2000) there is a clear relationship between the wind anomalies and anomalies in eddy flux divergence, a relationship which Lorenz and Hartmann (2001, 2003) found constituted a positive feedback. Since the eddy feedback plays a critical role in maintaining the annular mode patterns, it seems likely that the eddy feedback must likewise account for the forced responses shown in the model runs here.

This hypothesis is tested in this chapter, through the use of a zonally symmetric version of the model. By using the zonally symmetric model, I may prescribe the eddy fluxes as fixed values. Additionally, the applied forcing may be separated from the changes in eddy flux divergence from run to run. The direct effects of the forcing may therefore be examined in the absence of an eddy feedback.

Below, runs in which the torques or reference temperature perturbations are applied, but the eddy fluxes held fixed at the climatological control run values, are considered. The changes in climatology in these cases capture neither the shape nor the strength of the responses in the full model run properly. Instead, the changes in eddy fluxes must be included to produce both the proper magnitude and shape of the annular mode response.

6.2 Setup

For the results in this chapter, the model is run with a zonally symmetric setup, suppressing all longitudinal variation in the climatological variables. This is accomplished by calculating the climatological eddy fluxes from the control run and prescribing them to the model for all points in longitude, rather than allowing the tendencies of wind and temperature related to the eddy fluxes to be calculated anew at each longitude and time step. The resolution and values of the damping coefficients are identical to those used in the full model runs.

As the model is run in sigma coordinates, the form of the eddy flux tendencies in sigma coordinates must be considered. Following the discussion in Holton (1992), chapter 10, section 3, the eddy forcing terms are found to be

$$\begin{aligned}
\frac{\partial \overline{u}}{\partial t}_{eddy\ forc.} &= -\frac{1}{\overline{p_s} a \cos^2\phi}\frac{\partial}{\partial \phi}\overline{\left((vp_s)'\, u' \cos^2\phi\right)} - \frac{1}{\overline{p_s}}\frac{\partial}{\partial \sigma}\overline{\left((\dot{\sigma}p_s)'\, u'\right)} \qquad (6.1)\\
\frac{\partial \overline{T}}{\partial t}_{eddy\ forc.} &= -\frac{1}{a\cos\phi}\frac{\partial}{\partial \phi}\overline{\left((vp_s)'\, T' \cos\phi\right)} - \frac{\partial}{\partial \sigma}\overline{\left((\dot{\sigma}p_s)'\, T'\right)} - \kappa\overline{\left(\left(\frac{\partial \dot{\sigma}}{\partial \sigma}p_s\right)' T'\right)}\\
&\quad -\kappa\overline{(p_s D)'\, T'} + \kappa\left(\frac{\overline{(p_s\dot{\sigma})'\, T'}}{\sigma}\right), \qquad (6.2)
\end{aligned}$$

where $\dot{\sigma}$ is the pressure velocity analog in sigma coordinates, $\frac{D\sigma}{Dt}$, D the horizontal divergence, p_s the surface pressure, and other meteorological notation is as used earlier.

The zonally symmetric model is first run with the climatological eddy fluxes applied and using no external forcing. The climatology produced in this run is similar to that of the control, as will be shown below. Next, for each case shown in Chapters

4 and 5, the zonally symmetric model is run with the applied torque or the perturbed reference temperature, but holding the eddy fluxes from the control run fixed. These runs measure the direct effects of the forcing on the model's climatology by suppressing the effects of the eddy feedback. Finally, for each case, the model is run with both the applied forcing and time-mean eddy fluxes calculated from the forced run in the full model. The responses in these trials include the effects of the eddy, zonal-flow feedback.

As the zonally symmetric runs do not permit eddy fluxes to change with time, the climate is similarly invariant. In these runs, the model spins up until its climatology is reached; then the meteorological fields do not vary with time. In all the model results shown below, the results are averaged over the final 500 days of 2,000 day model runs, though this average is identical to the climatology on any individual day of that period.

6.3 Control Climatology of the Zonally Symmetric Run

In this section, a climatology obtained from the zonally symmetric trial is presented. This run is forced with the time-mean eddy fluxes calculated from the control full model run. All of the climatological fields derived from this run feature no longitudinal variation.

The temperature is relaxed to the control run's reference temperature profile, and no external forcing is applied. This run is therefore the zonally symmetric analog of the control full model run, shown in Chapter 3.

First I display the forcings of zonal wind and temperature due to the eddy fluxes calculated from Equations 6.1 and 6.2, respectively. These forcings are shown in Figures 6-1 and 6-2. The zonal wind forcing is strongly positive near the location of the jet in each hemisphere, with weaker centers of negative forcing on each flank. The temperature forcing in each hemisphere is positive through a large vertical column on the poleward side of each jet, with negative temperature forcings strongest at the ground, in the subtropics of each hemisphere.

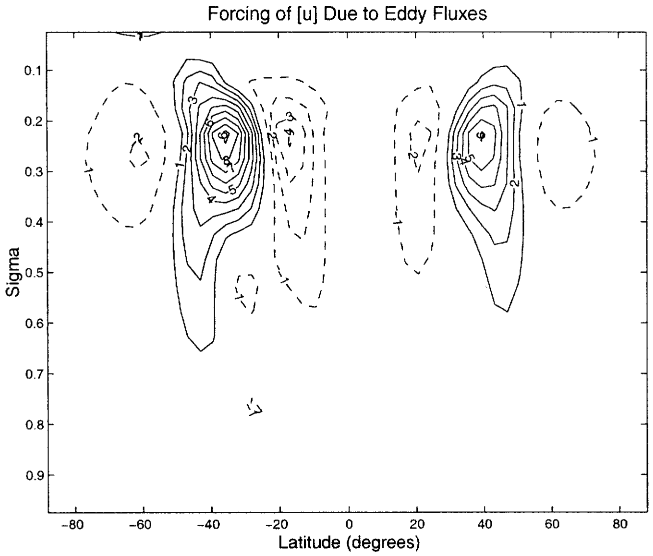

Figure 6-1: Forcing of zonal wind due to eddy flux terms calculated in Equation 6.1. Contour interval is 1 $m\ s^{-1}\ day^{-1}$ rate of change of zonal wind. Negative contours are dashed and zero contour is omitted.

The zonal wind found from the control run of the zonally symmetric model is shown in Figure 6-3. In each hemisphere a westerly jet similar to that of the control full model run has been produced in the mid-latitudes, with weak easterlies predominating equatorward of 30°. The jet maxima are similar in position to their locations in the full model run (Figure 3-1), though slightly equatorward in each hemisphere (35° here versus 37° in the full run for the SH jet, and 37° here versus 41° in the full run for the NH jet). The jet maxima are also somewhat stronger here (50 $m\ s^{-1}$ versus 43 $m\ s^{-1}$ in the SH; 36 $m\ s^{-1}$ versus 32 $m\ s^{-1}$ in the NH), but the profile of surface wind is similar to that of the full model.

The streamfunction produced by the zonally symmetric model is shown in Figure 6-4. It is similar to the streamfunction produced by the full model run (Figure 3-3). The most prominent cell is the tropical overturning cell, with its rising branch in the NH and sinking branch in the SH. This Hadley cell features a maximum transport of $23 \times 10^{10}\ kg\ s^{-1}$ at its center — a magnitude similar to that of the full run in Chapter 3. The weaker NH Hadley cell and Ferrel cells are also similar to those

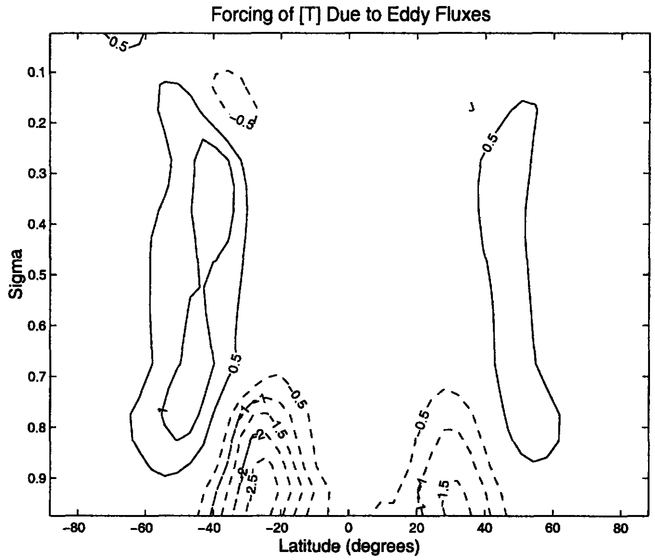

Figure 6-2: As in Figure 6-1, but for the forcing in temperature as calculated from Equation 6.2. Contour interval is 0.5 $K\ day^{-1}$ rate of change of temperature. Negative contours are dashed and zero contour is omitted.

produced from the full model run.

The temperature calculated by the zonally symmetric model is shown in Figure 6-5. Like the temperature profile from the full run (Figure 3-4), the warmest point is found north of the equator, and nearly-flat meridional temperature gradients still predominate in the tropical troposphere. The 20 K difference between temperatures at the North Pole and South Pole is also replicated here.

The zonally symmetric model produces a control climatology similar to that of the full model. In the next section, I will compare this climatology to those produced using the applied mechanical torques, but leaving the eddy fluxes from the control run fixed. These direct responses to the forcing capture neither the magnitude nor the structure of the annular mode response.

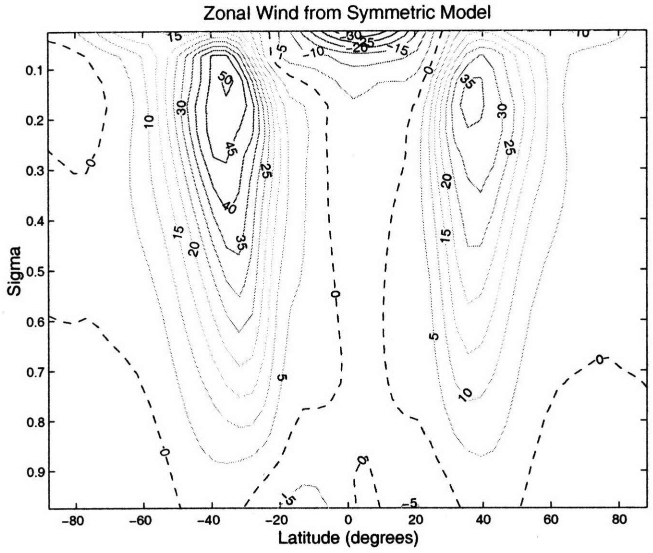

Figure 6-3: Zonal wind for the control zonally symmetric run. Contour interval is 5 $m\ s^{-1}$; zero contour is dashed.

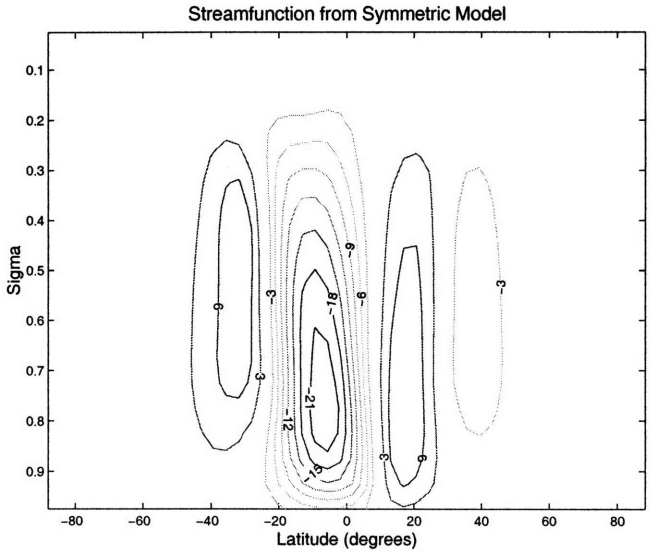

Figure 6-4: Streamfunction for the control zonally symmetric run. Contour interval is $3 \times\ 10^{10}$ $kg\ s^{-1}$; zero contour is omitted.

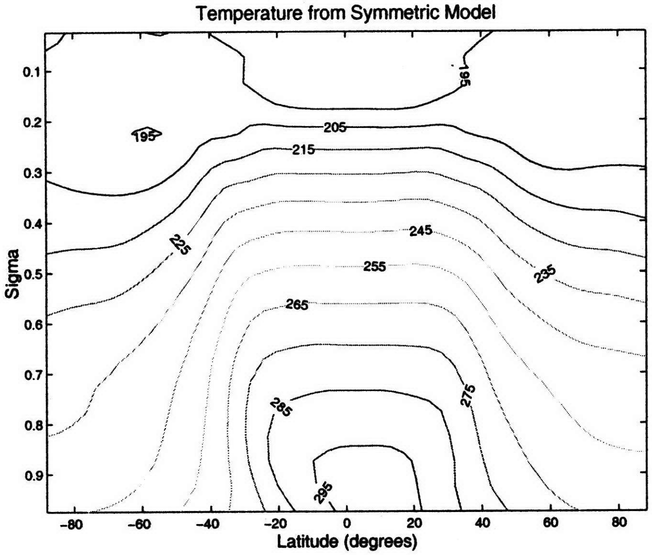

Figure 6-5: Temperature for the control zonally symmetric run. Contour interval is 10 K.

6.4 Results of the Zonally Symmetric Model for Mechanically Forced Trials

In this section, zonally symmetric runs are discussed in which the torques described in Chapter 4 are applied to the model. As stated above, for each torque two runs of the zonally symmetric model will be conducted. The first run adds only the torque, but none of the eddy flux changes found in the full model. These flux anomalies, along with the torque, are incorporated into the second run. As examples I will use Trials L3, L4, L5, and L6 to illustrate the responses of the zonally symmetric model, but runs using forcing from other trials displayed analogous behavior in their responses.

In the next few figures, runs of the zonally symmetric model are considered where the mechanical forcings are applied, but the eddy fluxes are held fixed at the control values. The changes in zonal wind between these runs and the control run of the zonally symmetric model are shown in Figure 6-6. In all cases, the response to the direct forcing alone is insufficient to explain either the magnitude or the structure of the annular mode-like responses in Figures 4-16 and 4-17. The response in Trial L3, for example, is much weaker than the annular mode response. It features its strongest

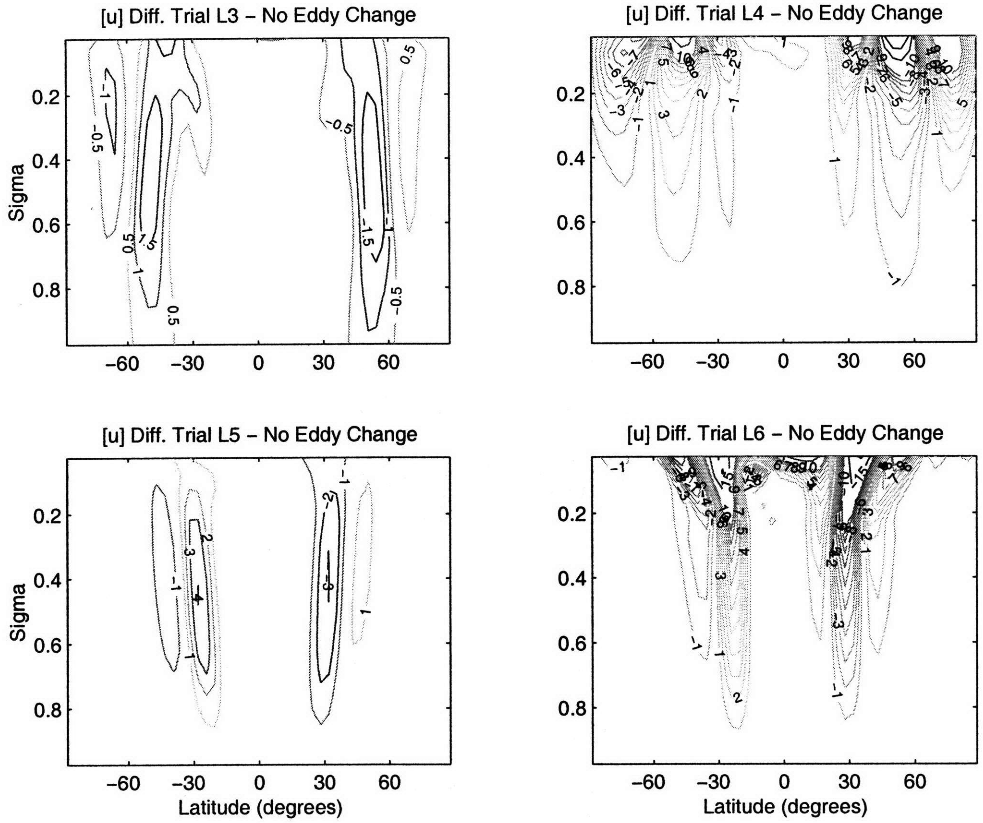

Figure 6-6: Change in zonal wind for the indicated trials versus the control for the zonally symmetric runs, including direct forcing only. Contour interval is 0.5 $m\ s^{-1}$ in top left panel and 1 $m\ s^{-1}$ in other panels; zero contour is omitted.

magnitude at about 50° in each hemisphere — the latitude at which the forcing was applied in Trial L3 — but the direct response does not include the opposite-signed lobe of anomalous wind on the other flank of the jet. The behavior in Trial L5 is somewhat similar — here while the opposite-signed lobes are generated on the other flank, the magnitudes of these lobes are weaker than those seen for the full annular mode response in the full model runs. The zonally symmetric responses in Trials L7 and L8 (not shown) are also too weak and do not represent the annular mode shape.

The direct responses to Trials L4 and L6 do not capture the appropriate shape or strength of the annular modes, either. While these trials produce strong wind changes in the upper troposphere, they are not as vertically coherent as the annular modes. In the full model run of Trial L4, for example, anomalous wind exceeding $1\ m\ s^{-1}$ reached the ground, while here the contours do not do so. As with the zonally symmetric responses to the forcing in Trials L3 and L5, the responses in these two cases are not dipolar about the latitude of the unforced jet, as in the analogous full model runs.

The changes in streamfunction between each trial in the zonally symmetric model and that of the control zonally symmetric run are shown in Figure 6-7. The streamfunction changes are particularly weak in Trials L3 and L4, which use poleward-flank forcing. Trial L5 features a somewhat stronger streamfunction response, but the response is not vertically coherent. In Trial L6, the direct streamfunction response is both the strongest of the four trials considered here, and more vertically coherent than Trial L5, with positively anomalous streamfunction extending from the ground to tropopause level. The change of magnitude of streamfunction, reaching a maximum of $2 \times 10^{10}\ kg\ s^{-1}$, is of the same order of magnitude as the changes seen in the full model run (Figure 4-19). While the direct response to Trial L6 is not annular mode-like, it is strong, unlike the weaker responses seen in the other trials.

The changes in temperature between the four zonally symmetric trials and their control run are shown in Figure 6-8. In no case does the change in temperature from the zonally symmetric run with direct forcing only resemble that of the full model run (Figures 4-20 and 4-21). Trials L3 and L5 feature cooling just poleward of the

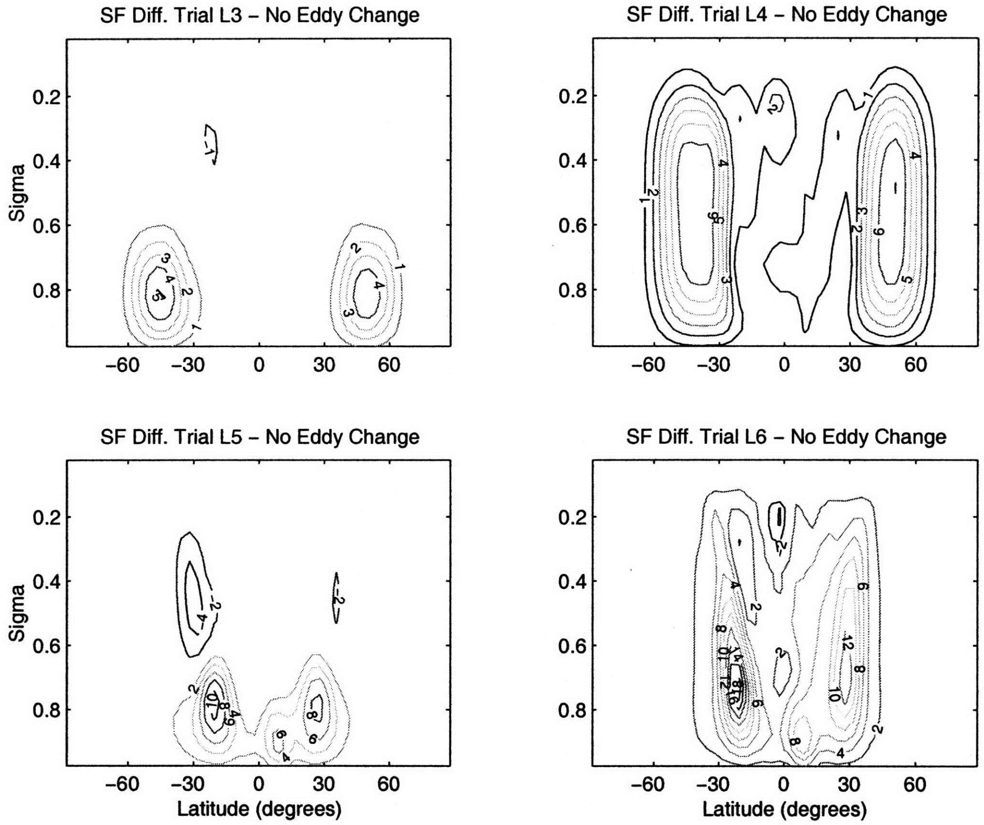

Figure 6-7: As in Figure 6-6, but for the streamfunction. Contour interval is $1 \times 10^9\ kg\ s^{-1}$ in top two panels and $2 \times 10^9\ kg\ s^{-1}$ in the bottom two panels. Zero contour is omitted.

positive forcing in the SH, and warming just poleward of the negative forcing in the NH. Trials L4 and L6 contain large temperature changes at the top of the model with cooling or warming extending downward from these features, but this pattern does not match the annular mode pattern either.

Having examined the responses of the zonally symmetric model to the direct forcing only, I now turn to the responses of the model under both the direct forcing and the eddy changes calculated from the full model run. These runs therefore include the effects of changes to the eddy feedback in the response.

The changes to eddy forcing of the zonal wind for the four trials are shown in Figure 6-9, and the changes to eddy forcing of temperature are shown in Figure 6-10. In each case there are anomalous centers of zonal wind forcing, which are especially strong for Trial L4. In Trials L3 and L4, which feature positive forcing on the poleward

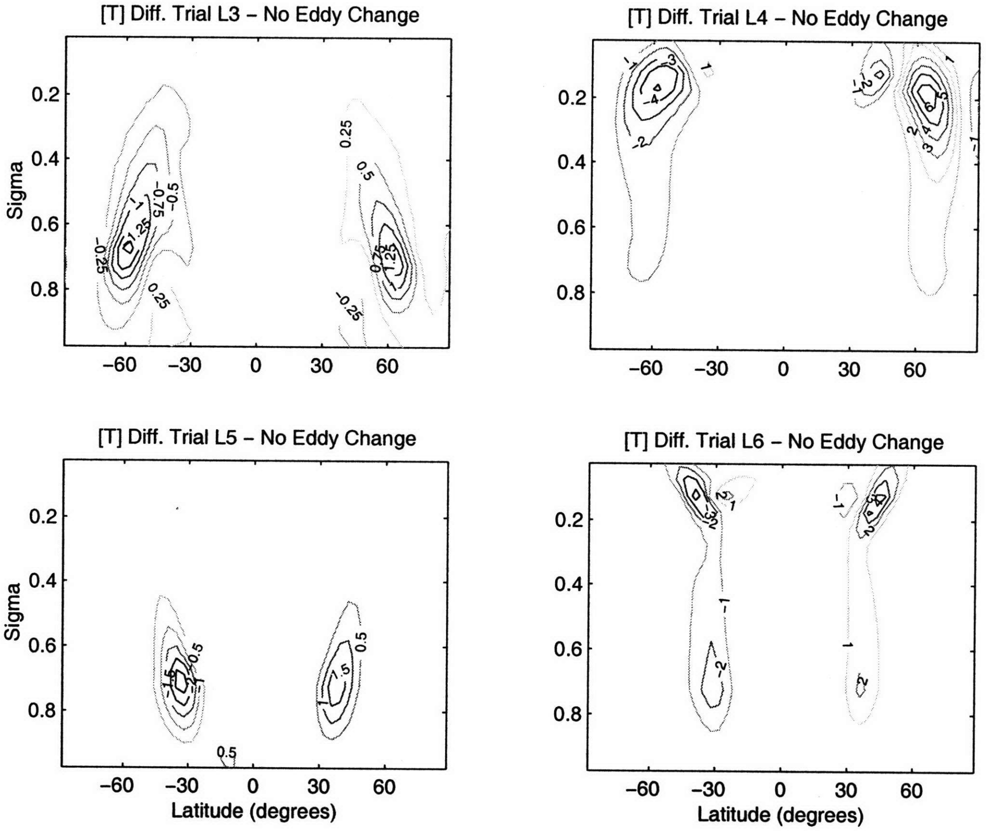

Figure 6-8: As in Figure 6-6, but for the temperature. Contour interval is 0.25 K in top left panel, 0.5 K in bottom left panel, and 1 K in right panels.

flank of the jet in the SH and negative forcing in the NH, there are westerly forcing anomalies poleward of the jet in the SH and easterly forcing anomalies equatorward of the jet in the SH, with the opposite occurring in the NH. The opposite pattern appears for Trials L5 and L6, whose westerly torque is equatorward of the jet in the SH, and whose easterly torque is equatorward of the jet in the NH.

The changes to eddy forcing of temperature in Figure 6-10 display similar patterns for the four runs. Trials L3 and L4 show warming tendencies in the SH mid-latitudes, with cooling tendencies on the equatorward sides. The opposite patterns appear in the NH. Likewise, the changes in Trials L5 and L6 are similar in shape, but opposite in sign, to those in Trials L3 and L4.

The change in zonal wind between each forced trial including eddy fluxes and the control zonally symmetric run is shown in Figure 6-11. These responses compare favorably to the responses in the full model shown in Figures 4-16 and 4-17. In Trials

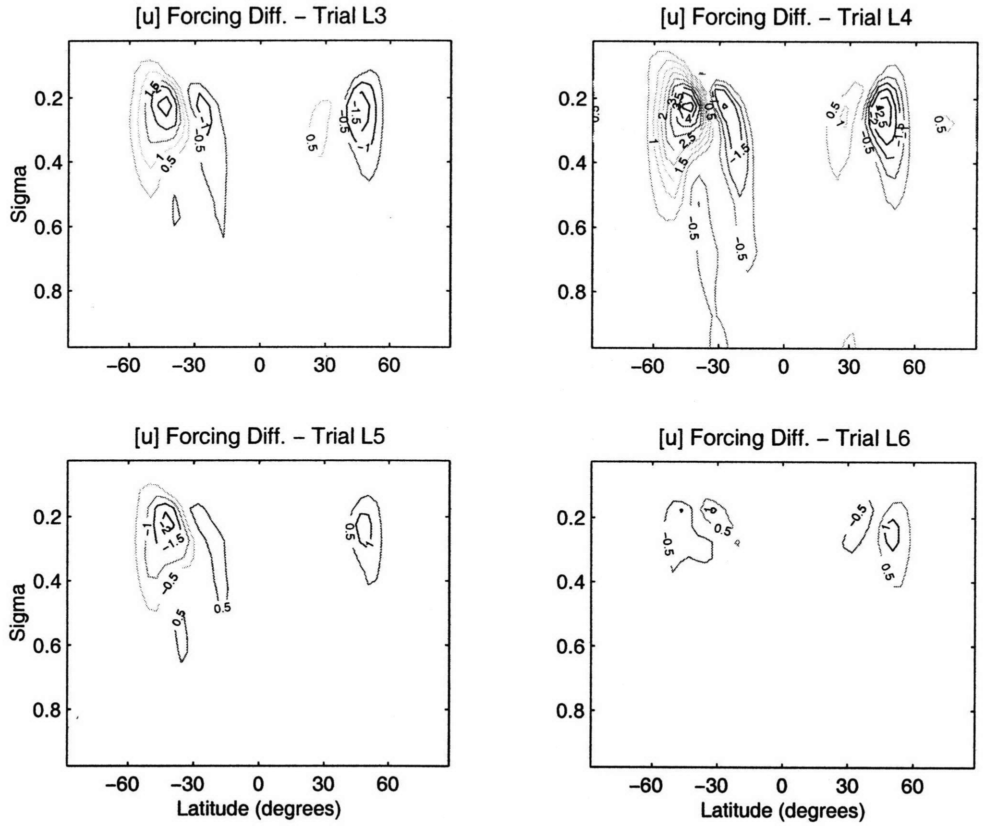

Figure 6-9: Changes in tendency of of zonal wind due to eddy flux terms for each trial versus the control. Contour interval is 0.5 $m\ s^{-1}\ day^{-1}$ rate of change of zonal wind. Zero contour is omitted.

L3, L4, and L5, the response is now clearly annular mode-like, with responses of one polarity on one side of the jet, and responses of opposite polarity on the other side of the jet. The magnitudes compare favorably to the trials in Chapter 4 as well. Note that the inclusion of the changes to the eddy fluxes has amplified the magnitude of the responses in Trials L3 and L5. Trial L4 already featured a strong direct response in the upper atmosphere, but the magnitude of the response in the lower atmosphere has been amplified by the eddies.

Of the four trials, the one which produces results the least like the annular modes is Trial L6, which used forcing in the upper troposphere on the equatorward flanks of the jets. However, recalling the results from Chapter 4, this was a run for which the annular mode response was weak as compared to most of the other runs. And, as shown earlier in this chapter, this trial featured a very strong direct response to the

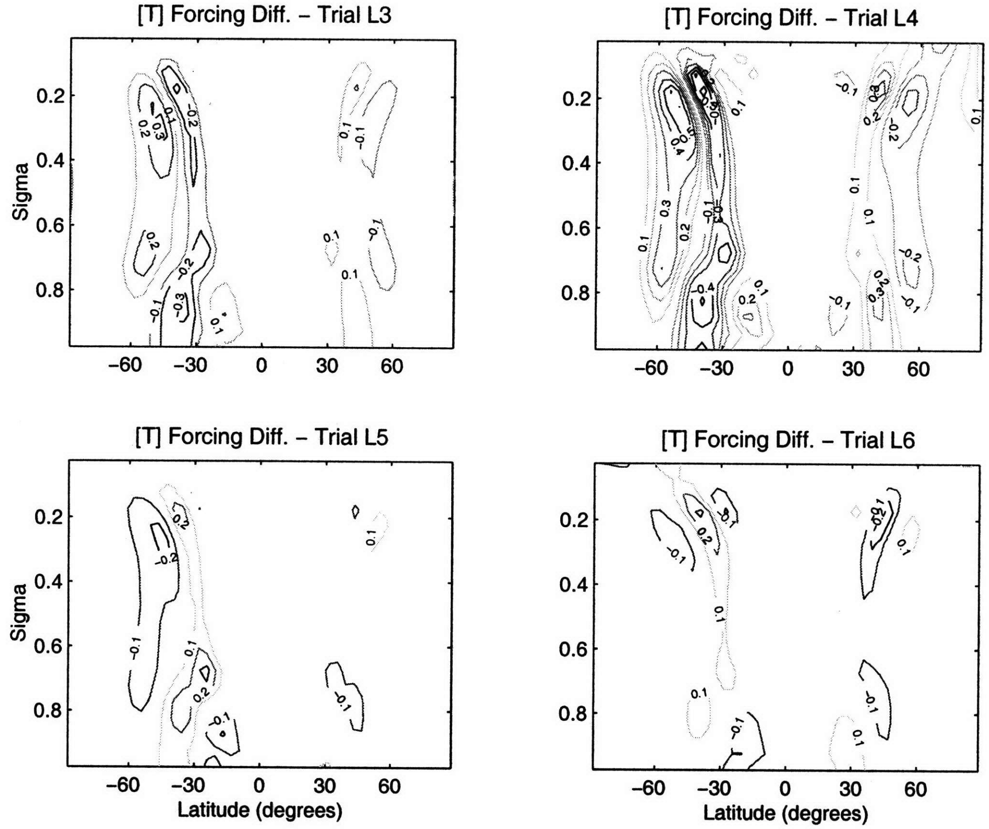

Figure 6-10: As in Figure 6-9, but for the changes in temperature tendency. Contour interval is 0.1 $K\ day^{-1}$. Zero contour is omitted.

applied forcing.

The changes in streamfunction for the four trials, with eddy flux changes included, versus the zonally symmetric control are shown in Figure 6-12. Again, the amplification of the response upon inclusion of the eddies is clear. In Trials L3 and L4 the streamfunction anomalies are no longer monopolar in each hemisphere but dipolar, and the magnitude of the maximum anomaly has jumped by almost an order of magnitude. The response in Trial L5 is now more vertically coherent, while of the four trials the change in streamfunction is most similar to that of the direct response for Trial L6. The magnitudes and shapes of the streamfunction changes, upon inclusion of the eddies, are similar to those of the full model run shown in Figures 4-18 and 4-19.

The changes in temperature for the four zonally symmetric trials are shown in Figure 6-13. Again, inclusion of the eddy feedback improves agreement with the patterns found from the full model and shown in Figures 4-20 and 4-21. In all four

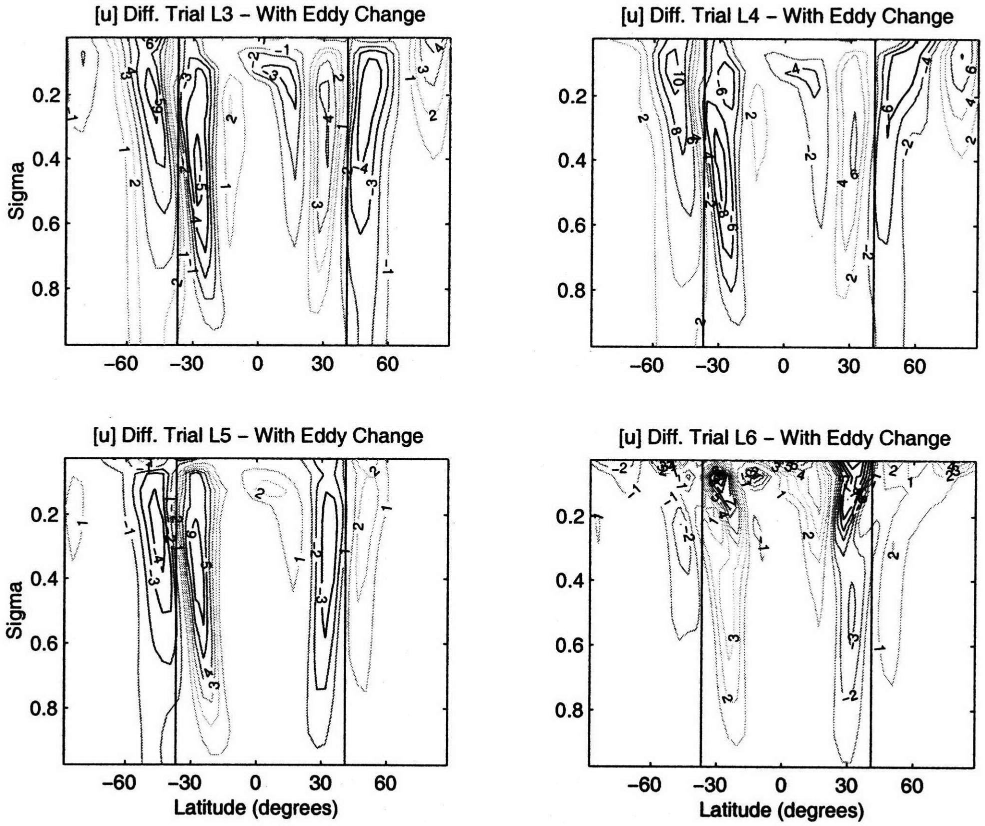

[u] Diff. Trial L3 - With Eddy Change

[u] Diff. Trial L4 - With Eddy Change

[u] Diff. Trial L5 - With Eddy Change

[u] Diff. Trial L6 - With Eddy Change

Figure 6-11: Change in zonal wind for the indicated trials versus the control for the zonally symmetric runs, including both direct forcing and changes in eddy fluxes. Contour interval is 2 $m\ s^{-1}$ in the top right panel and 1 $m\ s^{-1}$ in the other panels. Vertical lines are positions of time-mean jets.

trials, the ribbon of dynamic warming or cooling extending from tropopause level to the surface is now the prominent feature. Also similar to the full model responses in Chapter 4, there is an opposite-signed temperature response poleward of the dynamic ribbon in Trials L3 and L4, but that is much less prominent in Trials L5 and L6.

In these trials, the direct forcing is insufficient to capture either the correct strength or the correct shape of the patterns from the full model run. The changes to eddy feedback must be included in the zonally symmetric model in order to reproduce the correct pattern. For three of these trials (Trials L3, L4, and L5), this pattern was a robust annular mode. As noted in Chapter 4, however, the annular mode response was weaker in Trial L6. The zonally symmetric trials suggest that a more dominant direct response may be the cause of this discrepancy.

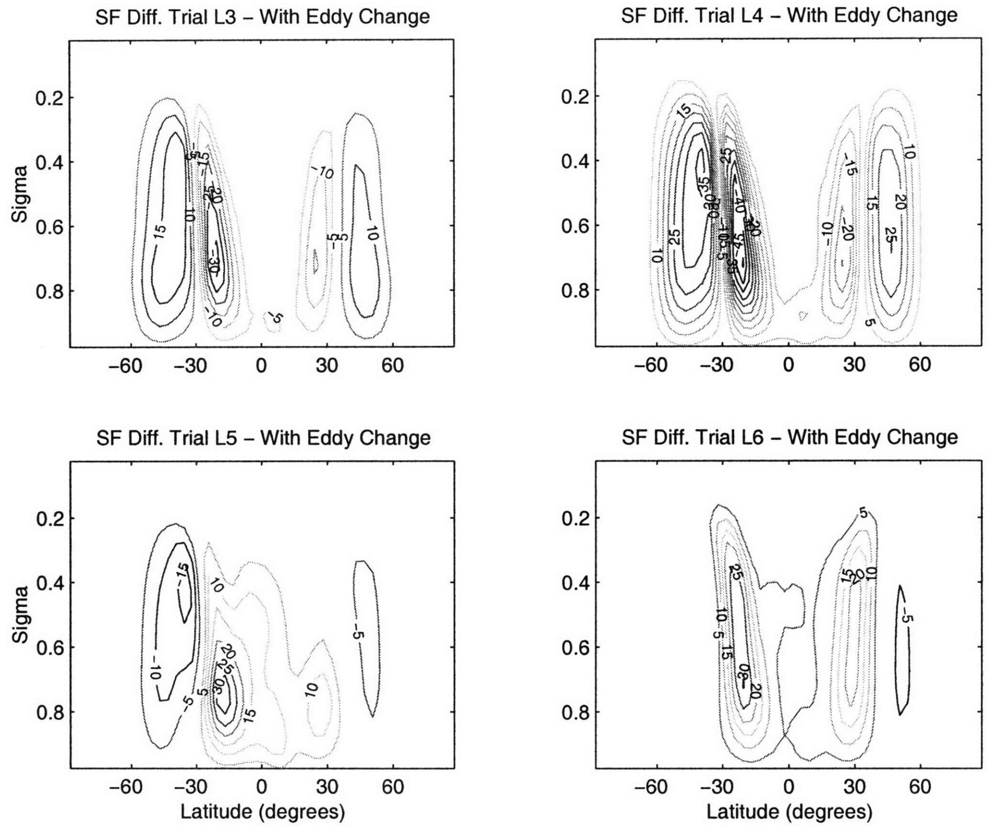

SF Diff. Trial L3 – With Eddy Change

SF Diff. Trial L4 – With Eddy Change

SF Diff. Trial L5 – With Eddy Change

SF Diff. Trial L6 – With Eddy Change

Figure 6-12: As in Figure 6-11, but for the streamfunction. Contour interval is $5 \times 10^{9} kg\ s^{-1}$ in all panels.

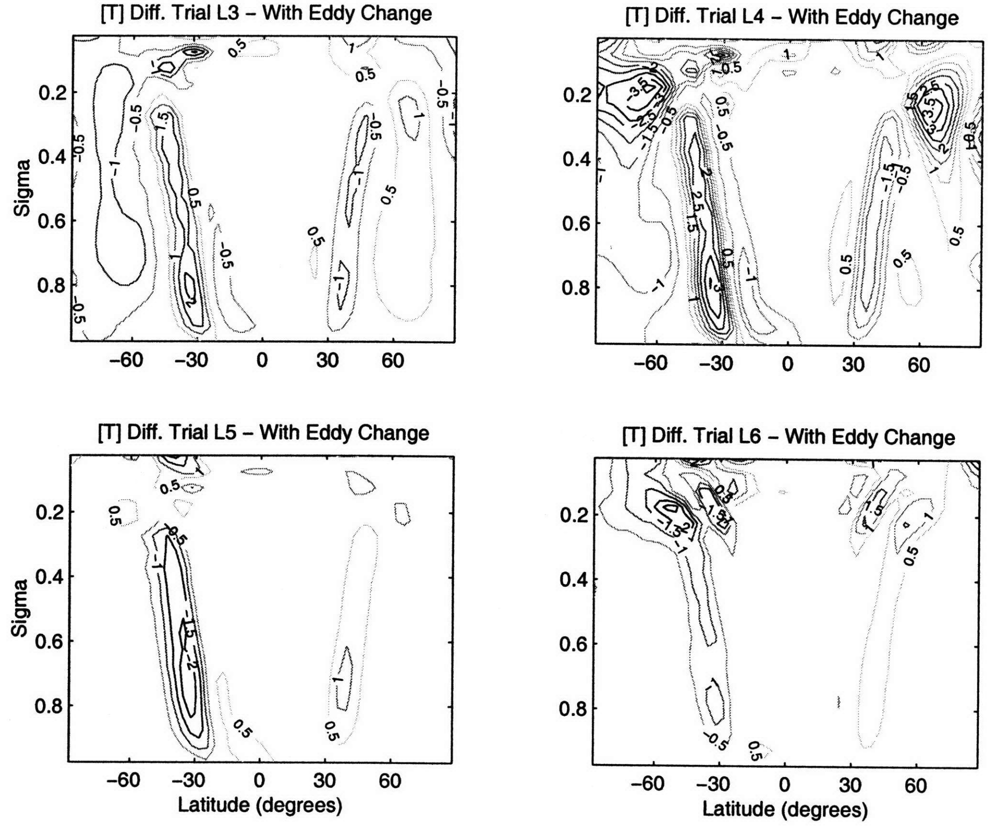

[T] Diff. Trial L3 - With Eddy Change

[T] Diff. Trial L4 - With Eddy Change

[T] Diff. Trial L5 - With Eddy Change

[T] Diff. Trial L6 - With Eddy Change

Figure 6-13: As in Figure 6-11, but for the temperature. Contour interval is 0.5 K in all panels.

Consider the following transformed Eulerian-mean momentum balance:

$$\frac{\partial u}{\partial t} + v^* \left(\frac{\frac{\partial (u \cos\phi)}{\partial \phi}}{a \cos\phi} - f \right) + \omega^* \frac{\partial u}{\partial p} = -c_d u + \frac{1}{a \cos\phi} \nabla \bullet F + G. \tag{6.3}$$

For a steady-state response to an external forcing G away from the frictional boundary layer which includes no changes to the E-P flux divergence $\nabla \bullet F$, G must be balanced by changes in the meridional circulation (primarily v^*). But, as the magnitude of the absolute vorticity decreases as one draws closer to the equator, the direct response of the meridional velocity must be larger for a forcing placed closer to the equator than for the same strength of forcing placed closer to the pole. Also, the torques placed closer to the equator overlap with the Hadley cell, introducing factors into the dynamics other than the extratropical eddy, mean-flow interaction that is crucial to the annular modes.

The direct streamfunction response shown in Figure 6-7 is far stronger for Trial L6 than for the other three trials. Comparing the response upon inclusion of the eddy flux changes, as in Figure 6-12, demonstrates that the smallest change among the four trials between the direct response and that with eddy feedback has occurred for Trial L6. While Trial L5 also features forcing placed on the tropical flank of the jet, its direct streamfunction response is not vertically coherent. Instead overturning anomalies extend only up to $\sigma = 0.7$; and weaker, opposite-signed anomalies actually occur above that. Of the four trials, only Trial L6 has produced a strong, Hadley-like direct response, and the strength of this direct response obscures the annular mode dynamics seen more clearly in the other panels.

6.5 Results of the Zonally Symmetric Model for Thermally Forced Trials

In the previous section, I have shown that the directly applied torques are not sufficient to produce either the shape or the strength of the annular-mode like response in the zonally symmetric model. Instead the changes to the eddy feedback are necessary to capture both the proper magnitude and pattern of the wind response.

In this section, I force the zonally symmetric model with the perturbations to reference temperature, rather than the mechanical torques. For each case, a similar procedure is used. The model is first run with the anomalous relaxation temperature profile applied, but with the eddy fluxes held constant from the control run. Then, a run is conducted using both the change in reference temperature, and the changes in eddy fluxes. As in the previous cases, the former runs do not reproduce properly the annular mode patterns, and the changes to the eddy feedback contained in the latter runs is necessary. For examples here I will choose Trials P1, P2, P5, and P6, although several other thermally forced trials were also tested in the zonally symmetric model, with the direct forcing alone again found insufficient to reproduce the annular mode patterns.

The directly forced changes in zonal wind for the trials using 2 K and 4 K reference temperature changes, limited to poleward of 45°, are shown in Figure 6-14. The annular mode-like responses seen in Figures 5-8 and 5-9 are not found in these trials, which use the direct forcing only. In each case the wind response is monopolar in each hemisphere, with a weakening of the westerlies for polar warming cases (P1 and P2) and a strengthening of the westerlies in polar cooling cases (P5 and P6).

As seen in Figure 6-15, the changes in streamfunction are extremely weak in these four cases, when only the direct forcing is applied. For the 4 K changes shown in Figures P2 and P6, the maximum changes in streamfunction, found in the mid-latitudes near the surface, are about 1×10^9 $kg\ s^{-1}$ — a pittance compared to the magnitudes of the changes in the full model run (Figures 5-10 and 5-11).

The temperature changes in these zonally symmetric runs, shown in Figure 6-16, show no evidence of a dynamic reorganization of the temperature field as in Figures 5-12 and 5-13. Instead the difference field simply mimics the difference in reference temperature between each case and the control run.

In the rest of this section, I consider the changes in the thermally forced cases from the zonally symmetric model, including both the responses to the direct forcing

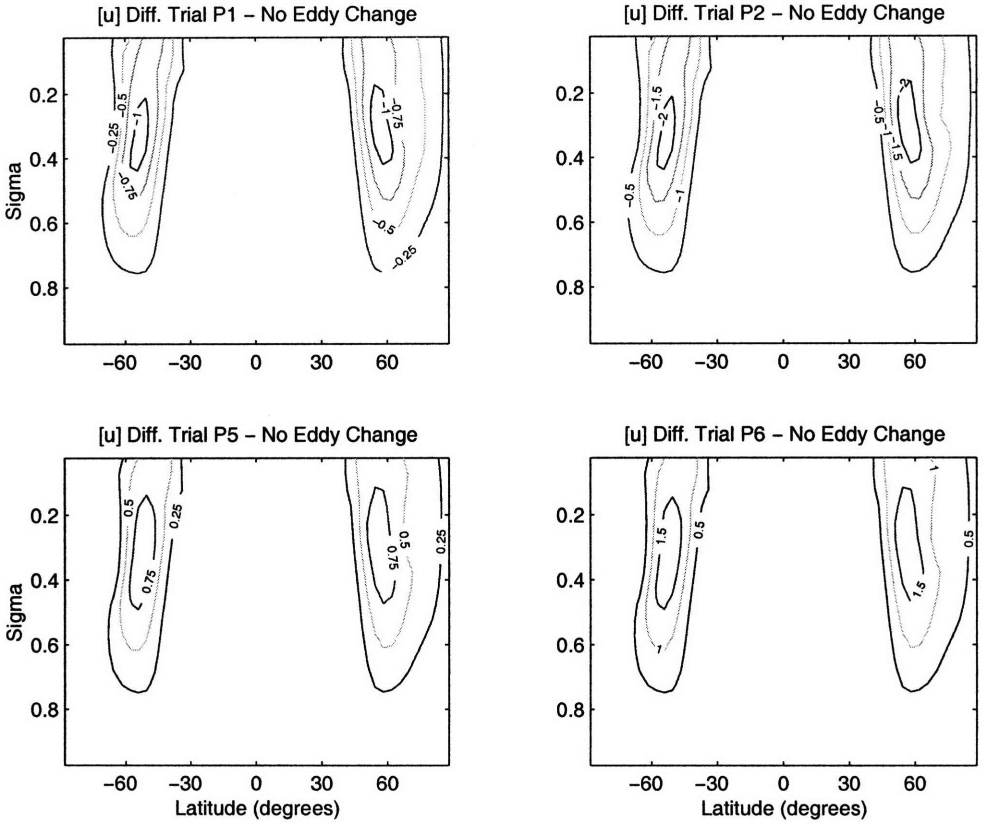

Figure 6-14: Change in zonal wind for the indicated trials versus the control for the zonally symmetric runs, including direct forcing only. Contour interval is 0.25 $m\ s^{-1}$ in left panels and 0.5 $m\ s^{-1}$ in right panels.

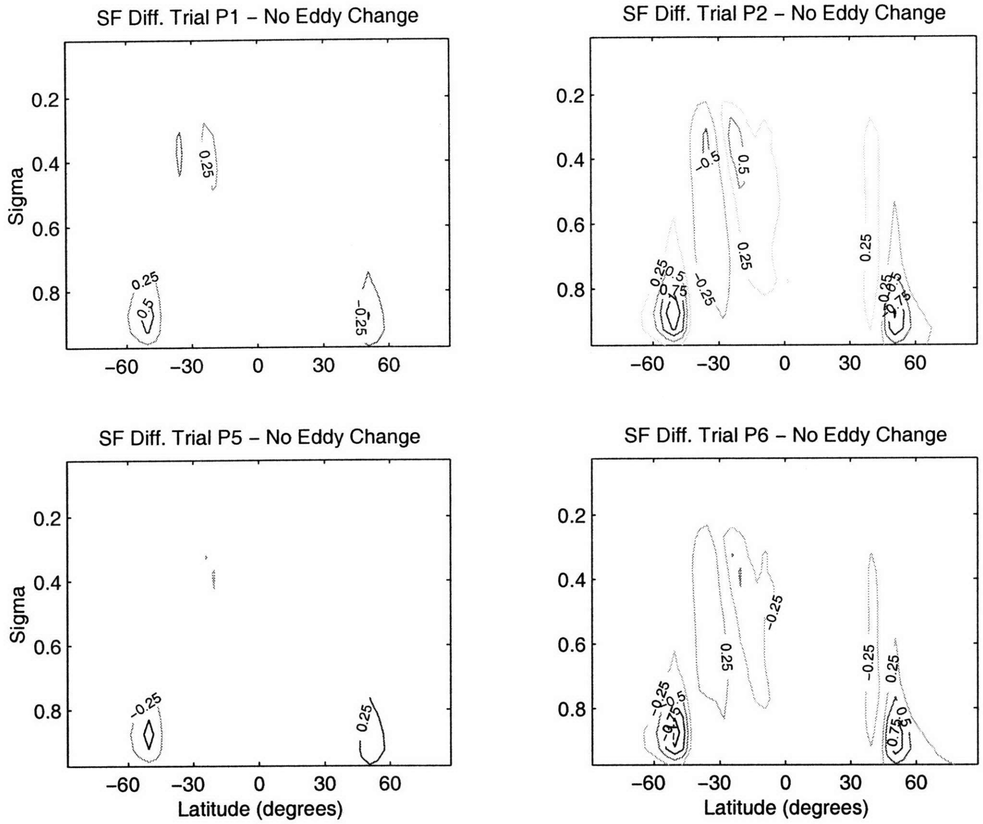

Figure 6-15: As in Figure 6-14, but for the streamfunction. Contour interval is $0.25 \times 10^9 kg\ s^{-1}$ in all panels. Zero contour is omitted.

and the changes to eddy fluxes. The changes to the eddy fluxes between these runs and the directly forced runs are shown in Figures 6-17 and 6-18. The structure of the changes to the eddy fluxes are similar to those in the mechanically forced trials. The changes in zonal wind forcing are focused about opposite-signed anomalies near the tropopause, about the position of the unforced jet. The temperature forcing anomalies include a strand of one polarity of forcing in the subpolar region; and a strand of opposite polarity of forcing on its equatorward side.

The changes in zonal wind from the zonally symmetric model, for cases including the change in both the reference temperature and the eddy feedback, are shown in Figure 6-19. Unlike for the cases shown in Figure 6-14, the annular mode patterns are reproduced here, with results comparing favorably to those shown for the full model in Figures 5-8 and 5-9. The dipolar shape is now produced, and the magnitudes of the responses are amplified. For example, in Trials P2 and P6, anomalies of up to

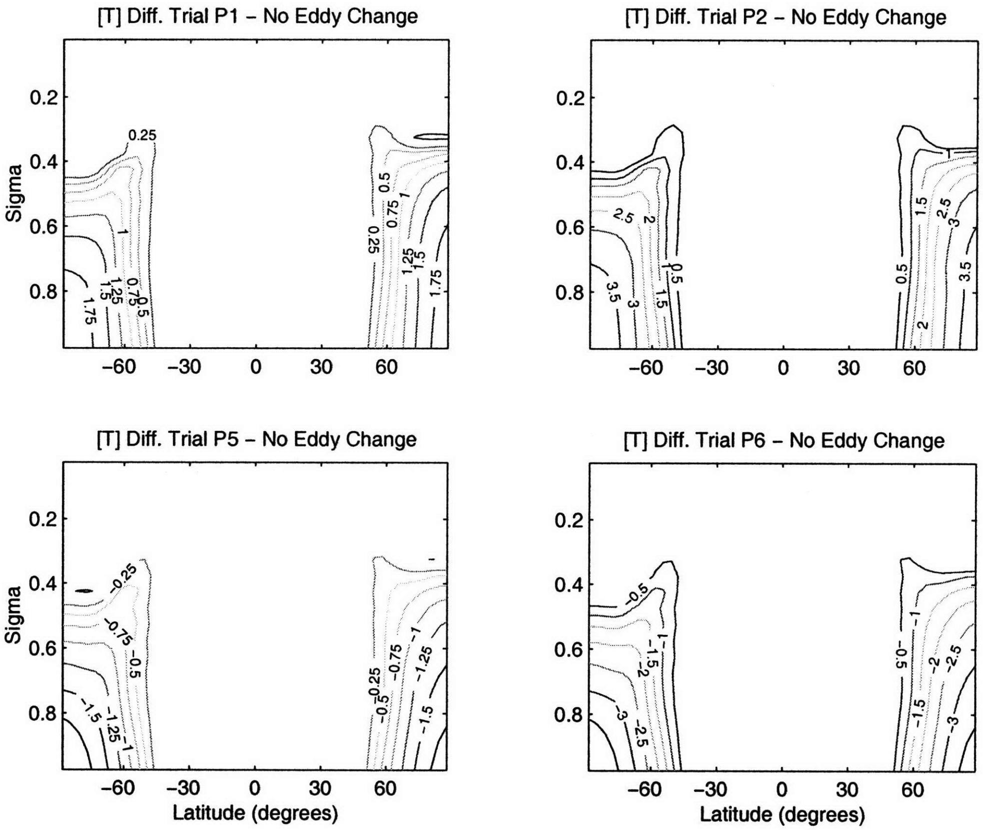

Figure 6-16: As in Figure 6-14, but for the temperature. Contour interval is 0.25 K in left panels and 0.5 K in right panels.

5 $m\ s^{-1}$ are found upon inclusion of the eddy feedback. This strength of the anomalies compares well to the full model results in Chapter 5, and is much stronger than those found in Figure 6-14.

The changes in streamfunction shown in Figure 6-20 are much different compared to their solely directly forced counterparts in Figure 6-15. The magnitudes of the responses are much enhanced — changes in streamfunction now easily exceed $10 \times 10^9\ kg\ s^{-1}$, which is consistent with the strength of the responses found in the full model trials in Figures 5-10 and 5-11. Additionally, the cells of anomalous streamfunction in Figure 6-20 are much more vertically coherent than their counterparts in Figure 6-15; the changes here reach from the surface to the upper troposphere.

Figure 6-21, which shows the temperature changes among the indicated zonally symmetric runs, with included eddy changes, and the control, shows the dynamic warming or cooling in mid-latitudes associated with changes in the overturning circu-

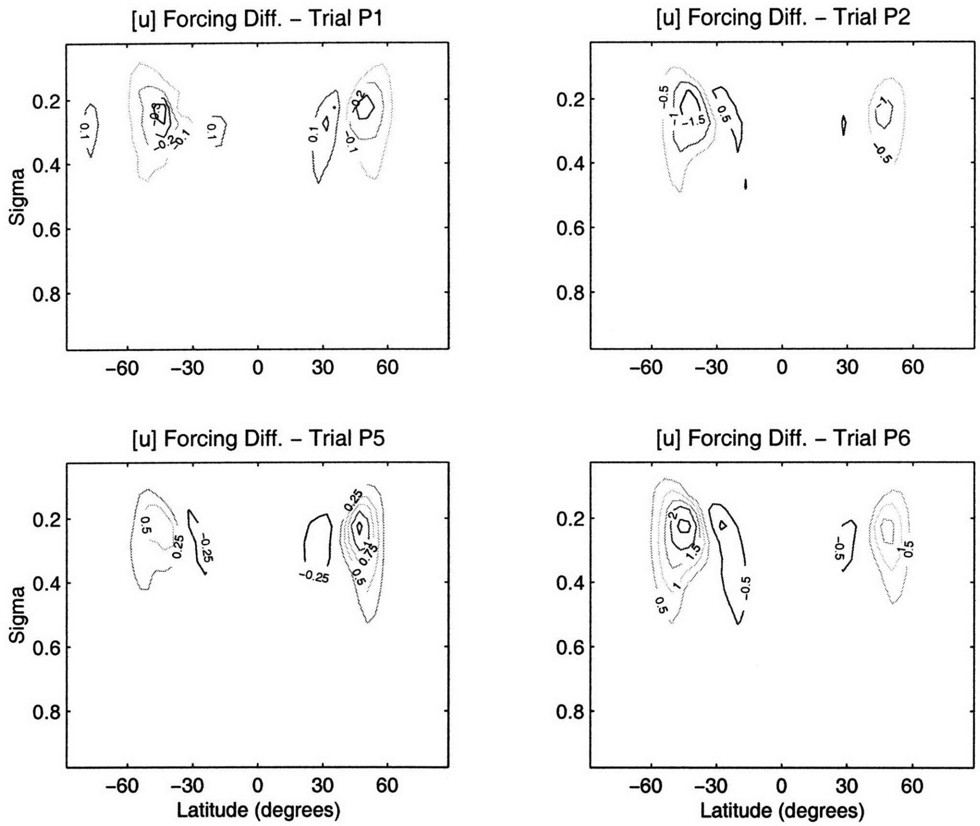

Figure 6-17: Changes in forcing of of zonal wind due to eddy flux terms for each trial versus the control. Contour interval is 0.1 $m\ s^{-1}\ day^{-1}$ rate of change of zonal wind in top left panel; 0.25 $m\ s^{-1}\ day^{-1}$ in bottom left panel, and 0.5 $m\ s^{-1}\ day^{-1}$ in right panels. Zero contour is omitted.

lations. These features were absent in Figure 6-16, where only the direct temperature changes were included. Again, the inclusion of the changes in eddy fluxes has vastly improved the agreement of the zonally symmetric responses with their full model counterparts shown in Figures 5-12 and 5-13.

6.6 Summary

In this chapter, a zonally symmetric model is used to determine the direct response of the model to solely the applied forcings, and separately, the response of the model to the forcings with the changes in climatological eddy fluxes from the full model run included.

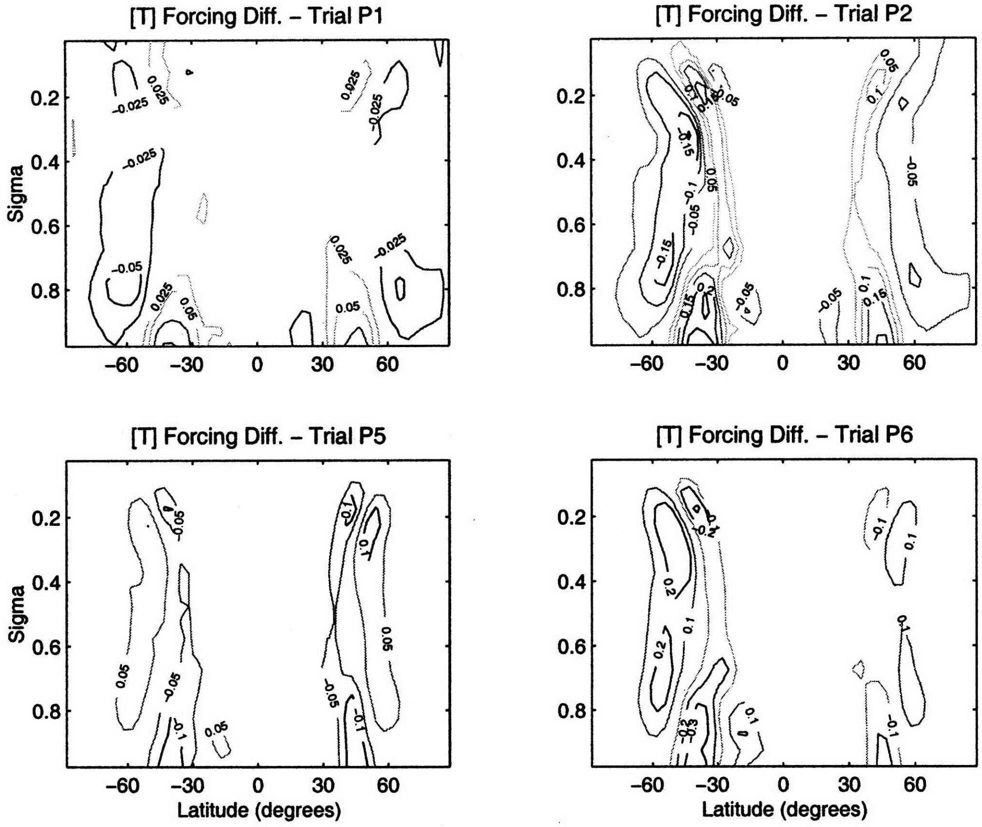

Figure 6-18: As in Figure 6-17, but for the changes in temperature forcing. Contour interval is 0.025 $K\ day^{-1}$ in top left panel; 0.1 $K\ day^{-1}$ in bottom right panel; and 0.05 $K\ day^{-1}$ in other panels. Zero contour is omitted.

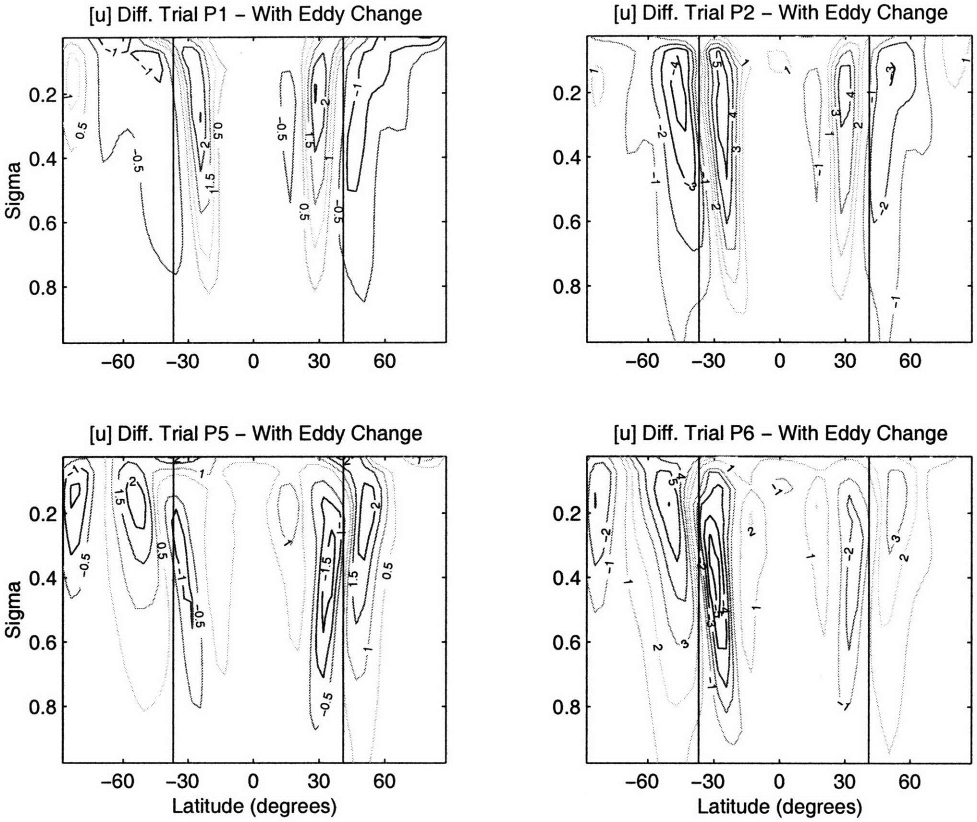

Figure 6-19: Change in zonal wind for the indicated trials versus the control for the zonally symmetric runs, including both direct forcing and changes in eddy fluxes. Contour interval is 0.5 $m\ s^{-1}$ in the left panels and 1 $m\ s^{-1}$ in the right panels. Vertical lines are positions of time-mean jets.

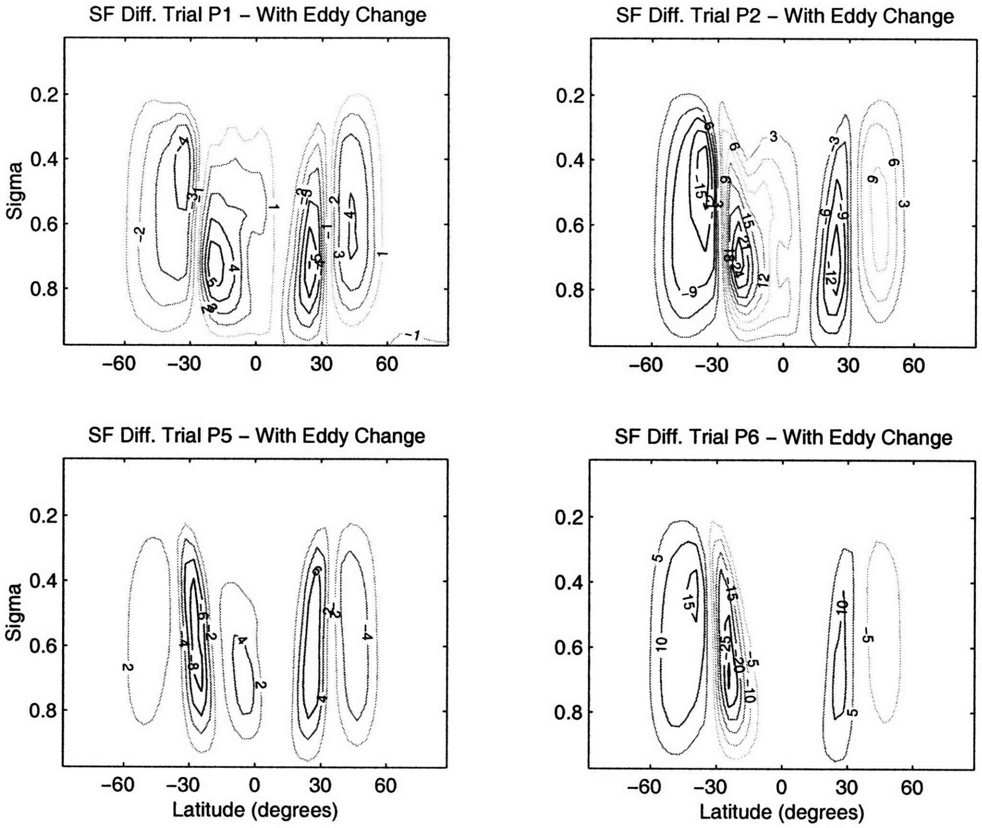

Figure 6-20: As in Figure 6-19, but for the streamfunction. Contour interval is $1\times10^9\ kg\ s^{-1}$ in the top left panel, $2\times10^9\ kg\ s^{-1}$ in the bottom left panel, $3\times10^9\ kg\ s^{-1}$ in the top right panel, and $5\times10^9\ kg\ s^{-1}$ in the bottom right panel.

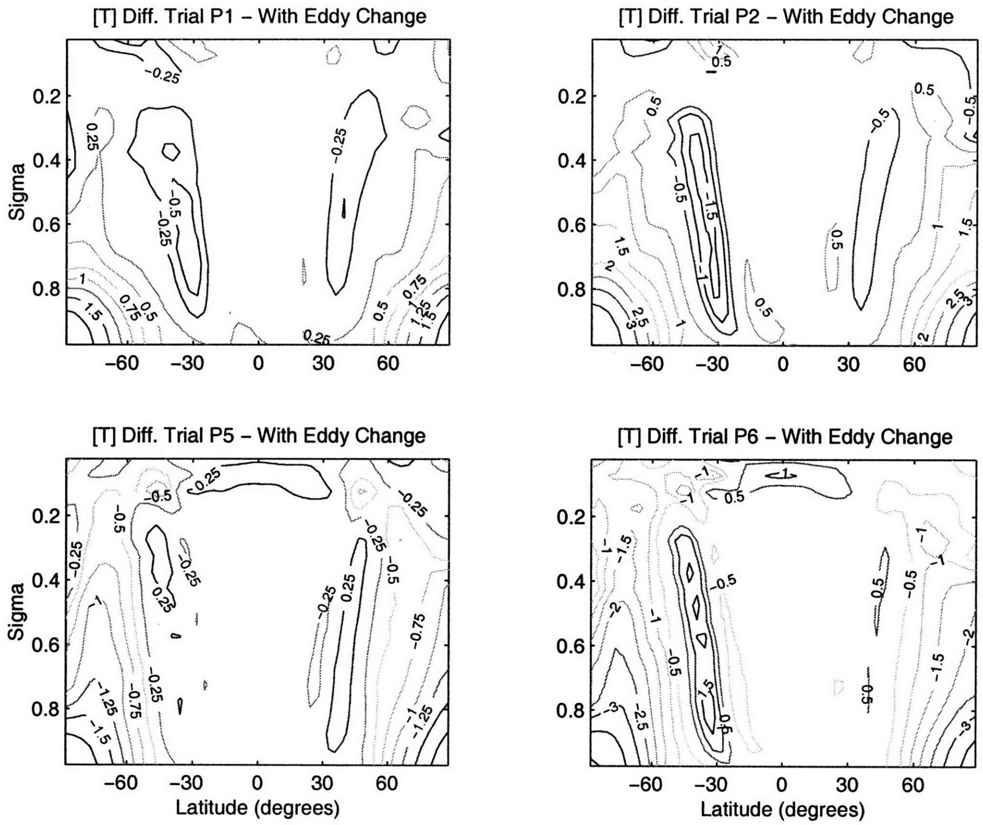

Figure 6-21: As in Figure 6-19, but for the temperature. Contour interval is 0.25 K in left panels and 0.5 K in right panels.

The runs using only the directly applied torques or changes to reference temperature, without the changes to eddy fluxes, failed to produce either the correct shape or strength of the annular mode patterns. For the cases with applied torque, the direct responses tended to be monopolar or tripolar, and the strength of the response tended to be too weak in the lower and middle troposphere (and the upper troposphere as well, for trials where the forcing was placed at 750 hPa). Similarly, the trials forced thermally produced direct responses which were weaker and a poor match for shape as compared to the results from the full model run.

However, including the changes in eddy fluxes, and therefore allowing the changes to the eddy, zonal-flow feedback to be represented in the zonally symmetric model, produced results which generally matched the full model results as well. The dipole, with a positive lobe on one side of the jet's time-mean position and a negative lobe on the other side, was consistently produced, and the wind anomalies were appropriately stronger as compared to the runs with direct forcing only. The eddy feedback processes found by Lorenz and Hartmann (2001, 2003) to maintain the annular mode patterns in Earth's atmosphere are necessary in this model for producing the anomalous forced patterns which look like the annular modes.

Chapter 7

Comparison of Forcing and Response Strengths

7.1 Introduction

The results of Chapters 4 and 5 illustrate that the annular modes arise in this simple GCM as a response to a variety of forcings, demonstrating that they are a preferred response of the model atmosphere to the forcings.

The previous results show that the wind responses are generally larger as the magnitude of the forcing is increased. Additionally, recalling the experiments from Chapter 4, the strength of the annular mode response is much greater for trials whose forcings coincided with the flanks of the jet than the center of the jet. As the flanks of the jet contain maximum EOF magnitude, while the center of the jet coincides with a nodal line of the EOF, it appears that the strength of the response also varies with the projection of the torque on the annular mode pattern.

In this chapter, I will explore the relationship between strength and location of the forcing, and strength of the annular mode response, using the fluctuation-dissipation theory. While these comparisons are simple for trials of one particular forcing type (mechanical or thermal), it is more difficult to cross-compare results using different types of forcings.

As an attempt to accomplish this comparison, I will consider an effective forcing which includes both the directly applied torque, and the torque arising through the action of the instantaneous overturning response. Both the mechanical and thermal forcings will alter the meridional and pressure velocities of the system, and these instantaneous variations themselves will seek to accelerate or decelerate the zonal wind. In this way, it is possible to formulate a "torque" even for the thermally forced cases, where no mechanical forcing is applied. I then try to analyze the control problem as a stochastically forced problem, comparing to the runs using the effective torque derived in this chapter as the forcing. However, as will be seen below, this formulation will encounter several difficulties, and potential reasons for these will be discussed.

Before turning to the mathematical formulation of this generic forcing, I consider a simpler comparison of forcing and response strength as motivation for examining the relationship between the two quantities.

7.2 Fluctuation-Dissipation Theory

As noted in the introduction to this chapter, the annular mode response in the forced trials may be increased through two processes: either by increasing the strength of the forcing, or by improving the projection of the forcing on the unforced annular modes. The results suggest the model may respond according to the fluctuation-dissipation theory (Leith, 1975).

The fluctuation-dissipation theory states that the forced response of a system may be related to its unforced variability. Specifically, fluctuation-dissipation theory relates the regression matrix for prediction of the forced response to the lagged covariance of the variability in the unforced model.

While the theory had been used in other physical sciences earlier, Leith (1975) first applied the theory to the atmospheric sciences. He formulated the theory for a forced-dissipative system, with two quadratic integrals of motion with equilibrium spectra and a normal probability distribution. While noting these conditions would not hold strictly for the atmosphere, Leith (1975) postulated the fluctuation-dissipation theory could be used if the probability distribution were approximately normal.

The fluctuation-dissipation theory has become an active area of research in the atmospheric sciences. Majda et al. (2005) recently obtained promising results applying the fluctuation-dissipation theory to varied chaotic systems with no damping but different autocorrelation decay rates for different scales of motion; the theory was found to predict the results accurately. Turning to a system including forcing and damping, Majda et al. (2005) found results qualitatively in agreement with fluctuation-dissipation theory, although the theory's predicted response was too strong for some choices of forcing. The theory has also been explored in systems closer to those found in nature, for example by Gritsun and Branstator (2007), who found in their model that the fluctuation-dissipation theory correctly predicted the response to imposed heating in most, though not all, of their trials.

In a later section of this chapter, I will compare the forced responses of the model to its unforced variability. The mathematics on which the analysis is based come from Penland (1989), whose analysis makes different assumptions on the system than does Leith (1975)'s analysis, although both authors find that the forced response is related to the lagged covariance. First, however, to inspire a more methodical analysis, I consider a simpler comparison of the forcing and response strength.

7.3 Simple Comparisons of Forcing and Response Strength

The simplest way to compare the forcing and response is to take a simple inner product of the response and unforced annular mode, examined against the inner product of torque and unforced annular mode. These results are shown in Figure 7-1 for the SH, and Figure 7-2 for the NH.

To obtain the results in these figures, the mechanical forcings described in Tables 4.1, 4.2, and 4.3 are projected against the non-dimensional versions of the EOF patterns shown in Figure 3-11 and compared to the wind responses from Chapter

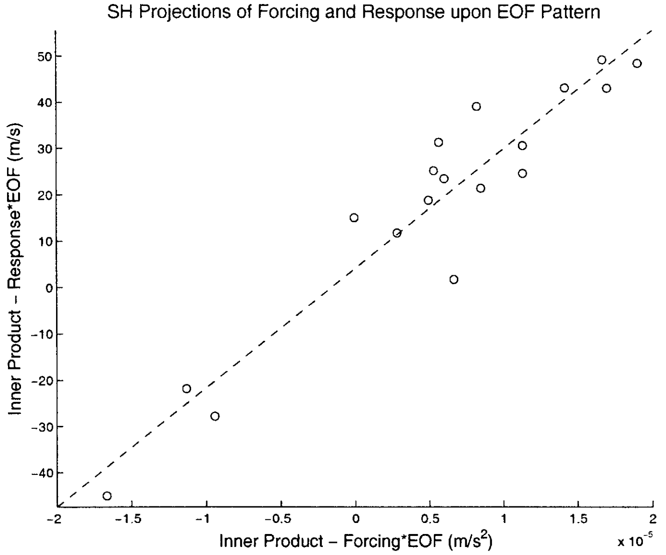

Figure 7-1: Projection of SH zonal wind response on SAM of the unforced model run versus the forcing projected on SAM of unforced model run, for the mechanically forced trials. Dashed line is best linear least-squares fit.

4 projected upon the EOFs. Trials L6, B3, and B4, which featured poorer annular mode-like responses because of a more tropically-dominant response, are excluded from this plot, but all other runs shown in Chapter 4 are included. In both hemispheres the relationship between forcing and response appears to be linear. The slope of the best least-squares fit is 30.0 days in the SH, and 28.6 days in the NH.

The next step is to include the response of the thermally forced trials, shown in Chapter 5, in the projections. This is not straightforward, because while the mechanical forcing has units of acceleration, the thermal forcing has units of Kelvin per unit time. In order to facilitate a comparison, for each case the applied mechanical forcing is non-dimensionalized by the variance of the zonal wind field of the unforced run, and the applied thermal forcing non-dimensionalized by the variance of the temperature field of the unforced run. While this is a crude method of comparing the mechanically and thermally forced trials, it allows for a simple first comparison to be made.

It is also necessary to obtain a pattern onto which the temperature forcings may be projected. To find this pattern, an SVD analysis of the cross-covariance between the zonal wind and temperature anomalies is conducted. As with the SVD of the

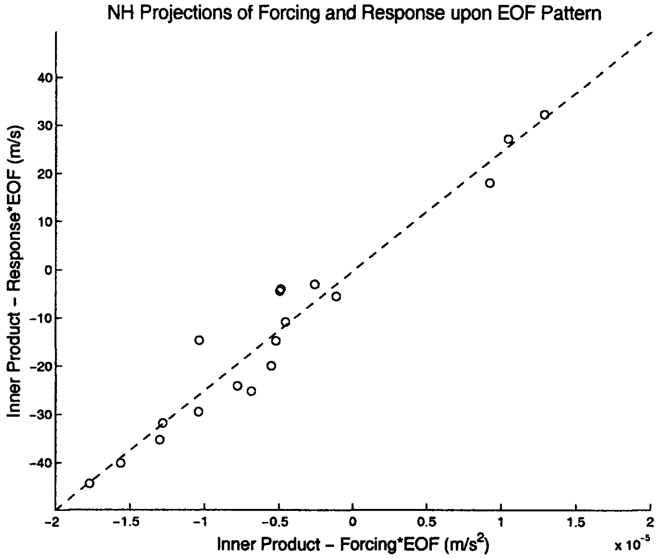

Figure 7-2: As in Figure 7-1, but for the NAM and NH.

cross-covariance of wind and E-P flux divergence anomalies reported in Chapter 3, the spatial patterns of wind emerging from the SVD analysis are virtually identical to the EOFs of wind. The spatial patterns emerging for the temperature are shown in Figure 7-3.

Following the procedure from Chapter 3, I plot both the first and second patterns on one plot, as there is little spatial overlap between the two. The main feature of each pattern is a region of anomalous temperature, centered between $30 - 35°$ in the SH and $35 - 40°$ in the NH, reaching from the tropopause level to the ground. Opposite-signed, weaker anomalies are found poleward of the main feature in each hemisphere. Not surprisingly, these SVD patterns are similar to the changes in temperature from the full model run associated with the annular mode-like responses in Chapters 4 and 5.

It may also be noted that the trials with hemisphere-scale forcing from Chapter 5 will have forcing which projects poorly on these patterns. The wide latitudinal extent of the forcing results in a large degree of cancellation, as some forcing projects on the positive centers and some on the negative centers. The restriction of the forcing to poleward of 45°, however, will not result in this cancellation. Those forcings will project on the secondary centers in this pattern in the subpolar regions.

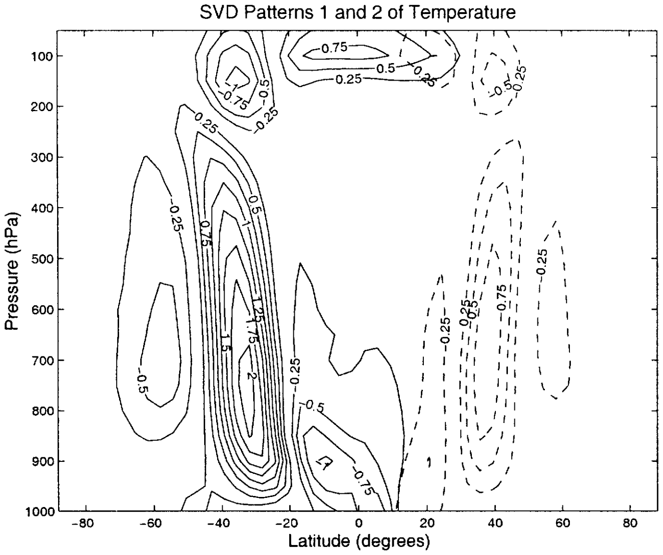

Figure 7-3: First and second SVD patterns of temperature anomalies found from cross-covariance with zonal wind anomalies. Solid lines indicate leading pattern; dashed lines indicate second pattern. Contour interval is 0.25 K; zero contours are omitted.

Figures 7-4 and 7-5 show the relationship between forcing and response, including both the mechanically and thermally forced cases. For each case, the wind response is normalized by the zonal wind variance of the unforced run, the temperature response is normalized by the temperature variance of the unforced run, and the two quantities are summed to produce the overall response. The response is again linear in each hemisphere, with the thermally forced cases scattering about the same line as the mechanically forced cases.

While the results in Figures 7-4 and 7-5 suggest a linear relationship between the strength of forcing and the strength of the response, consistent with expectations from fluctuation-dissipation theory, the rough nature (variance weighting) used to combine the mechanically and thermally forced trials for the comparison must be noted. Additionally, the projections here are performed against the EOFs of the system, which are statistical patterns. As will be shown below, it is possible to obtain the eigenvectors of the system's dynamical operator, which offer a more justifiable basis for the projection of forcing and response.

Despite these limitations, the results here encourage a more thorough examination

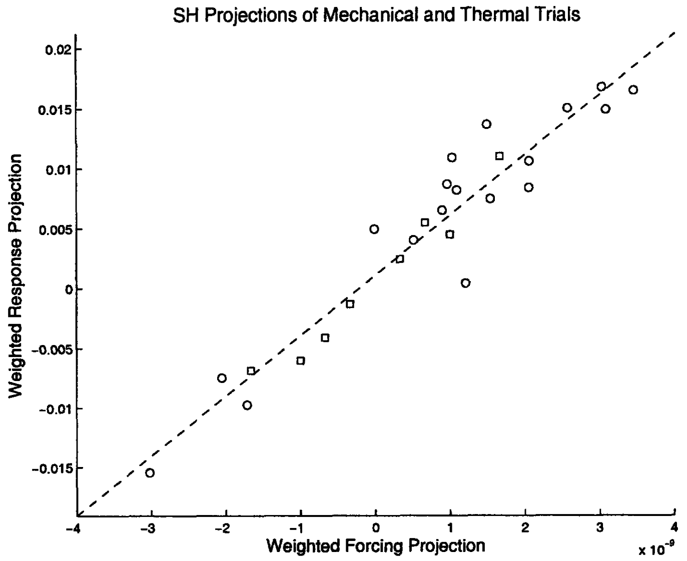

Figure 7-4: Projection of SH response versus projection of forcing. Response includes the temperature anomaly of each run weighted by the variance of the temperature of the unforced run and the zonal wind anomaly of each run weighted by the variance of the zonal wind of the unforced model run. Forcing is also weighted by the appropriate variance. Circles indicate mechanically forced trials; squares thermally forced trials. Dashed line is best linear least-squares fit.

of the relationship between the forcing and response. In the next section, I attempt a more theoretical construction to link the mechanically and thermally forced cases.

7.4 Mathematical Formulation of the Effective Forcing

My goal in this section is to derive an "effective torque" which includes both the applied momentum perturbations and the instantaneous effects of the forcing. As discussed by Eliassen (1951), an anomalous overturning circulation will be established in response to the forcing, in order to maintain a thermal wind balance. If the establishment of this overturning circulation occurs very rapidly, as suggested by Eliassen (1951), then it may be considered as part of an "instantaneous" response to the forcing, while the timescale on which steady-state, balanced changes occur (owing to the actions of the eddy-zonal wind feedback, as well as radiational and

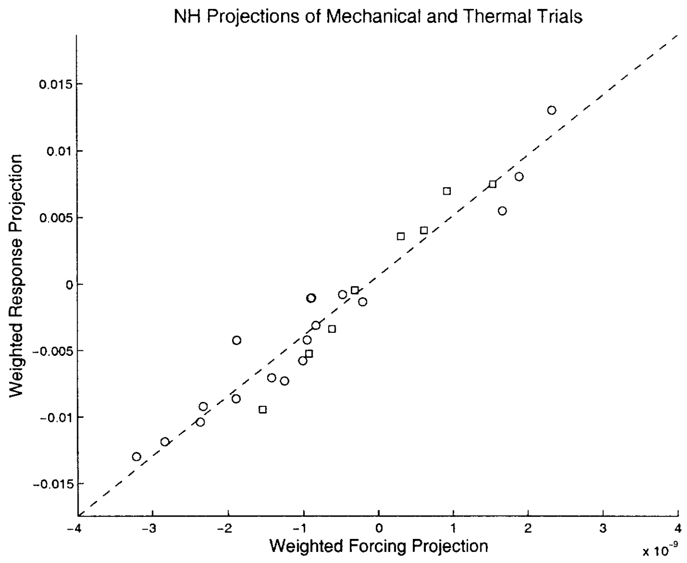

Figure 7-5: As in Figure 7-4, but for the NH.

frictional adjustment) is much longer. The thermally forced cases produce this overturning as well as the mechanically forced cases, so in both types of forced cases there are terms, acting on timescales shorter than the changes in eddy fluxes, which seek to accelerate or decelerate the zonal wind.

The initial mathematical formulation is similar to other studies, such as Plumb (1982) and Haynes and Shepherd (1989), although they use quasi-geostrophic equations while primitive equations are used here. Specifically, the starting point of this formulation is the zonal-mean equations of absolute angular momentum $(M+m)$ and buoyancy $(B+b)$. Linearizing these equations, and representing the basic state of meteorological variables with capital letters, and perturbations with lowercase letters, the equations are written:

$$\begin{aligned}
\frac{\partial m}{\partial t}+\frac{V}{a}\frac{\partial m}{\partial \phi}+\Omega\frac{\partial m}{\partial p}+\frac{v}{a}\frac{\partial M}{\partial \phi}+\omega\frac{\partial M}{\partial p} &= -d_m+h-\alpha_m m && (7.1)\\
\frac{\partial b}{\partial t}+\frac{V}{a}\frac{\partial b}{\partial \phi}+\Omega\left(\frac{\partial b}{\partial p}-\frac{\kappa b}{p}\right)+\frac{v}{a}\frac{\partial B}{\partial \phi}+ & \\
\omega\left(\frac{\partial B}{\partial p}-\frac{\kappa\left(B+g\right)}{p}\right) &= -d_b-\alpha_b\left(b-b_e\right) && (7.2)
\end{aligned}$$

The anomalous eddy momentum flux divergence is d_m, while the anomalous buoyancy flux divergence is d_b. The torque per unit mass is h. The dissipation coefficients for momentum and buoyancy are represented by α_m and α_b, respectively.

The buoyancy of the basic state may be represented as $B = \frac{g(T_{basic}-T_*)}{T_*}$, while the perturbation buoyancy is $b = \frac{g(T-T_{basic})}{T_*}$. The forcing of the buoyancy equation is the relaxation to the reference buoyancy; I write the reference buoyancy as $B_e = \frac{g\left(T_{e,basic}-T_*\right)}{T_*}$ and the perturbation which constitutes the forcing as $b_e = \frac{g\left(T_e-T_{e,basic}\right)}{T_*}$. T_* is a reference temperature, taken here to be 255 K.

By using the streamfunction, Equations 7.1 and 7.2 may be combined into a single equation. Hence it is necessary to introduce χ, where

$$
\begin{aligned}
v &= \frac{\partial \chi}{\partial p} && (7.3)\\
\omega &= -\frac{1}{a\cos\phi}\,\frac{\partial\left(\chi\cos\phi\right)}{\partial\phi}. && (7.4)
\end{aligned}
$$

χ, as written here, does not have the dimensions of streamfunction ($kg\ s^{-1}$) as used in the previous chapters, but it serves the same purpose in providing a statement of continuity. Substituting $\chi \rightarrow \frac{g}{2\pi a\cos\phi}\psi$ returns the equations for mass streamfunction ψ.

It is also necessary to introduce a linearized balance equation. Beginning with the primitive equation for the material rate of change of meridional velocity,

$$
\frac{Dv_T}{Dt} = -\frac{1}{a}\frac{\partial\Phi}{\partial\phi} - 2\Omega\sin\phi\; u_T - \frac{u_T^2}{a}\tan\phi;^{1} \tag{7.5}
$$

one may postulate a gradient wind balance where $\frac{Dv_T}{Dt}$ is negligible, by which the meridional gradient of geopotential Φ is related to the zonal velocity u_T,

$$
\frac{\partial\Phi}{\partial\phi} = -2a\Omega\sin\phi\; u_T - u_T^2\tan\phi. \tag{7.6}
$$

Substituting total angular momentum $M_T = M + m = a\cos\phi\left(u_T + \Omega a\cos\phi\right) =$

---

[1] The subscripts T are used to indicate these velocities are not the perturbation velocities u and v; rather Equation 7.5 is true for total zonal and meridional velocities.

$a \cos\phi \left(U + u + \Omega a \cos\phi\right)$ yields

$$\frac{\partial \Phi}{\partial \phi} = -\frac{\sin\phi}{a^2 \cos^3\phi}\left(M_T^2 - M_{planetary}^2\right), \tag{7.7}$$

Hydrostatic balance may also be applied,

$$\frac{\partial \Phi}{\partial p} = -\frac{1}{\rho}. \tag{7.8}$$

The equations may be cross-differentiated, resulting in

$$\frac{\partial}{\partial \phi}\frac{1}{\rho} = \frac{\sin\phi}{a^2 \cos^3\phi}\frac{\partial}{\partial p}\left(M_T^2\right), \tag{7.9}$$

upon which further substitution and linearization of M_T results in the balance equation in terms of buoyancy, introducing ϵ,

$$\begin{aligned} \frac{1}{a}\frac{\partial b}{\partial \phi} &= \frac{2\sin\phi}{a^3\cos^3\phi}\,\frac{p}{H_*}\,\frac{\partial\left(Mm\right)}{\partial p} \\ \frac{1}{a}\frac{\partial b}{\partial \phi} &= \epsilon\,\frac{\partial\left(Mm\right)}{\partial p}. \end{aligned} \tag{7.10}$$

Now, the equation for streamfunction may be obtained by differentiating Equation 7.2 with respect to ϕ and dividing by a, multiplying Equation 7.1 by M, then differentiating with respect to p and multiplying by ϵ, and subtracting the latter equation from the former. This yields:

$$\begin{aligned} -\frac{1}{a}d_{b,\phi} - \frac{1}{a}\left(\alpha_b\left(b - b_e\right)\right)_\phi - \epsilon\left(\left(-d_m + h - \alpha_m m\right)M\right)_p &= \\ \left(\partial_t + \frac{V}{a}\partial_\phi + \Omega\partial_p\right)\frac{1}{a}b_\phi + \frac{1}{a^2}\left(V_\phi b_\phi\right) + \frac{1}{a}\left(\Omega_\phi b_p\right) - \frac{\kappa}{ap}\left(\Omega b\right)_\phi & \\ + \frac{1}{a^2}\left(B_\phi \chi_p\right)_\phi + \frac{1}{a^2}\left(S\frac{1}{\cos\phi}\left(\chi\cos\phi\right)_\phi\right)_\phi - \left(\partial_t + \frac{V}{a}\partial_\phi + \Omega\partial_p\right)\left(\epsilon\left(Mm\right)_p\right) & \\ -\epsilon V_p M\frac{1}{a}m_\phi + \epsilon V\left(\frac{1}{a}M_\phi m\right)_p - \epsilon\Omega_p M m_p + \epsilon\Omega\left(M_p m\right)_p & \\ + \left(\frac{V}{a}\epsilon_\phi + \Omega\epsilon_p\right)\left(Mm\right)_p - \epsilon\left(\chi_p M\frac{1}{a}M_\phi\right)_p + \epsilon\left(\frac{1}{\cos\phi}\left(\chi\cos\phi\right)_\phi\frac{1}{a}MM_p\right)_p, & \end{aligned} \tag{7.11}$$

where the stability $S = \kappa(B+g)/p - B_p$.

Substituting the balance equation (7.10) for $\frac{1}{a}\frac{\partial b}{\partial \phi}$ will eliminate the derivatives with respect to time. Then, rearranging yields a diagnostic equation for χ,

$$\begin{aligned}
&\frac{1}{a^2}\left(B_\phi \chi_p\right)_\phi + \frac{1}{a^2}\left(\frac{S}{\cos\phi}\left(\chi\cos\phi\right)_\phi\right)_\phi - \epsilon\left(\chi_p \frac{1}{a} M M_\phi\right)_p + \\
&\epsilon\left(\frac{1}{a\cos\phi}\left(\chi\cos\phi\right)_\phi M M_p\right)_p - \epsilon V_p \frac{1}{a} M m_\phi + \epsilon V\left(\frac{1}{a} M_\phi m\right)_p \\
&-\epsilon\Omega_p M m_p + \epsilon\Omega\left(M_p m\right)_p + \left(\frac{V}{a}\epsilon_\phi + \Omega\epsilon_p\right)\left(Mm\right)_p \\
&-\epsilon\left(\alpha_m m M\right)_p + \left(\frac{1}{a}V_\phi - \frac{\kappa}{p}\Omega + \alpha_b\right)\frac{1}{a}b_\phi + \frac{1}{a}\Omega_\phi\left(b_p - \frac{\kappa b}{p}\right) + \frac{1}{a}\left(\alpha_b\right)_\phi b \\
&= \epsilon\left(M d_m\right)_p - \frac{1}{a}d_{b,\phi} + \frac{1}{a}\left(\alpha_b b_e\right)_\phi - \epsilon\left(hM\right)_p . \qquad (7.12)
\end{aligned}$$

Several other terms may be eliminated through use of reasonable assumptions. I will assume that the term $\frac{1}{a}\Omega_\phi\left(b_p - \frac{\kappa b}{p}\right)$ is small.[2] In the model runs in Chapters 3 through 5, α_b was not a function of latitude, so the term depending on its meridional gradient is zero. After these simplifications, the remaining terms involving the perturbation buoyancy are all dependent not on b itself, but its meridional gradient b_ϕ, which may be related to momentum perturbations through the balance equation. So, there are two types of terms on the left-hand side of Equation 7.12: those which are linear in χ, and those which are linear in m. Introducing operators A and C to act upon the streamfunction and perturbation momentum, respectively, Equation 7.12 may be written as

$$A\chi + Cm = \epsilon\left(M d_m\right)_p - \frac{1}{a}d_{b,\phi} + \frac{1}{a}\left(\alpha_b b_e\right)_\phi - \epsilon\left(hM\right)_p . \qquad (7.13)$$

The terms on the right-hand side are the eddy momentum flux divergence, the eddy buoyancy flux divergence, the perturbation buoyancy forcing, and the applied torque.

The next step is to consider simplifications to the eddy divergences. It will be assumed here that eddy feedback operators E, which act only on the anomalous momentum and not the anomalous buoyancy, may be defined. This simplification assumes that the eddy feedback operators are not sensitive to the static stability. Additionally, the simplification assumes the fluxes are related to the instantaneous and not the lagged values of the wind, though this latter point should not be problematic given the persistence of the annular modes in this model. Further, the operators shall be assumed to be linear.

---

[2] In most places this term is small; its value is largest around 30 – 40° latitude. Calculating the term using output from the model runs and including it as a component of the forcing did not appreciably alter the projections to be shown below.

$$M d_m = E_m m; \; d_b = E_b m. \tag{7.14}$$

Then,

$$A\chi + Cm = \epsilon \left(E_m m\right)_p - \frac{1}{a}\left(E_b m\right)_\phi + \frac{1}{a}\left(\alpha_b b_e\right)_\phi - \epsilon \left(hM\right)_p, \tag{7.15}$$

reduces the number of terms not dependent on either χ or m to just two — the applied buoyancy and momentum perturbations.

Combining the eddy feedback operators into a single term operating on m

$$E_\chi = \epsilon E_{m,p} - \frac{1}{a} E_{b,\phi} + \epsilon E_m \partial_p - \frac{1}{a} E_b \partial_\phi \tag{7.16}$$

allows the equation for streamfunction to be written

$$A\chi = -Cm + E_\chi m + \frac{1}{a}\left(\alpha_b b_e\right)_\phi - \epsilon \left(hM\right)_p, \tag{7.17}$$

or, inverting for the streamfunction,

$$\chi = A^{-1}\left(E_\chi - C\right) m + A^{-1}\left(\alpha_b \frac{1}{a} b_{e,\phi} - \epsilon \left(hM\right)_p\right). \tag{7.18}$$

The solution for χ may be substituted into Equation 7.1.

$$\frac{\partial m}{\partial t} + \left(\frac{V}{a} m_\phi + \Omega m_p + \alpha_m m\right) + \chi_p \frac{1}{a} M_\phi - \frac{1}{a}\frac{1}{\cos\phi}\left(\chi \cos\phi\right)_\phi M_p = -E_m m + h. \tag{7.19}$$

Introducing the operators G and H,

$$G = \frac{V}{a}\frac{\partial}{\partial\phi} + \Omega\frac{\partial}{\partial p} + \alpha_m \tag{7.20}$$

$$H = \frac{1}{a}M_\phi\frac{\partial}{\partial p} - \frac{1}{a}M_p\frac{\partial}{\partial\phi} + \frac{1}{a}M_p\tan\phi \tag{7.21}$$

Equation 7.19 may be re-written as

$$\frac{\partial m}{\partial t} + (G + E_m)\, m + H\chi = h. \tag{7.22}$$

Then, substituting in the expression for χ from Equation 7.18 returns

$$\frac{\partial m}{\partial t} + \left(G + E_m + HA^{-1}\left(E_\chi - C\right)\right) m = h - HA^{-1}\left(\alpha_b\frac{1}{a}b_{e,\phi} - \epsilon\left(hM\right)_p\right). \tag{7.23}$$

Defining several operators, I write the expression

$$\frac{\partial m}{\partial t} + Lm + Em = q \tag{7.24}$$

where the operator $L = G - HA^{-1}C$, and the total eddy feedback operator $E = E_m + HA^{-1}E_\chi$. The net forcing is, in general,

$$q = \left(I + HA^{-1}\epsilon\partial_p\left(M\times\right)\right) h - HA^{-1}\alpha_b\frac{1}{a}\partial_\phi b_e. \tag{7.25}$$

The net forcing q is equated to changes in momentum, but it depends on both the mechanical forcing and the reference buoyancy perturbations. While h, the applied torque, appears in the expression for q, so do terms related to the overturning circulation generated by the anomalous χ. The effects of the mechanical and thermal forcings have been united.

In order to calculate the effective forcing, I take the perspective of the Eliassen (1951) problem — that is, I consider the "instantaneous" response in which an anomalous overturning circulation is established in response to the forcing while holding the changes in perturbation momentum, which occur more slowly, fixed. Then, recalling

Equation 7.18, the equation for the "instantaneous" streamfunction response is

$$\chi_i = A^{-1}\left(\alpha_b \frac{1}{a} b_{e,\phi} - \epsilon \left(hM\right)_p\right). \tag{7.26}$$

Then, returning to Equation 7.25, the net forcing under these circumstances is

$$q_i = h - H\chi_i. \tag{7.27}$$

In order to solve for q_i, I use a two-dimensional model which solves the elliptic Equation 7.26. $\omega = 0$ is prescribed as the top boundary condition and $v = 0$ as the side boundary conditions. The bottom boundary condition is more complex.

As discussed by Haynes and Shepherd (1989), the commonly-used bottom boundary condition $\omega = 0$ is not appropriate, although for cases where the surface pressure change is small it may be an acceptable substitute. For these runs, which seek "instantaneous" solutions, the surface pressure tendency may be large and therefore $\omega = 0$ is a poor assumption. Instead I use the boundary condition introduced by Haynes and Shepherd (1989), which is that the material derivative of geopotential Φ vanish. Linearizing this condition in primitive coordinates, the bottom boundary condition of the 2-D model is

$$\frac{\partial \Phi'}{\partial t} + \frac{v}{a}\frac{\partial \Phi_o}{\partial \phi} + \omega \frac{\partial \Phi_o}{\partial p} = 0. \tag{7.28}$$

The responses of the model are then considered through the perspective of this effective applied forcing q_i, which includes both the applied torque and the instantaneous overturning response. While the thermally forced cases have no torque, they do have an overturning response, so through this procedure an effective forcing has been obtained which allows for a comparison between the mechanically and thermally forced cases.

In Figure 7-6 I show a few examples of the streamfunction anomalies calculated by the 2-D elliptic model. Trial L4, which uses torques placed in the upper troposphere on the jets' poleward flanks, produces positive streamfunction anomalies in

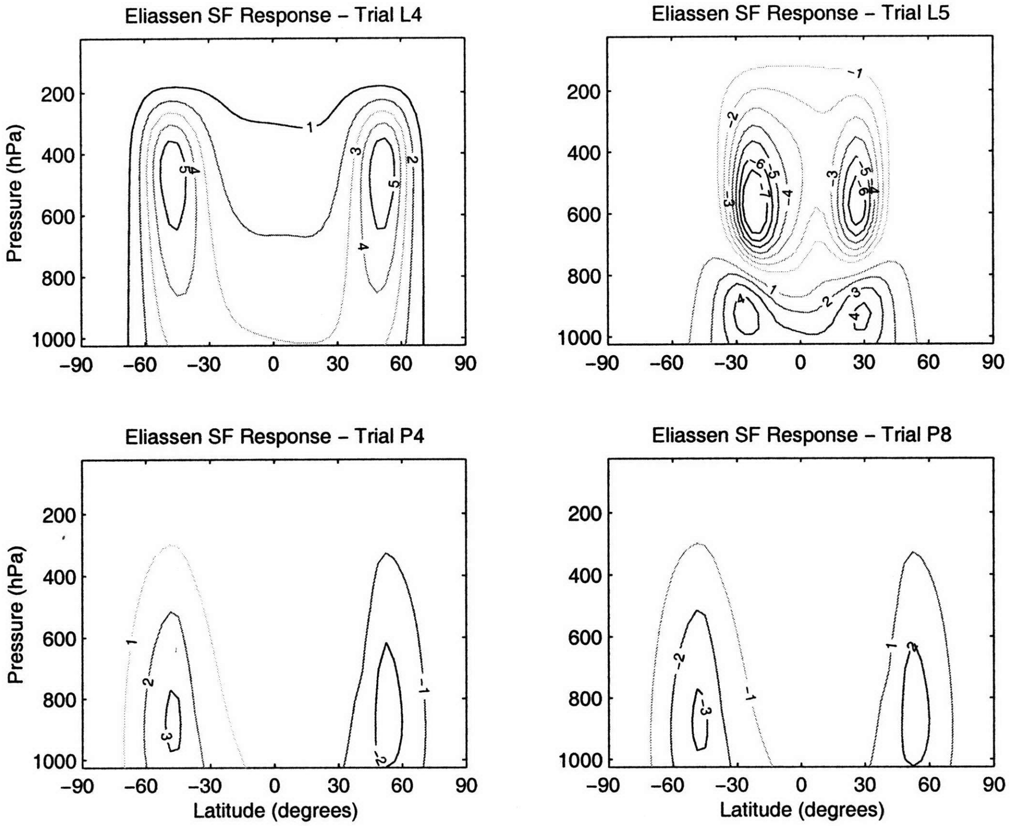

Figure 7-6: Instantaneous streamfunction response to indicated forcings in the 2-D elliptic model. Contour interval is $1 \times 10^9 kg\ s^{-1}$.

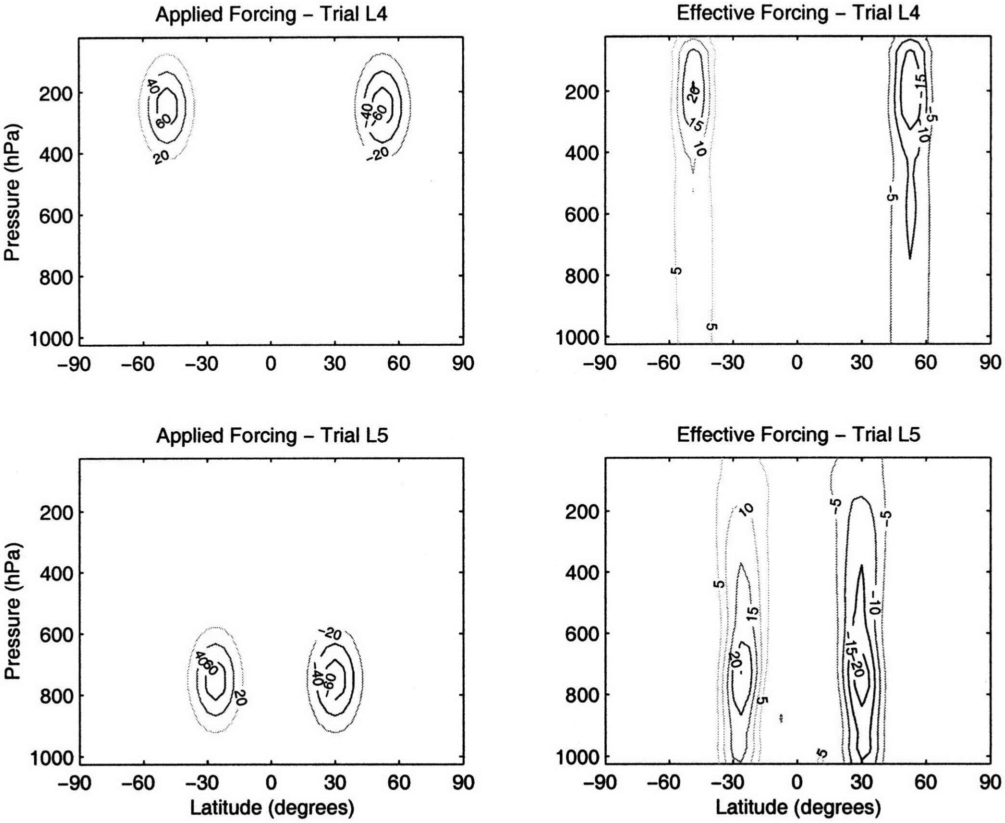

Figure 7-7: Applied torques (left panels) and "effective forcings" (right panel) for the indicated trials. Units are $m^2\ s^{-2}$ in each panel.

each hemisphere. The strength of the responses in each hemisphere is similar, but not exactly alike, as the background state included in the calculations is not identical in each hemisphere. The same behavior is found at the forcing locations in Trial L5 (the lower troposphere on the jets' equatorward flanks). However in Trial L5 there are streamfunction anomalies of opposite sign in the middle-to-upper troposphere, and in both trials a substantial amount of the streamfunction anomaly appears to go into the ground. Neither of these features, however, are worrisome as these are the instantaneous Eliassen (1951) responses to the forcing, not the steady, downward-control solutions of Haynes et al. (1991).

The responses to two thermally forced cases are shown in the lower panels. In the two cases the responses are similar in magnitude, but opposite in polarity, for the warming (Trial P4) or cooling (Trial P8) of T_{ref} in the polar regions.

The streamfunctions are now used to calculate the effective forcings, according to

Equation 7.27. The effective forcings for Trials L4 and L5, which are representative of the other cases, are shown in Figure 7-7. They are plotted alongside the original torques. In both cases the effects of the overturning circulation have smoothed the forcing vertically. Rather than being concentrated in a bullseye, the torque is now more barotropic. While in each case the magnitude is still strongest near the level of the forcing, the strength there has been much reduced.

The effective forcing for two thermally forced cases (P4 and P8) is shown in Figure 7-8. They are shown alongside the buoyancy forcing in each case. A cautionary note must be applied: As the effective forcing has units of $m^2\ s^{-2}$ and the buoyancy forcing has units of s^{-3} the buoyancy forcing and effective forcing of each case are not directly comparable as in Figure 7-7.

In each case, the buoyancy forcing is concentrated at the ground, in the midlatitude and subpolar region. The effective forcing resulting as a consequence of the applied buoyancy anomalies, however, has a much different shape. In both trials the main feature in both hemispheres is a broad region of effective torque in the midlatitudes of the free troposphere, with torques of opposite sign in smaller regions at the surface.

Through use of the 2-D elliptic model, I have obtained a set of "effective forcings" for each trial, combining both the applied torques and the effects of the overturning circulation of the instantaneous response. These effective torques may be used to complete a comparison of forcing and response strength, as will be done below.

7.5 Principal Oscillation Pattern Analysis

In this section, I pursue an analysis of the forced problem using the principal oscillation pattern (POP) analysis introduced by von Storch et al. (1988) and further employed by Penland (1989). The "POPs" are the eigenvectors of a deterministic feedback matrix; hence they indicate the spatial properties of the feedback. Because they contain information on the dynamics of the system, the POPs are a superior basis for projection of the forcing and response than the EOFs, which are statistical

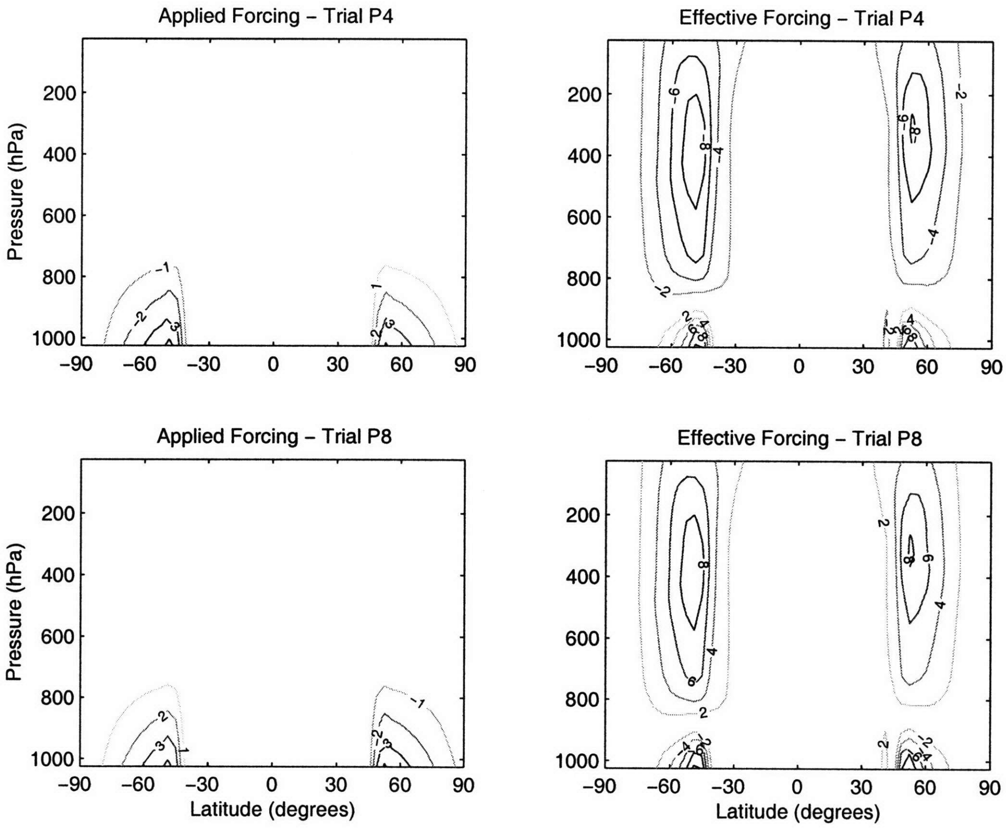

Figure 7-8: Buoyancy forcing (left panels, units 10^{-13} s^{-3}) and "effective forcing" (right panels, units m^2 s^{-2}) for the indicated trials.

patterns that do not contain dynamical information. As noted by Penland (1989), the POP analysis also indicates the timescales on which the feedback should act.

My system appears to be a good candidate for POP analysis. As shown in Chapter 6, the changes in eddy fluxes among the model runs are absolutely necessary for producing both the correct shape and the correct amplitude of the annular mode patterns. In the previous section, I hypothesized a mathematical formulation of the problem using the eddy feedback.

In order to use the POP analysis, I assume that the changes in eddy fluxes, occurring on more rapid timescales, result in the changes to the zonal wind structures on longer timescales. An analysis of the dynamical operators found in the section above will produce the leading POPs and their timescales.

For a system with a state vector x, a forcing f and a dynamical operator D,

$$\frac{\partial x}{\partial t} + Dx = f. \tag{7.29}$$

The solutions may be expanded in terms of V, the eigenvectors of D. Then, for each location i,

$$(x_i, f_i) = \sum_{\alpha} V_{i\alpha} \left(y_\alpha, g_\alpha\right) \tag{7.30}$$

If each eigenvector V_α has an associated eigenvalue λ_α, then this reduces to, for each mode,

$$(\partial_t + \lambda_\alpha)\, y_\alpha = g_\alpha. \tag{7.31}$$

For a steady, forced system, the solutions become

$$y_\alpha = \lambda_\alpha^{-1} g_\alpha \tag{7.32}$$

Hence a large response to forcing y is indicated by a large projection of the forcing g, and a small eigenvalue λ.

In my control run, there is no steady forcing f. However, the eddies themselves may be considered as a stochastic forcing of the system. This stochastic forcing may be written as

$$f_i = V_{i\alpha} c_\alpha \phi_\alpha(t); \tag{7.33}$$

where c_α is the strength of the projection on the mode α, and the time-dependence term ϕ is scaled such that its zero-lag correlation is 1. Then the time-dependent equation becomes

$$(\partial_t + \lambda_\alpha)\, y_\alpha = c_\alpha \phi_\alpha(t). \tag{7.34}$$

Equation 7.34 may be integrated in order to obtain the correlation function of the response. It may be shown that this function decays exponentially with time, with decay timescale λ_α^{-1}. The mathematical formalism is contained in the Appendix.

Hence, there is a second, independent way of obtaining the timescale of the two leading modes. Instead of simply calculating the autocorrelation timescale of the EOF patterns, the timescale of the decay should also be found through considering the slope of the forcing projections on the dynamical operator's eigenvectors versus the response projections on the dynamical operator's eigenvectors. In Section 7.4, the state vector was reduced from one containing zonal wind and temperature, to one containing solely zonal wind, with the accompanying effective torques. Using this basis, I return to the steady forced problem, but seek the eigenvectors of the dynamical operator, rather than the simple EOFs, for purposes of the projection.

The starting point is the dynamical problem for angular momentum, using the effective torque derived in the previous section as the forcing. Recall Equation 7.24; which may be alternatively written as

$$\frac{\partial u}{\partial t} + \mathsf{B}u = f, \tag{7.35}$$

where $f = (a\cos\phi)^{-1} q$ and $\mathsf{B}_{ij} = (\cos\phi_i)^{-1}(L_{ij} + E_{ij})\cos\phi_j$. The equation describing the system reduces to a forced eigenvalue problem for B, an operator combining the dynamical and eddy feedback terms. Determining the eigenvectors of this operator will be the crux of the problem.

Any matrix may be decomposed, by eigenvalue decomposition,

$$\mathsf{B} = \mathsf{V}\Lambda\mathsf{W}^{\mathsf{T}}, \tag{7.36}$$

where Λ is a diagonal matrix of eigenvalues, V contains the eigenvectors of B, and W contains the eigenvectors of the transpose of B. It then follows that

$$\mathsf{V}\mathsf{W}^{\mathsf{T}} = \mathsf{V}^{\mathsf{T}}\mathsf{W} = \mathsf{I}, \tag{7.37}$$

where I is the identity matrix.

It is impossible to calculate V directly, as the exact nature of the operator B is unknown. However, following the POP analysis allows one to obtain V through other means. This is the topic of the following discussion.

The methods used here are presented in Penland (1989) and will be outlined briefly here. Some details of this presentation may be found in the Appendix.

I begin by defining the lagged covariance in physical space,

$$\mathsf{C}_\tau = \left\langle u\left(t+\tau\right) u^T\left(t\right)\right\rangle, \tag{7.38}$$

where the angle brackets denote a time average.

Mapping u and f into POP space by projecting onto the eigenvectors of B yields,

$$u = \mathsf{V}\overline{u};\ \overline{u} = \mathsf{W}^{\mathsf{T}}u \tag{7.39}$$

$$f = \mathsf{V}\overline{f};\ \overline{f} = \mathsf{W}^{\mathsf{T}}f \tag{7.40}$$

In the notation here, the quantities presented with overbars are in the POP space, while those without overbars are in physical space.

The lagged covariance in POP space is,

$$\overline{\mathsf{C}}_\tau = \left\langle \overline{u}\left(t+\tau\right)\overline{u}^T\left(t\right)\right\rangle = \mathsf{W}^{\mathsf{T}}\mathsf{C}_\tau\mathsf{W}. \tag{7.41}$$

Then Equation 7.35, in POP space, becomes, for each mode α,

$$\frac{\partial \overline{u}_\alpha}{\partial t} + \lambda_\alpha \overline{u}_\alpha = \overline{f}_\alpha \tag{7.42}$$

Integrating Equation 7.42 and plugging into the expression for covariance is the next step. Assuming that the lagged covariance of the forcing decays much more quickly than the lagged covariance of u, it is found that

$$\overline{\mathsf{C}}_\tau = \overline{\mathsf{C}}_\mathsf{o}\Gamma_\tau,\ \tau \ < \ 0 \tag{7.43}$$

$$\overline{\mathsf{C}}_\tau = \Gamma_\tau^{-1}\overline{\mathsf{C}}_\mathsf{o},\ \tau \ > \ 0, \tag{7.44}$$

where Γ_τ is a diagonal matrix with elements $e^{\lambda\tau}$ on the diagonal, and zeros off the diagonal.

Returning to physical space, the lagged covariance in physical space must be

$$\mathsf{C}_\tau = \mathsf{V}\overline{\mathsf{C}}_\tau\mathsf{V}^\mathsf{T}. \tag{7.45}$$

But, Equation 7.44 may be used to substitute, yielding

$$\mathsf{C}_\tau = \mathsf{V}\Gamma_\tau^{-1}\overline{\mathsf{C}}_\mathsf{o}\mathsf{V}^\mathsf{T} \tag{7.46}$$

$$\mathsf{C}_\tau = \mathsf{V}\Gamma_\tau^{-1}\mathsf{W}^\mathsf{T}\mathsf{V}\overline{\mathsf{C}}_\mathsf{o}\mathsf{V}^\mathsf{T} \tag{7.47}$$

$$\mathsf{C}_\tau = \mathsf{G}_\tau\mathsf{C}_\mathsf{o}, \tag{7.48}$$

where

$$\mathsf{G}_\tau = \mathsf{V}\Gamma_\tau^{-1}\mathsf{W}^\mathsf{T}. \tag{7.49}$$

The matrices V and W contain the eigenvectors of G and G^T, and are termed the "principal oscillation patterns" of G and G^T. However, as seen in Equation 7.36, they also contain the eigenvectors of B and B^T. So instead of solving for the eigenvectors of B directly, the procedure of Penland (1989) allows instead for the manipulation of

G. As seen from Equation 7.48, G is simply

$$\mathsf{G} = \mathsf{C}_\tau \mathsf{C}_o^{-1} \tag{7.50}$$

So, to find G, it is simply necessary to calculate the zero-lag covariance matrix and a lagged covariance matrix, and multiply the two matrices.

In the figures below, I show the eigenvectors of G for several cases. The eigenvectors are similar to the EOFs of the unforced model.

While in principle one can calculate the covariance matrices using the entire dataset, Penland (1989) recommends projecting the data u onto a smaller number of EOFs. She notes that this reduces the number of degrees of freedom, making the calculations more efficient. The covariance matrices of the full data here are very large (960×960 elements), so I will focus on reducing the number of EOFs.

In Figures 7-9 and 7-10, I show the first and second POPs of G, at 10- and 40-day lag, respectively. These eigenvectors are calculated for a lagged covariance matrix containing information from the first four EOFs of the unforced run. For both time lags shown, the leading POP is similar to the leading EOF, describing primarily a dipole in the SH about the unforced jet's position. The second POP is similar to the second EOF, with the variability centered in the NH. The eigenvectors found for the two different lags are similar, as are the eigenvectors calculated at other lags (not shown). Since the eigenvectors should not depend on the time lag chosen, this is an expected result.

One potential concern, however, is the poorer separation of features between the two hemispheres. For the EOFs calculated in the previous chapters, the features were always confined to one hemisphere. Here, however, there is a larger residual amplitude in the hemisphere opposite the primary pattern. This behavior was noted for the eigenvectors calculated for other time lags as well.

As another test, I examine the POPs produced upon retention of a larger number of EOFs. These results agree with those of the four-EOF system, to a point. Shown are the first and second POPs, for a 10-day lag, for a six-EOF and eight-EOF system,

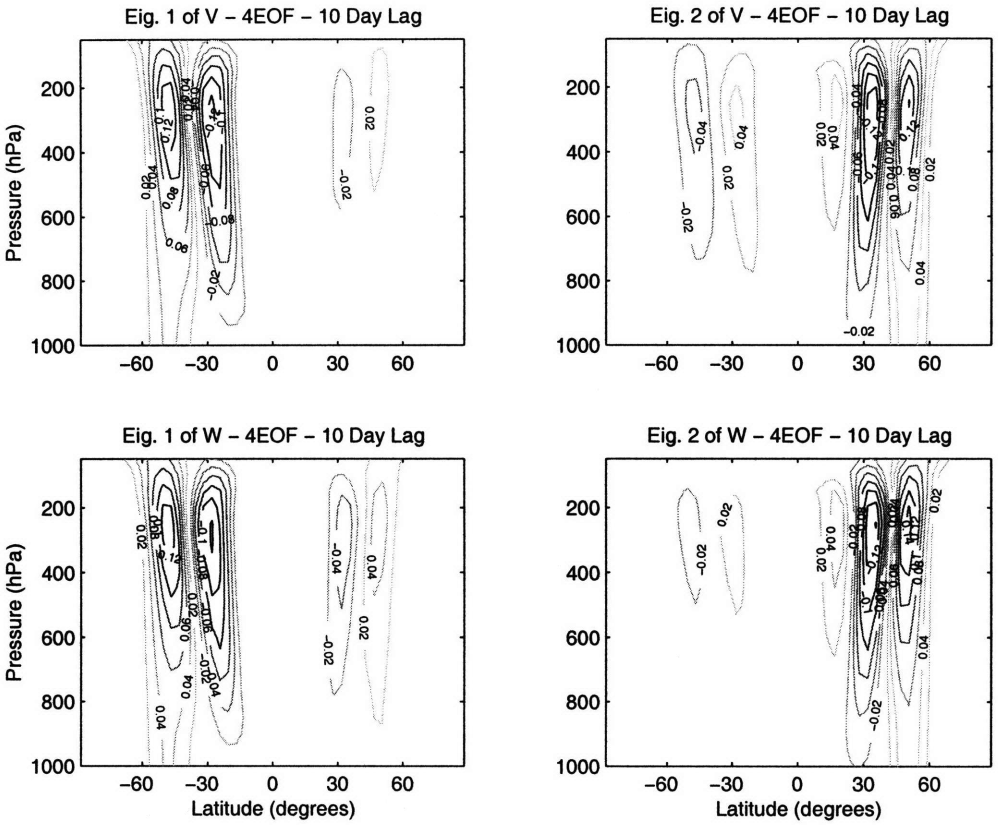

Figure 7-9: First and second eigenvectors of V and W for the four-EOF system, using a 10-day lag. Units are nondimensional.

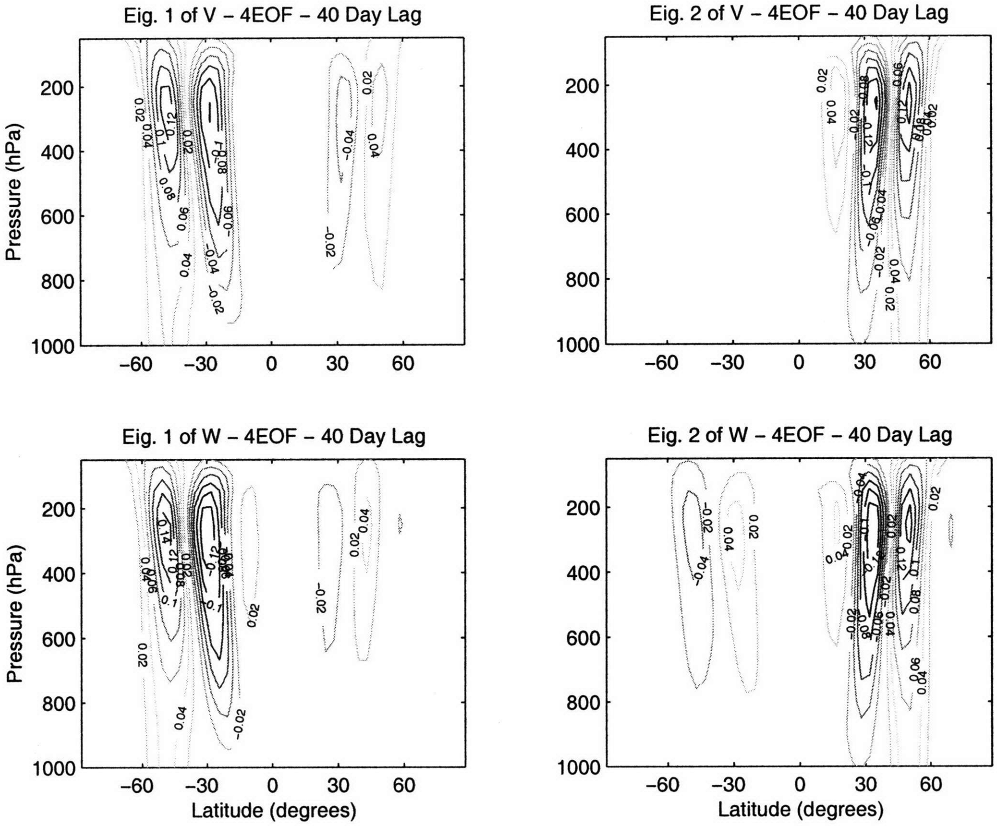

Figure 7-10: As in Figure 7-9, but for a 40-day lag.

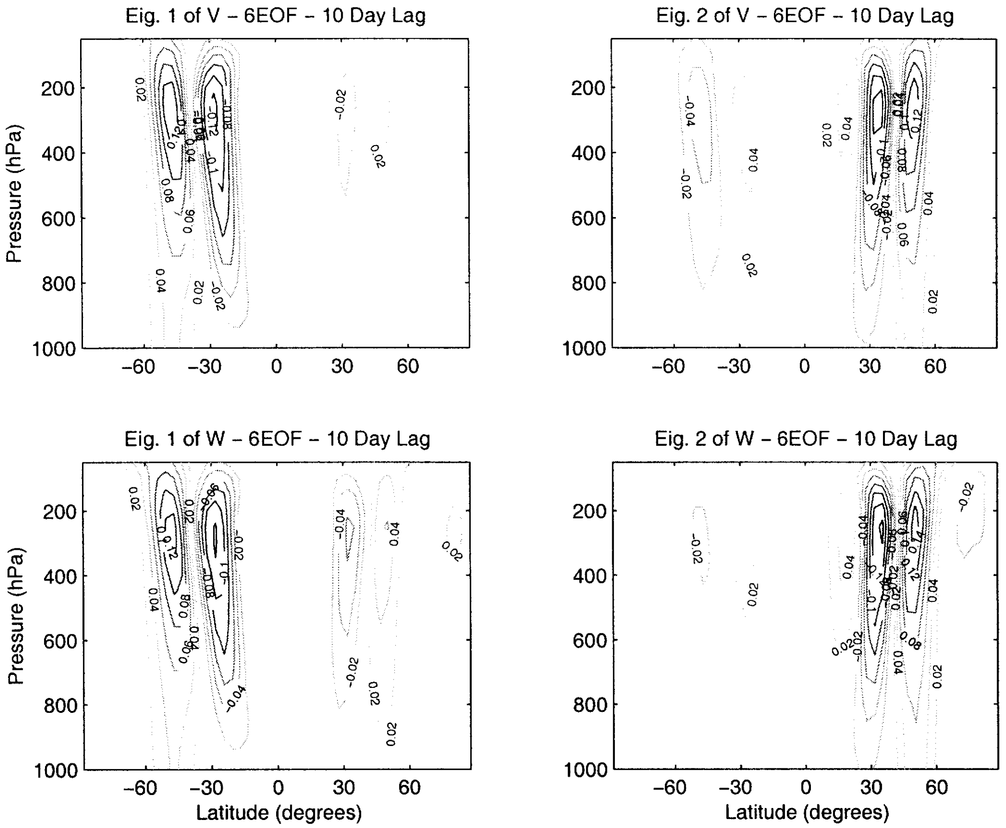

Figure 7-11: As in Figure 7-9, but for a six-EOF system.

in Figures 7-11 and 7-12. These eigenvectors are similar to those shown in Figures 7-9 and 7-10 above, with the POPs primarily describing the same shape as the EOFs, with the larger residual amplitude in the opposite hemisphere as noted above.

After expanding the system to 12 EOFs, the agreement becomes much poorer, as the system appears to become ill-posed. The POP analysis instead generates complex eigenvalues and eigenvectors, which do not resemble those of the annular mode patterns.

While it is worrisome that the system becomes ill-posed after the addition of about one dozen EOFs, fortunately these higher EOFs describe very little variance of the unforced run. In fact, the first four EOFs contain 85 percent of the variability in the zonal wind field. The first eight EOFs describe collectively 90 percent of the variability, and the first twelve EOFs contain 93 percent of the variability. So, narrowing the data to the first four EOFs does not result in a large loss of variability

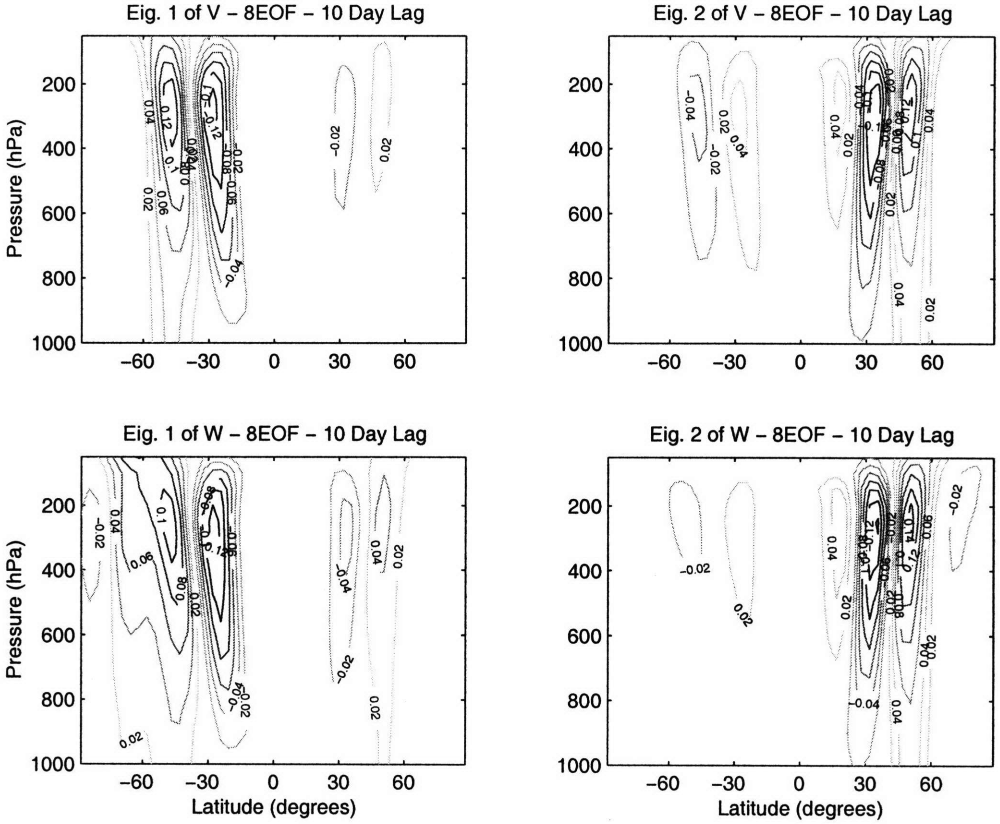

Figure 7-12: As in Figure 7-9, but for an eight-EOF system.

EOFs Retained	Lag	Value of λ_1^{-1} (days)	Value of λ_2^{-1} (days)
4	10	58	41
4	40	66	51
8	10	60	41
8	40	65	51

Table 7.1: Eigenvalues of B for the indicated trials.

while offering speedy computations. That is what will be done here.

At this point it is also possible to check the eigenvalues λ^{-1} derived from the principal oscillation patterns. These should match the decorrelation times of the leading EOFs of the unforced run, if we can think of the problem as stochastically forced. The eigenvalues do generally match the decorrelation times (58 days in the SH and 48 days in the NH), as shown in Table 7.1. The results in this table are typical of those for other lags or numbers of EOFs retained.

Returning to the steady, forced problem, recall Equation 7.35. If the solution is steady this simply reduces to

$$\mathsf{B}u = f. \tag{7.51}$$

Using the eigenvector expansion of B, this may be re-written as

$$u = \mathsf{V}\Lambda^{-1}\mathsf{W}^{\mathsf{T}}f. \tag{7.52}$$

Multiplying by W^{T} on the left of each side of the equation yields for each mode

$$\overline{u}_{\alpha} = \lambda_{\alpha}^{-1}\overline{f}_{\alpha}. \tag{7.53}$$

This equation predicts that the slope of the line containing the projections of the forcing onto W^{T}, and the wind response onto W^{T}, should be linear with slope λ^{-1}.

With this in mind, I return to the projections of response and forcing examined earlier, this time inspired by the POP analysis. Following the procedure here, the wind response in each hemisphere will be projected onto W^{T}, as will be the effective forcing, and the relationship between these two projections compared.

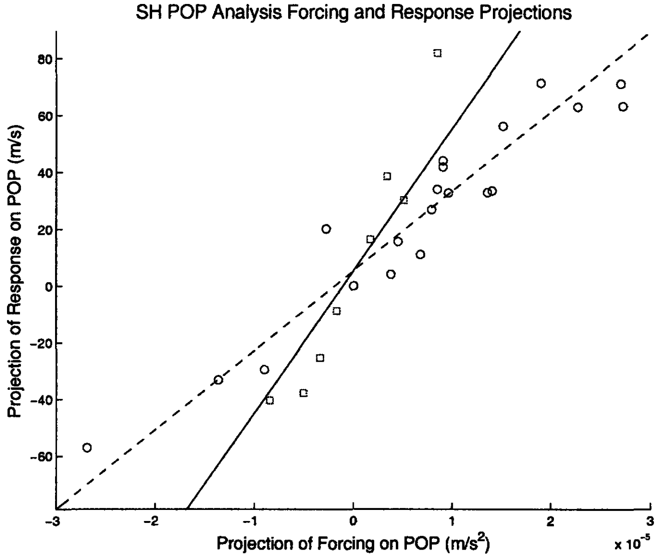

Figure 7-13: SH zonal wind response projected on W^T of the unforced model run versus the forcing projected on same pattern. Circles indicate mechanically forced trials; squares indicate thermally forced trials. Dashed line is best least-squares fit; solid line is prediction based on decorrelation time of pattern in unforced run.

In both hemispheres, however, the results (Figures 7-13 and 7-14) are not as simple as those obtained from the more trivial projections shown earlier (Figures 7-1 and 7-2). While in each case the mechanically forced trials appear to have a linear projection, and the thermally forced trials appear to have a linear projection, the slopes of the projections between the two trials are different.

Neither the slope of the mechanically or thermally forced trials alone, nor the slope of the best least-squares fit including all the trials, matches the decorrelation timescales predicted from the POP analysis. The slopes obtained from the best fit including all trials (dashed lines in Figures 7-13 and 7-14) are 32 days in the SH and 17 days in the NH, comparing poorly with the decorrelation times of 58 days in the SH and 48 days in the NH (solid lines). The slopes of the best linear fits to the mechanically forced trials are 31 days in the SH and 15 days in the NH. The best fits to the thermally forced trials feature slopes of 85 days in the SH and 100 days in the NH.

In Figures 7-15 and 7-16, only those trials whose strength of response projection was below the median value of all trials are plotted, and the fit based on those lines

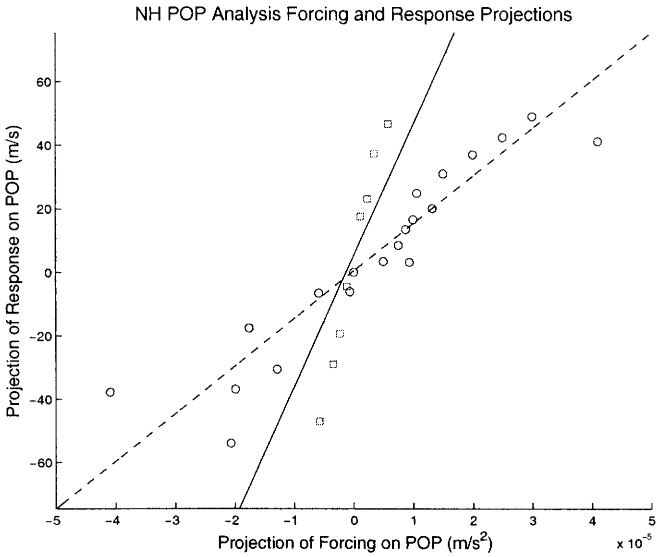

Figure 7-14: As in Figure 7-13, but for the NAM and NH.

considered. In each case the value of the slope for the best fit is only slightly changed (now 31 days in the SH and 15 days in the NH). As in the examination of the projections using all the trials, the difference in behavior between mechanically and thermally forced trials is still evident.

7.6 Discussion

It is clear from the analysis in Figures 7-13 through 7-16 that the POP analysis is problematic in explaining the relationship between forcing and response observed in the simpler projections. It is worthwhile to consider potential reasons why that is the case.

As noted above, there are two areas of concern with the POP analysis performed here. First, the POP analysis does not produce robust results if too many EOFs are included. While the system has no trouble handling the four or six EOF system, when beyond 12 EOFs the system does not find physically meaningful solutions. While the heavy weighting of the variability of the unforced run toward the first few EOFs would hopefully make the higher EOFs irrelevant, the computational difficulty must be noted here.

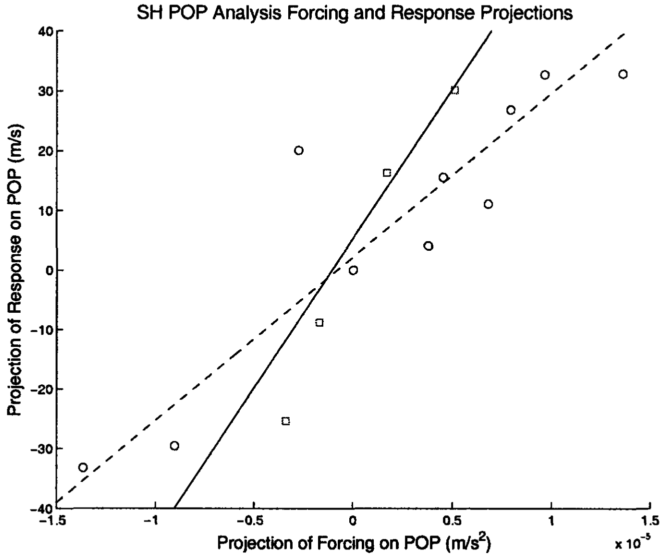

Figure 7-15: As in Figure 7-13, but for the points with strengths of response projection below the median value.

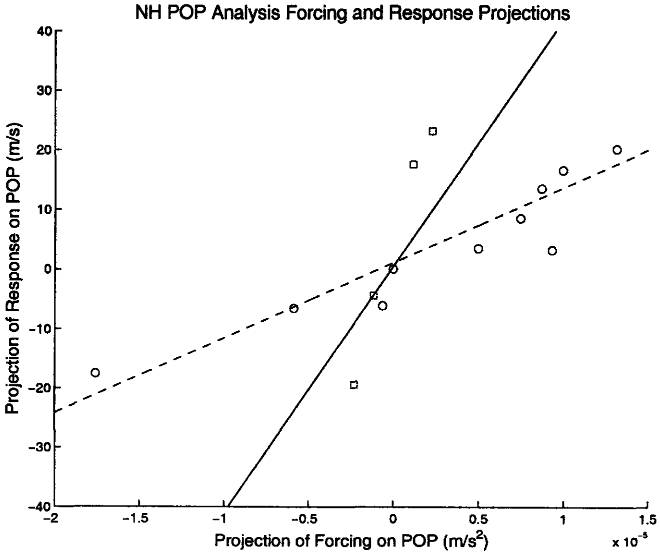

Figure 7-16: As in Figure 7-15, but for the NAM and NH.

A second problem arising from the POP analysis, as specified above, is the poorer separation of amplitude between the hemispheres. In the EOF analysis of earlier chapters, there was always a clean separation of variability between the hemispheres. The amplitude of EOF1 was virtually zero everywhere in the NH, and the strength of EOF2 was virtually zero everywhere in the SH. However, as seen above, the separation of amplitude is not as clean with the POP analysis. While in every case the eigenvectors of V and W display maximum amplitude in the expected hemisphere, there are weaker but noticeable centers of amplitude in the opposite hemisphere, which were clearly not visible in the EOF analysis of earlier chapters. Their appearance here is disquieting, but it seems quite robust as it occurs for the different lags and numbers of retained EOFs considered.

It is also possible that some of the assumptions made in the mathematical formulation are invalid. The analysis in Section 7.4 assumed that a linear eddy feedback operator could be defined which acted only on the perturbation momentum. It is certainly plausible, however, that changes to static stability materially effect the eddy fluxes, requiring the eddy feedback to be treated as a function of perturbation buoyancy as well. Inclusion of the perturbation buoyancy would make the mathematical problem much less tractable, denying the opportunity for a simple solution. Nonetheless, it may be that the static stability perturbations are indispensably linked to the eddy feedback in the model.

Alternatively, the problem encountered by the POP analysis may simply be a reflection of non-linearity in the system. For the trials selected in Chapters 4 and 5, the response of the model to the applied forcing was typically of the order of the internal variability of the system, as expressed through the magnitude of the EOFs of the unforced model run. This strength of response could potentially be too great to allow a linear relationship between forcing and response. Included in the analysis above are some trials with weaker magnitudes of forcing, and a fuller suite of such trials would be useful in discerning whether the typical forcings used here are too strong to insure linear behavior. Unfortunately, such trials are extremely difficult to perform in this setup as the long decorrelation timescales of the EOFs in the model, combined with the slow speed of numerical integration, would require impractical lengths of integration. However, examination of a greater number of trials with small magnitudes of forcing is a logical next step to test the analysis.

In summary, I have shown that the strength of the annular mode response to forcing in the model is increased either by increasing the magnitude of the forcing applied, or by improving the projection of the forcing on the annular mode pattern. A simple projection, uniting the mechanically and thermally forced cases by weighting each by its respective variance, suggests a linear relationship between forcing and response. However, uniting the two types of forcing by determining an "effective torque" and projecting upon the eigenvectors of the dynamical operator through use of POP analysis does not duplicate this result. The reasons for this discrepancy are not understood, although an improper assumption in the mathematical formulation is possible, as is the presence of non-linear effects at the strengths of forcing used here.

Chapter 8

Conclusions

8.1 Introduction

In this thesis, I have studied whether the annular modes are a preferred response of a simple atmospheric general circulation model to applied forcings. The differences in climatologies among the forced runs and a control trial are annular mode-like in most cases, so the annular modes are indeed a preferred response of the model.

In this final chapter of the thesis, I wish to summarize the results of the trials conducted as part of the thesis work, as well as offer suggestions for future work. Finally, returning to the inspiration of this thesis — the appearance of the annular modes in relation to a number of real-world forcings of the atmosphere — I briefly discuss the implications of the simple model results in the context of the Earth's atmosphere.

8.2 Summary

This thesis has used a simple general circulation model to explore whether the annular mode patterns are a preferred response of the atmospheric circulation to generic forcings.

In this study, the dynamical core of the GFDL atmospheric general circulation model has been employed. For the trials here, a T30 spectral resolution and 20 equally-spaced sigma-levels have been used. Newtonian cooling, Rayleigh friction, and hyperdiffusion constitute the model's dissipation schemes.

A control climatology produced by the model is fairly similar to that of Earth. The most notable climatological feature in each hemisphere is a westerly jet. In both the Southern (winter) and Northern (summer) Hemisphere, the maximum amplitude of each jet is similar to that observed on Earth. The locations of each jet in latitude are close to those observed on Earth as well. Other climatological fields also parallel those observed on Earth. Perhaps most notably, the structure of the Eliassen-Palm fluxes and divergence are like those observed in real life.

The dominant feature of variability in each hemisphere is an annular mode. In the zonal wind field, the annular mode straddles the eddy-driven jet, with a dipole of positive and negative amplitude centered about a nodal line coincident with the jet. This matches the zonal wind variability in each hemisphere of Earth's atmosphere (e.g. Lorenz and Hartmann, 2001, 2003). The annular mode may be seen in the model's pressure and geopotential fields as well.

The model is subjected to a series of torques, and the climatologies of the model under the influence of the various torques are compared to that of the control. The torques are chosen to be monopolar in each hemisphere so as to have a different spatial structure as compared to the dipolar annular modes.

In most of the trials, the response in each hemisphere to these monopolar forcings is dipolar and annular mode-like, with opposite-signed wind anomalies centered about the position of the control time-mean jet in each hemisphere. The responses to the mechanical forcing are generally stronger for an increased strength of forcing, or an improved projection of the forcing on the annular mode patterns. Whenever an annular mode-like response is found in the wind field, the changes in eddy flux divergence are similar to the patterns found through singular value decomposition of the covariance matrix of eddy-zonal wind anomalies in the control trial. This suggests eddy feedback processes cited by Lorenz and Hartmann (2001, 2003) as responsible for maintaining the annular modes in Earth's atmosphere are also responsible for the appearance of the forced patterns in these model runs.

In some of the mechanically forced trials with the torques placed on the jets' equatorward flanks, the annular mode response was not as strong as would otherwise be expected from the projection of the forcing on the mode. In these trials, there was substantial interference with the Hadley circulation, leading to a stronger direct response that obscured the indirect eddy-mean flow changes which are critical to the annular mode response.

The response of the model to thermal forcings is also tested by perturbing the reference temperature profile and comparing these climatologies to that of the control run. Model runs with broad, hemisphere-scale perturbations to the reference temperature did not successfully reproduce the annular mode patterns. As with the mechanically forced trials using equatorward-flank torques, the direct responses here tended to be stronger. Additionally, the wide geographical range over which the temperature varied resulted in a poor projection on the annular mode patterns. However, temperature perturbations confined poleward of 45° did robustly reproduce the dipolar wind anomalies. With the region of variation in the reference temperature more confined, the projection of the forcing was greatly improved, and the annular mode response more robust.

A zonally symmetric version of the model is used to test whether the changes found in the full model runs are due to the direct effects of the forcing, or changes to the eddy feedback processes. The eddy fluxes are calculated from the full model climatologies and input into the zonally symmetric model but held fixed at each time step. Then, the applied forcing alone may be added to discern the response caused directly by the forcing. In all cases, this response matches neither the structure nor the magnitude of the response found in the full model run. Then, the eddy fluxes from the forced full model runs are calculated and prescribed to the zonally symmetric model, and the zonally symmetric model is run with the applied forcing and these forced eddy fluxes. In these runs, the zonally symmetric model is able to reproduce the correct shape and strength of patterns found in the full model runs, showing that changes to the eddy feedback processes are needed to produce properly the forced annular mode patterns.

8.3 Suggestions for Future Work

While a substantial number of model runs, testing the annular mode response to both mechanical and thermal forcings, has been conducted in this thesis, there are of course a number of extensions which could be made to understand further the response of the annular mode patterns to applied forcings. Below I suggest several avenues for further work which I believe would prove worthwhile.

The largest unresolved question presented in this thesis is the relationship between the strength of the forcing and the strength of the response, and it is therefore an obvious candidate for further examination.

From the results of this simple GCM, the relationship between the projection of the forcing and the projection of the response in the mechanically forced trials appears to be linear. Likewise, a linear relationship may be discerned between the forcing and response projections in the thermally forced trials. However, the two sets of trials suggest lines with different slopes, and an attempt to unify the two sets of trials by considering the Eliassen (1951) response as the effective torque did not resolve the differences in slope.

The perspective used in Chapter 7 was to compare the forced cases with the unforced run, using fluctuation-dissipation theory, in order to learn more about the behavior of the responses. From the unforced case, I obtained the EOF patterns of the zonal wind anomalies as well as their decorrelation times. Additionally, the principal oscillation pattern (POP) analysis techniques were used to determine the eigenvectors and eigenvalues of the feedback matrix. The eigenvectors derived from the POP analysis are close to those found through EOF analysis, though in the POP analysis there is residual amplitude in the opposite hemisphere which does not occur in the EOFs. The timescales derived from the eigenvalues of the POP analysis agree well with the decorrelation times found through EOF analysis.

Then, turning to the forced cases, the projections on the POPs of the "effective torques" derived through analysis of an instantaneous response to the forcing are considered and compared to the response projections. While the mechanically forced cases taken individually or the thermally forced cases taken individually appear linear, they do not follow the same line, and neither slope matches the eigenvalue of the POP analysis.

It was assumed in the dynamical formulation that the eddy feedback operator was not sensitive to changes in static stability, so if stability changes are important this is a potential source of trouble in the analysis. Additionally, it was hypothesized the operators depended on the instantaneous value of the perturbation momentum, and not the lagged value. However, given the long decorrelation times of zonal wind in the model runs, this assumption seems to be reasonable.

The POP analysis does rely on linearity, and it is possible that the forcings used here are too strong and the assumptions of linearity are violated. One remedy for this situation would be to conduct an additional number of trials with forcings weaker than those typically used here to see if linearity can be established in response to the reduced forcings. Unfortunately, such trials are difficult to perform here. The practical constraints of my system — long decorrelation times and slow computing power — make examination of cases with very weak forcing difficult, as very long model runs would be needed to produce statistically robust data. However, such trials may be of interest to those who wish to examine this project further.

In this thesis, I have conducted a number of trials with forcings placed in the troposphere. Both mechanical and thermal trials have been employed, and the forcings have been varied in strength, location, and spatial structure. While one can obviously design an infinite number of forcings to examine in the model, I believe I have been thorough in my examination of tropospheric forcings.

A particularly interesting follow-up of this work would be to examine the results of trials with forcing placed in the stratosphere, which has not been done in this thesis. As noted in the Introduction, the extratropical stratosphere and troposphere are coupled in each hemisphere at certain times of the year, and during those times the annular mode signal is observed to extend past the tropopause into the middle atmosphere (Thompson and Wallace, 2000). During these times, Arctic Oscillation anomalies have been observed to descend downward from the stratosphere to the troposphere and affect weather patterns at Earth's surface (Baldwin and Dunkerton, 1999, 2001).

A few studies have examined the response of stratosphere-resolving model atmospheres to selected mechanical (Song and Robinson, 2004) or thermal (Kushner and Polvani, 2004) forcings, in an attempt to understand better the dynamical linkage between the stratosphere and troposphere. However these studies have used a limited number of forcings and did not employ a broad array of forcings at different locations as was done here. It would be worthwhile to see if the annular modes are a preferred response to stratospheric forcing, as they are in this model for tropospheric forcing, and whether there is a consistent downward propagation of the anomalies. A reasonable hypothesis would be that a forcing which projects upon the stratospheric extensions of the annular mode patterns, or produces a meridional circulation response which in turn projects well, would result in this type of behavior. A thorough suite of trials placing mechanical and thermal forcings in the stratosphere would elucidate the role of the annular mode patterns in the middle atmosphere and their role in stratosphere-troposphere coupling.

8.4 Implications for Earth's Atmosphere

In the Introduction to this thesis, I discussed several problems in weather and climate to which the annular modes appear as a response. Based on the results obtained from this model, it appears that the annular modes should be examined when considering the response of Earth's atmosphere to a generic forcing. I wish to close with some discussion of the implications of the results of this study for the climate system of Earth.

As stated earlier, the annular mode signal has appeared in relation to global warming in both reanalysis data (e.g. Thompson et al., 2000) and model studies (e.g. Rind et al., 2005). If the annular modes are a preferred response of the Earth's climate system to the thermal forcing, as they have been for the simple model here, then it is imperative to consider the effects of annular modes when predicting future climate change.

Model trials in Chapter 5, conducted with the thermal forcing confined to be poleward of 45°, showed a strong annular-mode like response. The forcings in these trials are qualitatively similar to those of global warming scenarios for both the observed and predicted modern trends and the reconstructed climatologies from paleoclimate.

Other factors besides the annular mode patterns contribute to the greater polar sensitivity to climate changes. The ice albedo feedback, of course, is one important cause (Budyko, 1969; Sellers, 1969). As Earth warms and ice melts, the albedo of the planet is reduced, and the surface therefore absorbs more solar energy, resulting in a further impetus for warming.

The strong projection of temperature changes concentrated in polar regions on the annular modes suggested in this model may be another source of the high-latitude sensitivity to climate changes. Recall that in this model there is no ocean or cryosphere so the ice albedo feedback cannot operate, yet the model is still sensitive to thermal forcing in the polar regions. In Chapter 5 of this thesis, reference temperature anomalies confined poleward of 45° produced robust annular mode-like responses. Such changes in temperature concentrated in the high latitudes appear to be occurring under the current hypothesized warming scenarios and have occurred during warm periods in Earth's history. As noted by the IPCC (2001a), the rise in climatological temperatures in the twentieth century in the Arctic region outpaced those in other parts of the world. Most modeling scenarios examined by the IPCC suggest that the Arctic land areas will similarly warm more rapidly under predicted changes in the twenty-first century as compared to the globe as a whole. The greater sensitivity in the polar regions to climate change is also consistent with reconstructions of historical climate data for warm periods such as the Cretaceous (e.g. Barron, 1983), where the rise in temperature in the polar regions was disproportionately high as compared to the tropics.

Should the polar amplification of temperature anomalies project well on the annular modes of Earth's real atmosphere as it did for the model runs of Chapter 5, then the impacts known to be associated with different phases of the annular modes must be considered when making predictions of future climate change.

Another forcing, which as discussed in Chapter 1 appears to be linked to the annular mode pattern, is the radiative effects of ozone depletion. This is a thermal forcing in the stratosphere, as the absence of ozone allows for anomalously low temperatures to be observed in the polar regions of the stratosphere. While no runs involving stratospheric forcing have been conducted here, analyses of annular mode-like changes to the polar vortex show they are related to ozone loss (Thompson and Solomon, 2002), and the recent climate trends in the SH have been modeled by Gillett and Thompson (2003) using ozone depletion as their forcing. Hence, any predictions about changes in the stratospheric circulation which stem from either continued ozone loss or ozone recovery should be reflected in geopotential anomalies or wobbles of the polar night jet which are signatures of the annular mode in that field.

The results of this thesis suggest that mechanical forcings should also be able to induce a response in Earth's atmosphere that resembles the annular mode patterns. As found in Chapter 4, the addition of artificial, monopolar torques to the model atmosphere generally produced a dipolar, annular mode-like wind response. Hence, it is reasonable to hypothesize that mechanical forcings in Earth's real atmosphere should also result in annular mode-like responses.

Changes to eddy fluxes are central in producing the annular mode patterns. As seen through use of the zonally symmetric model in Chapter 6, the eddy feedback processes found by Lorenz and Hartmann (2001, 2003) to sustain the unforced annular modes are also responsible for producing the forced patterns here. While the monopolar torques tested here obviously do not appear in Earth's atmosphere, there are of course changes to the eddy fluxes in real life. And, a forcing which produces changes to the patterns of Eliassen-Palm flux and divergence may therefore cause changes to the annular mode patterns of Earth's atmosphere, if the extension of the model results to the real atmosphere proves accurate.

E-P flux divergence and convergence are associated with the generation and dissipation of waves in Earth's atmosphere. The behavior of waves may be affected by any number of phenomena, so it appears the annular modes may similarly be affected. An anomalously high (or low) rate of eddy generation at the surface results in anomalously high (or low) E-P flux divergence, and is therefore a mechanical forcing which could effect the annular modes. An unusually active (or quiet) storm track is an example of this type of forcing. Waves favor propagating toward regions of high refractive index (Matsuno, 1970), so forcings affecting the refractive index of the atmosphere will change where waves propagate and ultimately dissipate and may affect the annular modes as well. Similarly, changes to the background state of Earth's atmosphere may cause waves to be evanescent (Charney and Drazin, 1961), again affecting their direction of propagation and dissipation characteristics. Since eddies are crucial to the transport of momentum in the extratropics of Earth's atmosphere, a forcing which changes the distribution of eddy momentum flux convergence and divergence may affect the annular modes similarly to the model's response to the addition of artificial torques.

In summary, the annular modes have proven to be a preferred response of the model's circulation to both mechanical and thermal forcings whose spatial structure does not resemble that of the annular modes. While the physical parameterizations present in the model are much simpler than the complex processes in Earth's atmosphere, the model results do suggest that the annular modes may indeed be a preferred response of Earth's atmosphere as well. The prominence of the annular modes as a model response suggests they are more than a statistical artifact but instead represent patterns of dynamical importance. The attention paid to the annular modes in the past few years has been well-deserved, and the response of the annular modes should be investigated when considering the large-scale response to forcings in the extratropics of Earth's atmosphere.

Appendix A

Reference Temperature Profile

This appendix highlights the formulae used to calculate the reference temperature in the model runs used here. Recall that the profile of reference temperature is plotted in Figure 2-3. It is based on the Held and Suarez (1994) default from the GFDL circulation model, but there are a few modifications.

I begin by defining background temperatures at the ground, and in the stratosphere. The stratosphere's reference temperature is chosen to be a constant 195 K. For the ground temperature, the following formula is applied. The ground temperature consists of its polar value, a term varying as the fourth power of cosine of latitude whose maximum value is slightly off the equator, and a term which is asymmetric about the equator. The second term results in the point of maximum reference temperature being displaced slightly into the Northern Hemisphere, while the third term imparts different equator-pole temperature gradients to the two hemispheres. Together, these changes result in a reference temperature profile qualitatively similar to a perpetual July.

$$T_{ground} = T_{pole} + T_{grad} \cos^4(\phi - \phi_o) + T_{seas} \sin \phi \tag{A.1}$$

For the runs shown in this thesis, $T_{pole} = 255\ K$, $T_{grad} = 60\ K$, $T_{seas} = 10\ K$, and $\phi_o = 2.8°$. As a test of model sensitivity, several trials were conducted using small perturbations to these coefficients, and the climatologies produced were similar to that using the chosen parameters.

To obtain the vertical variation in the reference temperature T_{ref}, the default scheme employed in the GFDL model is used. The following formulae apply, and the model's default choice of 10 K for Δ_v is used.

$$T_1(\phi, p) = \left(T_{ground} - \Delta_v \cos^4(\phi - \phi_o) \ln\left(\frac{p}{1000\ hPa}\right)\right) \tag{A.2}$$

$$T_2(\phi, p) = T_1(\phi, p) \left(\frac{p}{1000\ hPa}\right)^{\frac{2}{7}} \tag{A.3}$$

Finally, the model selects the maximum of T_2 and T_{strat} at each point to be the reference temperature T_{ref}. This is the profile shown in Figure 2-3 and used for the control run in Chapter 3, and the mechanically forced trials in Chapter 4.

In the thermally forced model trials of Chapter 5, the prescribed change in reference temperature is added to or subtracted from the control's surface value. The change in reference temperature with altitude follows the variation used in the two equations above, and as the maximum of T_2 and T_{strat} is still selected, the change in reference temperature reaches zero at the tropopause for all cases.

Appendix B

Mathematical Formulation of the POP Analysis

In this appendix, I present several details of the principal oscillation pattern (POP) analysis, expanding on the briefer discussion in Chapter 7.

In Section 7.4, it is shown (Equation 7.34) that if the control run with no external forcing may be considered to be stochastically forced by the eddies, then the time-dependent equation for the system may be written as,

$$(\partial_t + \lambda_\alpha)\, y_\alpha = c_\alpha \phi_\alpha(t), \tag{B.1}$$

where λ is the eigenvalue of each mode α, c the projection onto each mode, and ϕ the scaled time-dependence.

Here I wish to show that the correlation function of the response decays exponentially with timescale λ^{-1}.

To begin, I define the correlation function of the forcing C_F

$$C_{F,\alpha}(\tau) = \langle \phi_\alpha(t)\phi_\alpha(t+\tau)\rangle\,. \tag{B.2}$$

It will be assumed $C_F(\tau) = C_F(-\tau)$. The pointed brackets <> indicate a time-average.

The decorrelation time T is then

$$T_\alpha = \int_0^\infty C_{F,\alpha}(\tau) d\tau \tag{B.3}$$

The correlation function of the response $C_R = \langle y(t)y(t+\tau)\rangle$ may be found by integrating Equation 7.34 and substituting for y.

$$y_\alpha(t) = c_\alpha \int_{-\infty}^t e^{\lambda_\alpha(t'-t)}\phi_\alpha(t')dt' = c_\alpha \int_{-\infty}^0 e^{\lambda_\alpha s}\phi_\alpha(t+s)ds \tag{B.4}$$

$$C_{R,\alpha}(\tau) = c_\alpha^2 \int_{-\infty}^0 \int_{-\infty}^0 e^{\lambda_\alpha(s+s')} C_{F,\alpha}(\tau + s' - s)\ ds\ ds'. \tag{B.5}$$

Assuming that the forcing correlation decays exponentially, $C_{F,\alpha}(\tau) = e^{-T_\alpha^{-1}|\tau|} = e^{-\mu|\tau|}$, then

$$C_{R,\alpha} = c_\alpha^2 \int_{-\infty}^0 e^{\lambda_\alpha s} \left(\int_{-\infty}^0 e^{\lambda_\alpha s'} e^{-\mu|\tau+s'-s|} ds' \right) ds. \tag{B.6}$$

Consider $\tau > 0$ (since C_R is symmetric with respect to τ). Noting that $s < 0$, the expression in parentheses may be split into two pieces.

$$\int_{-\infty}^0 e^{\lambda_\alpha s'} e^{-\mu|\tau+s'-s|} ds' = \int_{-\infty}^{s-\tau} e^{\lambda_\alpha s'} e^{\mu(\tau+s'-s)} ds' + \int_{s-\tau}^0 e^{\lambda_\alpha s'} e^{-\mu(\tau+s'-s)} ds' \tag{B.7}$$

After integrating each piece and rearranging,

$$\int_{-\infty}^0 e^{\lambda_\alpha s'} e^{-\mu|\tau+s'-s|} ds' = \frac{1}{\lambda_\alpha - \mu} e^{-\mu(\tau-s)} - \frac{2\mu}{\lambda_\alpha^2 - \mu^2} e^{-\lambda_\alpha(\tau-s)} \tag{B.8}$$

Then, plugging back in to Equation B.6,

$$C_{R,\alpha} = \frac{c_\alpha^2 e^{-\mu\tau}}{\lambda_\alpha - \mu} \int_{-\infty}^0 e^{(\lambda_\alpha+\mu)s} ds - \frac{2\mu c_\alpha^2 e^{-\lambda_\alpha \tau}}{\lambda_\alpha^2 - \mu^2} \int_{-\infty}^0 e^{2\lambda_\alpha s} ds \tag{B.9}$$

$$C_{R,\alpha} = \frac{c_\alpha^2}{\lambda_\alpha^2 - \mu^2} \left(e^{-\mu\tau} - \frac{\mu}{\lambda_\alpha} e^{-\lambda_\alpha \tau} \right) \tag{B.10}$$

If the decorrelation time of the forcing (noise) is short, so that $\mu >> \lambda_\alpha$, then the second term of C_R dominates, and the decay time is exponential, with decay time λ_α^{-1}.

While the analysis above assumed that the forcing decorrelation was exponential, a more general expression may in fact be found. It will still be assumed that $C_F(\tau) = C_F(-\tau)$, and that $T_\alpha << \lambda_\alpha^{-1}$, but the form of the forcing correlation function will otherwise not be assumed.

Then, returning to the response correlation function,

$$C_{R,\alpha}(\tau) = c_\alpha^2 \int_{-\infty}^{0} \int_{-\infty}^{0} e^{\lambda_\alpha (s+s')} C_{F,\alpha}(\tau + s' - s)\ ds\ ds'. \tag{B.11}$$

Instead, the variables may be rotated and redefined, $(\xi, \eta) = \frac{1}{\sqrt{2}}(s + s', s - s')$. ξ will be less than 0. Then,

$$C_{R,\alpha} = c_\alpha^2 \int_{-\infty}^{0} \left(\int_{\xi}^{-\xi} C_{F,\alpha}(\tau - \eta\sqrt{2}) d\eta \right) e^{\sqrt{2}\lambda_\alpha \xi} d\xi. \tag{B.12}$$

If ζ is defined to be $\tau - \eta\sqrt{2}$, then the integral in parentheses may be rewritten as

$$\left(\int_{\xi}^{-\xi} C_{F,\alpha}(\tau - \eta\sqrt{2}) d\eta \right) = \frac{1}{\sqrt{2}} \int_{\tau+\xi\sqrt{2}}^{\tau-\xi\sqrt{2}} C_{F,\alpha}(\zeta) d\zeta. \tag{B.13}$$

Here I will make use of an assumption on C_F — that the function is very narrow. This is an extension of the assumption that $T_\alpha << \lambda_\alpha^{-1}$. Then, as extending the limits of integration where C_F is small will not appreciably alter the result, I find

$$\left(\int_{\xi}^{-\xi} C_{F,\alpha}(\tau - \eta\sqrt{2}) d\eta \right) \approx \frac{1}{\sqrt{2}} \int_{\tau+\xi\sqrt{2}}^{\infty} C_{F,\alpha}(\zeta) d\zeta. \tag{B.14}$$

Defining $\Psi_\alpha(s) = \int_s^\infty C_{F,\alpha}(\zeta) d\zeta$, then

$$\left(\int_{\xi}^{-\xi} C_{F,\alpha}(\tau - \eta\sqrt{2}) d\eta \right) = \frac{1}{\sqrt{2}} \Psi_\alpha(\tau + \sqrt{2}\xi), \tag{B.15}$$

and

$$C_{R,\alpha} = \frac{1}{\sqrt{2}} c_\alpha^2 \int_{-\infty}^{0} \Psi_\alpha(\tau + \sqrt{2}\xi) e^{\sqrt{2}\lambda_\alpha \xi} d\xi. \tag{B.16}$$

Again, the nature of the forcing decorrelation may be used to simplify the expression. As the correlation function C_F is very narrow, its integral $\Psi(s)$ will resemble a step function $H(-s)$ in the integral below. So,

$$C_{R,\alpha} \sim \int_{-\infty}^{0} \Psi_\alpha(\tau + \sqrt{2}\xi) e^{\sqrt{2}\lambda_\alpha \xi} d\xi. \sim \int_{-\infty}^{-\tau/\sqrt{2}} e^{\sqrt{2}\lambda_\alpha \xi} d\xi. \tag{B.17}$$

So, performing the final integration to learn the variation of C_R with τ for $\tau > 0$,

$$C_{R,\alpha} \sim e^{-\lambda_\alpha \tau}, \tag{B.18}$$

and, using the symmetry of C_R with respect to τ,

$$C_{R,\alpha} \sim e^{-\lambda_\alpha |\tau|}. \tag{B.19}$$

So, the decorrelation time of the annular mode patterns decays exponentially with lag λ^{-1}, so long as the stochastic forcing has short memory. As shown in Chapter 7, in the steady forced problem λ should also be reflected in the slope of the response versus forcing projections. So the fluctuation-dissipation analysis suggests the decay timescale λ^{-1} may be found independently two separate ways, if indeed this analysis is appropriate to the problem.

In Chapter 7, POP analysis was used to obtain the eigenvalues of the feedback matrix and the spatial properties of the feedback. Some of the formalism is in the main body, but there I cite in Equation 7.44 results for the lagged covariances C_τ. I would like to develop those more formally here.

Recall from Chapter 7 the lagged covariance in POP space is,

$$\overline{\mathsf{C}}_\tau = \left\langle \overline{u}\left(t+\tau\right) \overline{u}^T\left(t\right) \right\rangle = \mathsf{W}^\mathsf{T} \mathsf{C}_\tau \mathsf{W}. \tag{B.20}$$

Also, Equation 7.42 describes the system in POP space for each mode α,

$$\frac{\partial \overline{u}_\alpha}{\partial t} + \lambda_\alpha \overline{u}_\alpha = \overline{f}_\alpha \tag{B.21}$$

Integrating Equation 7.42, and assuming $\overline{u}_\alpha$ goes to 0 as t goes to $-\infty$, then

$$\overline{u}_\alpha(t) = \int_{-\infty}^{t} e^{\lambda_\alpha (s-t)} \overline{f}_\alpha(s) ds. \tag{B.22}$$

Defining $\mathsf{\Gamma}_\mathsf{t}$, the diagonal matrix with elements $e^{\lambda t}$ on the diagonal, and zeros off the diagonal, this becomes

$$\overline{u}_\alpha(t) = \int_{-\infty}^{0} \mathsf{\Gamma}_s \overline{f}_\alpha(s+t) ds. \tag{B.23}$$

Now, returning to the expression for lagged covariance, I substitute for $\overline{u}_\alpha$.

$$\overline{\mathsf{C}}_\tau = \int_{-\infty}^{0} \int_{-\infty}^{0} \mathsf{\Gamma}_{s'} \left\langle \overline{f}\,(s'+t+\tau)\, \overline{f}^T\,(s''+t) \right\rangle \mathsf{\Gamma}_{s''}\; ds'\; ds'', \tag{B.24}$$

or, using $\mathsf{F}_\tau = \left\langle \overline{f}(t+\tau) \overline{f}^T(t) \right\rangle$,

$$\overline{\mathsf{C}}_\tau = \int_{-\infty}^{0} \int_{-\infty}^{0} \mathsf{\Gamma}_{s'} \mathsf{F}_{\tau+s'-s''} \mathsf{\Gamma}_{s''}\; ds'\; ds''. \tag{B.25}$$

Again, it is necessary to invoke the short decorrelation time of forcing as compared to the response patterns. If this is so, then F_τ will be nonzero only near $\tau = 0$. As a result, if $s' > -\tau$,

$$\int_{-\infty}^{0} \mathsf{F}_{\tau+s'-s''} \mathsf{\Gamma}_{s''}\; ds'' = 0. \tag{B.26}$$

But, if $s' < -\tau$,

$$\int_{-\infty}^{0} \mathsf{F}_{\tau+s'-s''} \mathsf{\Gamma}_{s''}\; ds'' = \mathsf{D}\mathsf{\Gamma}_{s'+\tau}, \tag{B.27}$$

where D is the integral of F_s over ds, from negative infinity to infinity. Since $\mathsf{\Gamma}_{s'+\tau} = \mathsf{\Gamma}_{s'}\mathsf{\Gamma}_\tau$, then if $\tau < 0$,

$$\overline{\mathsf{C}}_\tau = \int_{-\infty}^{0} \mathsf{\Gamma}_{s'} \mathsf{D} \mathsf{\Gamma}_{s'+\tau}\; ds' = \left(\int_{-\infty}^{0} \mathsf{\Gamma}_{s'} \mathsf{D} \mathsf{\Gamma}_{s'} ds' \right) \mathsf{\Gamma}_\tau. \tag{B.28}$$

Conversely, if $\tau > 0$,

$$\overline{\mathsf{C}}_\tau = \int_{-\infty}^{-\tau} \mathsf{\Gamma}_{s'} \mathsf{D} \mathsf{\Gamma}_{s'+\tau}\; ds' = \int_{-\infty}^{0} \mathsf{\Gamma}_{s''-\tau} \mathsf{D} \mathsf{\Gamma}_{s''} ds'' \tag{B.29}$$

$$\overline{\mathsf{C}}_{\tau} = \Gamma_{-\tau}\left(\int_{-\infty}^{0} \Gamma_s \mathsf{D} \Gamma_s ds\right) \tag{B.30}$$

Finally, it may be noted the expression in parentheses for the equations immediately above, for both $\tau < 0$ and $\tau > 0$, is simply equal to $\overline{\mathsf{C}}_o$, the lag-zero covariance in POP space. That, and noting that $\Gamma_{-\tau} = \Gamma_{\tau}^{-1}$, yields the equations for lagged covariance, quoted in Chapter 7.

$$\overline{\mathsf{C}}_{\tau} = \overline{\mathsf{C}}_{\mathsf{o}}\Gamma_{\tau}, \ \tau \ < \ 0 \tag{B.31}$$

$$\overline{\mathsf{C}}_{\tau} = \Gamma_{\tau}^{-1}\overline{\mathsf{C}}_{\mathsf{o}}, \ \tau \ > \ 0, \tag{B.32}$$

Returning to the discussion in Chapter 7, these equations are then used to find the matrix G, whose eigenvectors contain the principal oscillation patterns.

Bibliography

Ambaum, M. H. P., B. J. Hoskins, and D. B. Stephenson, 2001: Arctic Oscillation or North Atlantic Oscillation? *J. Climate*, **14**, 3495–3507.

Angström, A., 1935: Teleconnections of climate changes in present time. *Geog. Ann.*, **17**, 242–258.

Baldwin, M. P. and T. J. Dunkerton, 1999: Propagation of the Arctic Oscillation from the stratosphere to the troposphere. *J. Geophys. Res.*, **104**, 30,937–30,946.

— 2001: Stratospheric harbingers of anomalous weather regimes. *Science*, **294**, 581–584.

Baldwin, M. P., D. B. Stephenson, D. W. J. Thompson, T. J. Dunkerton, A. J. Charlton, and A. O'Neill, 2003: Stratospheric memory and skill of extended-range weather forecasts. *Science*, **301**, 636–640.

Barron, E. J., 1983: A warm, equable Cretaceous: The nature of the problem. *Earth Sci. Rev.*, **19**, 305–338.

Black, R. X., 2002: Stratospheric forcing of surface climate in the Arctic Oscillation. *J. Climate*, **15**, 268–277.

Bretherton, C. S., C. Smith, and J. M. Wallace, 1992: An intercomparison of methods for finding coupled patterns in climate data. *J. Climate*, **5**, 541–560.

Budyko, M. I., 1969: The effect of solar radiation on the climate of the earth. *Tellus*, **21**, 611–619.

Cash, B. A., P. J. Kushner, and G. K. Vallis, 2002: The structure and composition of the annular modes in an aquaplanet general circulation model. *J. Atmos. Sci.*, **59**, 3399–3414.

Charney, J. G. and P. G. Drazin, 1961: Propagation of planetary-scale distrurbances from the lower into the upper atmosphere. *J. Geophys. Res.*, **66**, 83–109.

Chen, G., I. M. Held, and W. A. Robinson, 2007: Senstivity of the latitude of the surface westerlies to surface friction. *J. Atmos. Sci.*, **64**, 2899–2915.

Deser, C., 2000: On the teleconnectivity of the "Arctic Oscillation". *Geophys. Res. Lett.*, **27**, 779–782.

DeWeaver, E. and S. Nigam, 2000: Zonal-eddy dynamics of the North Atlantic Oscillation. *J. Climate*, **13**, 3893–3914.

Edmon, H. J., Jr., B. J. Hoskins, and M. E. McIntyre, 1980: Eliassen-Palm cross-sections for the troposphere. *J. Atmos. Sci.*, **37**, 2600–2616.

Eliassen, A., 1951: Slow thermally or frictionally controlled meridional circulation in a circular vortex. *Astrophys. Norveg.*, **5**, 19–60.

Feldstein, S. B., 2000: The timescale, power spectra and climate noise properties of teleconnection patterns. *J. Climate*, **13**, 4430–4440.

— 2002: The recent trend and variance of the annular mode. *J. Climate*, **15**, 88–94.

Feldstein, S. B. and S. Lee, 1996: Mechanisms of zonal index variability in an aquaplanet GCM. *J. Atmos. Sci.*, **53**, 3541–3555.

— 1998: Is the atmospheric zonal index driven by an eddy feedback? *J. Atmos. Sci.*, **55**, 3077–3086.

Fyfe, J. C., G. J. Boer, and G. M. Flato, 1999: The Arctic and Antarctic Oscillations and their projected changes under global warming. *Geophys. Res. Lett.*, **26**, 1601–1604.

Gerber, E. P. and G. K. Vallis, 2005: A stochastic model for the spatial structure of annular patterns of variability and the North Atlantic Oscillation. *J. Climate*, **18**, 2102–2118.

Gerber, E. P., S. Voronin, and L. M. Polvani, 2007: A test of the intraseasonal variability in simple atmospheric general circulation models. *Mon. Wea. Rev.*, submitted.

Gillett, N. P., M. R. Allen, R. E. McDonald, C. A. Senior, D. T. Shindell, and G. A. Schmidt, 2002: How linear is the Arctic Oscillation response to greenhouse gases? *J. Geophys. Res.*, **107**, doi:10.1029/2001JD000589.

Gillett, N. P. and D. W. J. Thompson, 2003: Simulation of recent Southern Hemisphere climate change. *Science*, **302**, 273–275.

Gong, D. and S. Wang, 1999: Definition of Antarctic Oscillation index. *Geophys. Res. Lett.*, **26**, 459–462.

Gritsun, A. and G. Branstator, 2007: Climate response using a three-dimensional operator based on the fluctuation-dissipation theorem. *J. Atmos. Sci.*, **64**, 2558–2575.

Hartley, D. E., J. T. Villarin, R. X. Black, and C. A. Davis, 1998: A new perspective on the dynamical link between the stratosphere and the troposphere. *Nature*, **391**, 471–474.

Hartmann, D. L. and F. Lo, 1998: Wave-driven zonal flow vacillation in the Southern Hemisphere. *J. Atmos. Sci.*, **55**, 1303–1315.

Haynes, P. H., C. J. Marks, M. E. McIntyre, T. G. Shepherd, and K. G. Shine, 1991: On the "downward control" of extratropical diabatic circulations by eddy-induced mean zonal forces. *J. Atmos. Sci.*, **48**, 651–678.

Haynes, P. H. and T. G. Shepherd, 1989: The importance of surface pressure changes in the response of the atmosphere to zonally-symmetric thermal and mechanical forcing. *Quart. J. Roy. Meteor. Soc.*, **115**, 1181–1208.

Held, I. M. and M. J. Suarez, 1994: A proposal for the intercomparison of the dynamical cores of atmospheric general circulation models. *Bull. Amer. Meteor. Soc.*, **75**, 1825–1830.

Holton, J. R., 1992: *An introduction to dynamic meteorology*. Academic Press, San Diego.

IPCC, 2001a: *Climate Change 2001: Impacts, adaptation, and vulnerability*. Cambridge Univeristy Press, Cambridge.

— 2001b: *Climate Change 2001: The scientific basis*. Cambridge Univeristy Press, Cambridge.

Karoly, D. J., 1990: The role of transient eddies in low-frequency zonal variations of the Southern Hemisphere circulation. *Tellus*, **42A**, 41–50.

Kidson, J. W., 1988a: Indices of the Southern Hemisphere zonal wind. *J. Climate*, **1**, 183–194.

— 1988b: Interannual variations in the Southern Hemisphere circulation. *J. Climate*, **1**, 1177–1198.

Kodera, K. and H. Koide, 1997: Spatial and seasonal characteristics of recent decadal trends in the northern hemispheric troposphere and stratosphere. *J. Geophys. Res.*, **102**, 19,433–19,447.

Kodera, K., K. Yamazaki, M. Chiba, and K. Shibata, 1990: Downward propagation of upper stratospheric mean zonal wind perturbation to the troposphere. *Geophys. Res. Lett.*, **17**, 1263–1266.

Kuroda, Y. and K. Kodera, 1999: Role of planetary waves in the stratosphere-troposphere coupled variability in the Northern Hemisphere winter. *Geophys. Res. Lett.*, **26**, 2375–2378.

Kushner, P. J., I. M. Held, and T. L. Delworth, 2001: Southern Hemisphere atmospheric circulation response to global warming. *J. Climate*, **14**, 2238–2249.

Kushner, P. J. and L. M. Polvani, 2004: Stratosphere-troposphere coupling in a relatively simple AGCM: The role of eddies. *J. Climate*, **17**, 629–639.

Lee, S. and S. B. Feldstein, 1996: Mechanism of zonal index evolution in a two-layer model. *J. Atmos. Sci.*, **53**, 2232–2246.

Leith, C. E., 1975: Climate response and fluctuation dissipation. *J. Atmos. Sci.*, **32**, 2022–2026.

Limpasuvan, V. and D. L. Hartmann, 2000: Wave-maintained annular modes of climate variability. *J. Climate*, **13**, 4414–4429.

Loewe, F., 1937: A period of warm winters in western Greenland and the temperature see-saw between western Greenland and Europe. *Quart. J. Roy. Meteor. Soc.*, **63**, 365–371.

Lorenz, D. J. and D. L. Hartmann, 2001: Eddy-zonal flow feedback in the Southern Hemisphere. *J. Atmos. Sci.*, **58**, 3312–3327.

— 2003: Eddy-zonal flow feedback in the Northern Hemisphere winter. *J. Climate*, **16**, 1212–1227.

Lorenz, E. N., 1951: Seasonal and irregular variations of the Northern Hemisphere sea-level pressure profile. *J. Atmos. Sci.*, **8**, 52–59.

Majda, A. J., R. V. Abramov, and M. J. Grote, 2005: *Information theory and stochastics for multiscale nonlinear systems (CRM monograph series 25)*. American Mathematical Society.

Marshall, J., Y. Kushnir, D. Battisti, P. Chang, A. Czaja, R. Dickson, J. Hurrell, M. McCartney, R. Saravanan, and M. Visbeck, 2001: North Atlantic climate variability: phenomena, impacts, and mechanisms. *Int. J. Clim.*, **21**, 1863–1898.

Matsuno, T., 1970: Vertical propagation of stationary planetary waves in the winter Northern Hemisphere. *J. Atmos. Sci.*, **27**, 871–883.

Namias, J., 1950: The index cycle and its role in the general circulation. *J. Atmos. Sci.*, **7**, 130–139.

North, G. R., T. L. Bell, R. F. Cahalan, and F. J. Moeng, 1982: Sampling errors in the estimation of empirical orthogonal functions. *Mon. Wea. Rev.*, **110**, 699–706.

Osborn, T. J., K. R. Briffa, S. F. B. Tett, P. D. Jones, and R. M. Trigo, 1999: Evaluation of the North Atlantic Oscillation as simulated by a coupled climate model. *Clim. Dyn.*, **15**, 685–702.

Penland, C., 1989: Random forcing and forecasting using principal oscillation analysis. *Mon. Wea. Rev.*, **117**, 2165–2185.

Perlwitz, J. and N. Harnik, 2003: Observational evidence of a stratospheric influence on the troposphere by planetary wave reflection. *J. Climate*, **16**, 3011–3026.

Plumb, R. A., 1982: Zonally symmetric Hough modes and meridional circulations in the middle atmosphere. *J. Atmos. Sci.*, **39**, 983–991.

Plumb, R. A. and K. Semeniuk, 2003: Downward migration of extratropical zonal wind anomalies. *J. Geophys. Res.*, **108**, doi: 10.1029/2002JD002773.

Polvani, L. M. and P. J. Kushner, 2002: Tropospheric response to stratospheric perturbations in a relatively simple general circulation model. *Geophys. Res. Lett.*, **29**, doi:10.1029/2001GL014284.

Rind, D., P. Lonergan, N. K. Balachandran, and D. Shindell, 2002: $2\times CO_2$ and solar variability influences on the troposphere through wave-mean flow interactions. *J. Met. Soc. Japan*, **80**, 863–876.

Rind, D., J. Perlwitz, P. Lonergan, and J. Lerner, 2005: AO/NAO response to climate change: 2. Relative importance of low- and high- latitude temperature changes. *J. Geophys. Res.*, **110**, doi:10.1029/2004JD005686.

Robinson, W. A., 1994: Eddy feedbacks on the zonal index and eddy-zonal flow interactions induced by zonal flow transience. *J. Atmos. Sci.*, **51**, 2553–2562.

— 1996: Does eddy feedback sustain variability in the zonal index? *J. Atmos. Sci.*, **53**, 3556–3569.

— 2000: A baroclinic mechanism for the eddy feedback on the zonal index. *J. Atmos. Sci.*, **57**, 415–422.

Rogers, J. C. and H. van Loon, 1982: Spatial variability of sea level pressure and 500 mb height anomalies over the Southern Hemisphere. *Mon. Wea. Rev.*, **110**, 1375-1392.

Rossby, C.-G., 1939: Relations between variations in the intensity of the zonal circulation of the atmosphere and displacements of the semipermanent centers of action. *J. Mar. Res.*, **2**, 38–55.

Sellers, W. D., 1969: A global climatic model based on the energy balance of the earth atmosphere system. *J. Appl. Meteor.*, **8**, 391–400.

Shindell, D. T., R. L. Miller, G. A. Schmidt, and L. Pandolfo, 1999: Simulation of recent northern winter climate trends by greenhouse-gas forcing. *Nature*, **399**, 452–455.

Shindell, D. T., G. A. Schmidt, R. L. Miller, and D. Rind, 2001: Northern Hemisphere winter climate response to greenhouse gas, ozone, solar, and volcanic forcing. *J. Geophys. Res.*, **106**, 7193–7210.

Shiotani, M., 1990: Low-frequency variations of the zonal mean state of the Southern Hemisphere troposphere. *J. Met. Soc. Japan*, **68**, 461–471.

Simmons, A. J. and D. M. Burridge, 1981: An energy and angular-momentum conserving vertical finite-difference scheme and hybrid vertical coordinates. *Mon. Wea. Rev.*, **109**, 758–766.

Son, S. W. and S. Lee, 2005: The response of westerly jets to thermal driving in a primitive equation model. *J. Atmos. Sci.*, **62**, 3741–3757.

— 2006: Preferred modes of variability and their relationship with climate change. *J. Climate*, **19**, 2063–2075.

Song, Y. and W. A. Robinson, 2004: Dynamical mechanisms for stratospheric influences on the troposphere. *J. Atmos. Sci.*, **61**, 1711–1725.

Szeredi, I. and D. J. Karoly, 1987: The horizontal structure of monthly fluctuations of the Southern Hemisphere troposphere station data. *Aust. Met. Mag.*, **35**, 119–129.

Thompson, D. W. J., J. C. Furtado, and T. G. Shepherd, 2006: On the tropospheric response to anomalous stratospheric wave drag and radiative heating. *J. Atmos. Sci.*, **63**, 2616–2629.

Thompson, D. W. J. and S. Solomon, 2002: Interpretation of recent Southern Hemisphere climate change. *Science*, **296**, 895–899.

Thompson, D. W. J. and J. M. Wallace, 1998: The Arctic Oscillation signature in the wintertime geopotential height and temperature fields. *Geophys. Res. Lett.*, **25**, 1297–1300.

— 2000: Annular modes in the extratropical circulation. Part I: Month-to-month variability. *J. Climate*, **13**, 1000–1016.

Thompson, D. W. J., J. M. Wallace, and G. C. Hegerl, 2000: Annular modes in the extra-tropical circulation. Part II: Trends. *J. Climate*, **13**, 1018–1036.

Vallis, G. K., E. P. Gerber, P. J. Kushner, and B. A. Cash, 2004: A mechanism and simple dynamical model of the North Atlantic Oscillation and annular modes. *J. Atmos. Sci.*, **61**, 264–280.

von Storch, H., T. Bruns, I. Fischer-Bruns, and K. Hasselmann, 1988: Principal oscillation pattern analysis of the 30- to 60-day oscillation in general circulation model equatorial troposphere. *J. Geophys. Res.*, **93**, 11,022–11,036.

Walker, G. T., 1924: Correlation of seasonal variations in weather IX: A further study of world weather. *Mem. Indian Meteor. Dep.*, **24**, 275–332.

Walker, G. T. and E. W. Bliss, 1932: World Weather V. *Mem. R. Meteorol. Soc. IV*, **36**, 53–84.

Wallace, J. M., 2000: North Atlantic Oscillation/annular mode: Two paradigms — one phenomenon. *Quart. J. Roy. Meteor. Soc.*, **126**, 791–805.

Wallace, J. M. and D. S. Gutzler, 1981: Teleconnections in the geopotential height field during the Northern Hemisphere winter. *Mon. Wea. Rev.*, **109**, 784–812.

Wallace, J. M. and D. W. J. Thompson, 2002: The Pacific center of action of the Northern Hemisphere annular mode: Real or artifact? *J. Climate*, **15**, 1987–1991.

Yoden, S., M. Shiotani, and I. Hirota, 1987: Multiple planetary flow regimes in the Southern Hemisphere. *J. Met. Soc. Japan*, **65**, 571–586.

Yu, J.-Y. and D. L. Hartmann, 1993: Zonal flow vacillation and eddy forcing in a simple GCM of the atmosphere. *J. Atmos. Sci.*, **50**, 3244–3259.

Zorita, E. and F. Gonzales-Rouco, 2000: Disagreement between predictions of the future behavior of the Arctic Oscillation as simulated in two different climate models: Implications for global warming. *Geophys. Res. Lett.*, **27**, 1755–1758.